UNIVERSIDADE DO ALGARVE

Faculdade de Ciências e Tecnologia

Dynamics of resonant tunneling diode optoelectronic oscillators

Bruno Miguel Patarata Romeira

Doutoramento em Física

2012

UNIVERSIDADE DO ALGARVE

Faculdade de Ciências e Tecnologia

Dynamics of resonant tunneling diode optoelectronic oscillators

Bruno Miguel Patarata Romeira

Advisory Committee/Tese orientada por:

Prof. Doutor José M. L. Figueiredo, Universidade do Algarve

Prof. Doutor Charles N. Ironside, University of Glasgow

Prof. Doutor José M. Quintana, University of Seville

Doutoramento em Física

2012

Title/Título: Dynamics of resonant tunneling diode optoelectronic oscillators

Author/Autor: Bruno Miguel Patarata Romeira

Host institutions/Instituições de acolhimento:

Centro de Eletrónica Optoeletrónica e Telecomunicações (CEOT), Departamento de Física, Universidade do Algarve, Portugal

School of Engineering, University of Glasgow, United Kingdom

Microelectronics Institute of Seville (IMSE-CNM), University of Seville, Spain

Dissertation submitted to the Faculty of Science and Technology of the Universidade do Algarve in partial fulfillment of the requirements for the degree of Doctor in Physics and the title of European Doctorate.

Dissertacão apresentada à Faculdade de Ciências e Tecnologia da Universidade do Algarve para cumprimento dos requisitos necessários à obtencão do grau de Doutor em Física e o título de Doutoramento Europeu.

Apoio financeiro da Fundação para a Ciência e Tecnologia (FCT), Portugal, bolsa de doutoramento SFRH/BD/43433/2008. Financiamento comparticipado pelo Programa Operacional Potencial Humano/Fundo Social Europeu (POPH/FSE) e por fundos nacionais do MCTES.

FCT Fundação para a Ciência e a Tecnologia
MINISTÉRIO DA EDUCAÇÃO E CIÊNCIA

POPH PROGRAMA OPERACIONAL POTENCIAL HUMANO

QREN QUADRO DE REFERÊNCIA ESTRATÉGICO NACIONAL PORTUGAL 2007.2013

UNIÃO EUROPEIA
Fundo Social Europeu

I would like to dedicate this thesis to my loving parents Adelaide and Luís, to my sister Milene, and to Inês.

Esta tese é dedicada aos meus pais, Adelaide e Luís, à minha irmã Milene e à Inês.

Acknowledgements

I would like to thank all those whose support and advice in the past few years made the realization of this work possible. Without their assistance it would have been very difficult for me to achieve the objectives of this project. In particular, I would like to express my immense gratitude to my supervisor Prof. José Figueiredo, for offering me the opportunity to carry out research and his continuous belief in this work. I will always remember the long afternoon discussions and brainstorming ideas that came out from our meetings that helped me to become a more independent researcher.

I wish to express my sincere appreciation to my co-supervisor Prof. Charlie Ironside for accepting me as a visiting PhD student at his research group at the Optoelectronics Group of the University of Glasgow. I am particularly grateful to Prof. Ironside for his insightful guidance and to share with me his exciting scientific ideas. I also would like to thank my co-supervisor Prof. José Quintana for receiving me at the Microelectronics Institute of Seville (IMSE-CNM), and for his help and important contribution to the work on numerical simulation of circuit topologies using resonant tunneling diodes.

I would like to express my appreciation to people working at Centro de Electrónica, Optoelectrónica e Telecomunicações (CEOT) and Departamento de Física of the Universidade do Algarve. I thank Prof. Robertus Potting at the Physics Department, and the directors of CEOT, Prof. Henrique Gomes, Prof. Carmo Medeiros, and more recently Prof. Rui Guerra, for providing me the institutional support as a graduate junior researcher and as a PhD student. A special thank to my friend Hugo Silva for useful discussions in many topics, particularly on low-dimension nanostructures. I also thank the technicians from the Departamento de Física, Paulo Silva and Mário Freitas, and lecturers, colleagues, and friends in the FCT faculty that supported my work or who were nice friends around, Ana Carolina, Vitor Cunha, Ana Cavaco, Artur Neves (and the tea break), Ricardo Avó, Peter Stallinga, José Argain, Custódia Fonseca, José Rodrigues, José Mariano, José do Carmo... thank you all... I am sorry if I forgot someone.

ACKNOWLEDGEMENTS

During my visits to the Optoelectronics Research Group of the Glasgow University, I have received help from a number of people around me from the very start. A special thank to Dr Thomas Slight, who shared with me his knowledge on optoelectronic devices employing resonant tunneling devices, from the basics to the tips and tricks. I thank Liquan Wang (Leo) and Dr Edward Wasige for their contributions and useful discussions on the stability of resonant tunneling devices, Dr Tony Kelly for helping me in the lab during the characterization of devices, and Dr Chong Li, Dr Ata Khalid, and Dr Gary Ternent for our discussions on negative differential resistance devices. Thanks to Dr Kris Seunarine for his contribution to the work, particularly in the fabrication of RTD devices with photo-detection capabilities by the end of my PhD. I also thank Dr Horacio who shared with me his knowledge and experience on the design, implementation, and characterization of high speed electronic circuits, and Dr Julien Javaloyes for his help and important contribution to the work on the numerical simulation methods of time-delayed systems. I thank the technical support staff of the Department of Engineering, and I would like to express my gratitude to all the other lecturers, researchers, colleagues and friends within the Optoelectronics Group, Barry, Gabor, Philippe, Moss, Piotr, Pepe, Sonia, Jehan, Chidi, Vincenzo, Carla, Corrie, Marc Sorel, Lianping, Marco, Piero... I am sorry if someone's missing.

I am grateful to Prof. Henrique Salgado for receiving me at the Optoelectronics and Telecommunications laboratory in the Institute for Systems and Computer Engineering (INESC) of Porto. I would like to express my gratitude to all the PhD and PostDoctoral researchers within the Optoelectronics and Telecommunications research group, namely Luís Pessoa, Mário (Pico), Sérgio, and João Oliveira, who shared with me their knowledge and experience on several aspects of telecommunication systems. I am also extremely grateful to Prof. Paulo Monteiro and Filipe Ferreira for receiving me at the research facilities of Nokia Siemens Networks, in Lisbon-Amadora. As a young researcher, it was a privilege to experience the environment of such an international recognized R&D Center.

I am extremely grateful to my supervisor José Figueiredo for providing the pre-existing material and resonant tunnelling diode optical waveguide devices, without which this work couldn't be possible, and also to Essient Photonics, Scotland, for providing the pre-existing material utilized in the fabrication of resonant tunnelling diode photo-detector devices by the end of my PhD project. I also thank Dr Wyn Meredith from Compound Semiconductor Technologies Global Ltd., Scotland, for providing the laser diode commercial prototype devices.

I am in debt with Fundação para a Ciência e Tecnologia for their funding of my

doctoral years (SFRH/BD/43433/2008), conference attendances, and of the research project WOWi - wireless-optical-wireless interfaces for picocellular access networks (PTDC/EEA-TEL/100755/2008). I am very grateful for the opportunity to attend national and international recognized conferences. Most of them could not be possible to attend without the financial support of the following institutions: Calouste Gulbenkian Foundation, Luso-American Development Foundation (FLAD), IEEE LEOS Student Travel Grant from the Photonics Society (formerly LEOS society), USA, and the European Physical Society, France.

I am also extremely grateful with Calouste Gulbenkian Foundation, Portugal, for the "2009 Young Researchers Incentive Programme" award, and with IEEE Photonics Society, USA, for the "2011 IEEE Photonics Society Graduate Student Fellowship".

On a personal note, I would like to express my deep appreciation to my friends, particularly my friends from D&A and ACF-Fuseta, Domingos, Carlinhos, Bruno Bx, Btr, Gustavo, Silvio... we had really crazy and stressful moments, also to my friends Ângelo, Liliana, Vera, and Marta, to my parents and my sister, who supported me, and to Inês for her patience and for being always by my side.

ACKNOWLEDGEMENTS

Abstract

The nonlinear dynamics of optoelectronic integrated circuit (OEIC) oscillators comprising semiconductor resonant tunneling diode (RTD) nanoelectronic quantum devices has been investigated. The RTD devices used in this study oscillate in the microwave band frequency due to the negative differential conductance (NDC) of their nonlinear current voltage characteristics, which is preserved in the optoelectronic circuit. The aim was to study RTD circuits incorporating laser diodes and photo-detectors to obtain novel dynamical operation regimes in both electrical and optical domains taking advantage of RTD's NDC characteristic.

Experimental implementation and characterization of RTD-OEICs was realized in parallel with the development of computational numerical models. The numerical models were based on ordinary and delay differential equations consisting of a Liénard's RTD oscillator and laser diode single mode rate equations that allowed the analysis of the dynamics of RTD-OEICs. In this work, several regimes of operation are demonstrated, both experimentally and numerically, including generation of voltage controlled microwave oscillations and synchronization to optical and electrical external signals providing stable and low phase noise output signals, and generation of complex oscillations that are characteristic of high-dimensional chaos.

Optoelectronic integrated circuits using RTD oscillators are interesting alternatives for more efficient synchronization, generation of stable and low phase noise microwave signals, electrical/optical conversion, and for new ways of optoelectronic chaos generation. This can lead to simplification of communication systems by boosting circuits speed while reducing the power and number of components. The applications of RTD-OEICs include operation as optoelectronic voltage controlled oscillators in clock recovery circuit systems, in wireless-photonics communication systems, or in secure communication systems using chaotic waveforms.

ABSTRACT

Keywords: laser diodes, nonlinear systems, optoelectronic circuits, oscillators, photo-detectors, resonant tunneling diodes, synchronization.

Resumo

Este trabalho consistiu no estudo da dinâmica não-linear de circuitos osciladores opto-electrónicos integrados constituídos por dispositivos semicondutores nano-electrónicos quânticos, os díodos de efeito túnel ressonantes (RTD, acrónimo de "Resonant Tunneling Diode").

Os dispositivos RTD utilizados neste trabalho oscilam na banda de frequências das microndas devido à condutância diferencial negativa intrínseca ao RTD, apresentando no seu funcionamento eléctrico uma elevada não-linearidade, a qual é preservada no circuito opto-electrónico. O objetivo foi estudar os osciladores RTD integrados com díodos de laser e foto-detectores para obter novos regimes de funcionamento nos domínios eléctrico e óptico utilizando os métodos de perturbação externa injecção eléctrica e óptica e realimentação optoelectrónica. Quando o oscilador é perturbado externamente é possivel obter sincronização, geração de portadoras caóticas e geração de oscilações estáveis controladas por tensão na banda de frequências das microondas e com uma melhoria significativa do ruído de fase.

O comportamento opto-electrónico não-linear observado é descrito por um sistema dinâmico de equações diferenciais equivalente a um oscilador forçado de Liénard associado às equações das taxas do laser de díodo. O modelo constitui um exemplo da teoria de sistemas não-lineares e explica os regimes de funcionamento registados.

Os circuitos opto-eletrónicos semicondutores integrados empregando osciladores RTD fornecem soluções para a simplificação e redução do consumo de energia dos sistemas de comunicação devido à sincronização, conversão elétrica/óptica mais eficiente e melhoria substancial do ruído de fase dos sinais microondas gerados. Para além disso, é possível obter novas funcionalidades, como por exemplo, a geração de portadoras caóticas ópticas e eléctricas, utilizando um número reduzido de componentes. As aplicações dos dispositivos opto-electrónicos incluem o seu uso em redes de nova geração de rádio sobre fibra para a conversão de sinais microondas para o domínio óptico e vice-versa, a implementação de circuitos para aplicações digitais de recuperação

do relógio tirando vantagem das características de sincronização e a implementação de novos sistemas de comunicação tirando partido dos sinais ópticos e eléctricos caóticos na transmissão de informação confidencial.

Palavras chave: circuitos opto-electrónicos, díodos de efeito túnel ressonantes, foto-detectores, lasers de díodo, osciladores, sincronização, sistemas não-lineares.

List of Publications

During the course of this project, a number of book chapters, journal papers, conference proceedings, and public presentations have been made which are based on the work presented in this thesis. They are listed here for reference.

Book Chapters

- **B. Romeira**, J. M. L Figueiredo, C. N. Ironside, and J. Javaloyes (2013). "Dynamics of Liénard Optoelectronic Oscillators," Book Chapter In: Selected Topics in Nonlinear Dynamics and Theoretical Electrical Engineering, Kyandoghere Kyamakya, Wolfgang A. Halang, Wolfgang Mathis, Jean Camberlain Chedjou, and Zhong Li (Eds.), Studies in Computational Intelligence, Vol. 459, ISBN 978-3-642-34559-3, Springer Berlin/Heidelberg.

- J. M. L. Figueiredo, **B. Romeira**, T. J. Slight, and C. N. Ironside (2010). "Resonant Tunnelling Optoelectronic Circuits," Book Chapter In: Advances in Optical and Photonic Devices, Ki Young Kim (Ed.), ISBN 978-953-7619-76-3, InTech.

- **B. Romeira** and J. M. L Figueiredo (2010). "Optoelectronic oscillators for communication systems," *Emerging Trends in Technological Innovation*, Camarinha-Matos, Luis M.; Pereira, Pedro; Ribeiro, Luis (Eds.), IFIP International Federation for Information Processing, Vol. 314, ISBN: 978-3-642-11627-8, Springer Berlin/Heidelberg.

Peer reviewed journal papers

- H. I. Cantú, **B. Romeira**, A. E. Kelly, C. N. Ironside, and J. M. L. Figueiredo, "Modulation accuracy of binary phase-shift keying signal broadcast after injection

locking of a resonant tunnelling diode microwave oscillator," to be published in *Microw. Opt. Techn. Let.*.

- **B. Romeira**, J. Javaloyes, J. M. L. Figueiredo, C. N. Ironside, H. I. Cantú, and A. E. Kelly, "Delayed Feedback Dynamics of Linard-type Resonant Tunneling-Photo-Detector Optoelectronic Oscillators," *IEEE J. Quantum Electron.*, vol. 49, no. 1, pp. 31-42, 2013.

- H. I. Cantú, **B. Romeira**, A. E. Kelly, C. N. Ironside, and J. M. L. Figueiredo, "Resonant tunneling diode optoelectronic integrated circuits applications in radio over fiber networks," *IEEE Trans. Microw. Theory Tech.*, vol. 60, no. 9, pp. 2903-1912, 2012.

- **B. Romeira**, K. Seunarine, C. N. Ironside, A. E. Kelly, and J. M. L. Figueiredo, "A self-synchronized optoelectronic oscillator based on an RTD photo-detector and a laser diode," *IEEE Photonics Technol. Lett.*, vol. 23, no. 16, pp. 1148-1150, 2011.

- **B. Romeira**, J. M. L. Figueiredo, C. N. Ironside, A. E. Kelly, and T. J. Slight, "Optical control of a resonant tunneling diode microwave-photonic oscillator," *IEEE Photon. Technol. Lett.*, vol. 22, no. 21, pp. 1610–1612, 2010.

- **B. Romeira**, J. M. L. Figueiredo, C. N. Ironside, and T. J. Slight, "Chaotic dynamics in resonant tunneling optoelectronic voltage controlled oscillators," *IEEE Photon. Technol. Lett.*, vol. 21, no. 24, pp. 1819–1821, 2009.

- **B. Romeira**, J. M. L. Figueiredo, T. J. Slight, L. Wang, E. Wasige, C. N. Ironside, A. E. Kelly, and R. Green, "Nonlinear dynamics of resonant tunneling optoelectronic circuits for wireless/optical interfaces," *IEEE J. Quantum Electron.*, vol. 45, no. 11, pp. 1436–1445, 2009.

Peer reviewed conference proceedings (oral communications)

- **B. Romeira**, J. M. L. Figueiredo, C. N. Ironside, K. Seunarine, and J. Javaloyes, "Nonlinear dynamics of a Liénard delayed-feedback optoelectronic oscillator," *Joint conference Third International Workshop on Nonlinear Dynamics and*

Synchronization (INDS'11) and Sixteenth International Symposium on Theoretical Electrical Engineering (ISTET'11), Session: Nonlinear Dynamics, chaos and Synchronization - 2, Klagenfurt, Austria, July 25-27, 2011.

- **B. Romeira**, L. M. Pessoa, H. M. Salgado, S. Silva, and J. M. L. Figueiredo, "Clock recovery of an injection-locked resonant runneling diode microwave photonics oscillator," *13th International Conference on Transparent Optical Networks (ICTON 11)*, paper We.C5.6, Stockholm, Sweden, June 26-30, 2011.

- **B. Romeira**, K. Seunarine, C. N. Ironside, J. Javaloyes, A. E. Kelly, and J. M. L. Figueiredo, "A Liénard optoelectronic oscillator with time-delayed feedback," *The European Conference on Lasers and Electro-Optics (CLEO) and the European Quantum Electronics Conference (EQEC) Conference Digest, OSA Technical Digest (CD) (Optical Society of America, 2011)*, paper CI3.2, Munich, Germany, May 22-26, 2011.

- C. N. Ironside, M. Haji, L. Hou, J. Akbar, A. E. Kelly, K. Seunarine, **B. Romeira**, and J. M. L. Figueiredo, "Review of optoelectronic oscillators based on mode-locked lasers and resonant tunneling diode optoelectronics," *International Conference on Applications of Optics and Photonics (AOP11)*, Proc. SPIE 8001, 80011Q, Braga, Portugal, May 3-7, 2011.

- **B. Romeira**, J. M. L Figueiredo, K. Seunarine, and C. N. Ironside, "Optoelectronic oscillator topologies based on resonant tunneling diode fiber optic links," *International Conference on Applications of Optics and Photonics (AOP11)*, Proc. SPIE 8001, 80011T, Braga, Portugal, May 3-7, 2011.

- **B. Romeira**, K. Seunarine, C. N. Ironside, A. E. Kelly, T. J Slight, and J. M. L. Figueiredo, "An optoelectronic oscillator based on a resonant tunneling diode photo-detector integrated chip," *The 23rd Annual Meeting of the IEEE Photonics Society*, paper MD4, Denver, Colorado, USA, 7-11 November, 2010.

- C. N. Ironside, **B. Romeira**, K. Seunarine, , A. E. Kelly, T. J Slight, and J. M. L. Figueiredo, "Applications of laser diode sources with integrated resonant tunnelling diode technology," *Photonex2010 - Industry Programme*, C6: Novel Sources and detectors, Telford, UK, 3-4 November 2010.

- **B. Romeira**, T. J. Slight, A. E. Kelly, C. N. Ironside, and J. M L Figueiredo, "Microwave photonic oscillators for femtocellular access networks," *15th European*

Conference on Networks and Optical Communications (NOC 2010), Components and modulation strategies, Faro-Algarve, Portugal, 8-10 June, 2010.

- **B. Romeira**, J. M. L. Figueiredo, C. N. Ironside, A. E. Kelly, and T. J. Slight, "Optical injection locking of a resonant tunneling diode - optical waveguide photodetector," *15th European Conference on Integrated Optics (ECIO 2010)*, paper ThF4, Cambridge, United Kingdom, April 7-9, 2010.

- C. N. Ironside, J. M. L. Figueiredo, **B. Romeira**, T. J. Slight, L. Wang, and E. Wasige, "Resonant tunneling diode opto-electronic integrated circuits," *SPIE Photonics West 2010*, Nanotechnologies in Photonics: Quantum Sensing and Nanophotonic Devices VII, Session 4: Quantum Structures and Devices I, Proceedings of SPIE Volume 7608-17, San Francisco, CA, USA, 23-28 January, 2010.

- **B. Romeira**, J. M. L. Figueiredo, T. J. Slight, L. Wang, E. Wasige, and C. N. Ironside, "Wireless injection locking and phase noise reduction in a semiconductor laser driven by a resonant tunnelling diode nonlinear oscillator," *The European Conference on Lasers and Electro-Optics and the XIth European Quantum Electronics Conference (CLEO/Europe-EQEC)*, paper CI3.1, Munich, Germany, June 14-19, 2009.

- **B. Romeira**, J. M. L. Figueiredo, T. J. Slight, L. Wang, E. Wasige, and C. N. Ironside, "Wireless/photonics interfaces based on resonant tunneling diode optoelectronic oscillators," *Conference on Lasers and Electro-Optics (CLEO)/The International Quantum Electronics Conference (IQEC) (Optical Society of America, Washington, DC, 2009)*, paper CTuT4, Baltimore, Maryland, USA, May 31-June 5, 2009.

- J. M. L. Figueiredo, C. N. Ironside, **B. Romeira**, T. J. Slight, L. Wang, and E. Wasige, "Wireless-photonics-wireless interfaces based on resonant tunneling diode optoelectronic oscillators," *European workshop on photonics solutions for wireless, access, and in-house networks*, session 4: Radio-over-Fibre techniques, Duisburg, Germany, May 18-20, 2009.

- C. N. Ironside, J. M. L. Figueiredo, **B. Romeira**, T. J. Slight, E. Wasige, and L. Wang, "The resonant tunneling diode-laser diode optoelectronic integrated circuit operating as a voltage controlled oscillator," *SPIE Microtechnologies for the New Millennium*, Photonic Materials, Devices and Applications, session 8B:

Photonic Devices, Proceedings of SPIE Volume 7366-39, Dresden, Germany, May 4-6, 2009.

- **B. Romeira**, J. M. L. Figueiredo, T. J. Slight, L. Wang, E. Wasige, and C. N. Ironside, "Wireless to optical frequency locking and chaos using a resonant tunnelling - laser diode circuit," *IEEE/LEOS Winter Topicals Meeting Series (WIN 09)*, paper MB3.4, pp. 128-129, Innsbruck, Austria, January 12-14, 2009.

Peer reviewed conference proceedings (posters)

- H. I. Cantú, **B. Romeira**, K. Seunarine, A. E. Kelly, C. N. Ironside, and J. M. L. Figueiredo, "Conversion of phase modulated signals from optical network to wireless domain using resonant tunneling diode optoelectronic integrated circuits," *The Optical Fiber Communication Conference and Exposition and the National Fiber Optic Engineers Conference (OFC/NFOEC'12), OSA Technical Digest (Optical Society of America, 2012)*, paper JTh2A.19, Los Angeles, CA, USA, March 4-8, 2012.

Other Communications and Symposia

- **B. Romeira**, J. M. L. Figueiredo, and C. N. Ironside, "An Optoelectronic Resonant Tunneling Diode Oscillatory Circuit with an Optical Fiber Delayed Feedback," *The IEEE Photonics Society GOLD Session, IEEE Photonics Society Annual Conference 2011*, GOLD Poster Presentations, Arlington, Virginia, USA, 9th October 2011 (poster).

- J. M. L. Figueiredo, **B. Romeira**, T. J. Slight, and C. N. Ironside, "Microwave-photonic oscillators for radio-over-fibre access networks," *VIII Symposium On Enabling Optical Networks and Sensors (SEON 10)*, Porto, Portugal, 2010 (Symposium).

LIST OF PUBLICATIONS

List of Patents

During the course of this project, a number of national and international patent applications have been filled based on the work presented in this thesis. They are listed here for reference.

- Title: Methods and systems for optoelectronic oscillators; Patent application No: 104973, University of Algarve, Portugal; Inventor(s): **B. Romeira**, J. M. L. Figueiredo, C. N. Ironside, and T. J. Slight (submitted in February 17, 2010).
- Title: Interfaces and methods for wireless-optical and optical-wireless conversion; Publication No(s): GB2465184, WO/2010/052481; International Publication No.: PCT/GB2009/002637; Inventor(s): **B. Romeira**, J. M. L. Figueiredo, C. N. Ironside, and T. J. Slight (published in May 5, 2010).

Previous Publications

Before the course of this project, a number of journal papers, conference proceedings, and public presentations have been made which are related with the work presented in this thesis. They are listed here for reference.

Peer reviewed journal papers

- **B. Romeira**, J. M. L. Figueiredo, T. J. Slight, L. Wang, E. Wasige, C. N. Ironside, J. M. Quintana, and M. J. Avedillo, "Synchronisation and chaos in a laser diode driven by a resonant tunneling diode," *IET Optoelectron.*, vol. 2, no. 6, pp. 211–215, 2008.

- T. J. Slight, **B. Romeira**, L. Wang, J. M. L. Figueiredo, E. Wasige, and C. N. Ironside, "A Liénard oscillator resonant tunnelling-laser diode hybrid integrated circuit: model and experiment," *IEEE J. Quantum Electron.*, vol. 44, no. 12, pp. 1158–1163, 2008.

- J. M. L. Figueiredo, **B. Romeira**, T. J. Slight, L. Wang, E. Wasige, and C. N. Ironside, "Self-oscillation and period adding from a resonant tunnelling diode - laser diode circuit," *Electron. Lett.*, vol. 44, no. 14, pp. 876–878, 2008.

Peer reviewed conference proceedings (oral communications)

- **B. Romeira**, J. M. L. Figueiredo, T. J. Slight, L. Wang, E. Wasige, and C. N. Ironside, "Synchronizing optical to wireless signals using a resonant tunneling diode laser diode circuit," *21st Annual Meeting of the IEEE Lasers and Electro-Optics Society (LEOS 08)*, paper TuB1, pp. 145-146, Newport Beach, CA, USA, November 9-13, 2008.

- **B. Romeira**, J. M. L. Figueiredo, T. J. Slight, L. Wang, E. Wasige, and C. N. Ironside, "Optoelectronic integration of a resonant tuneling diode and a laser diode," *14th European Conference on Integrated Optics (ECIO 08)*, paper WeB4, pp. 41-44, Eindhoven, Netherlands, June 11-13, 2008.

- **B. Romeira**, J. M. L. Figueiredo, T. J. Slight, L. Wang, E. Wasige, C. N. Ironside, J. M. Quintana, and M. J. Avedillo, "Observation of frequency division and chaos behavior in a laser diode driven by a resonant tunneling diode," *Conference on Lasers and Electro-Optics (CLEO)/Quantum Electronics and Laser Science Conference and Photonic Applications Systems Technologies (QELS) (Optical Society of America, Washington, DC, 2008)*, paper CMY5, pp. 766-767, San Jose, CA, USA, May 4-9, 2008.

- **B. Romeira**, J. M. L. Figueiredo, T. J. Slight, L. Wang, E. Wasige, C. N. Ironside, J. M. Quintana, and M. J. Avedillo, "Synchronization and chaos in a laser diode driven by a resonant tunneling diode," *Conference on semiconductor and integrated optoelectronics (SIOE 08)*, paper 32, Cardiff, Wales, United Kingdom, March 31-April 2, 2008.

Posters and Symposia

- **B. Romeira**, J. M. L. Figueiredo, T. J. Slight, L. Wang, E. Wasige, and C. N. Ironside, "Generation of optical chaotic signals," *16th National Conference of Physics (PHYSICS 08)*, Lisbon, Portugal, September 3-6, 2008 (Poster).

- **B. Romeira**, J. M. L. Figueiredo, T. J. Slight, L. Wang, E. Wasige, C. N. Ironside, J. M. Quintana, and M. J. Avedillo, "Novel optoelectronics circuits employing resonant tunnelling diodes," *2nd International Conference on Advanced Nano Materials (ANM 08)*, Aveiro, Portugal, June 22-25, 2008 (Poster).

- **B. Romeira**, J. M. L. Figueiredo, T. J. Slight, L. Wang, E. Wasige, C. N. Ironside, J. M. Quintana, and M. J. Avedillo, "Chaotic behavior in optoelectronic circuits employing resonant tunneling diodes," *2nd Workshop on Low-Dimensional Structures: Properties and Applications (WLDS 08)*, Aveiro, Portugal, January 31-1 February, 2008 (Poster).

- J. M. L. Figueiredo, **B. Romeira**, T. J. Slight, L. Wang, E. Wasige, and C. N. Ironside, "Optoelectronic integrated circuits incorporating negative differential resis-

tance devices," *V Symposium On Enabling Optical Networks and Sensors (SEON 07)*, Aveiro, Portugal, 2007 (Symposium).

- J. M. L. Figueiredo, **B. Romeira**, and A. Brázio, "Optoelectronic characterization of structures based on tunnel junctions, tunnel barriers and quantum dots," *International School on Structural Characterization of Nanostructures (ISSCN 07)*, Aveiro, Portugal, January 25-27, 2007 (Poster).

PREVIOUS PUBLICATIONS

List of Acronyms

AC alternating current

BER bit-error-rate

BERT bit-error-rate test

BPSK binary phase shift keying

BS base station

CMOS complementary metal-oxide-semiconductor

CPW coplanar waveguide

CRO coaxial resonator oscillator

CS central station

CW continuous-wave

DBQW double barrier quantum well

DC direct current

DDE delay differential equation

DFB distributed feedback

EAM electro-absorption modulator

EDFA erbium-doped fiber amplifier

E/O electrical-to-optical

EVM error vector magnitude

FFT Fast Fourier Transform

FOM figure of merit

FP Fabry-Pérot

FSR free spectral range

FWHM full width at half maximum

GMSK Gaussian minimum shift keying

GSG ground-signal-ground

GSM global system for mobile communications

HBT heterojunction bipolar transistors

HIC hybrid integrated circuit

HPT hetero-junction phototransistors

ILO injection-locked oscillator

IMPATT impact avalanche and transit time

LAN local area networks

LASER light amplification by stimulated emission of radiation

LCE Lyapunov characteristic exponent

LD laser diode

LED light emitting diode

LO local oscillator

MBE molecular beam epitaxy

MOCVD metalorganic chemical vapor deposition

MWP microwave-photonics

MMIC monolithic microwave integrated circuits

NDC negative differential conductance

ODE ordinary differential equation

O/E optical-to-electrical

OEIC optoelectronic integrated circuit

OEO optoelectronic oscillator

OILO optical injection-locked oscillator

OVCO optoelectronic voltage controlled oscillator

OW optical waveguide

PCB printed circuit board

PD photo-detector

PDC positive differential conductance

PIC photonic integrated circuit

PRBS pseudorandom bit stream

PSD power spectral density

PSK phase shift keying

PVCR peak to valley current ratio

PVVR peak to valley voltage ratio

QAM quadrature amplitude modulation

QPSK quadrature phase shift keying

RF radio frequency

RIN relative intensity noise

RMS root-mean-square

RoF radio over fiber

RTD resonant tunneling diode

Rx receiver

RZ return-to-zero

SM single mode

SMA sub-miniature version A

SMSR single mode suppression ratio

SNR signal-to-noise ratio

SPICE Simulation Program Integrated Circuits Especially

SSB single sideband

SSM spectrum surveillance monitoring

TL transmission line

TRAPATT trapped plasma avalanche and transit time

Tx transmitter

VCO voltage controlled oscillator

VSA vector signal analyzer

VSG vector signal generator

WGM whispering gallery mode

WOWi wireless-optical-wireless interfaces for picocellular access networks

Contents

List of Figures

List of Tables

Chapter 1

Introduction

1.1 Motivation

In the past two decades there has been an increasing interest on nonlinear systems applied to microwave-photonics (MWP) systems. The main driving force behind this research interest is the desire to take advantage of the nonlinearities of electronic and optoelectronic devices to achieve novel functions in both electrical and optical domains. A nonlinear system with a proper perturbation can exhibit two opposite effects: either a destabilization effect, or a stabilization effect. In both cases, there are an increasing number of applications where one of these effects may be highly desired like, for example, in novel communication systems.

Within the frame of this thesis, we will place emphasis upon concepts and applications which are related to semiconductor optoelectronic integrated circuit (OEIC) technology based on resonant tunneling diode (RTD), laser diode (LD), and photodetector (PD) devices. The main motivation of this work is to enable a deep understanding, both experimentally and theoretically, of the various dynamical regimes and related phenomenologies that result of the combination of RTD, LD, and PDs subjected to electrical, optical, and optoelectronic perturbations. An emphasis will be also laid on the innovative technological applications that can be derived from the observed behaviors.

1.2 Oscillator systems

Oscillation is among the simplest of dynamic behaviors that has been used to study a wide variety of physical phenomena. Oscillatory phenomena are often found in the

life sciences. These include the beating of the heart, the oscillations of the membrane potential in the axons of the neurons, among many others. Physics is full of oscillatory behavior; electromagnetic waves composed of electric and magnetic oscillating fields, and atomic vibrations in solid state physics are examples of this kind of phenomena. Electrical and mechanical oscillators, as well vibrations in structures are everyday elements in the world of engineering.

The importance of oscillators in science and technology can be outlined by two milestones. First, the pendulum, examined in detail by Galileo Galilei in the sixteenth century, persisted as the time-measurement instrument (in conjunction with the Earth's rotation period) until the advent of the piezoelectric quartz resonator. Second, the radio frequency (RF) oscillator, the first integrated circuit built on a bar of germanium by Jack Kilby at the Bell Laboratories in September 1958.

In theoretical physics, the word oscillator refers to a physical object or quantity oscillating sinusoidally - or at least periodically - for a long time, ideally forever, without losing its initial energy. Conversely, in experimental science the word oscillator stands for an artifact that delivers a periodic signal, powered by a suitable source of energy. Oscillators are indeed of major importance in a number of applications such as communications, high-speed digital electronics, radars and space research.

1.2.1 Electrical and optical oscillators

An important type of oscillator widely used today is the electronic oscillator that converts direct current (DC) power into RF. The first electronic oscillator was invented by Lee De Forest [1] in the early 1900s, shortly after the development of the vacuum tube. In this triode based device, also known as the van der Pol oscillator [2], the flux of electrons emitted by the cathode towards to the anode is modulated by the potential on the control grid. This potential is derived from the feedback of the current in the anode circuit containing an energy storage element (a frequency selecting LC filter) to the grid.

The rapid progress in crystal growth and microfabrication technologies in the second half of the last century have led to the development of novel semiconductor devices that replaced the old vacuum tubes in most of the applications. Today the solid state counterparts of these valve oscillators based on transistors and other semiconductor devices are in virtually every day applications from electronic instrumentation and communication systems to consumer electronics.

At the late 1950s, it was understood that a system associating an optical gain

media and an appropriate optical resonator would produce an optical oscillator. This optical oscillator was named light amplification by stimulated emission of radiation (LASER). In the optical domain the semiconductor laser is among the most widespread optical oscillator systems. Like all lasers, they are constituted by a gain medium which amplifies light by stimulated emission of radiation, and an optical resonator which also couples out the coherent light produced. Because of their characteristics, semiconductor lasers are the principal sources of coherent light in optical telecommunications and are widely used in many other applications such as laser printers, bar-code readers, and data storage, to cite only a few.

1.2.2 Injection locking

The concept of injection locking refers to a state of an oscillator when its frequency and phase, often known as the slave oscillator, are locked via direct coupling or injection to another oscillator, known as the master oscillator. This concept applies to all kinds of oscillators, from mechanical oscillators to electronic oscillators, and of course to optical oscillators.

Injection locking was first observed and described by Huygens in 1665 [3]. He recorded the phenomenon that two pendulum clocks (mechanical oscillators) hanging on the same wall could synchronize to each other even when they started with different frequencies and phases. In 1927 van der Pol [4] used this phenomenon to create a forced electronic oscillator. Adler [5] further developed the technique in 1945, which is currently addressed in electronics and communications as the injection-locked oscillator (ILO) technique.

In the 1966s, after the invention of lasers, Stover and Steier [6] studied injection locking on He-Ne lasers, which is considered the first demonstration of optical injection locking. With the development of high efficient semiconductor lasers, optical injection-locked oscillator (OILO) techniques entered a new era where the properties of the laser were found to be strongly dependent on external light injection, particularly the modulation bandwidth characteristics, which are critical for communication applications.

Microwave oscillators can be also controlled optically. This is an alternative to signal detection approach and uses the optical signal to control or introduce signals directly into microwave devices. This approach has several attractions. First, no extra electronic circuits are required to process the optical detected signals before application to the microwave device, nor any circuit parasitics are introduced, which may improve response speed. Second, optical control introduces an extra control port to the mi-

crowave device. The basic process used in direct optical control of microwave devices is photogeneration of carriers within the device by the incident optical signal, usually through intrinsic absorption. The main forms of oscillator control are optical switching, optical tuning, and optical injection locking [7]. Optical control of a wide range of microwave devices has been demonstrated for oscillators incorporating avalanche photodiodes [8, 9], heterojunction bipolar transistors (HBT) integrated with photodiodes [10], and RTDs [11], to mention only a few.

1.3 Oscillators for microwave photonics systems

Microwave photonic systems use optical waves as carriers to transport RF/microwave signals through optical fibers to remote locations taking advantage of optical fibers low loss, light weight, high capacity, high security and immunity to electromagnetic interference. This technology is beginning to be used in local access networks to provide private users with ultra-wideband communications. The development of novel methods and systems combining optical techniques and OEIC devices can significantly simplify and augment the capacity of RF/microwave photonic systems. Their high-frequency and ultra-pure microwave signal generation capabilities allow the development of novel communication systems such as radio over fiber (RoF) networks [12, 13].

1.3.1 Methods of generating microwave signals in the optical domain

Since microwave resonator-based oscillator technology can not match all advantages of photonic systems, there has been a great search of configurations capable to generate microwave carriers in both electrical and optical domains. In a versatile oscillator for photonic systems it should be also possible to synchronize or control the oscillator by both electrical and optical signals.

There are several methods for generating a microwave signal in the optical domain. In Fig 1.1 we give examples of just a few which are based in direct or external modulation of a laser diode. The direct modulation examples, Fig. 1.1(a), are in general the lowest cost solutions. The external modulation, Fig. 1.1(b), uses a laser diode, an external electro-optic modulator and a stable microwave signal from a local oscillator (LO). This method provides higher performance with a trade-off between high cost and power consumption.

The basic configurations using direct and external modulation to generate microwave signals can be further optimized for higher performance using perturbation methods based on injection locking and delayed feedback techniques such as optical

injection [14, 15], optical feedback [16–18], and optoelectronic feedback [19]. In the optical injection scheme, Fig. 1.1(c), external injected coherent light in a master-slave configuration is used to provide bandwidth enhancement, chirp and noise reduction for optical communication applications [14]. The optical feedback scheme consists of optical re-injection of a fraction of the light produced by the laser into its active region. In this case the round-trip time of light in the external cavity introduces a delay in the system that is utilized to control and adjust the desired behavior [20]. In the optoelectronic feedback scheme a fast responding photodiode is used to produce a current that is an image of the laser output power and that is added, after a delay, to the laser injection current to control the laser output [21].

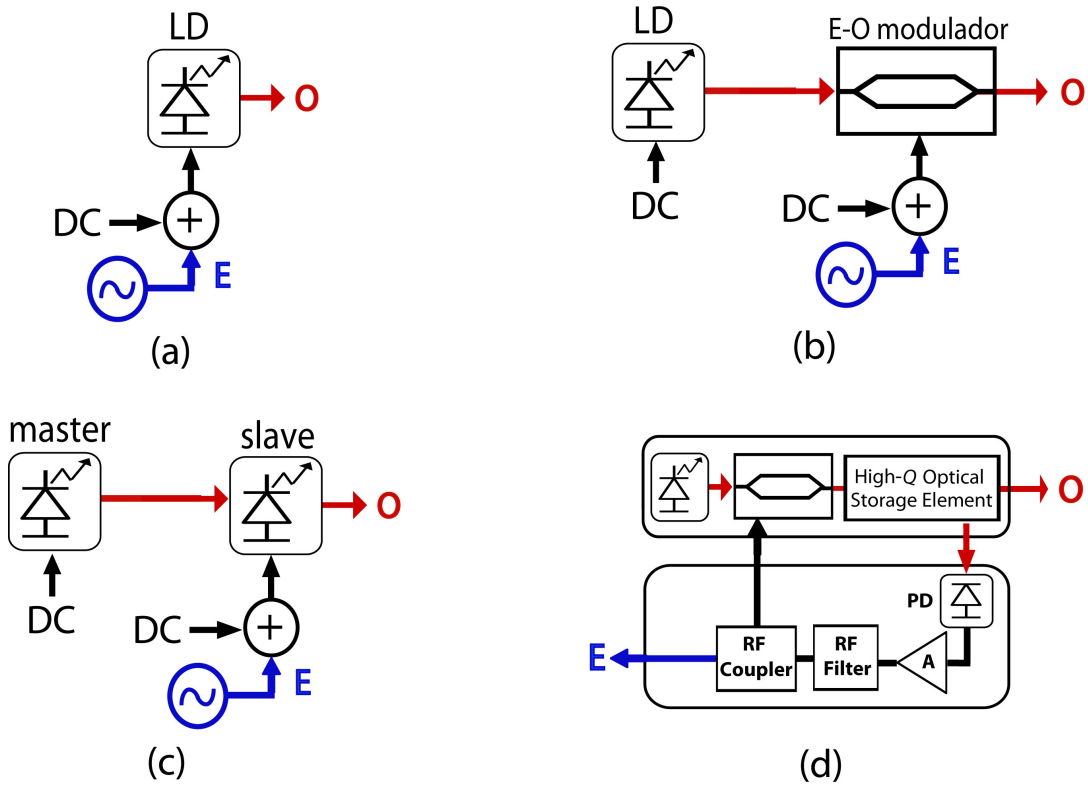

Figure 1.1: Methods of generating microwave electrical (E) signals in the optical (O) domain. (a) Direct modulation. (b) External modulation. (c) Optical injection-locking of a directly modulated laser. (d) The optoelectronic oscillator (PD: photo-detector; A: amplifier).

Of increasing interest is the optoelectronic oscillator (OEO) system, Fig 1.1(d), that can generate highly pure signals in both electrical and optical domains [22, 23]. A

typical OEO consists of a nonlinear system, an element to compensate for any losses, and a time-delayed feedback loop that can function in the frequency range from tens of GHz down to few kHz. In a OEO system, external elements such as electro-optic modulators are used to produce nonlinearities, with laser diodes being used only as light sources. Using this configuration, it was demonstrated that delayed feedback OEOs provide very high-quality MWP signals [24, 25].

The aforementioned examples not only produce high-frequency microwave signals in the optical domain but also, with appropriate perturbation, can exhibit highly complex dynamics capable to produce broadband chaotic carriers. Optoelectronic feedback topologies have been receiving great attention due to generation and control capabilities of chaotic carriers that can be used in the security of optical communication systems [26, 27]. The dynamics of such systems can be easily synchronized and controlled adjusting either the external perturbation or feedback parameters [28–30]. Despite the variety of advantages, the resulting systems presented in Fig 1.1 can be either bulky, inefficient, complicated, or costly for some applications. Therefore, a great deal of work on oscillators for photonic microwave systems is underway to provide not only simple and high-performance microwave and millimeter-wavelength oscillators, but also to take advantage of the rich dynamical outputs to deliver novel applications and functionalities in MWP.

The aim of this work is the demonstration of a novel class of much less complex OEO topologies due to the use of resonant tunneling diode structures.

1.3.2 Resonant tunneling diodes for microwave photonics systems

Resonant tunneling diode structures have been the focus of broad interest since Chang, Esaki, and Tsu observed experimentally electron-wave resonance in double barrier structures in 1974 [31]. Since then, the RTD has emerged as one of the most important testing grounds for modern theories of transport physics, and is central to the development of new types of semiconductor nanostructures.

Basic RTDs consist of nano-electronic structures that use vertical stacking of epitaxial layers of semiconductor alloys with the active regions consisting of a double barrier quantum well (DBQW) structure, in total, about 10 nm thick, that act as like a Fabry-Pérot (FP) interferometer for the electron wavefunctions. The FP effect gives rise to a highly nonlinear and N-shaped current versus voltage (I-V) characteristic which provides the occurrence of negative differential conductance (NDC). Furthermore, the I-V characteristics can be tailored by appropriate bandgap engineering to provide the

desired shape and properties. The conduction mechanism of DBQW-RTDs is based on quantum transport phenomena which provides many compelling merits such as extremely fast response speed, high frequency operation, and low power consumption, to mention a few.

Since resonant tunneling can be a very fast effect the most promising application of the DBQW-RTD is as high speed switching devices [32], either electronically or optically switched [33]. The operating frequency of such devices can go up to several THz [34–36] which make them the fastest purely electronic devices operating at room temperature. Furthermore, the intrinsic nonlinearities provides the basis for self-organized formation of current density patterns. Consequently, a large variety of complex spatiotemporal dynamics has been observed, e.g., limit cycle self-sustained oscillations [37] and also chaotic behavior when the DBQW-RTD is externally perturbed [38].

DBQW-RTDs can be integrated with conventional electronic and photonic devices [39–41]. Approaches to light modulation, light detection and light generation at microwave and millimeter-wave frequencies have been investigated by combining DBQW-RTDs with optical waveguides [42, 43], semiconductor lasers [44], and photo-detectors [33]. RTD-based OEICs can enhance devices and circuits characteristics by reducing power consumption and offering novel functionalities and significant improvements in the modulation/detection performance, circuit reliability, and speed.

The RTD-based OEIC combine the electrical non-linearities of RTD oscillators with PDs and LD light sources. An example of a RTD-OEIC is depicted in Fig. 1.2 showing a voltage controlled OEO with both electrical and optical output ports operating at a natural frequency f_0. Since the RTD-OEO emulates the RTD wideband NDC region, high frequency oscillations and generation of stable low-phase noise electrical and optical signals are expected, with both being controllable by electrical or optical injection signals. In Fig. 1.2(a) the OEO comprises a RTD device containing an intrinsic region for photo-detection, i.e., it can be controlled either electrically or optically, and a LD device as a source of light that is driven electrically by the RTD NDC current oscillations. Additional control of the RTD-OEO can be provided taking advantage of a time delayed feedback as shown in Fig. 1.2(b) which enriches the dynamics of the system [23].

As discussed throughout this thesis, OEO topologies based on RTDs can be operated in a wide variety of regimes. These operation modes include novel optoelectronic voltage controlled oscillator (OVCO) circuits, with potential to simplify clock recovery schemes, improve control of microwave photonics oscillators, generate electrical and optical aperiodic waveforms, and as electrical-to-optical (E/O) and optical-to-

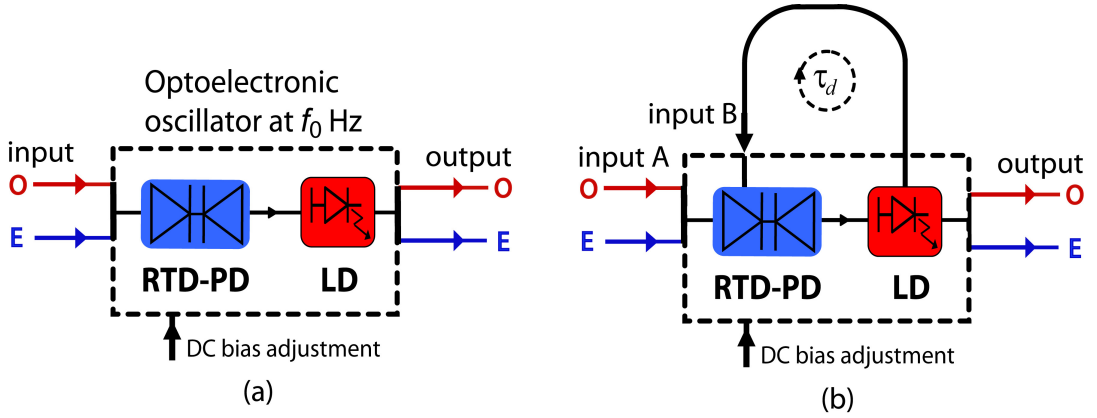

Figure 1.2: Schematic of an a optoelectronic integrated circuit system consisting of RTD-PD and LD elements operating at a natural frequency f_0 with both electrical and optical outputs. (a) Control of the RTD-based OEO using electrical (E) and optical (O) injection locking techniques. (b) Time-delay feedback control of the RTD-based OEO with time delay τ_d.

electrical (O/E) converters for RoF systems. The main potential advantages of utilizing the RTD-OEO system instead of optical injection or feedback of optoelectronic/laser systems as described previously with help of Fig. 1.1 include the simple implementation, compact solution, tunability of RTD oscillator, and possibility to exploit novel dynamical regimes taking advantage of the nonlinearities of both RTD and LD devices.

1.4 Aims of the work

The aim of this work is to provide a comprehensive study on the nonlinear dynamics and applications of OEIC circuits that combine RTD, PD, and LD components, Fig. 1.2. More specifically, this work developed around the following milestones:

- Implement RTD-based oscillator topologies combined with laser diodes and photodetector devices to obtain operation regimes in both electrical and optical domains taking advantage of RTD's nonlinear behavior.
- Investigate the dynamics of electrically and optically injection locked RTD-based oscillators, and subjected to time delayed feedback.
- Develop and evaluate numerical models based on ordinary and delay differential equations consisting of a Liénard's RTD oscillator model, and laser diode rate

equations model for the analysis of the dynamics of RTD and LD-based systems, respectively.

1.5 Thesis outline

The thesis is divided into six chapters. In this introductory chapter, the motivation and aims of the research work have been explained, with a brief overview on RTD and LD oscillators, and the main perturbation control schemes. The remaining of the thesis is devoted to the presentation and discussion of computational simulations and characterization of implemented RTD-PD-LD oscillator topologies. The remaining chapters are organized as follow:

- **Chapter 2** provides an overview on some pertinent theory of nonlinear dynamic systems with special emphasis on the resonant tunneling diode and the laser diode, the key components utilized in this work. A system of ordinary differential equations called the Liénard RTD oscillator model is introduced which provides a general framework for the analysis of the nonlinear operation regimes of RTD-based systems. Furthermore, the laser diode is discussed using the single mode rate equations model. Finally, a review of the main dynamical regimes of both RTD and LD oscillator systems are presented.

- **Chapter 3** will give a detailed description of the experimental key steps needed for producing the RTD-OEICs investigated in this project. We give particular attention to the processes needed to obtain a high-frequency RTD oscillator driving a laser diode, the RTD-LD, in the form of a hybrid integrated circuit (HIC). Then, we demonstrate the RTD-LD generates synchronized and chaotic signals in both optical and electrical domains when driven by periodic electrical signals. The RTD-LD behaviors are analyzed using the Liénard RTD-LD numerical model, to obtain additional insight on the dynamics of the implemented circuits.

- **Chapter 4** reports on the characteristics of DBQW-RTD optical waveguide photo-detectors. An optically controlled RTD-PD oscillator taking advantage of the photo-detection characteristics of the DBQW-RTD structures is then investigated, and the corresponding dynamical regimes are further explained utilizing an optically controlled Liénard oscillator model. Furthermore, optical and electrical injection locking is discussed for novel applications in MWP systems including in optoelectronic clock-recovery circuits and transmission of modulated signals in wireless/photonis links.

- **Chapter 5** describes a delayed feedback OEO comprising a self-synchronized RTD-PD oscillator using optical delay lines with lengths of hundreds of meters (in both single and dual loop configurations) to provide stability of free-running oscillations and phase noise reduction. The RTD-OEO dynamics is investigated as function of re-injected optical power and fiber length. The experimental results will be compared with the numerical simulations of the time delayed feedback Liénard oscillator model.

Ultimately, the main results of this thesis, the conclusions, and future work are presented in **Chapter 6**.

1.6 Main achievements

The main scientific contributions that have arisen from the PhD work are summarized as follows.

- Experimental demonstration of RTD-LD optoelectronic voltage controlled oscillators producing both electrical and optical self-sustained oscillation signals at microwave frequencies [45, 46].

- Development of the Liénard RTD nonlinear oscillator model to study the dynamical behaviors of autonomous and non-autonomous RTD-LD oscillators [46, 47].

- Experimental demonstration and numerical simulation of fundamental and harmonic injection locking, period-adding bifurcation, quasi-periodic and chaotic behaviors in non-autonomous RTD-LD oscillators [48, 49].

- Proposal and experimental demonstration of a novel optically controlled RTD-OEIC oscillator with both optical and electrical input and output ports, and a DC voltage control port, forming the RTD-PD-LD oscillator [50].

- First experimental implementation of wireless/photonics [51, 52] and clock recovery [53] schemes employing electrical and optical injection locking of RTD-PD-LD oscillators.

- First demonstration of a time delayed feedback RTD-OEO comprising a self-synchronized RTD-PD oscillator, a LD, and optical delay lines [54, 55].

- Development of a numerical model consisting of a time delayed-feedback Liénard oscillator incorporating a Gaussian white noise source, to obtain a more realistic study of the dynamics of RTD-OEO systems [56, 57].

Chapter 2

Dynamics of resonant tunneling and laser diode semiconductors

2.1 Introduction

The study of irregular phenomena including chaos is part of the broader theory of nonlinear dynamical systems [58, 59]. The beginning of the science of the dynamical systems goes back to Isaac Newton and the invention of differential calculus. Since then, physicists have believed that periodic solutions are sufficient to describe the oscillatory behavior of dynamical systems. However, the research performed by Henri Poincaré at the end of the nineteenth century showed that simple dynamical systems can led to complex behavior, that we now call chaos. But it was only at the end of the 1960s, mostly because of the pioneering studies of Edward Lorenz while simulating irregular oscillations in fluid convection in the atmosphere [60], that the scientific community drew its attention towards chaos and related phenomena. In parallel to the increasing attention on the theory of dynamical systems and chaos, the widespread use of computers has enabled to observe and model chaotic behaviors in a large number of scientific fields. Since then scientists have discovered that chaos can appear in a large number of biological, chemical, physical, and information systems [61, 62], with novel applications in chaos control and synchronization [63–65].

In the field of semiconductor physics, nonlinear generation-recombination processes [66], and nonlinear optical effects [67] may give rise to many nonlinear behaviors. They manifest themselves as electric instabilities such as switching between a non-conducting and a conducting state, or spontaneous oscillations of the current or voltage, if sufficiently high electric or magnetic fields, injected currents, or optical or microwave power

is applied.

Semiconductor structures nowadays can be designed and fabricated by modern epitaxial growth technologies with almost unlimited flexibility. This means, by controlling the thickness of those structures in the nanometer scale, systems with specific electric and optical properties can be tailored to show pronounced nonlinear transport properties that may be applied in electronic and optical oscillating and switching devices.

This chapter provides a theoretical framework for the analysis of complex nonlinear spatio-temporal dynamics and chaotic behavior in circuits based on RTD and LD devices, the two key semiconductor components utilized on this work. RTDs are one of the few quantum-transport devices that operate effectively at room temperature, and are well known for their high-speed and switching characteristics associated with the NDC region. LDs are the principal sources of coherent light in optical telecommunications. They are widely used in optical storage devices, and in laser pointers, to cite only a few applications. Altogether, the scientists realized that the large variety of dynamical regimes produced by these semiconductor devices could be exploited in new type of applications, by taking advantage of their nonlinearities.

2.2 Aim and objectives

The aim of this chapter is to provide dynamical system theory tools to investigate the nonlinear charge transport of RTD-based devices and LDs, for the analysis of the nonlinear operation regimes of RTD and LD-based circuits. This was achieved through the following objectives:

- Review of RTD's features that include a description of its pronounced nonlinear current-voltage (I-V) and high-speed operation characteristics.
- Describe the RTD oscillator circuit using a ordinary differential equation (ODE) system forming the Liénard RTD oscillator model.
- Investigate the complex dynamics of Liénard RTD oscillator systems.
- Investigate the dynamical regimes of laser diodes using single mode rate equations model.

2.3 Chapter overview

After a brief discussion on semiconductor nonlinear dynamic systems we will introduce the basic notions of RTD structure characteristics and charge transport mechanisms. Then the RTD's nonlinear DC characteristic and models are discussed with special emphasis upon the interaction of the RTD with an external circuit. Using this approach, a coupled system of ODEs forming the Liénard RTD oscillator model which provides a general framework for the analysis of the nonlinear operation regimes of RTD-based circuits is then investigated. Finally, the characteristics of LD systems and the nonlinear dynamic regimes of directly modulated lasers using single mode rate equations are described.

2.4 Semiconductor nonlinear dynamic systems

With the advent of modern semiconductor-growth technologies such as molecular beam epitaxy (MBE) and metalorganic chemical vapor deposition (MOCVD), artificial structures composed of different materials with layer thicknesses of only a few nanometers have been grown, and it has become possible to design and fabricate semiconductor structures whose dimensions are controlled down to one monolayer ($\sim$ 0.3 nm), required for devices such as the RTD. This has given the unprecedented capability to tailor devices with novel electric and optical properties.

Modern semiconductor structures whose structural and electronic properties vary on a nanometer scale provide an abundance of examples of nonlinear transport processes. In these structures nonlinear transport mechanisms are given, for instance, by quantum mechanical tunneling through potential barriers and is particularly pronounced in the cases of semiconductor heterostructures and low-dimensional structures, in which abrupt junctions between different materials on an atomic length scale cause conduction band discontinuities resulting in potential barriers and wells to the charge. In these examples the local charge accumulation in the potential wells and the nonlinear processes for transport of charge across the barriers have been found to provide a number of nonlinearities.

Although the features described above have been known for a long time, the view of a semiconductor device as a nonlinear dynamic system is a fairly recent development. Such nonlinear dynamic systems can exhibit a variety of complex behaviors including bifurcations, self-sustained oscillations, and deterministic chaos. These behaviors are characteristic of dissipative dynamic systems, i.e., a steady state can be maintained only

by a continuous flux of energy, and possibly matter, through them. Mathematically, this is described by a suitable space of dynamic variables. Unlike an isolated, closed system, which after a perturbation always returns to an equilibrium state characterized by maximum entropy, an open dissipative nonlinear system may exhibit a process of self-organization, in which the entropy is locally decreased. Such processes usually involve qualitative changes in the state of the system, similar to phase transitions and have been noted in a great number of very different dissipative systems occurring in physics, chemistry, biology, ecology, and even economics and social sciences.

The introduction of concepts and methods from nonlinear dynamics subsequently stimulated a large amount of experimental and theoretical work in a variety of semiconducting materials essential for modern high-speed electronic and optoelectronic nanometric devices, such as DBQW-RTD structures [68, 69], semiconductor superlattices [70, 71], and semiconductor lasers [20]. In all those structures space charges confined on nanometer scales and sharp electric potential gradients lead to strong electric fields and far-from-equilibrium conditions that give rise to a number of nonlinear transport phenomena.

In the remaining of this chapter, we provide a brief introduction on some basic background theory and modeling relevant for the nonlinear dynamics of DBQW-RTD structures and laser diodes investigated in this work.

2.5 Resonant tunneling diodes

A semiconductor DBQW-RTD consists of a low band-gap semiconductor layer (the quantum well, typically from 5 nm to 10 nm wide) surrounded by two thinner layers of higher band-gap material (barriers, typically from 1.5 nm to 5 nm), both sandwiched between lower band-gap n-type material layers, usually the well material [40]. Figure 2.1(a) shows an example of the schematic energy diagram of a double barrier quantum well formed by InGaAs/AlAs semiconductor compounds. When both sides are terminated by highly doped semiconductor layers for electrical connection (the emitter and the collector contacts) the structure is called resonant tunneling diode.

Resonant tunneling diode is a DBQW low-dimensional structure that has gained considerable attention because of the strong NDC effect that is displayed in different semiconductor material systems and over a wide range of current density, Fig. 2.1(b). The NDC is a result of the nonlinear processes for transport of charges across the DBQW substructure. In practical applications, the RTD is remarkable because it is one of the few quantum transport devices that operates at room temperature. This has

facilitated its characterization at high speeds and has allowed the NDC region to be used in switching devices and high frequency oscillators when included in a resonant tank (e.g. a *RLC* circuit). The RTD capability to operate as an oscillator has great interest in many topics of nonlinear dynamics because of the strong non-linearity and the anti-symmetry of its I-V characteristic.

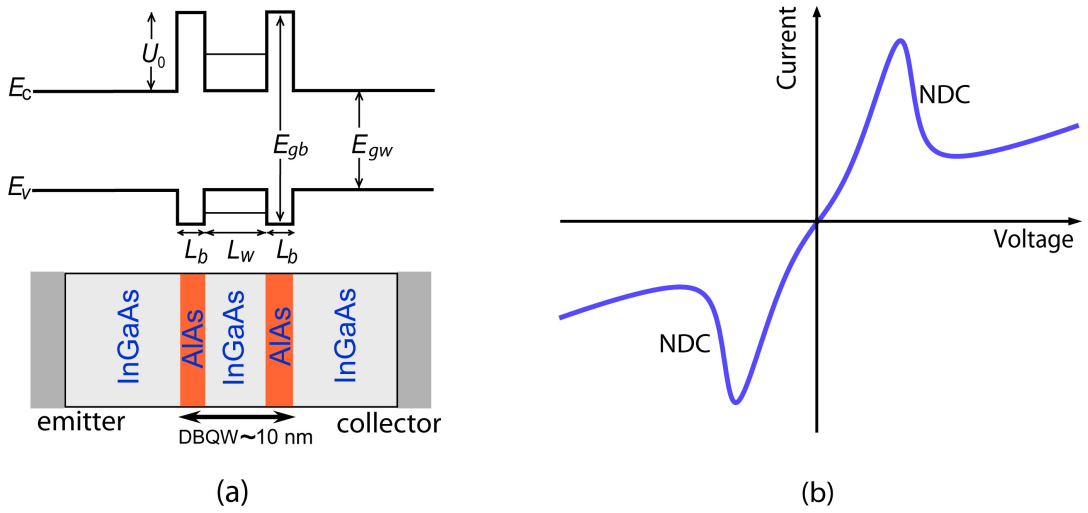

Figure 2.1: (a) Schematic diagram (*top*) of a double barrier quantum well band profile formed by InGaAs/AlAs semiconductor compounds (*bottom*). The energy diagram shows the lowest conduction band E_c and the highest valence band E_v profiles. E_{gb} e E_{gw} represent the energy band gaps of the barriers and quantum well, respectively, and U_0 is the potential barrier height. (b) Typical DBQW-RTD room-temperature current-voltage characteristic exhibiting negative differential conductance.

In this section, the nonlinear charge transport mechanism in DBQW resonant tunneling diodes is discussed, as well a physics-based I-V characteristic model, and an equivalent circuit model for the study of the dynamics of RTD-based systems.

2.5.1 Double barrier quantum well RTD

Resonant tunneling is an important mechanism for instabilities in DBQW semiconductor structures. Resonant tunneling through double potential barriers was predicted by Bohm [72], and latter Iogansen [73] discussed the possibility of resonant transmission of an electron through double barriers formed in semiconductor crystals. They concluded that structures with identical barriers show tunneling transmission coefficients of one when the particles incident energy equals the structure resonant energies, however

small the transmission through the individual barriers may be [40]. Figure 2.2 compares schematically the transmission coefficient $T(E)$ for single and symmetrical double barrier structures as a function of incident carrier energy. The transmission coefficient lobs broadens with increasing energy because the barriers become more transparent [39]. Because of the finite height of the energy barriers, the allowed energy states in the well region become quasi-bound or resonant states rather than true bound states as it happens with thicker barrier quantum wells [39]. In consequence, tunneling of charge carriers through the barriers is strongly enhanced when their energy equals one of well energy levels, reaching much higher values than the product of the two individual barrier transmission coefficients at the energy values of the system resonant levels, see Fig. 2.2. In this structure, the resonant tunneling mechanism is analogous to tunneling between two adjacent wells.

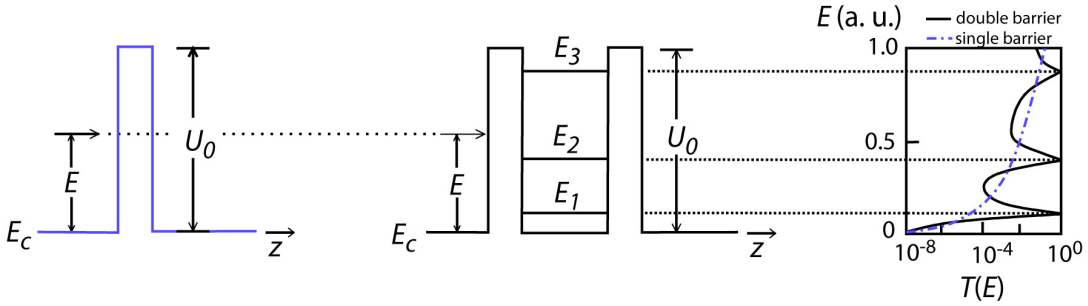

Figure 2.2: Transmission coefficients, $T(E)$, of single (*left*) and double (*center*) barrier quantum well structures as a function of incident carrier energy E.

Under applied bias, the overall carrier flow through a DBQW-RTD is qualitatively different from that of a single barrier diode since the double barrier structure acts as a FP filter to charge carrier energy distribution [40]. This filter action is exploited applying a voltage across the DBQW structure to control the number of carriers that can take part in the conduction through resonant levels. The carrier transmission coefficient maxima shown in Fig. 2.2 give rise to I-V characteristics with regions of strong NDC. The resonant tunnelling phenomenon in AlGaAs DBQW structures was first predicted in 1973 [74], and demonstrated experimentally in 1974 by Chang et al. [31]. In 1983, Sollner et al. [75] demonstrated resonant tunneling through quantum wells at frequencies up to 2.5 THz, and NDC characteristic at room temperature has been measured for the first time in 1985 [76, 77].

Figure 2.3 shows a schematic of a n-type DBQW-RTD lowest conduction band profiles at around zero volt, at the peak voltage (resonance), and in the valley voltage

region (off resonance). The RTD I-V characteristic can be understood with the help of the lowest conduction band profile Γ. The main carrier flow processes in a DBQW-RTD is schematically represented in Fig. 2.3. When the applied bias is small, i.e., $V << V_p$ (peak voltage, also referred as resonance voltage), the Γ-conduction band profile is not much affected, remaining almost flat, see Fig. 2.3(a) (i). The first resonant level is well above the emitter Fermi level, and little current flows. As voltage is increased, the energy of the first resonant level is moved downwards to the emitter Fermi level, leading to an almost linear current increase with the voltage, the first positive differential conductance (PDC) region, till reaching a local maximum I_p, ideally, at $V \simeq 2E_{n=1}/q$, when the overlap between the emitter electron Fermi sea energy spectrum and the transmission coefficient around the first resonant level reaches a local maximum, as shown in Fig. 2.3(a) (ii). A further increase in the applied voltage pulls the first resonant level towards the bottom of the Γ-valley and into the forbidden gap, where there are no longer carriers available to efficiently cross the DBQW. This leads to a sharp current decrease, giving rise to the first negative NDC portion of the device I-V characteristic, Fig. 2.3(b). At a given voltage, known as the valley voltage V_v, with $V_v > V_p$, the current reaches a local minimum I_v, Fig. 2.3(a)(iii). An additional increase on the bias voltage will further lift up the emitter Fermi level and tunneling through higher resonant levels or through the top regions of the barriers will lead to new current rise, similar to the classical diode I-V characteristic, Fig. 2.3(b).

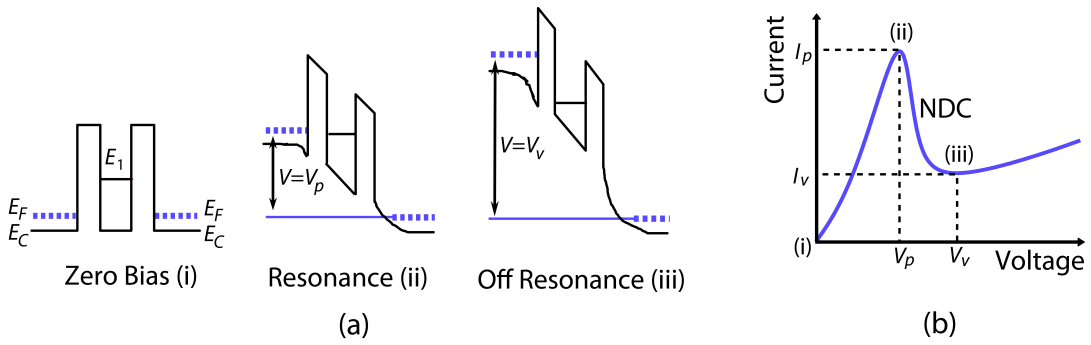

Figure 2.3: (a) Lowest conduction band profile under applied voltage. (b) Negative differential conductance current voltage characteristic.

2.5.2 Negative differential conductance

In the negative differential conductance region, the current density decreases with increasing voltage (increasing electric field across the DBQW), which in general corres-

ponds to an unstable regime. The actual electric response depends, for instance, upon the contact conditions and the attached circuit, which in general contains - even in the absence of external load resistors - unavoidable resistive and reactive components such as lead resistances, lead inductances and package inductances and capacitances. The global I-V characteristic of an RTD can be calculated from the local current density $j(\varepsilon)$ relation, where ε represents the local electric field across the DBQW, by integrating the current density j over the cross-section A of the current flow:

$$I = \int_A \boldsymbol{j}\, dxdy \tag{2.1}$$

and the electric field ε over the length L of the sample:

$$V = \int_0^L \varepsilon dz \tag{2.2}$$

where z is the direction of current flow and x and y are the perpendicular directions. Unlike the $j(\varepsilon)$ relation, the I-V characteristic is not only a property of the semiconductor material, but also depends on the geometry, the boundary conditions, and the contacts of the sample. The I-V relation is said to display NDC when:

$$\frac{dI}{dV} < 0. \tag{2.3}$$

For a useful representation of the RTD non-linear I-V characteristic, it is necessary to considerer a wide variety of device structures and materials available, that is, a suitable modeling of the RTD I-V characteristic has to include, as much as possible, RTD physical parameters such as material properties, layer dimensions, energy levels, dopant concentrations, and the device geometry.

Since a quantum mechanics based model that includes a full description of RTD features[1] can be a complex and time-demanding task for circuit design purposes [41], several attempts have been made to incorporate the full pronounced nonlinear I-V and RTD high-speed operation characteristics into circuit simulation packages such as Simulation Program Integrated Circuits Especially (SPICE) or related tools [78]. Different RTD models have been developed to model RTD's large signal I-V curves. The following is a brief list of these approaches: piecewise linearly approximation technique [79], the equation approximating the I-V curve with one Gaussian function and one exponential

[1] Simulation packages such as Wingreen provides an integrated simulation environment for simulation of quantum transport in layered semiconductors based on Green's functions. The simulator is capable of generating output for the selfconsistent potential, the quantum charge density, the local density of states, the current density, and the transmission probability of DBQW-RTDs.

function [80], the equation approximating the I-V curve with three Gaussian and/or exponential functions [81], and a physics-based RTD current voltage equation [82]. All these methods have a common character - they are curve-fitting procedures. There are no relations between RTD I-V expression and device physics for all models stated above, except the model of Schulman et al. [82], which is derived from the quantum model. The model of Schulman et al. consists of a mathematical function which provides a satisfactory I-V shape characteristic for InGaAs/AlAs and GaAs/AlAs DBQW-RTD semiconductor compounds. The expression obtained contains physical quantities originated from the quantum formalism, that can also be treated as empirical parameters for fitting purposes.

In the Schulman et al. I-V model the resonant tunneling current density is expressed within the effective mass approximation [39], which includes nonzero temperature, Fermi-Dirac statistics and the transmission coefficient $T(E,V)$ approximated by a Lorentzian function. Therefore, the current density of the RTD reduces to the formula:

$$J = \frac{qm^* k_B T \cdot \Delta E_r}{4\pi^2 \hbar^3} \ln\left[\frac{1+e^{(E_F - E_r + qV/2)/k_B T}}{1+e^{(E_F - E_r - qV/2)/k_B T}}\right]\left[\frac{\pi}{2} + \tan^{-1}\left(\frac{E_r - qV/2}{\Delta E_r/2}\right)\right] \tag{2.4}$$

where $E = E_r - qV/2$ is the energy measured up from the emitter conduction band edge, E_r is the energy of the resonant level relative to the bottom of the well at its centre, and ΔE_r is the resonance width. The parameters q and k_B are unit electric charge and Boltzmann constants, respectively. Equation 2.4 can be rewritten providing the description of the resonant term $J_R(V)$ of the NDC:

$$J_R(V) = A \ln\left[\frac{1+e^{q(B-C+n_1 V)/k_B T}}{1+e^{q(B-C-n_1 V)/k_B T}}\right]\left[\frac{\pi}{2} + \tan^{-1}\left(\frac{C - n_1 V}{D}\right)\right] \tag{2.5}$$

where the parameters A, B, C, D, and n_1 can be used to shape the curve to match the first PDC and the NDC regions of the measured I-V characteristic, having at the same time a well-defined physical interpretation: A and B are related, among other parameters, with resonance width ΔE_r and Fermi level energy E_F, respectively, and allow adjustment of the RTD peak current and PVCR; C and n_1 determine essentially the RTD peak voltage, correlated with the energy of the resonant level relative to the bottom of the well E_r and how much of the voltage drops across the quantum well, respectively; finally, D is related with the resonance width ΔE_r.

In order to represent the increasing valley current due to tunneling through higher

resonances or thermal excitation over the barriers, an additional current density component, identical to the classical diode current, the non-resonant term $J_{NR}(V)$, is included:

$$J_{NR}(V) = H\left(e^{n_2 qV/k_B T} - 1\right) \tag{2.6}$$

Parameters H and n_2 adjust the peak to valley current ratio (PVCR) and the exponential growth in the second PDC. The final form of the RTD I-V curve is then given by:

$$I(V) = I_R(V) + I_{NR}(V) = M[J_R(V) + J_{NR}(V)] \tag{2.7}$$

where the multiplying factor M is used to scale equation (2.7), in order to take into account the device area. Figure 2.4 shows examples of typical experimental I-V curves of (a) GaAs/AlAs, and (b) InGaAs/AlAs DBQW-RTD devices and the corresponding fittings given by Eq. (2.7). The fitting parameters are shown in Table 2.1 assuming a temperature of operation $T = 300$ K and a multiplying factor $M = 2 \times 10^{-6}$ cm^2. We can see that very good agreement between the model and measurements has been achieved, especially for regions before peak and after valley, as well as the peak and valley points. From the analysis of the fitting parameters it is possible to identify, for example, that higher values of parameters A and B are used in the InGaAs/AlAs fitting due to RTD higher peak current and higher PVCR. Parameter D was identical in both fittings due to similar peak to valley voltage ratio (PVVR) values.

Table 2.1: Description of the typical physical parameters of the experimental I-V curves fitting.

Semiconductor compounds	A (Acm^{-2})	B (V)	C (V)	D (V)	H (Acm^{-2})	n_1	n_2
GaAs/AlAs	1950	0.05	0.0874	0.0073	18343	0.0352	0.0031
InGaAs/AlAs	3800	0.068	0.1035	0.0088	4515	0.0862	0.0127

The formalism of the numerical fitting presented here is special useful for circuit design because of the flexibility and small effort necessary to fit experimental data and to incorporate additional effects when desired. Taking advantage of the relative good description of the RTD DC I-V characteristic presented here, the Schulman et al. I-V model can be included together with an RTD equivalent circuit (described in the next subsection) to model alternating current (AC) behavior including self-sustained oscillations.

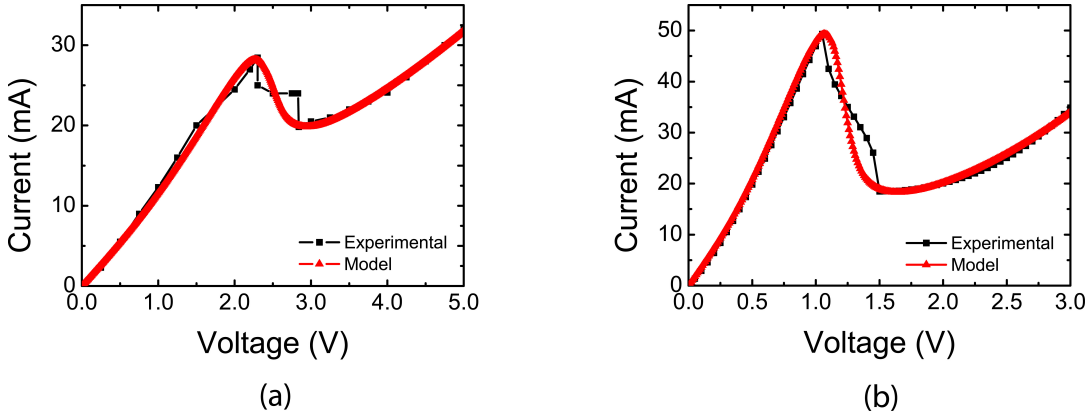

Figure 2.4: RTD experimental I-V curves and numerical fitting for (a) GaAs/AlAs and (b) InGaAs/AlAs semiconductor compounds.

2.5.3 RTD equivalent circuit

RTDs can work very fast because of the nanometric device dimension, fast electron escape rates across the barriers and short RC time constant. Because of the $N-$shaped I-V characteristic along with their capability of high-speed operation RTDs can generate oscillations at very high frequency when included in a resonant cavity [34]. Two important milestones demonstrating RTDs operating above 1 THz have been recently reached [35, 36] confirming the RTD is the fastest purely electronic solid state device operating at room temperature.

Although these oscillation records give a direct and unmistakable proof of the speed of these devices, in this work we are focus on the study of RTD-based circuits where circuit elements, particularly, the series resistance, the device capacitance, and inductance parasitics (e.g. bond wires) must be considered for circuit applications. These elements restrict the RTD operation at relative moderate frequencies in the microwave part of the spectrum. The theoretical identifications of an accurate equivalent circuit model for RTD-based circuits is important from the oscillator design perspective. Maximizing the power-frequency product, extracting individual component characteristics from experimental measurements, and insight for structural changes to the RTD which will lead to novel behaviors, are some of the possibilities that can be explored at the circuit level.

Until now equivalent circuits in several forms have been introduced to represent the small-signal behaviors of the RTD. The simplest equivalent circuit model introduced to represent a DBQW-RTD is the parallel combination of RTD conductance and ca-

pacitance, as represented in Fig. 2.5(a). The reason this simple model is employed is the following. When a DC bias is applied to the collector and emitter the RTD starts conducting and current flows though the device. At the same time the collector side starts to deplete because of the applied bias. As a result of the applied bias, the RTD conductance G_0 and the capacitance C due to depletion of the collector side appears in the RTD equivalent model. The fact that voltage leads current inside RTD motivated Brown et al. [83] to modify the simple equivalent circuit of Fig. 2.5(a) by introducing an inductance L_{qw}, Fig. 2.5(b), in series with the RTD conductance. Brown et al. considered if the applied bias is changed by a step function than the current through RTD needs some time to accommodate the change in bias. The time taken by the RTD current to reach its new value corresponding to the changed applied voltage is nothing but the quasibound state lifetime τ_d, and the inductance L_{qw} is related with the nth resonant state lifetime by the following relation $L_{qw} = \tau_d/G_0$. Since RTD current lags behind the applied voltage so intuitively the inductance comes in series with the RTD conductance, as shown in Fig. 2.5(b).

RTDs can sustain oscillation at very high frequency only physically limited by the resonant state lifetime, the depletion layer transit time, and the device RC time. Typical RTD switching times are in general dominated by the effects of current densities and capacitances, i.e., by the circuit RC time constant [78]. Considering the device is operating at moderate frequencies, and thus neglecting the resonant tunneling time delay, i.e., assuming L_{qw} to be negligibly small, self-sustained oscillations in the microwave range can be studied using the simple series inductance equivalent circuit model of Fig. 2.5(c): the RTD conductance G_0 in parallel with the diode capacitance C, where R_S and L_S account to the RTD external circuit resistance and inductance, respectively. This model contains the following general characteristics: parameters G_0 in parallel with the diode capacitance C obtained from the static NDC conductance and RTD emitter-collector capacitance, respectively. A resistance R_S associated with the highly doped bulk regions on either side of the DBQW structure and external lead resistances associated to the contacts, wires and other bias circuit components. Finally, a series inductance L_S which in this case accounts for the lead inductances of the circuit connections (e.g. bond wires).

The highest frequency f_{max} at which a particular diode can oscillate, independent of the circuit, can be found in a first approximation using the lumped equivalent circuit shown in Fig. 2.5(c), consisting of the negative differential conductance G_0, the parasitic series resistance R_S, and a capacitance C. If we assume that all of the elements are frequency independent, the real part of the terminal impedance of this circuit is

negative up to a frequency given by [84]:

$$f_{max} = \frac{1}{2\pi C}\sqrt{\frac{-G_0}{R_S} - G_0^2}, \tag{2.8}$$

where G_0 varies rapidly from a maximum negative value G_{max} near the center of the NDC region to zero at the peak and valley points. The imaginary part of the impedance becomes zero at

$$f_{osc} = \frac{1}{2\pi}\sqrt{\frac{1}{L_S C} - \frac{G_0^2}{C^2}}, \tag{2.9}$$

which corresponds to the RTD oscillation frequency. In most of the double-barrier diodes of interest, both R_S and C are also nearly independent of bias voltage throughout the NDC region, with $C = \epsilon A/L_{depl}$, where ϵ is the dielectric constant, A is the cross sectional area of the device and L_{depl} is the depletion region width.

The voltage range over which the NDC exists for these devices limits the output power of oscillators that use them. It has been shown that the maximum output power, assuming a sinusoidal voltage waveform, is $P_{max} = (3/16)\Delta I \Delta V$, where ΔI and ΔV are the current and voltage ranges of the negative resistance [85]. This relation gives that diodes of larger area can produce more output power.

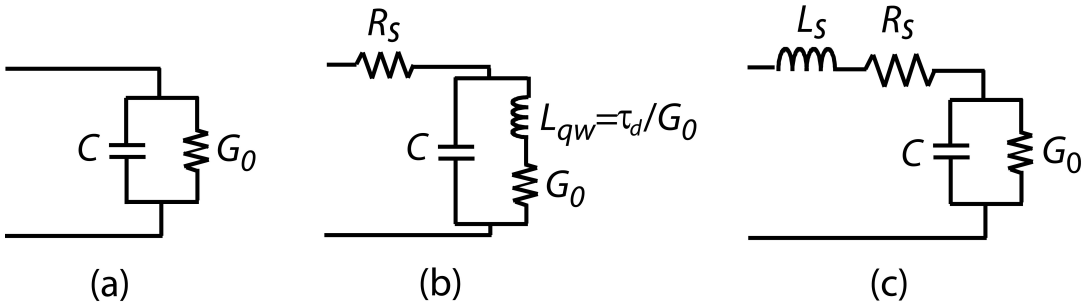

Figure 2.5: (a) RC equivalent circuit. (b) RLC equivalent circuit by Brown et al. (c) RLC equivalent circuit.

Although the previous analysis gives relevant information of RTD devices for circuit applications, in a real setup, the maximum attainable frequency and power are mainly determined by parasitics, including the inductance between the RTD and the external circuitry. In the next section, we investigate the dynamic regimes of InGaAs/AlAs DBQW-RTDs with the help a Liénard-type of oscillator model derived from the analysis of the RLC equivalent circuit of Fig. 2.5(c). The Liénard system models RTD-based RLC nonlinear oscillators and can be generalized to other type of RTD materials and

even NDC devices to explain a broad range of rich dynamics observed in these systems.

2.6 Dynamics of Liénard RTD oscillators

In this section we describe the RTD oscillator circuit using a coupled system of ODEs forming a Liénard-type model system. Such systems were first studied during the advent of the radio and vacuum tubes since certain oscillating circuits can be modeled as Liénard oscillator systems [86]. They are currently used in many areas of physics and engineering and have been the object of intensive analysis by numerous authors in nonlinear dynamical systems (see [87, 88] and the references cited therein). Among the more relevant dynamic behaviors of such systems are the existence of periodic solutions in the form of limit cycles and bifurcations (see Appendix A).

A particular example of a Liénard system is the Van der Pol oscillator. Balthasar van der Pol [2] devised the van der Pol oscillator to analyze the nonlinear oscillations in a parallel RLC circuit linked to a triode valve as the amplifier, with the anode current in the triode being a nonlinear function of the lumped voltage. The van der Pol equation can describe self-sustained oscillations in the form of limit cycles [4], not only in electronic circuits but also in many other dissipative structures including chemical reactions, biological and optical systems.

2.6.1 Liénard RTD oscillator model

Using the theory of nonlinear oscillations in terms of differential equations, here we formulate a nonlinear dynamic model from the equivalent electrical circuit shown in Fig. 2.6(a) to analyze the dynamics of the RTD oscillator. This approach follows a similar analysis performed by Quintana et al. [89] where the dynamics of a novel circuit topology able to implement frequency divider circuits based on RTDs is investigated.

In the model represented in Fig. 2.6(a), the RTD nonlinear I-V characteristic is represented by a voltage dependent current source $F(V)$, Fig. 2.6(b), in parallel with RTD intrinsic capacitance C. The resistor R and inductor L correspond to the circuit series and parasitic lead resistances and inductances, respectively. By applying Kirchhoff's rules to the circuit of Fig. 2.6(a), the voltage $V(t)$ across the capacitance C and the current $I(t)$ through the inductor L are given by the following system of two first-order differential equations:

$$\frac{dV(t)}{dt} = \frac{1}{C}\left[I(t) - F(V)\right] \tag{2.10}$$

$$\frac{dI(t)}{dt} = \frac{1}{L}\left[V_{DC} - RI(t) - V(t)\right] \tag{2.11}$$

where V_{DC} is the DC bias voltage. Since the knowledge of variables $V(t)$ and $I(t)$ completely specifies the behavior of this system, and because time itself does not explicit appear in this set of first-order differential equations, we say that the system is a two-dimensional autonomous system. The RTD oscillator modeled by Eqs. (2.10) and (2.11) is an example of a autonomous Liénard-type system [46].

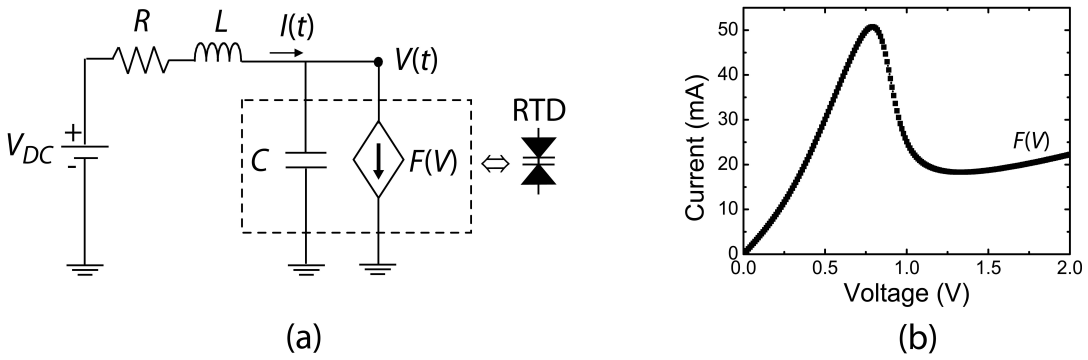

Figure 2.6: (a) Equivalent circuit configuration used in nonlinear oscillator study of RTD-based circuits. (b) InGaAs/AlAs RTD I-V characteristic given by Eq. 2.7.

The autonomous Liénard system of Eqs. (2.10) and (2.11) can be further extended to include an external electrical perturbation $V_{AC}\sin(2\pi f_{in}t)$. In this case the system is said to be nonautonomous due to the explicit dependence of time in the expression for excitation signal V_{AC}, and periodic with period $T = 1/f_{in}$, and is given by:

$$\frac{dV(t)}{dt} = \frac{1}{C}\left[I(t) - F(V)\right] \tag{2.12}$$

$$\frac{dI(t)}{dt} = \frac{1}{L}\left[V_{DC} + V_{AC}\sin(2\pi f_{in}t) - RI(t) - V(t)\right] \tag{2.13}$$

For purposes of simulation, we normalize Eqs. (2.12) and (2.13), choosing V_0 and I_0 as scale parameters with physical dimensions of current and voltage ($V_0 = 1$ V and $I_0 = 1$ A), respectively, and rescale $V(t) = x(t)V_0$, $I(t) = y(t)I_0$, $t = \tau\sqrt{LC}$, $V_{DC} = \upsilon_0 V_0$, $V_{AC} = \upsilon V_0$, $f_{in} = \Omega\omega_0$, $\omega_0 = (\sqrt{LC})^{-1}$, and $R = \gamma(V_0/I_0)$. Then $x(t)$, $y(t)$, Ω, and

τ are dimensionless. By defining the new variable $z(t) = 2\pi\Omega t$ which transforms the non-autonomous system of Eqs. (2.12) and (2.13) into an autonomous one, now with three equations, and redefining τ as t, the time scaled differential equations become:

$$\frac{dx(t)}{dt} = \frac{1}{\mu}\left[y(t) - f(x)\right], \tag{2.14}$$

$$\frac{dy(t)}{dt} = \mu\left\{\upsilon_0 + \upsilon\sin[z(t)] - \gamma y(t) - x(t)\right\}, \tag{2.15}$$

$$\frac{dz(t)}{dt} = 2\pi\Omega \tag{2.16}$$

In Eqs. (2.14)-(2.16), the function $f(x)$ comes from the normalization of $F(V)$ and $\mu = V_0/I_0\sqrt{C/L}$ is dimensionless. The dynamics of the forced Liénard RTD oscillator system now depends on parameters μ, γ, υ_0, υ, and Ω.

The Liénard RTD oscillator system subject to an external time-dependent force provides an additional degree of freedom and new possibilities emerge from the three-dimensional system described by Eqs. (2.14)-(2.16). Foremost of these new possibilities is chaos. In what follows we discuss the types of dynamical regimes that can occur in the forced Liénard RTD oscillator.

2.6.2 Self-sustained oscillations

The Liénard oscillator described by the differential equations (2.14)-(2.16) is a system with at least two dimensions, which means that it is possible to have cyclic or periodic behavior represented by closed loop trajectories in the state space: the limit cycle solution (see Appendix A). The motion on a limit cycle in state space represents oscillatory, repeating motion of the Liénard system, which in our case represents the formation of self-sustained microwave oscillations in the electrical domain.

The analysis of the Liénard oscillator starts with the investigation of limit cycles without external injection ($\upsilon = 0$) by analyzing the location of its fixed points. Fixed points (equilibria) of Eqs. (2.14) and (2.16) occur when $dx(t)/dt = 0$ and $dy(t)/dt = 0$. These points are obtained solving the following equations:

$$y = f(x) \tag{2.17}$$

$$y = \frac{1}{\gamma}(\upsilon_0 - x) \tag{2.18}$$

Equation 2.17 is the I-V characteristic of the RTD, and Eq. (2.18) is the load line. Fixed points occur at the points of intersection of these pair of curves. Since Eq. (2.17) describes a curve with two turning points and Eq. (2.18) is a straight line, the general configuration of the fixed points can be deduced.

Figure 2.7(a) shows an example of a limit cycle when the load line intersects the downward sloping section of $f(x)$. Self-sustained oscillations occur when there is a stable periodic orbit. This is the Van der Pol-like situation which results in a stable oscillation if the downward sloping section of $f(x)$ is sufficiently steep. The $f(x)$ and load line curves presented in Fig. 2.7(a) describe the situation where γ is small, that is, when the series resistance, R, is such that $R < |dF(V)/dV|$. In this situation, the load line is steep and the curves only intersect at a single point in the NDC region as υ_0 is increased from zero, and self-sustained oscillations build up. Intersections on the other sections of the curve give stable equilibria and no oscillations are present (e.g. dashed load line in Fig. 2.7(a) intersects PDC region of the I-V).

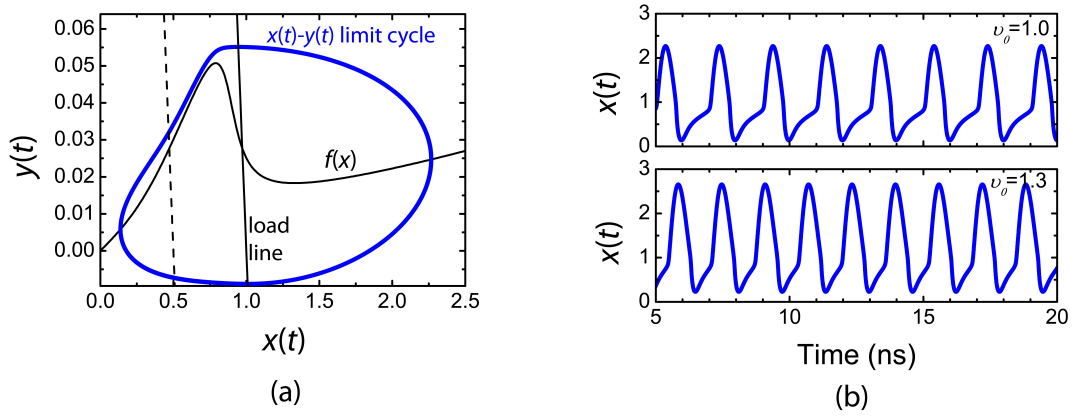

Figure 2.7: (a) I-V characteristic $f(x)$ function, load lines and $x(t) - y(t)$ limit cycle at $\upsilon_0 = 1.0$. (b) Self-sustained relaxation oscillations of voltage $x(t)$ output in time domain at $\upsilon_0 = 1$ and $\upsilon_0 = 1.3$.

To obtain the plot of the limit cycle we employed numerical integration (Runge Kutta methods [90]) of the ODE system of Eqs. (2.14)-(2.16) with the following electrical circuit parameters $R = 1\ \Omega$, $L = 9$ nH, $C = 5.5$ pF, and biasing in the NDC region of $f(x)$ (in this case $\upsilon_0 = 1.0$). Both current and voltage normalized outputs (excluding the time domain variable) are plotted in the limit cycle graph of Fig. 2.7(a). The analysis of the phase portrait confirms the existence of a stable limit cycle in the $x(t)$-$y(t)$ phase plane. Circular limit cycles correspond to sinusoidal oscillations. In

the example of Fig. 2.7(a) the self-sustained oscillations produced are of the type of relaxation oscillations, which are characteristic of negative resistance-type of oscillators (e. g. van der Pol oscillator). This type of motion involves in the limit cycle two time scales, a fast horizontal movement and a slow vertical motion, in which its shape is a direct consequence of the strong nonlinearity and anti-symmetry of the I-V curve. Likewise the characteristics of the oscillations are determined by parameters μ and υ_0.

Figure 2.7(b) shows typical relaxation oscillations in time domain for the same set of electrical circuit parameters varying the parameter υ_0: 0.498 GHz oscillation frequency when $\upsilon_0 = 1$ and 0.616 GHz when $\upsilon_0 = 1.3$. As shown in Fig. 2.7(b), because this change in the parameter υ_0 will cause the amplitude and frequency of the oscillation to change, the Liénard oscillator exhibits a frequency tunability as a function of bias voltage which has interesting applications for novel types of voltage controlled oscillator (VCO) systems, discussed later in this thesis (Chapter 3).

2.6.3 Synchronization

Synchronization (or frequency locking) of an oscillator is a common phenomenon whenever two or more oscillation frequencies (within the same physical system or physically distinct oscillators) interact nonlinearly [3].

Considering the Liénard oscillator, the mechanism of locking can be illustrated as follows. In the absence of the driving signal, the dynamics evolves towards a period attractor (limit cycle) as described in the previous subsection, with Ω_0 being the proper frequency of the attractor. If a driving signal is perturbing the system at frequency Ω, and if the two frequencies are commensurate over some range of control parameter values (e.g., amplitude of the driving signal), that is:

$$\frac{\Omega}{\Omega_0} = \frac{p}{q} \tag{2.19}$$

with p and q integers. Then we say the frequencies are frequency locked over this parameter range, at a given amplitude of the driving signal. How close Ω has to be a rational multiple of Ω_0 depends on the amplitude and on the multiple itself.

In order to study the frequency locking dynamics, we consider the case of electrical injection of a periodic signal $\upsilon \sin(2\pi\Omega t)$, where υ is the external amplitude and Ω the external frequency. The overall dynamic response considering both control parameters - external frequency and amplitude - was mapped solving the differential equations (2.14)-(2.16) and plotting the results in the $\upsilon - \Omega_p$ plane to illustrate the range of frequency ratios over which locking occurs, where Ω_p is the frequency ratio Ω/Ω_0 (Ω_0

was set to 0.1109 corresponding to the oscillator natural frequency of 0.498 GHz).

In Fig. 2.8 are presented the $2D$ locking maps for two fixed bias voltage. In either map each wedge-shaped colored region corresponds to a tongue and is related with a periodic region signed with its corresponding number p/q ratio. As υ increases, the frequency locking regions expand to fill finite intervals along the Ω_p interval. The main tongues in Fig. 2.8(a) are marked with $1:1$, $2:1$, and $3:1$, corresponding to the fundamental and harmonic frequency-locking regions. These regions were called Arnold tongues after the Russian mathematician who pioneered the study of frequency-locking [91]. As shown in Fig. 2.8(b), by increasing the bias voltage, the frequency-locking intervals are reduced due to the increase of the amplitude of free-running oscillations. Between each large locking region one can find several types of behavior, including sub-harmonic locking with narrower tongue regions and aperiodic outputs, namely quasi-periodic signals and chaos. In the graphics of Fig. 2.8 the white regions between tongues correspond to the aperiodic outputs.

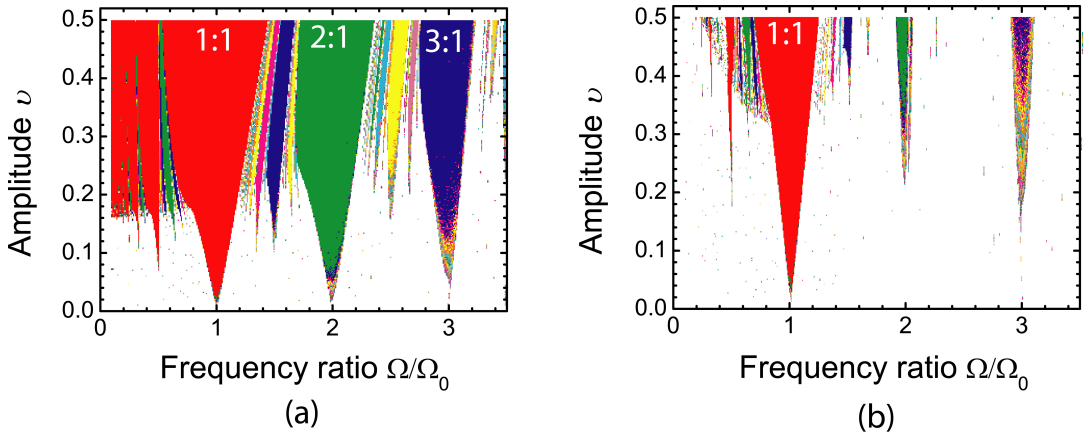

Figure 2.8: Arnold tongues map for electrical injection of a periodic signal at a fixed bias voltage (a) $\upsilon_0 = 1.0$ and (b) $\upsilon_0 = 1.3$.

In order to map with more detail the locked and unlocked regions, the dynamics of the Liénard oscillator was analyzed using $1D$ bifurcation maps. The bifurcation maps were constructed by calculating the time series of a given system variable, such as the voltage or current, and plotting the corresponding peak heights as a function of a given circuit control parameter, for example external frequency. In Fig. 2.9(a) we present the bifurcation map for the voltage $x(t)$ output as a function of frequency ratio Ω_p, for the frequencies between $0.002 < \Omega < 0.55$ at a fixed amplitude $\upsilon = 0.2$. As pictured in Fig. 2.9(a), increasing the external frequency Ω from close to DC until $\Omega = 0.55$,

a stable periodic signal marked with 1:1 is obtained, followed by a aperiodic region, then a stable 2:1 region, followed by a aperiodic region, and so on. This phenomenon is known as period-adding bifurcation (also referred as frequency division operation [89] or frequency demultiplication [4]), and is similar to the behavior found in the van der Pol oscillator system [4]. The period-adding sequence presented in the bifurcation map in Fig. 2.9(a) follows the broader locking regions related with the fundamental and harmonic natural frequencies of the Liénard oscillator.

In a close analysis of the bifurcation maps, Fig. 2.9(b), we find a fine structure of locking as a result of the competition between the self-sustained oscillation and the external injected signal. As shown in Fig. 2.9(b), the sub-harmonic frequency locking regions decrease in length (along the Ω axis) when the denominator in the fraction p/q increases. For example, the sub-harmonic locking region $5:3$ is shorter than the sub-harmonic locking region $3:2$. These regions can be easily mapped by constructing the so-called Farey tree that is based in the theory of numbers [92]: if we have two rational fractions p/q and p'/q', the rational fraction that lies between and has the smallest denominator is the rational fraction $(p+p')/(q+q')$.

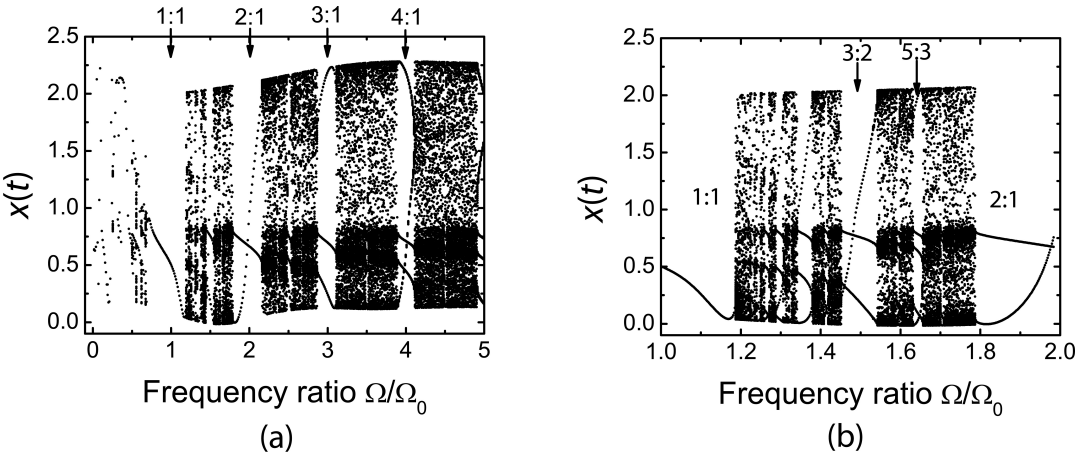

Figure 2.9: (a) Bifurcation map for electrical injection of a periodic signal at fixed amplitude $\upsilon = 0.2$. (b) Detailed bifurcation map in the region of frequencies $0.1 < \Omega < 0.22$ showing an example of the Farey tree sequence.

In Fig. 2.10 are shown some examples of locked and unlocked signals in the (a) time domain, (b) phase space, and (c) Fourier domain using power spectral density (PSD) computed by means of Fast Fourier Transform (FFT) technique of the time series output (see Appendix A). Clear trajectories are observed in phase space when the

Liénard oscillator is locked. The power spectrum is characterized by sharp peaks at the fundamental frequency and its harmonics [three of them appear in the locked region 1:1 of Fig. 2.10(c)]. When the system is not frequency locked and the ratio of frequencies cannot be expressed as a ratio of integers, then the ratio is called irrational and the motion is said to be aperiodic or quasi-periodic because it never exactly repeats itself, and it is composed of an infinite set of trajectories which belong to an invariant closed curve [Fig. 2.10(b) at $\Omega = 0.142$]. The corresponding FFT [Fig. 2.10(c)(*bottom*)] shows a rich harmonic content, which is typical in a quasi-periodic signal.

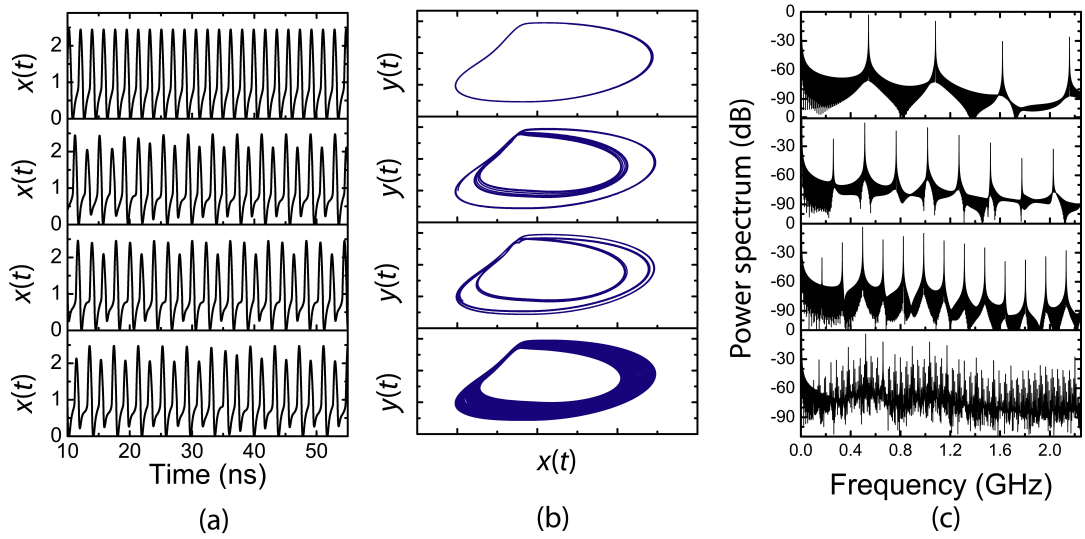

Figure 2.10: (a) Time series of voltage $x(t)$ output, (b) phase space plots onto the $x(t) - y(t)$ plane, and (c) the power spectra plots of $x(t)$ for the following locking regions (from *top* to *bottom*): 1:1 ($\Omega = 0.12$), 3:2 ($\Omega = 0.17$), 5:3 ($\Omega = 0.182$), and aperiodic region at $\Omega = 0.142$.

2.6.4 Quasi-periodic route to chaos

Here we analyze the route to chaos found in the Liénard oscillator. The system follows the quasi-periodic route to chaos scenario and begins with a limit cycle trajectory. As a control parameter is increased, for example the external frequency Ω, a second periodicity appears in the behavior of the system. If the ratio of the period of the second type of motion to the period of the first is not a rational ratio, then we say, as described previously, that the motion is aperiodic or quasi-periodic. Under some circumstances,

if the control parameter is increased further, the motion becomes chaotic.

The strongest evidence of the chaotic dynamics is provided by the evolution of different trajectories. In Fig. 2.11(a) is an example where two time series for $x(t)$ started at initial conditions (x_0, y_0, z_0), whose difference was about 1%. Up to $t \approx 70$ ns the time series are practically identically, however for times longer than 70 ns they evolve independently. This means that for an initial condition measured with an error of 1%, predictability of its future state becomes lost at $t \approx 70$ ns. This loss of predictability is the essential feature of chaos.

Another characteristic of chaos is that although an aperiodic orbit starting at different initial conditions will result in different trajectories, the structure of the two trajectories will remain essential the same, Fig. 2.11(b). This illustrates that despite its aperiodicity, the non periodic solutions have some invariant structure. Another strong evidence the system shows chaotic outputs is provided by its power spectrum, Fig. 2.11(c), which is broadband and continuous, a signature of a chaotic signal. The remaining peaks observed in Fig. 2.11(c) correspond to the injected external signal, the free-running signal and to minor vestiges of some quasi-periodicity, which are an indication that the system dynamics evolves into a quasi-periodic route to chaos.

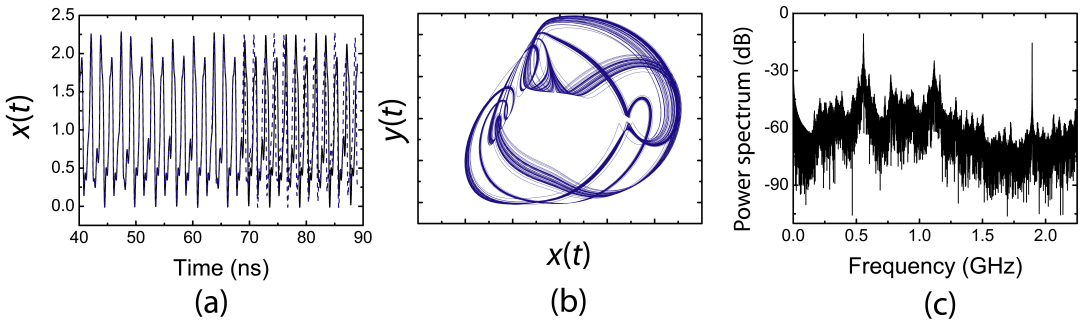

Figure 2.11: (a) Two time series of $x(t)$ output at close initial conditions, (b) phase space plots onto the $x(t) - y(t)$ plane, and (c) the power spectrum plot of $x(t)$ for a chaotic region at $\Omega = 0.421$.

In order to characterize chaotic orbits, the analysis continues further with the determination of the system's Lyapunov exponents (see Appendix A). Lyapunov exponents measure the rate of divergence of nearby trajectories, and is a key component of chaotic dynamic studies. A positive Lyapunov exponent is taken as the defining signature of chaos. The Lyapunov exponents also discriminate between the different dynamics: a limit cycle will have one zero exponent, with the others being negative; a $m-$frequency

quasi-periodic orbit will have m zero exponents, with the remaining negative (in the case of the forced Liénard system $m = 2$), and a chaotic signal will have one positive exponent, one zero exponent and one negative. Figure 2.12(a) presents the three Lyapunov exponents of the Liénard RTD system evaluated accordingly to the numerical algorithm computation package presented in [93]: there is a minimum exponent, always negative, there is a null exponent for all values of the frequency, and a third exponent that can take negative and positive values. Figure 2.12(b) shows the largest Lyapunov exponent as a function of the frequency ratio calculated from the Lyapunov characteristic exponent (LCE) of the forced Liénard RTD oscillator system. Under these conditions, in the Ω interval considered, chaotic states with positive exponent occur between windows of periodic and quasi-periodic regions. These chaotic transitions become more evident increasing the amplitude of the driving signal.

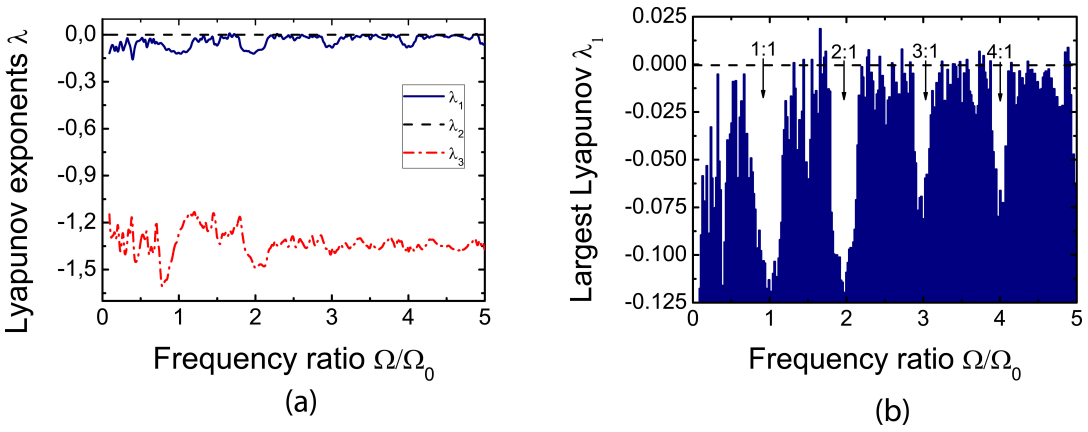

Figure 2.12: (a) The Lyapunov exponents as a function of the external injected frequency parameter at $\upsilon = 0.2$ showing the three exponents. (b) Histogram with a detailed view of the largest Lyapunov exponent λ_1.

As a final note, the injection locking phenomenon, the existence of the Arnold tongues, and the route to chaos studied numerically for the forced Liénard RTD oscillator are found in similar mathematical models that study electronic circuits, such as the van der Pol equation, the Chua circuit, among others. The van der Pol equation is a particular type (it is obtained by setting $f(x)$ by a third order polynomial function) of the Liénard equation. Because we are interested in the exact structure of the Arnold tongues, which is strongly depended on the particular form of the nonlinear system under study, the Liénard model provides a theoretical framework for the analysis of the nonlinear dynamics of circuits employing RTD devices.

2.7 Semiconductor lasers

The main application of semiconductor lasers is as sources for optical communication systems. A unique feature of semiconductor lasers is that, unlike other lasers that are modulated externally, the semiconductor laser can be modulated directly by current injection. This is especially important in view of the possibility of monolithic integration of the laser and the driver electronic circuit. In this section, we outline the theoretical study of the nonlinear dynamics in directly modulated lasers using single mode laser rate equations which provides a general framework for the analysis of the nonlinear operation regimes of LD-based systems.

2.7.1 Instabilities in directly modulated lasers

The structure of semiconductor lasers is based on the $p-n$ junction of the semiconductor materials and the laser oscillation is realized by the emission of light due to carrier recombination (equivalently the population inversion) between the conduction and valence bands (an extensive review can be found, for example, in the books of Agrawal and Dutta [94], and Petermann [95]). Semiconductor lasers are intrinsically stable, however, they can be destabilized by external perturbations such as current injection, optical feedback and optical injection. For example, in laser diodes with optical feedback successive sub-harmonic bifurcation and quasi-periodic routes to chaos have been observed (an extensive review can be found in [20, 21]).

Semiconductor lasers can be directly modulated through the injection current. The direct modulation is simple, efficient, and applicable to high-speed modulation which are important features that allows a variety of applications, namely for optical communications. A modulation for the injection current itself introduces an extra degree of freedom to the semiconductor laser system that can induce instability and chaos in its output. In directly modulated semiconductor lasers route to chaos through period-doubling bifurcations has been found in non-self-pulsing lasers [96], and route to chaos via quasi-periodicity has been investigated for self-pulsing lasers [97]. The chaotic phenomena occurs because of the interaction between temporal changes in the carriers and photons where the relaxation oscillation plays a crucial role for the modulation properties in semiconductor lasers. Applications of chaotic lasers are still growing and developing for secure optical chaos communications [27, 98].

2.7.2 Outline of laser rate equations

Modeling lasers may be realized with different levels of sophistication. Rigorously it requires a full quantum treatment but many laser dynamical properties may be captured by semiclassical or even purely classical approaches. Here we present a basic framework of analysis provided by the rate equations, a set of coupled ODEs to describe the behavior of the laser.

In their simplest version, they apply to an idealized active system consisting of only two energy levels coupled to a reservoir. They were originally introduced as soon as the laser was discovered to explain intensity spikes commonly seen with solid state lasers. They capture the essential features of the response of a single mode laser and they may be modified to account for specific effects such as the modulation of a parameter or optical feedback.

The rate equations presented here describe class B lasers that can only show coupled electric field-carrier density oscillations, the relaxation oscillations [21]. Edge-emitting type of lasers such as FP type with a monolayer of the active region, and other edge-emitting lasers such as multi-quantum well lasers and distributed feedback (DFB) lasers, can be treated in a similar manner. Although these lasers present different structures, the derivation of the rate equations for laser operations is similarly given and almost the same equations are obtained. Therefore, the macroscopic features of these lasers show the same behaviors from the point of view of chaotic dynamics, although the parameters in the rate equations may vary from one laser to other to account the characteristics strongly depend on the laser structure and the particular values of the device parameters.

The assumptions that go into formulating the rate equations are that the laser oscillates in a single mode and the population inversion is homogeneous. The rate equations for the photon $S(t)$ and injected carrier $N(t)$ densities in the active region are given by [99]:

$$\frac{dN(t)}{dt} = \frac{I_m(t)}{qV_{act}} - \frac{N(t)}{\tau_n} - g_0[N(t) - N_0][1 - \epsilon_N S(t)]S(t), \tag{2.20}$$

$$\frac{dS(t)}{dt} = \Gamma g_0[N(t) - N_0][1 - \epsilon_N S(t)]S(t) - \frac{S(t)}{\tau_p} + \Gamma\beta\frac{N(t)}{\tau_n}, \tag{2.21}$$

where $I_m(t)$ is the injection current, q is the unit electric charge, V_{act} is the active region volume, τ_n and τ_p are the spontaneous electron and photon lifetimes, respectively, the spontaneous emission factor β is the fraction of the spontaneous emission that is coupled

to the lasing mode; the gain function is linearized around the transparency density N_0, and the parameter g_0 is the differential gain; ϵ_n is the value for the nonlinear gain compression factor, and Γ is the optical confinement. In the model we have included the phenomenological parameter ϵ_n to account for additional nonlinearities that exist between the input current and the output photon relationship in real semiconductor lasers, so that we can approximate the gain as $g \cong g_0[1 - \epsilon_n S(t)][N(t) - N_0]$, where g_0 is the gain in the absence of any stimulated emission. When the photon density $S(t)$ in the laser cavity starts to increase, the gain of the laser starts to decrease and it becomes increasingly harder to generate a high power from the device. Not all nonlinearities exhibited by semiconductor lasers can be modeled simply by using the parameter ϵ_n (for example nonlinearities from coherent reflected waves from the laser mirror facets). Despite this, the rate equations in the form of Eqs. (2.20) and (2.21) are generally accepted to form a good mathematical model for single mode semiconductor lasers. In the model we have also included the effect of spontaneous emission β, adding the term $\beta\Gamma N(t)/\tau_n$ in the photon rate equation. As will be discussed later, ϵ_n and β are key control parameters in the description of the laser dynamics.

In Table 2.2 are presented laser rate equation parameters and typical values. The laser output power P_f is calculated using the equation:

$$\frac{S(t)}{P_f} = \frac{\Gamma\tau_p\lambda_0}{V_{act}\eta_{ld}hc}, \tag{2.22}$$

where η_{ld} is the differential quantum efficiency per facet, λ_0 is the emission wavelength, h is Planck's constant, and c is the speed of light in a vacuum.

For directly modulated semiconductor lasers the rate equations (2.20) and (2.21) mathematically relate the interaction between electrons and photons within the laser cavity and thus describe some of the nonlinearity in the input-output relationship between the current driving the laser, and the light output. The model based on rate equations easily facilitates the simulation of complicated input signals. Moreover, the rate equations parameters are easily identifiable and the effects of changing them can be easily seen in the laser output. In a semiconductor laser with external current injection, Eq. (2.20), a sinusoidal injection current modulation is applied to the bias injection current and $I_m(t)$ is given by:

$$I_m(t) = I_b\{1 + m\sin(2\pi f_{in}t)\}, \tag{2.23}$$

where f_{in} is the modulation frequency, m is the modulation index, and I_b is the DC bias current.

The small-signal response of rate equations behavior is similar to that of a *RLC* parallel oscillator circuit. The dynamical response can be, in a first approximation, characterized by the relaxation-oscillation frequency f_{ro} which is given by:

$$f_{ro} = \frac{1}{2\pi}\left(\frac{\Gamma g_0}{qV_{act}}\right)^{1/2}(I_{dc} - I_{th})^{1/2}, \tag{2.24}$$

where I_{th} is the laser threshold current:

$$I_{th} = qV_{act}[N_0 + (\Gamma g_0 \tau_p)^{-1}]/\tau_n, \tag{2.25}$$

Relaxation oscillation in a semiconductor laser occurs because the carrier cannot follow the photon decay rate. The presence of the relaxation oscillation gives rise to complex dynamics when the laser is perturbed by external disturbances as discussed in this section.

For numerical purposes Eqs. (2.20) and (2.21) are rescaled making use of the normalized carrier density $n(t)$ and the normalized photon density carrier $s(t)$, setting $N(t) = n(t)N_{th}$ and $S(t) = s(t)S_0$, and $t = \tau\tau_n$, where $S_0 = \Gamma(\tau_p/\tau_n)N_{th}$ and $N_{th} = N_0 + (\Gamma g_0\tau_p)^{-1}$ is the threshold carrier density. Redefining τ as t, the time scaled differential rate equations become:

$$\frac{dn(t)}{dt} = \frac{i_b}{i_{th}}\{1 + m\sin(z)\} - n - \frac{n(t)-\delta}{1-\delta}[1 - \epsilon s(t)]s(t), \tag{2.26}$$

$$\frac{ds(t)}{dt} = T_n\left[\frac{n(t)-\delta}{1-\delta}[1-\epsilon s(t)]s(t) - s(t) + \beta n\right], \tag{2.27}$$

$$\frac{dz(t)}{dt} = 2\pi\Omega_m, \tag{2.28}$$

where $\delta = N_0/N_{th}$ and $\epsilon = \epsilon_n S_0$ are two dimensionless parameters, i_{th} is the laser diode threshold current, and the parameter $T_n = \tau_n/\tau_p$ comes from the time rescaling. On the right-hand side of Eq. (2.26), the first term, $i_b + i_m\sin(\omega_m t)$, is the injection current, composed of a constant bias term i_b and of a sinusoidally varying modulation, with normalized angular frequency $\omega_m = 2\pi f_{in}\tau_n$ (f_{in} is the applied modulation frequency). The bias and modulation levels are defined, respectively, by the bias index, $p = i_b/i_{th}$, and modulation index $m = i_m/i_b$.

Table 2.2: Description of the standard laser rate equations parameters and the typical values used in the numerical simulation.

Symbol	Parameter	Value
V_{act}	active region volume	6.75×10^{-11} cm^3
τ_n	carrier lifetime	2×10^{-9} s
τ_p	photon lifetime	1.2×10^{-12} s
β	spontaneous emission	1×10^{-5}
g_0	gain coefficient	10^{-6} cm^3/s
N_0	optical transparency density	10^{18} cm^{-3}
ϵ_n	nonlinear gain compression	3.24×10^{-17} cm^3
Γ	optical confinement factor	0.44

2.7.3 Period-doubling bifurcation route to chaos

Several experimental and theoretical studies have shown the dynamics of lasers is strongly dependent on spontaneous emission and gain saturation. These results in various dynamic regimes in the laser output power included the observation of resonance frequency shift, bistability, and period-doubling bifurcations. In this section we analyze the laser rate equations, Eqs. (2.26)-(2.28), in the presence of sinusoidal injection current modulation and discuss the stability and instabilities in the laser system paying attention to the nonlinear gain saturation coefficient ϵ and the spontaneous emission factor β.

The output from a semiconductor laser faithfully follows an injection current modulation as far as the modulation index is small. On the other hand, for strong injection current modulation, the laser power clearly exhibits a number of nonlinear characteristics. We have numerically calculated the maps for the model of a standard edge-emitting laser with typical values given in Table 2.2. Figure 2.13 is the plot of the chaotic map using the injected frequency and modulation index as control parameters with bias index $i_b/i_{th} = 1.15$. In this condition, the relaxation oscillation frequency that depends on the bias injection current is around 1.56 GHz. The nonlinear gain saturation coefficient ϵ and the spontaneous emission factor β were set to $\epsilon = 1 \times 10^{-4}$ and $\beta = 1 \times 10^{-5}$, respectively.

The map of 2.13 shows that for low and moderate modulation index, and when the injected frequency is below the laser resonance frequency, the laser response has the same periodicity as the modulation, which corresponds to the region denoted as $period-1$. When both modulation frequency and index are large, $period-2$ oscillations emerge into the laser output, as shown in the map. Increasing further the modulation

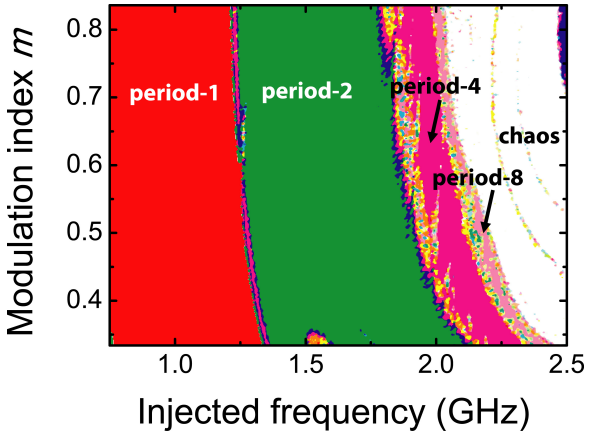

Figure 2.13: Simulated chaotic map for a bias current injection $i_b = 1.15 i_{th}$ at $\epsilon = 1 \times 10^{-4}$, and $\beta = 1 \times 10^{-5}$.

frequency, a period-doubling route to chaos is observed.

In Fig. 2.14 are plotted the corresponding laser output signals at $m = 0.5$ in the time domain (a), phase space (b), and Fourier domain (c) of the period-doubling route to chaos mapped in Fig 2.13. From *top* to *bottom* in Fig. 2.14 are plotted the graphics for $period-2$, $period-4$, $period-8$, and chaotic oscillations. These behaviors observed in the laser output are explained as follows: the laser exhibits intense pulses and the carrier number is abruptly decreased after the oscillations of intense pulses when the injection current is strongly modulated. If the modulation frequency exceeds the relaxation oscillation frequency, a longer recovery time than the modulation period is required to restore the carrier number enough for the laser oscillation. Then, the laser may oscillate at a frequency beyond the period of the modulation and result in $period-2$ oscillations and so forth.

Some types of laser dynamics are greatly affected by spontaneous emission of light which results in less effect for unstable oscillations induced by the injection current modulation. The theoretical analysis of the bifurcation maps of laser output provides a useful tool to identify the possible dynamics dependence on the spontaneous emission parameter. In Fig 2.15 are plotted the bifurcation diagrams of photon density outputs for similar conditions presented in Figs. 2.13 and 2.14. Fig. 2.15(a) shows an example of period-doubling route to chaos using a low value of the spontaneous emission coefficient. Fixing all the parameters and increasing β, we observe a suppression of the chaotic regions, Fig. 2.15(b). Increasing further the value of β, the periodic states of high order disappear and the laser follows the current modulation. These results have been

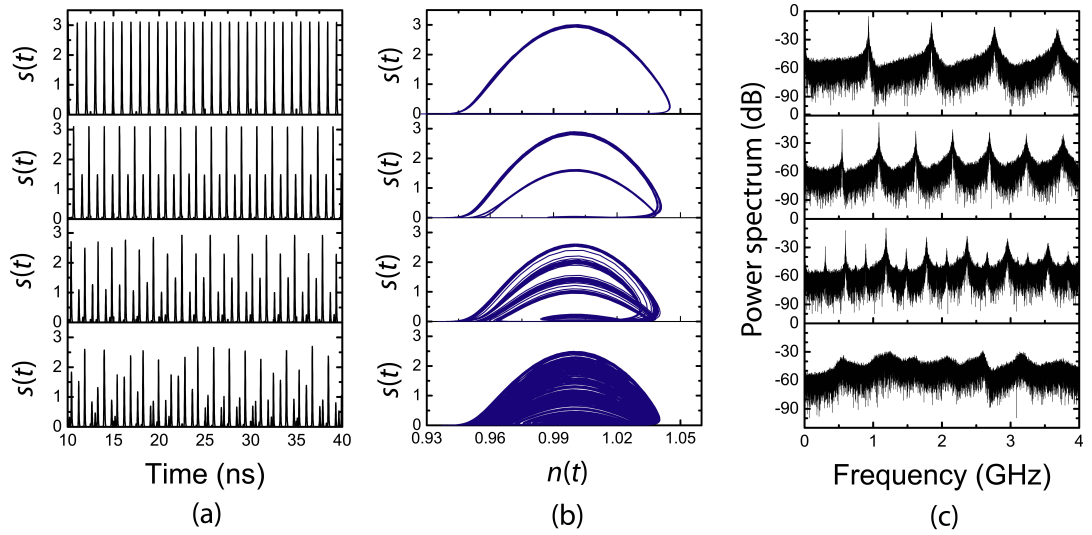

Figure 2.14: Numerical simulated (a) time series of $s(t)$ output, (b) $n(t) - s(t)$ phase space, and (c) power spectra for the following regions (from *top* to *bottom*): $period-2$ ($\Omega = 3.5$), $period-4$ ($\Omega = 4.0$), $period-8$ ($\Omega = 4.25$), and chaotic region at $\Omega = 4.5$. In all simulations the bias current injection was set to $i_b = 1.15 i_{th}$, $\epsilon = 1 \times 10^{-4}$, and $\beta = 1 \times 10^{-5}$.

also reported experimentally suggesting that period-doubling bifurcations and chaos in lasers are due to unusual low values of β measured in the lasers [96]. Several studies show the nonlinear gain saturation factor also suppress the bifurcations and chaos [20].

Despite the complex dynamics presented here, not all lasers show unstable oscillations for the injection current modulation. Some lasers show instabilities for strong injection current modulation, but others not. For example, the dynamics strongly depends on device structures such as the FP laser or the DFB laser. The important parameters for the nonlinear dynamics are the nonlinear gain saturation factor and the spontaneous emission factor. The nonlinear gain saturation factor is almost the same for the two types of lasers - usually the factor of DFB lasers is 1.5 times larger than that of FP lasers. On the other hand, the difference of the spontaneous emission coefficient can be 50 times larger in the FP type of lasers. These studies suggest that obtaining rich dynamics in the laser output is strongly dependent on LD characteristics. Thus, novel ways of producing complex dynamics in the laser output are being considered to fully take advantage of the efficiency and high-speed direct modulation capabilities of semiconductor lasers.

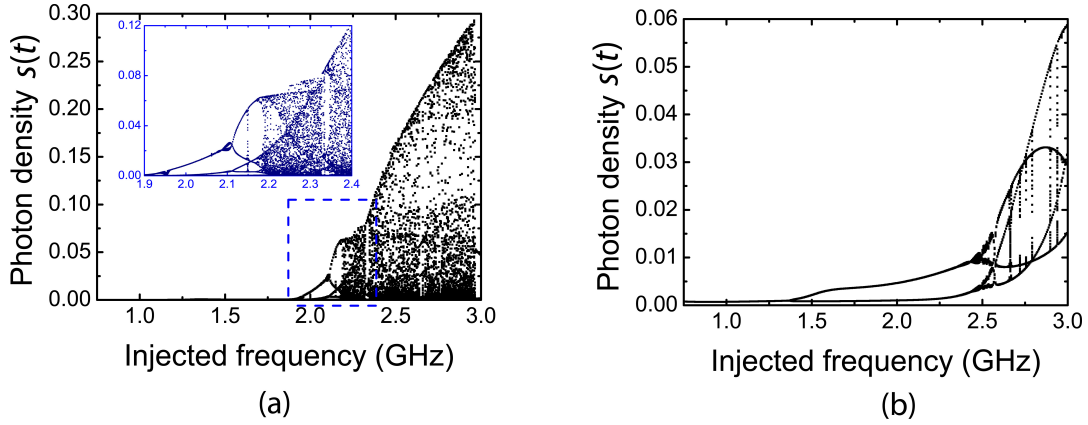

Figure 2.15: Bifurcation maps varying the external frequency. (a) Period-doubling route to chaos at $\beta = 1 \times 10^{-5}$. Inset is shown an enlargement of a small region indicated by a dashed rectangle. (b) Chaos suppression at $\beta = 1 \times 10^{-4}$. In both simulations $\epsilon = 1 \times 10^{-4}$ and $m = 0.5$.

2.8 Chapter summary

In this chapter we have presented a dynamical system theory to model nonlinear RTD-based systems in combination with circuit analysis. After a discussion on semiconductor nonlinear dynamic systems and an introduction on the basic notions of RTD devices, the nonlinear RTD oscillator system was analyzed using a coupled system of ODEs forming the Liénard RTD oscillator model. The dynamics of the Liénard oscillator was numerically investigated and it was found the dynamical regimes of these oscillator systems range from self-sustained-oscillations controlled by voltage to synchronization following a period-adding sequence behavior (also called frequency division), and chaos generation in a quasi-periodic route to chaos when subjected to external periodic injection.

Ultimately, we have investigated the dynamical regimes of directly modulated lasers using laser rate equations. The conditions for generation of bifurcations and chaos from edge-emitting semiconductor lasers under external perturbation were investigated. The period-doubling bifurcation routes to chaos are the predominant instabilities found in directly modulated lasers and the dynamics is strongly depended on devices' structures, including the factor of spontaneous emission and the nonlinear gain saturation.

Chapter 3

Synchronization and chaos in RTD-laser diode oscillators

3.1 Introduction

There is significant interest in developing transmitter and receiver sources with potential to meet future telecommunication and computing systems needs. The implementation of electro-optical and all-optical solutions taking in consideration the nonlinearity of semiconductor active devices (e.g. optoelectronic oscillators and laser diodes) attracted considerable attention in the last decade for synchronization and complex chaos generation, mainly because of their for applications in microwave-photonics systems [7] and secure optical chaos communications [27, 98].

In chaos-based communication systems the receiver is synchronized with the chaotic emitter to decode the message [65, 100]. The noise-like appearance of chaos is used to conceal the message leading to a better masking of the information-bearing signal. The use of chaotic carriers in communication allows steganography at the physical layer, improving the security of encryption techniques [101]. Most generators and receivers of optical chaotic carriers capable of synchronization are based on complex laser schemes where semiconductor laser operation is disturbed using either optical feedback [98], optoelectronic feedback [19, 102], direct modulation [103], or more recently using photonic integrated circuit (PIC) [104, 105] implementations, which induce instabilities in the laser that leads to the generation of chaotic optical outputs. These systems require a considerable number of linear and nonlinear optoelectronic components making them not practical configurations.

In this chapter, a hybrid optoelectronic circuit capable of synchronization and chaos

generation is investigated using OEIC devices. OEIC technology targets the integration of optical and electronic components on the same semiconductor chip. The objective is to emulate the success that silicon technology has demonstrated and produce chips with increased functionality, speed, reliability, and reduced size at low cost [106]. OEIC transmitter modules have been studied for optical communication systems, and comprise optical and electronic devices such as laser diodes and driver integrated circuits [107]. Due to the materials fabrication challenges presented by integration of very different components on a single chip, it is generally recognized OEIC modules can be assembled using a hybrid circuit approach, where we can redesign the devices and improve the processing pursuing simple packaging, or exploit the dynamical performance with more flexibility.

Here we investigate the nonlinear dynamics of optoelectronic HIC transmitter modules comprising RTD and LD devices. The progresses made on the hybrid RTD-LD modules established a new-type of RTD-based oscillator circuits that led to some significant breakthroughs including the demonstration of various dynamical regimes such as voltage controlled autonomous relaxation oscillations in both electrical and optical domains, as well as transitions between synchronization and chaos via pattern forming bifurcations when driven with a sinusoidal modulation voltage. The characterization of the implemented hybrid oscillator prototypes was carried out along with numerical simulations that confirmed the aforementioned dynamical scenarios. The experimental and modeling investigation has provided fundamental insight into the underlying physics and performance of the RTD-LD oscillator modules.

3.2 Aim and objectives

The aim of the work described in this chapter is to investigate the output dynamics of hybrid integrated RTD-LD oscillators consisting of discrete RTD and LD components, and validate the numerical model through computational simulation. These aims were achieved through the following objectives:

- Design, assemble, and connect in a printed circuit board (PCB) a HIC oscillator consisting of a DBQW-RTD connected electrically in series with a LD.
- Implement a bias stabilization circuit to solve low-frequency instabilities associated to RTD-based oscillator devices.
- Characterize and classify the electrical and optical operation regimes of RTD-LD oscillator circuits in terms of nonlinear dynamics.

- Utilize the Liénard oscillator and the laser rate equation numerical models introduced in the previous chapter to understand the dynamical behavior of RTD-LD oscillators.

3.3 Chapter overview

In this chapter, the constituent active components of the hybrid circuit (RTD and LD) and how they are assembled in a RTD-LD HIC are discussed, followed by a description of the electrical and optical characteristics of the RTD-LD, and principle of operation. Finally, the dynamical regimes in both electrical and optical outputs are described and demonstrated. The experimental results will be validated through computational numerical simulations using the coupled Liénard-laser diode oscillator model.

3.4 RTD-laser diode optoelectronic integrated circuits

A light-wave OEIC transmitter comprises a driving circuit and a light emitting diode (LED) or a laser diode which converts the electrical signal containing the information into an optical modulated signal. Alternatives to traditional laser diode transistor-driver circuits [108, 109] have been proposed based on the integration of DBQW based devices with semiconductor light sources, including the RTD-LED [110], vertically integrated semiconductor lasers with RTDs [111], resonant tunneling effect quantum-well lasers [112], and more recently the RTD monolithically integrated with an optical communications laser (the RTD-LD) [44].

Since DBQW layers fit well with the epitaxial layers that make up semiconductor light sources and because RTDs are high frequency semiconductor devices operating at room temperature with low power consumption, DBQW-RTD-based driving circuits are interesting alternatives to transistor-based driver circuits in OEIC transmitters and receivers.

3.4.1 Hybrid and monolithic RTD-LD oscillator circuits

High-speed OEICs can be implemented through two approaches, the hybrid OEIC and the monolithic OEIC. The monolithic approach uses vertical stacking of epitaxial layers of semiconductor alloy on the same semiconductor substrate. On the other hand, the hybrid approach is realized on a dielectric substrate, integrating all components which may be inserted as discrete lumped elements through wire bonding or surface mount techniques.

In recent work on a RTD-LD OEIC, a monolithic approach was used to integrate a DBQW-RTD and an optical communications laser operating at around 1500 nm [44]. The device consisted of a vertical integration of a DBQW on an InAlGaAs/InGaAs multiple quantum well laser structure. Such integration is straightforward as the RTD section requires only the growth of four to six extra epilayers above a laser structure grown on $p-$type InP substrate, allowing the RTD to be implemented on the laser junction $n-$type region. The DBQW was made of a 5 nm InGaAs well and 2 nm AlAs barriers [44]. The devices fabricated were ridge waveguides with the DBQW situated in the ridge between the laser section and the $n-$type contact. The results demonstrate the feasibility of monolithic integrated RTDs with LDs where both components can be realized on the same semiconductor substrate and made of similar epitaxial layer structure.

Although monolithic RTD-LDs are expected to show many advantages, potential unforseen effects in the monolithic devices related to the material growth (e.g. lattice mismatch leading to defects or incorrect doping levels) can compromise their expected performance. Further developments and optimization in wafer design and device fabrication are needed to achieve more efficiently transmitter functions like, for example, high-speed oscillations in both electrical and optical domains and RTD-LD operation at room temperature.

Following the foreseen operation regimes of RTD-LD oscillating circuits, in this work we have focus our efforts on the implementation of HIC versions using components similar to the targeted monolithic integrated device. Laboratory hybrid RTD-LDs are easier to implement than monolithic versions, allowing an extensive study of circuits' performance, assuming a compromise between limited high-speed operation due to packaging parasitics, and great flexibility in the implementation and testing of these type of circuits. In what follows, we provide a more detailed description of RTD and LD constituent components of hybrid RTD-LDs.

3.4.2 RTD description

The RTD component was a device fabricated from pre-existing material, the layer strucuture of which is given in [42]. The InGaAlAs RTD structure was grown by MBE in a Varian Gen II system on a n^+ InP substrate. It essentially consisted of two 2-nm-thick AlAs barriers separated by a 6-nm-wide InGaAs quantum well, embedded in a 1-μm thick InGaAlAs optical waveguide (OW) core, Fig. 3.1(a). This design was originally used to obtain a DBQW-RTD operating as an electro-absorption modulator (EAM)

[42]. A detailed description of the fabrication and electrical and optical characterization of InGaAlAs/InP RTD-EAMs can be found in [113]. Furthermore, these devices show potential to be explored to obtain novel photo-detector devices as will be described in Chapter 4. In this chapter, we discuss and exploit the electrical properties of the DBQW-RTDs. Besides the epi-layer structure shown in Fig 3.1(a), a δ-doped InGaAs cap layer was provided for formation of Au-Ge-Ni ohmic contacts. Ridges were fabricated by wet-etching after which ohmic contacts were deposited on top of the ridges. A SiO_2 layer was then deposited, and access contact windows were etched on the ridge electrodes allowing contact to be made to high frequency bonding pads [coplanar waveguide (CPW) transmission line (TL)].

The InP wafers upon which the MBE epi-growth takes place had approximately 400 μm thick. This gives the sample some mechanical strength and allows handling during the fabrication process without damage. However, this thickness may not be desirable in the finished device. The sample thinning is necessary to facilitate the cleaving process, in which the completed thinned sample is divided into individual RTDs. Thinning was carried out using a steel jig to hold the sample perpendicular to a plate glass sheet upon which has been spread abrasive powder mixed with water. Moving the jig across the plate in figure of eight motion ensures even grinding across the sample. Frequent measurements were made of sample thickness until a depth of approximately 150 μm.

Next, the thinned samples containing many RTD devices were separated in individual dies by mechanically scribing. Taking advantage of the crystallographic nature of the semiconductor structure, the cleaving procedure weakens the structure along one cleavage plane. In the cleaving process the sample is held by a vacuum chuck while a metal scribe is drawn over its surface to produce a shallow groove. The groove corresponds to the point at which the sample will break when a bending force is applied in its vicinity. The cleaving is completed with a gentle downwards pressure in either side of the sample over a razer blade. Using this technique individual RTD dies with typical dimensions of 500 μm$\times$400 μm, Fig. 3.1(a), were obtained for testing and assembling RTD-LD circuits. The quality of RTD devices was inspected though electric testing to verify their NDC characteristics and devices showing appropriate DC I-V characteristics were assembled in the HIC.

The DC electrical characteristics of the devices were measured using a HP 4145 parametric analyzer. In Fig. 3.1(b) are presented two typical I-V curves showing the NDC regions for devices of different active lengths and the same width, measured for both forward and reverse bias, showing the peak voltage rises as the active area increases. The RTD 150 μm $\times$ 4 μm shown in Fig. 3.1(b) has a peak current of

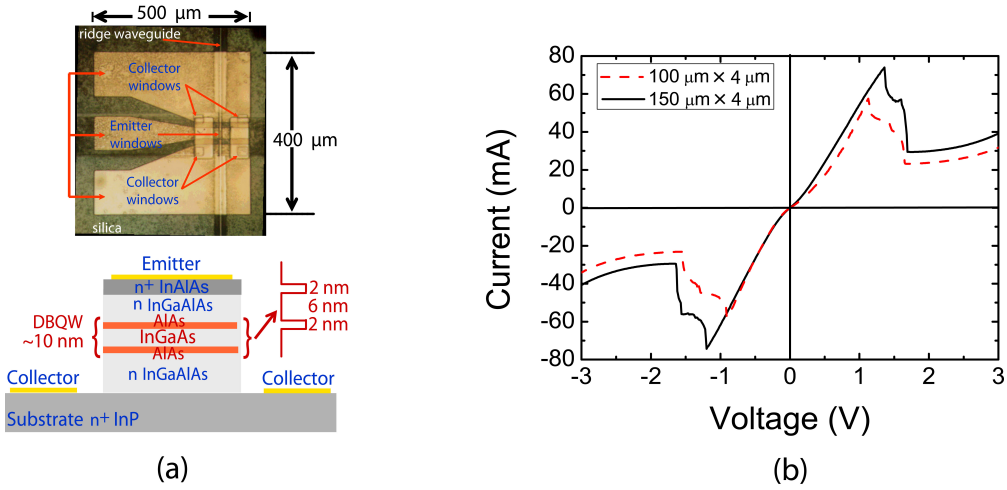

Figure 3.1: RTD component characteristics. (a) *Top*: RTD die top view showing the emitter and collector windows and the ridge waveguide (the ridge waveguide defines the device active area); *bottom*: schematic diagram (not scaled) of the RTD epi-layer structure. (b) Room-temperature InGaAlAs RTD I-V characteristics with the same ridge waveguide width.

58 mA and a PVCR of 2.5 (forward bias), with valley-to-peak voltage and peak-to-valley current differences, $\Delta V = V_v - V_p$ and $\Delta I = I_p(1 - PVCR^{-1})$, of 0.55 V and 35 mA, respectively. Another interesting feature of the I-V curves is that they are not completely anti-symmetric, the peak voltage in the reverse region is smaller in magnitude compared to the positive voltage side. This behavior may be related to the unsymmetrical nature of the layer structure and the different electrical characteristics of the InAlAs alloy, compared to the InP substrate.

High-frequency characterization of these devices was previously investigated [114] to provide more information about RTD impedance versus frequency dependence for various bias voltage values in order to find the equivalent circuit parameters, Fig. 2.5(c), as described in Chapter 2. For a 45 MHz to 18 GHz frequency range the series inductance was found negligible and the samples with negative resistance $R \approx -15\ \Omega$ (estimated from the NDC region) showed RTD equivalent capacitance of $C_{RTD} \approx 1.5$ pF and RTD series resistance of $R \approx 3\ \Omega$. For these circuit parameters, one can estimate the typical maximum frequency of operation of RTD devices, $f_{max} \sim 14.15$ GHz, as given by Eq. (2.8) (see Chapter 2). Further measurements of the CPW contacts show that additional parasitics due to the RTD doped n^+ substrate further limits the high-speed operation of the RTD devices used in this work. Measurements show the

doped substrate will have an effect on the maximum oscillation frequency because of the additional 1 pF capacitance due to the CPWs shunting the RTD to the ground. Therefore, future RTD designs with semi-insulating substrates is also expected to have a great impact on the high-speed operation.

3.4.3 Laser diode description

The laser diodes employed were commercial prototype devices supplied by Compound Semiconductor Technologies Global Ltd., Scotland. The laser devices consisted of InGaAsP multi-quantum-well active region with an InP:Fe doped uncoated buried heterostructure and ridge mesas with approximately 1.2 μm wide, $\sim$ 3 μm deep, and 250 μm long cavity. The devices were design for continuous-wave (CW) emission centre wavelength around 1550 nm. The exact material structure for the laser was unknown but for purposes of this work this is unimportant - the DC optical characteristics and frequency response were all that was required. The threshold current of the laser was around 6 mA, with a slope efficiency (dL/dI) of 0.25 W/A, more than 10 mW optical output power when operated above the threshold and series resistance around 5 Ω. Figure 3.2(a) shows the light-current-voltage (L-I-V) characteristic measured at 25 °C. The devices have a 3-dB modulation bandwidth in excess of 10 GHz making possible to operate at high-speed conditions. Figure 3.2(b) presents the typical frequency response of the laser, showing the modulation bandwidth of the laser varies from 7 GHz to 13.6 GHz, depending on the bias current.

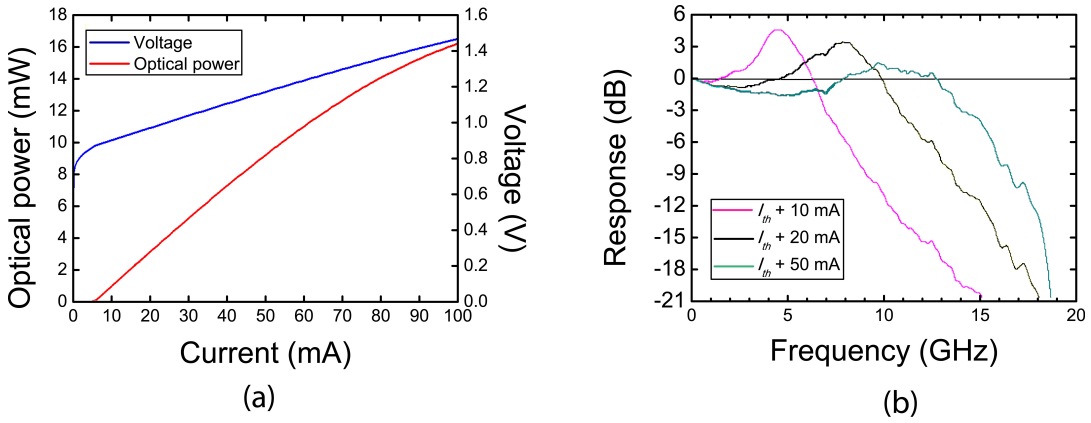

Figure 3.2: (a) L-I-V laser diode characteristics. (b) Frequency response of the laser.

The devices were supplied on a high-speed commercial sub-mount which provided a

suitable platform to wire bond the RTD device directly onto the high-speed bond pads of the platform and thus interconnecting the laser with the RTD.

3.5 RTD-LD hybrid oscillator circuit

The hybrid OEIC RTD-LD transmitter circuits discussed in this section form the basic circuit module configuration that is followed by the other RTD-based circuits discussed in the remaining chapters of this thesis. RTD and LD active components were selected and tested before combined with the rest of the circuit. Bond wires were used for connections among the various elements of the circuit. Variations in the characteristics of active components were compensated by manual tuning of some passive component parameters, namely the components that were part of the low frequency stabilization circuit. The hybrid implementation allows more control over the final characteristics of the circuit in the presence of diversity in RTD and LD component characteristics. Its drawbacks are the labor-intensive nature, relatively larger circuit sizes, and the inaccuracies and lower reliability associated with the bond wires.

3.5.1 RTD-LD description

The RTD-LD oscillator circuit module, represented schematically in Fig. 3.3(a), was realized using RTD and LD components attached directly onto the surface of a PCB containing a 50 Ω copper microstrip TL laminated onto the non-conductive PCB substrate. The printed TLs have distinct advantages, particularly because both active and passive devices may be readily incorporated and in-circuit characterization of devices is implemented straightforwardly. Other advantages include that DC and AC signals may be transmitted and that the structure is quite rugged and can withstand moderate high voltages and power levels. The TLs were realized in microstrip hybrid technology using Rogers substrate with a dielectric constant of 3.48 and a thickness of 0.762 mm. For this design implementation, a 15 mm 50 Ω microstrip TL corresponds approximately to an equivalent inductance of 4 nH. In the end terminals of the 50 ohm microstrip line high frequency sub-miniature version A (SMA) connectors for use up to 18 GHz were utilized to provide the RF input and output ports.

Another advantage of HICs using printed TLs is that discrete lumped components, such as surface mount chip resistors, inductors, or capacitors, can be externally inserted into the hybrid circuit and shunt connections are quite easy to be made. This advantage was very useful to test the RTD-based oscillator bias low frequency stability. In the oscillator circuit, thin-film resistors and capacitors were utilized as part of the bias

circuit of the oscillator to reduce the spurious oscillations and to act as a short circuit for the RF signals generated by the RTD-LD (the details of the low-frequency stability circuit are discussed in subsection 3.5.3). In Fig. 3.3(a) is shown schematically the shunt capacitor connected in parallel to the RTD device in series with the LD component and placed physically close of the RTD - the minimum distance between the RTD die and the thin-film capacitor node was below 2 mm. In order to test the influence of the shunt component in the stability of the RTD-LD oscillator, via holes separated by 10 mm along the microstrip TL were used to provide local grounding.

Conductive silver epoxy resin and bond wires where used to connect electrically the RTD emitter contact in series to the LD, and the RTD collector contact to the 50 Ω microstrip TL, as schematically represented in Fig. 3.3(a). The process of chip bonding of both RTD and LD chip devices consisted to attach the substrate with a high conductivity adhesive. The orientation of the laser was taken in consideration in the layout disposition and in the process of chip bonding in the PCB to ensure good alignment to an optical fiber and heat dissipation. The RTD was attached physically close of the LD, as shown in Fig. 3.3(b), to reduce wire bond interconnections, and thus reduce parasitics. When both LD and RTD dies where properly aligned using a die inspection and placement machine, silver epoxy glue (either cured at room temperature or at 100 °C) was applied to provide good adhesion. Furthermore, silver epoxy, if not yet cured, could be easily removed using acetone. After the chip bonding, silver dag painted down in the laser tile was applied to provide the ground connection, and solder wire connections from the RTD-LD to the microstrip TL were realized before the wire bonding final step.

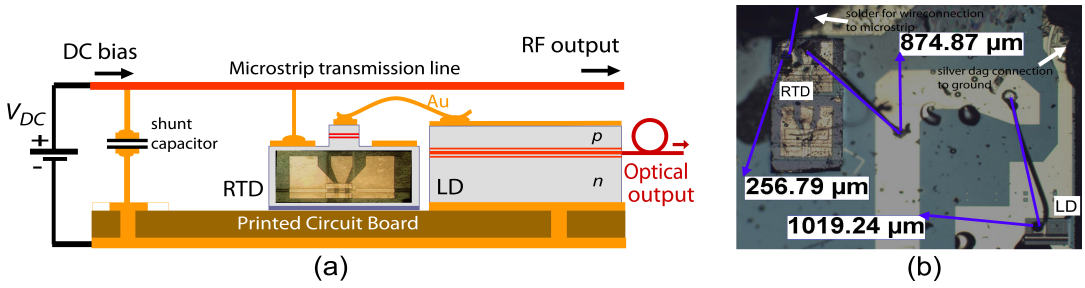

Figure 3.3: Hybrid RTD-LD oscillator module. (a) Illustration of the module (not scaled). (b) Picture of RTD, LD, and wire connections onto gold pads.

The final step was the connection between the RTD device CPW high frequency pads and the gold contacts pads of the laser device chip. The connections were realized

with gold wire, about 25 μm diameter, that linked the RTD and LD devices. The process was carried out under a microscope, using a commercial ultrasonic wire bonding machine (wedge bonder - model 4123). To obtain high speed operation, several factors to reduce parasitics were taken in account in the process of packaging and connection including a good common ground plane and minimizing wire bends to eliminate stray inductances. In fact, wire bond wires have been shown to be the limiting factor in high-speed HIC transmitters. In [115] it is shown that a 25 μm diameter with 2 mm length has an approximate inductance of 1.8 nH. Fig. 3.3(b) presents a picture of the RTD and LD connected by gold wires with an estimated total length around 2.1 mm. Furthermore, the gold wires contribute also to the total series resistance of the RTD-LD module. From the bond wire manufacturers (Mueller Feindraht AC) data sheet information, a 2 mm bond length corresponds to 0.49 ohm series resistance.

3.5.2 DC electrical characteristics

Figure 3.4 shows an example of the I-V characteristics of the individual RTD and laser diode devices, and of the RTD in series with the LD. The effect of adding a laser diode does not change the basic shape of the RTD I-V characteristic, just shifts the peak and valley regions to higher voltages - a shift of around 0.85 V, i.e., the voltage drop across the laser $p-n$ junction - but the current values are left unchanged (I_p = 41 mA, I_v = 12 mA). The device DC principle of operation is as follows. The individual RTD-LD exhibits NDC because the NDC is preserved in the hybrid integrated circuit, i.e., as the voltage rises above a threshold value, the peak voltage (V_p), the current drops steeply from its peak (I_p) to a lower value (I_v), before rising again. By ensuring that the LD threshold current is below the RTD's valley current ($I_p > I_v > I_{th}$), the LD operates in CW mode as the RTD-LD voltage is sweep across the NDC region. In the implemented RTD-LD circuits we have chosen RTD and LD components in order that $I_{th} < I_v$, that is, when the RTD-LD was DC biased in the NDC region the lasers were operating well above the threshold current.

The experimental RTD I-V characteristic was fitted using the model proposed by Schulman et al. [82], as discussed in Chapter 2. Figure 3.4 presents the RTD I-V model fit (dotted line) using the fitting parameters A = 3240 Acm^{-2}, B = 0.0875 V, C = 0.1449 V, D = 0.02132 V, H = 395 Acm^{-2}, n_1 = 0.1902, and n_2 = 0.0284. From the point of view of electrical simulation, when the laser is operating above the threshold, it can be modeled using an ideal diode in series with a voltage source and a current-limiting resistor R_l (typical lasers have around 5 Ω). Using SPICE circuit

simulator one can easily verify this aspect of the RTD-LD behavior. SPICE [116] is a widely used general-purpose electronic circuit simulator capable of performing AC, DC, and transient analysis on circuits consisting of several elements. First, we have simulated the laser diode characteristic, which is shown in Figure 3.4 using $R_l = 6\ \Omega$ with a threshold voltage of 0.85 V. Then, combining the model of the RTD derived from Shulman et al. [82] in series with the laser electrical characteristic simulated previously, we obtain the RTD-LD DC model fit presented in Fig. 3.4 which shows a close match to the experimental I-V characteristic. This simple approach simulated here confirms the RTD-LD DC electrical characteristics can be simply derived from the RTD electrical characteristic. As described in the next section, dedicated to the AC model of the RTD-LD oscillator, this simplifies considerably the circuit model without having a great affect in the description of the observed dynamical regimes.

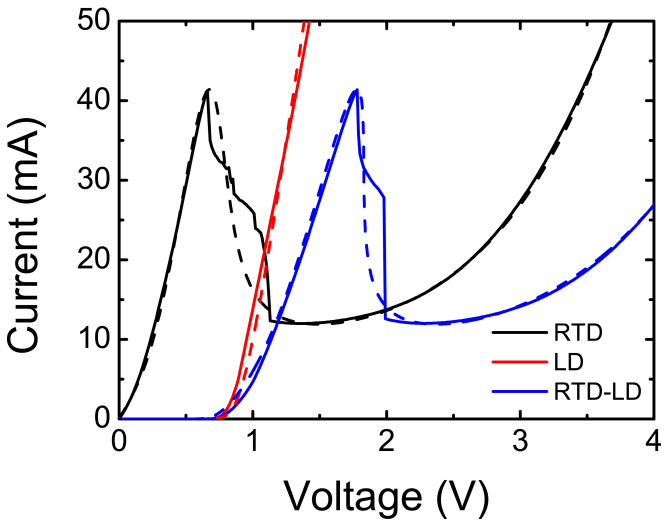

Figure 3.4: The I-V experimental electrical characteristics of the RTD-LD module overlaid with the model fit (dotted lines) derived from Schulman et al.

In the RTD and RTD-LD NDC regions a current shoulder is present where the current does not reduce suddenly but reaches a plateau before dropping steeply again. This arises as a result of oscillations caused by the drive circuit impedance and NDC. This is a result of the averaging of the oscillating signal by the RTD and RTD-LD from the source voltage meter. In the model this effect was not considered although modeling the RTD bias circuit oscillation may be carried out given accurate values of source impedance.

3.5.3 RTD-LD low-frequency stability

It has been demonstrated that in RTD-based devices the nonlinearity and NDC extends from DC to beyond the operating frequency of RTD device (up to the THz range [75]). This has led to the proposal of using RTDs for very high-frequency operation. However, potential problems can arise from the low-frequency or bias circuit oscillations [117]. For most practical applications, this means RTD-based devices in combination with the bias circuit should be stable at low frequencies when biased in the NDC region. In the RTD-LD practical circuit, the bias circuit, that includes the power source impedance and various parasitics elements, introduces parasitic oscillations with unwanted low-frequency signals which are not useful for high-frequency operation.

Proposed methods for suppression of parasitic low-frequency oscillations include RTD multivibrator oscillator [118] or RF excitation [119], both requiring a drive signal to initiate oscillation at the desired frequency. Another common method to solve the bias instability problem is to employ a stabilizing circuit using RTDs connected in series [120], or using a shunt resistor/capacitor connected directly across the tunneling diode [121, 122]. In the shunt resistor example, the stabilizing circuit is chosen such that the combined resistance (at DC and low frequencies) is positive when the tunneling diode is biased in the NDC region in order that:

$$\frac{1}{R_s} > G_0 \tag{3.1}$$

where R_s is the value of the shunt resistor and G_0 is the absolute value of the NDC. The disadvantages of this method are that the NDC characteristic must be determined indirectly, the total power consumption of the decoupling circuit increase, and degrades oscillator DC-to-RF conversion efficiency.

The other method proposed uses a shunt capacitor connected across the device. Figure 3.5 shows the equivalent circuit containing an RTD in series with an LD as represented schematically in Fig. 3.3(a) including parasitic elements, where R_b and L_b are the source resistance and inductance of the power supply, respectively, and the bias signal is isolated from the RF load by the blocking capacitor C_{block}. In this example a stabilizing capacitor C_s is used to improve the low frequency stability without affecting the RF impedance seen by the device, i.e., the shunt C_s is chosen to be a short circuit at the design frequency. In this configuration, the inductance L of the interconnect between the capacitor and the RTD must be minimized. This aspect arises from the the necessary low-frequency stability criterion derived in detail in [122]. Assuming the RTD-LD circuit of Fig. 3.5 is equivalent to the RLC circuit of Fig. 2.5(c) (see Chapter

2), the criterion is given by:

$$L_s < R_0^2 C \tag{3.2}$$

where L_s is the sum of all inductances, and C and R_0, are the capacitance and resistance of the RTD device, respectively. The stability criterion demonstrated in [122] and summarized by Eq. 3.2 defines L to a few nH for RTDs with peak currents in the mA range, values of the negative resistance R_0 of tens of ohms, and equivalent capacitance of tens of pF. This means, the low-frequency instabilities are avoided if the shunt capacitor could be inserted physically near the RTD, minimizing the lead inductance. Considering the typical RTD capacitance values of the RTDs' utilized in this work ($C \sim$ 1.5 pF-3 pF) and the estimated wire bond equivalent inductance in the range of 1 nH-8 nH, for the majority of the RTD-based circuits implemented in this work, a shunt capacitor $C_s \sim 1$ μF was sufficient to eliminate spurious oscillations.

In some implemented circuits in order to fulfill the condition given in Eqs. (3.1) and (3.2), a shunt resistor R_s in parallel with the shunt capacitor C_s formed the decoupling circuit (stabilizer) to isolate the bias circuit (V_{DC}, R_b and L_b) from the RF oscillator circuit shown in Fig. 3.5. The values of R_s and C_s were chosen to provide DC stability to the bias circuit and an RF path to ground for the oscillator circuit, respectively.

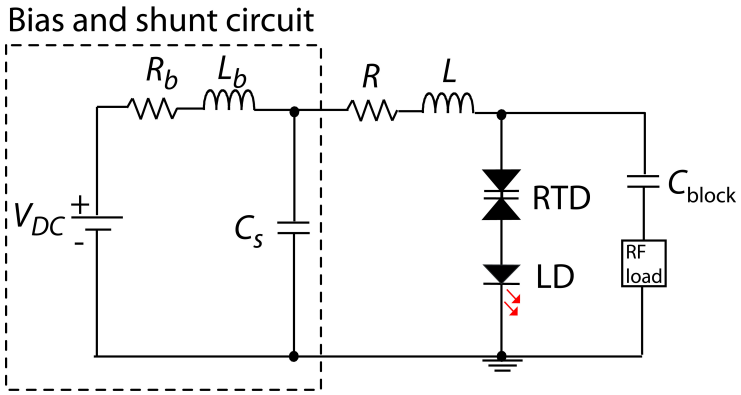

Figure 3.5: Circuit diagram of the RTD-LD equivalent circuit, and the DC bias and shunt circuit.

3.5.4 Liénard RTD-LD oscillator model

Using the theory of nonlinear oscillators in terms of differential equations, we formulate a dynamical model to investigate the dynamics of RTD-LD oscillators, derived from

the analysis of the RF circuit of Fig. 3.5. The RTD-LD model brings together the theory of Liénard-type oscillators and laser rate equations introduced in Chapter 2.

For purposes of analysis and numerical simulation of high-frequency oscillations, the RTD-LD schematic circuit presented in Fig. 3.5 can be reduced to the small-signal equivalent RLC circuit of Fig. 2.6(a) (see Chapter 2), because the shunt capacitor C_s acts as a short circuit at the frequencies under consideration. Since the capacitance of the laser diode is much larger than the RTD intrinsic capacitance, the RTD-LD module is modeled with the RTD estimated intrinsic capacitance and parasitics (see subsection 3.4.2) in parallel with a current dependent voltage source. This approximation seems reasonable since we have implemented single RTD hybrid circuits that showed identical range of frequency operation regimes whenever the lengths of the bond wires used to connect the RTD were similar to the RTD-LD hybrid circuit ones. In the RLC circuit of Fig. 2.6(a), R represents the equivalent resistance due to the devices (RTD and LD) and to account for the external lead resistances associated to the contacts, and L is the equivalent inductance to account for the lead inductances of the circuit connections (essentially determined by the gold bond wires total length).

Using the Kirchhoff's rules, we applied the same procedure discussed in Chapter 2 to obtain the two first-order differential equations that describe the RTD-LD electrical circuit. Then, coupling the electrical system to the laser diode rate equations to model the laser system, we obtain a ODE numerical model system for simulation of laser optical output driven by RTD current oscillations. The model is referred as the generalized nonlinear forced Liénard RTD-LD oscillator [46, 48, 123], which is given in the dimensionless form as:

$$\frac{dx(t)}{dt} = \frac{1}{\mu}\left[y(t) - f(x)\right] \tag{3.3}$$

$$\frac{dy(t)}{dt} = \mu\left\{\upsilon_0 + \upsilon\sin[z(t)] - \gamma y(t) - x(t)\right\} \tag{3.4}$$

$$\frac{dz(t)}{dt} = 2\pi\Omega \tag{3.5}$$

$$\frac{dn(t)}{dt} = \frac{1}{\tau_n'}\left[\frac{i_m(t)}{i_{th}} - n(t) - \frac{n(t)-\delta}{1-\delta}\{1-\epsilon s(t)\}s(t)\right] \tag{3.6}$$

$$\frac{ds(t)}{dt} = \frac{1}{\tau_p'}\left[\frac{n(t)-\delta}{1-\delta}\{1-\epsilon s(t)\}s(t) - s(t) + \beta n(t)\right] \tag{3.7}$$

where $V_{DC} - V_{TH} = \upsilon_0 V_0$, V_{TH} account to the LD voltage threshold, and V_{DC} account to the experimental RTD-LD bias voltage; $i_m(t)$ is the bias current with current modu-

lation in time $y(t)$ given by Liénard model, Eqs. (3.3)-(3.5), and i_{th} is the dimensionless laser diode threshold current. Note that time is normalized to the characteristic frequency of oscillation of the RTD-LD, $\omega_0 = (\sqrt{LC})^{-1}$, hence $\tau = \omega_0 t$. Therefore the parameters τ_n' and τ_p' in the laser system, Eqs. (3.6)-(3.7), come from the time rescaling. Because the electrical system operates in the GHz range, the time rescaling defined here has approximately the same order of magnitude as defined in Chapter 2 using $t = \tau\tau_n$. The remaining dimensionless parameters and variables in Eqs. (3.3)-(3.7) are identical to the ones described in Chapter 2. In Fig. 3.6 is depicted a block diagram with the corresponding mathematical representation of the coupled Liénard-laser diode system and includes a periodic signal $\upsilon \sin[z(t)]$ to account for the RTD-LD subjected to external electrical injection.

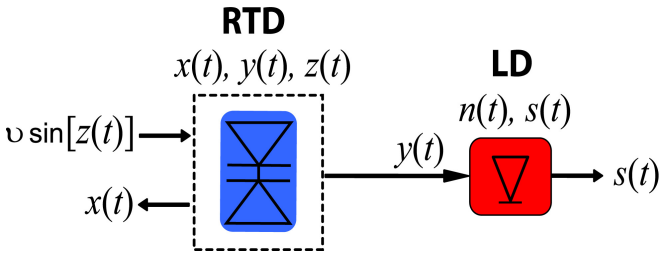

Figure 3.6: Block diagram of the forced Liénard RTD-LD oscillator dimensionless model.

3.6 Dynamics of RTD-LD voltage controlled oscillators

The NDC displayed by the DBQW-RTD forms the basis of the fast and simple RTD-LD oscillator investigated here, which is used in this work to implement a novel bistable or multistable circuit [124], the RTD-LD relaxation-type oscillator. In this section, we analyze and discuss the high-frequency RTD-LD self-sustained relaxation oscillator dynamics operating in the autonomous and non-autonomous electro-photonics regimes.

3.6.1 Experimental setup and principle of operation

In Fig. 3.7(a) is shown a photograph of an RTD-LD circuit, and in Fig. 3.7(b) is depicted the circuit's diagram and experimental setup used in this investigation showing both electrical input and outputs, and laser optical output. A DC voltage was supplied to the circuit's input through a wideband bias tee (45 MHz - 26.5 GHz). An Agilent E8257D RF signal generator was used to generate RF signals and was connected to

the RF input of the bias tee, providing external injection of the RTD-LD. The RTD-LD RF output was observed in the time domain using a high bandwidth oscilloscope (either a Agilent 86100C or a Tektronix 794D digital real time scope 2 GHz analog bandwidth) and in the frequency domain using a 40 GHz spectrum analyzer (either a HP 8564E or a Rohde & Schwarz FSV-40). The current through the RTD-LD branch of the circuit was driving the laser diode, and the corresponding modulated optical signal output was coupled into a single mode (SM) lensed fiber connected to a high bandwidth photo-detector (either a New focus 45 GHz IR PD model 1014 or a U^2T Photonics - XPDV2020R), the photo-detected output of which was measured in the frequency and time domain as for the RF output.

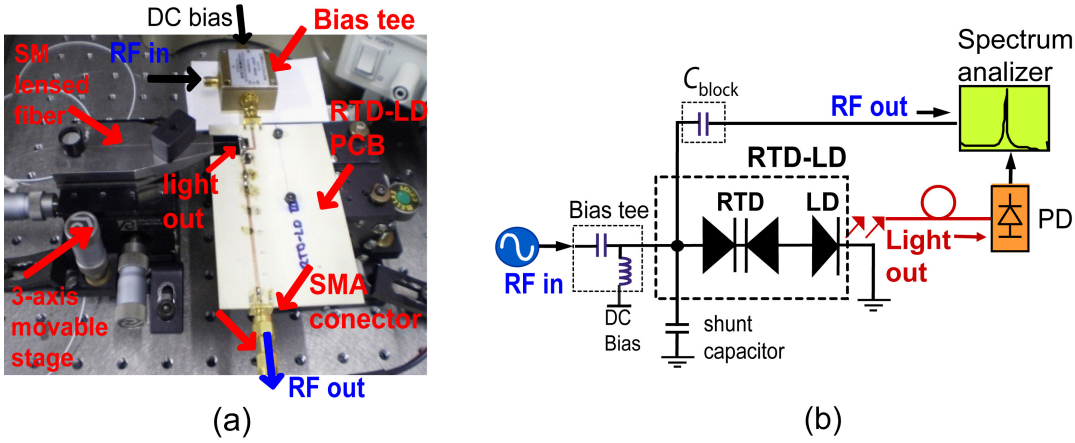

Figure 3.7: (a) Photograph of RTD-LD circuit. (b) Experimental setup and circuit schematic diagram.

The RTD-LD oscillator circuit operates as follow. The shunt capacitor provides stability at low-frequency oscillations, as explained in the previous section. Thus the circuit's free-running oscillation frequency is determined primarily by the round trip time of the AC feedback loop (effective length of equivalent TL from the shunt components to the RTD-LD module), in combination with the RTD and the LD parasitics (mainly the inductance from the wire bonding). Such an oscillator corresponds to a relaxation oscillator system since it operates by sequential transitions between two states. This principle of operation is based on the repetitive switching between DC-stable points lying below the peak point and above the valley point, which means the RTD dwells in either of its PDCs between switching events. The RTD successive switching events (relaxation oscillations) produce current oscillations that drive the laser output yielding

optical modulated outputs providing an image of the relaxation oscillations observed in the electrical domain. Under external injection of RF signals the NDC portion of the RTD nonlinear I-V characteristic responds to the injected varying voltages producing either periodic or aperiodic, including chaotic, current oscillations that modulate the laser diode optical output, converting electrical periodic or aperiodic signals into optical periodic or aperiodic sub-carriers, depending on the experimental conditions.

Using the experimental setup of Fig. 3.7, in what follows we investigate the dynamics of the RTD-LD in the autonomous and non-autonomous (forced) regimes. We also evaluate the dynamical system model comprising the Liénard's oscillator coupled to laser diode rate equations.

3.6.2 Optoelectronic voltage controlled oscillator

When an RTD is incorporated in a circuit resonator (or tank circuit) and biased into the NDC, oscillations are initiated due to small signal fluctuations occurring in the circuit oscillator or bias circuit (e.g. noise fluctuations due to voltage source). These oscillations are called relaxation oscillations. The operation frequency is determined to a first approximation by the circuit resonator frequency $1/2\pi\sqrt{LC}$ (see tank circuit of Fig. 2.6(a), Chapter 2). The oscillation frequency depends also on the nonlinear RTD impedance, which is a function of the DC bias voltage. Tuning the DC bias across the NDC region changes the RTD impedance and as consequence tunes the relaxation oscillation frequency in a regime of operation called VCO. In the RTD-LD circuit, since the NDC region is preserved and current relaxation oscillation waveforms flow through the laser diode, the circuit optical output emulates the electrical current relaxation oscillations: the laser output shows the same repetitive switching of the relaxation oscillation current. The RTD-LD circuit operates as an OVCO, that is, the RTD-LD biased in the NDC region produces electrical and optical oscillatory signals whose frequency is controlled by the bias voltage quiescent point. In what follows, we analyze the frequency tuning, time and Fourier domain outputs, and phase noise characteristics of the RTD-LD free-running OVCO.

3.6.2.1 Frequency tuning curves

Figure 3.8 shows two examples of the typical variation of RTD-LD oscillation frequency with DC bias voltage. As is shown in Fig. 3.8, the oscillation frequency does not vary monotonically with bias voltage. Instead, it increases with the bias voltage, reaches a maximum frequency, then slightly decreases until the RTD-LD is no longer biased in the

NDC region and the oscillations cease. The oscillation frequency tuning range varied over a few hundreds of megahertz for the circuits operating up to 2 GHz. The frequency of the RTD-LD circuit of Fig. 3.8(a) varied with the DC voltage from around 0.987 GHz to 1.247 GHz, that is, a frequency tuning range around 260 MHz; whereas the circuit of Fig. 3.8(b) oscillated from 1.977 GHz to 2.153 GHz, i.e., a tuning range of 176 MHz. The voltage tuning range of circuit in Fig 3.8(a) is larger than the circuit in Fig 3.8(a) as expected from higher PVVR measured in the I-V characteristic shown inset. Nevertheless, the tuning sensitivity expressed in frequency tuning range per voltage range was higher for circuit of Fig. 3.8(b). For stable oscillators, a linear deviation of frequency versus tuning voltage is desirable. In the RTD-LD oscillators analyzed, a linear deviation characteristic is attained considering voltages close to the peak voltage. Generally speaking, to have a wide DC operating range and therefore large tunability in a OVCO, a wide NDC (large difference between the peak and valley voltage) is desirable. The RTD-LD of Fig. 3.8(b) increased oscillation frequency mainly because a lower inductance contribution by reducing the bond wire length to 1-2 mm (down from $\sim$ 4 mm).

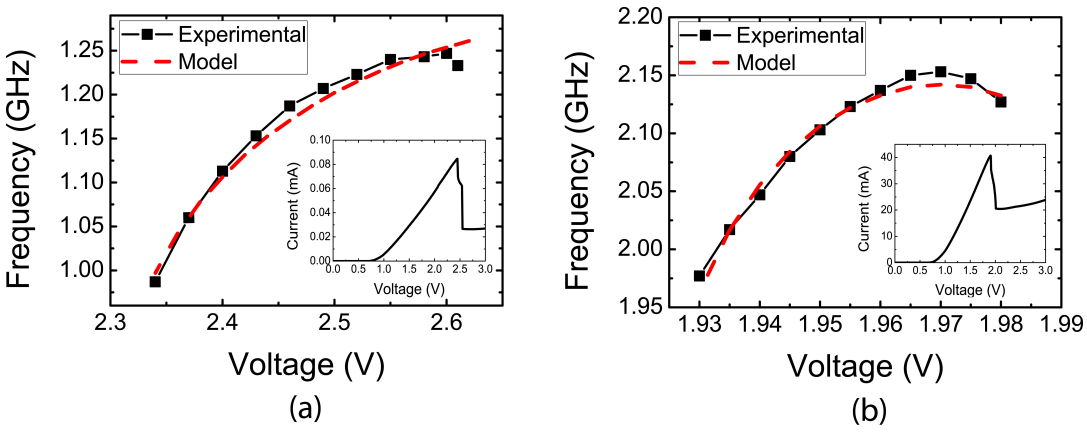

Figure 3.8: RTD-LD experimental and simulated frequency tuning curves as a function of voltage sweeping across the NDC region for RTD-LD oscillators operating up to (a) 1.247 GHz and (b) 2.15 GHz. Inset of each figure are the corresponding RTD-LD I-V characteristics.

For comparison of the experimental results with the numerical model, Fig. 3.8 presents also the simulated tuning frequency curves using the Liénard-laser diode model, Eqs. (3.3)-(3.7), in the autonomous regime, i.e., $\upsilon = 0$. The electrical circuit parameters used in the simulation of Fig. 3.8(a) were $R = 11.4\ \Omega$, $L = 3.31$ nH, and $C = 3$ pF.

The laser dynamics was modeled employing typical parameters of semiconductor laser described in Section 2 [99], with small adjustments to fit with experimental results $V_{act} = 6.75 \times 10^{-11}$ cm^3, $\tau_n = 3 \times 10^{-9}$ s, $\tau_p = 1.2 \times 10^{-12}$ s, $\beta = 1 \times 10^{-4}$, $g_0 = 10^{-6}$ cm^3/s, $N_0 = 10^{18}$ cm^{-3}, $\epsilon_n = 0.6 \times 10^{-17}$ cm^3, and $\Gamma = 0.44$. In Fig. 3.8(b) the same LD fitting parameters were employed and the electrical parameters used in the simulation were $R = 11.44\ \Omega$, $L = 0.92$ nH, and $C = 2.86$ pF. The simulations obtained by the Liénard-laser diode model describe reasonably well the experimental behavior of the RTD-LD circuit in the OVCO regime of operation.

3.6.2.2 Time and Fourier domain outputs

Figure 3.9 presents the experimental and simulated oscillations of RTD-LD electro-photonics outputs in both time and Fourier domains with the DC bias close to the peak voltage. Figure 3.9(a) shows RTD-LD voltage output waveform at free-running frequency around 0.987 GHz and the photo-detected laser optical output modulated by the current relaxation oscillations. As mentioned above, the repetition rate of the laser optical output was the same as the electrical circuit oscillation, confirming the laser diode operation was controlled by the RTD switching characteristics. The pulsed nature of the photo-detected laser optical output shown in Figure 3.9(a) confirms the capacitive characteristic of the current induced by the RTD switching (described in detail in [124]). The full width at half maximum (FWHM) of the photo-detected pulses is approximately 200 ps but this measurement is limited by the temporal acquisition resolution of the oscilloscope/photo-detector. Figure 3.9(b) shows the corresponding RF spectra of the electrical and optical outputs of RTD-LD circuit, confirming the pulse nature of the current relaxation oscillations with a high harmonic content (measured up to 10th harmonic). The spectrum of the photo-detector signal indicates that the laser output is modulated by the electrical self-sustained oscillation by an amount greater than 20 dB. The RTD-LD OVCO circuits can provide a simple way to convert fast, short electrical pulses with low timing jitter and phase noise, into fast, sharp optical pulses.

In Fig. 3.10(a) are shown the self-sustained voltage output and photo-detected optical waveforms of the RTD-LD circuit oscillating around 2.107 GHz when DC biased close to the valley voltage. In this region, which is nearest the region of great curvature of the NDC, the fundamental mode achieves its maximum efficiency, where the Fourier series has a predominant coefficient at the oscillation frequency, Fig. 3.10(b). As a result, the oscillation waveforms appear as sine wave-like shape.

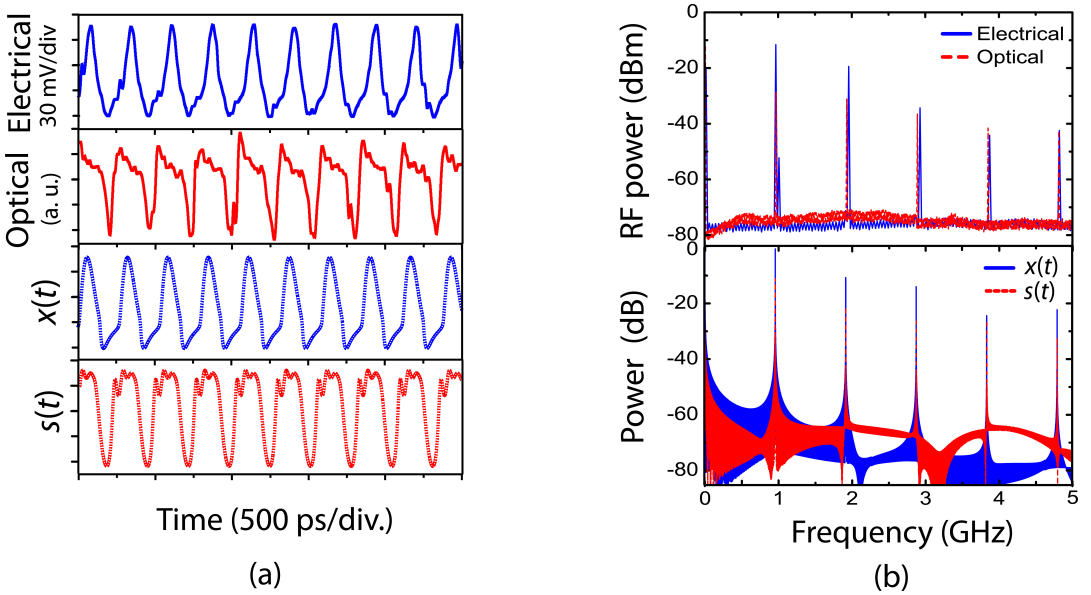

Figure 3.9: Experimental and simulated [$x(t)$ and $s(t)$] oscillations of RTD-LD electro-photonic outputs oscillating at 0.987 GHz (a) in time domain, and (b) in Fourier domain.

The experimental results in Figs. 3.9 and 3.10 were fitted to the numerical results (dashed lines) showing a good agreement between model and experiment, demonstrating the validity of the Liénard model. The OVCO frequency tuning curves, the waveforms and estimated power spectra presented here shows the the Liénard oscillator model coupled to laser rate equations can be used to describe the observed behavior in RTD-based driver circuits utilizing an optical communications semiconductor laser.

3.6.2.3 Phase noise characteristics

Ultimately, we analyze an important figure of merit (FOM) of the performance of oscillators, the phase noise characteristic. Figure 3.11(a) presents the RTD-LD free-running fundamental signal spectra operating around 1.2405 GHz with a span of 5 MHz. As shown in the spectrum surveillance monitoring (SSM) of both outputs [top inset of Fig. 3.11(a)], the free-running oscillation is of poor stability and suffer of frequency fluctuations. These fluctuations are commonly referred as phase noise which, like in many other conventional electronic devices, come from the active devices and other electrical noise sources.

The phase noise in an oscillator is mainly due to internal noise sources such as

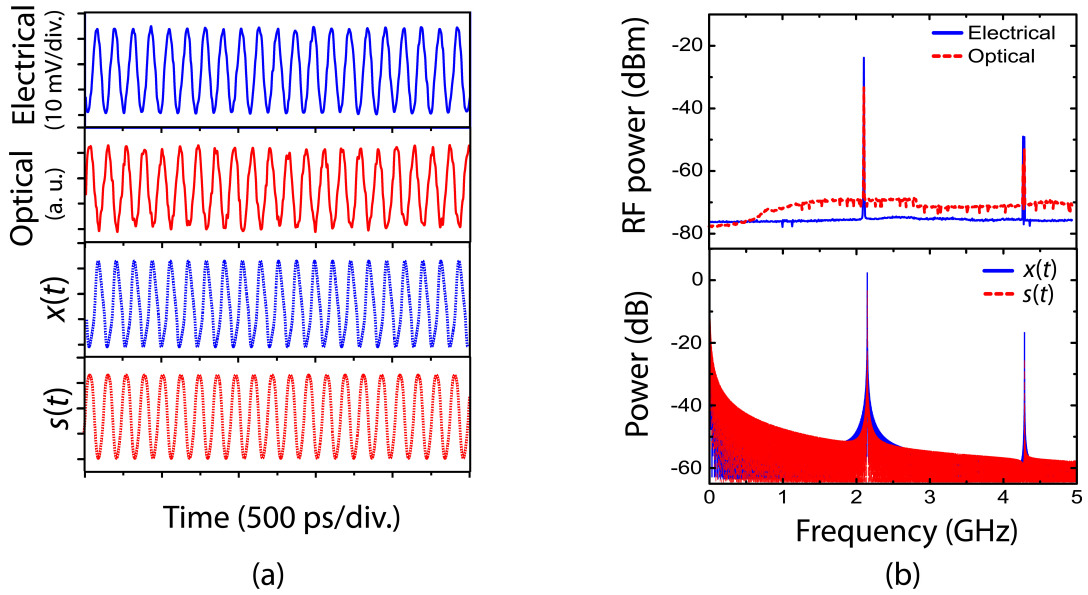

Figure 3.10: Experimental and simulated [$x(t)$ and $s(t)$] oscillations of RTD-LD electro-photonic outputs oscillating at 2.107 GHz (a) in time domain, and (b) in Fourier domain.

thermal noise and active device noise sources (flicker noise or $1/f$ shot noise). They are random in nature. The internal noise sources set a fundamental limit for a minimum obtainable phase noise in oscillator design. The spurious tones are due to external noise sources such as noise on control voltage, power supply, and bias current signals. They are deterministic in nature. There are many ways of quantifying these fluctuations (a comprehensive review of different standards and measurement methods is given in [125]).

A signal's short-term instabilities are usually characterized in terms of the single sideband (SSB) noise spectral density. SSB phase noise is defined as the ratio of noise power in a 1 Hz bandwidth at a given frequency offset, to the signal power. It has units of decibels below the carrier per hertz (dBc/Hz) and is given by:

$$L\{\Delta\omega\} = 10\log\left[\frac{P_{sideband}(\omega_0 + \Delta\omega, 1\text{Hz})}{P_{carrier}}\right] \tag{3.8}$$

where $P_{sideband}(\omega_0 + \Delta\omega,\ 1\ \text{Hz})$ represents the single sideband power at a frequency offset of $\Delta\omega$ from the carrier with a measurement bandwidth of 1 Hz, ω_0 is frequency of oscillation, and $P_{carrier}$ is the signal power.

Figure 3.11(b) presents the RTD-LD measured SSB phase noise measurements in

both electrical and detected optical outputs. At low offsets (100 kHz to 1 MHz) both electrical and optical outputs follow the same trend with a slope of around 20 dB/decade, which is a classical oscillator $1/f$ profile. The LD output follows this slope with a slightly inferior phase noise performance, -102.81 dBc/Hz at 1 MHz offset, essentially due to shot noise of the detector and laser relative intensity noise (RIN). At offsets above 10 MHz we found a region of nearly flat response usually called noise floor. In this region, the electrical and optical responses have about 8 dB difference at 100 MHz offset mainly because of the lower signal-to-noise ratio (SNR) of the detected laser output.

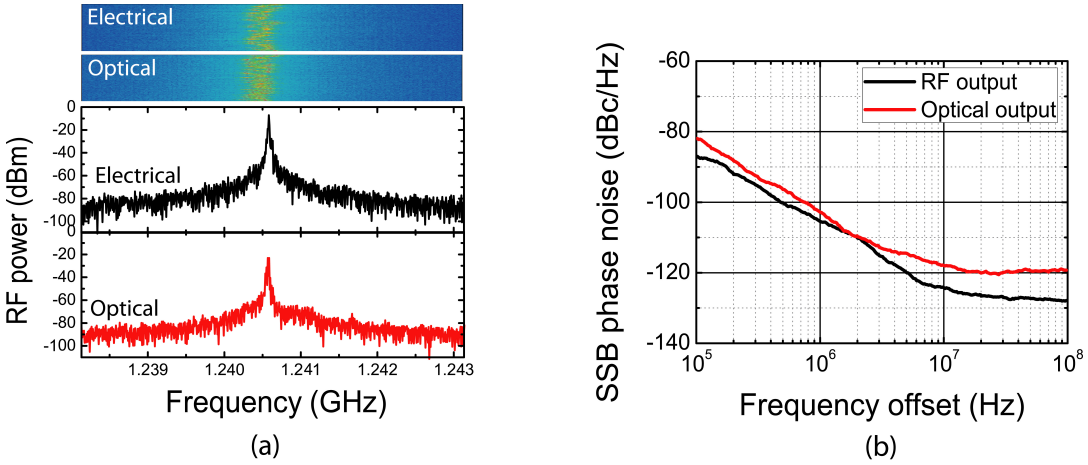

Figure 3.11: (a) RF spectra measurements of RTD-LD fundamental free-running oscillation in the electrical output and in the detected optical output (span of 5 MHz and RBW of 10 kHz, V_{DC} =2.485 V). On the top is a inset with the spectrum surveillance monitoring around 60 s time acquisition (time in the vertical axis). (b) SSB phase noise measurements of electrical and optical free-running oscillation outputs.

The phase noise regions observed in both electrical and optical outputs confirm the signals characteristics are mainly determined by the RTD electrical oscillator performance. The overall RTD-LD oscillator characteristics are summarized in Table 3.1 including operation frequency, typical oscillator tunability, and phase noise. The RTD-LD OVCO performance compares with recently reported RTD-based devices operating in the same range of frequencies and output power [11, 126]. Although the OVCO is still of inferior quality when compared with modified complementary metal-oxide-semiconductor (CMOS) VCO devices [127], and commercial available coaxial resonator oscillator (CRO) modules [128], further techniques including injection locking and self-synchronization can provide considerably improvements on the RTD-LD OVCO perfor-

mance, as demonstrated throughout this thesis. Moreover, improvements are expected by employing monolithic microwave integrated circuits (MMIC) circuits as reported in [129], which provide more control on the circuit parasitics, namely the wire bonding.

Table 3.1: Summary of RTD-LD free-running OVCO performance.

Parameter	Min.	Typ.	Max.	Units
Frequency f_0	0.987	-	1.247	GHz
Output power	-14.17	-	-8.5	dBm
Tuning frequency	-	260	-	MHz
Tuning frequency	-	21	-	%
Tuning voltage	2.34	-	2.61	V
SSB Phase noise@1 MHz	-	-105.43	-	dBc/Hz
SSB Phase noise@100 kHz	-	-86.93	-	dBc/Hz

3.6.3 Injection locking

Injection locking is a well-known phenomenon which is discussed in any standard textbook [58, 59] on nonlinear oscillators (see Chapter 2 and Appendix A), under one of various headings such as synchronization, phase locking, frequency entrainment, or forced oscillation. According to the oscillator model developed by Adler and described in its seminar paper [5], an oscillator can be locked in frequency by an external signal which is injected into the oscillator and the mechanism of the locking process depends upon the the initial frequency difference between the oscillator, the relative amplitude between the injected and the oscillator and the circuit parameters. In this subsection, we investigate the injection locking characteristics of RTD-LD oscillators subjected to RF signals close to the circuit's free-running fundamental mode.

The electrical signal was injected in the electrical input port using a bias tee and the output signal was measured in the LD optical output, Fig. 3.7(b). The RF spectra of the free-running and injection-locked RTD-LD oscillator outputs were measured with a RF spectrum analyzer, Fig. 3.12(a), and the oscillation frequency was set to around 1.2432 GHz. In Fig. 3.12(a) is presented the typical broad spectrum caused by the frequency fluctuations. The corresponding SSB phase noise measurements are shown in Fig. 3.12(b). The photo-detected free-running signal had a single-sided noise power density of -81.96 dBc/Hz at 100 kHz offset. Adding a RF signal frequency close to the free-running oscillation frequency (even using very low power levels, in this case -43 dBm) the RTD electronic oscillation was pulled to the the same repetition rate, and the photo-detected LD output spectrum collapsed to match that of the reference

synthesizer with -85.86 dBc/Hz noise suppression at 100 kHz offset when injection locked. On top of Fig. 3.12(a) is inset the spectrum surveillance confirming the spectral stability of the locked signal. The pull or locking range Δf was also measured. Under this level of power the locking range was around 300 kHz. For power levels much lower than the RTD-LD oscillator power the locking range was found to be approximately proportional to $\sqrt{P_i/P_0}$, where P_i is the injected power and P_0 is the RTD-LD RF output power [48]. This behavior follows Adler theory [5], and is the same as that observed for injection locking of conventional negative-resistance oscillators operating in the small-signal limit.

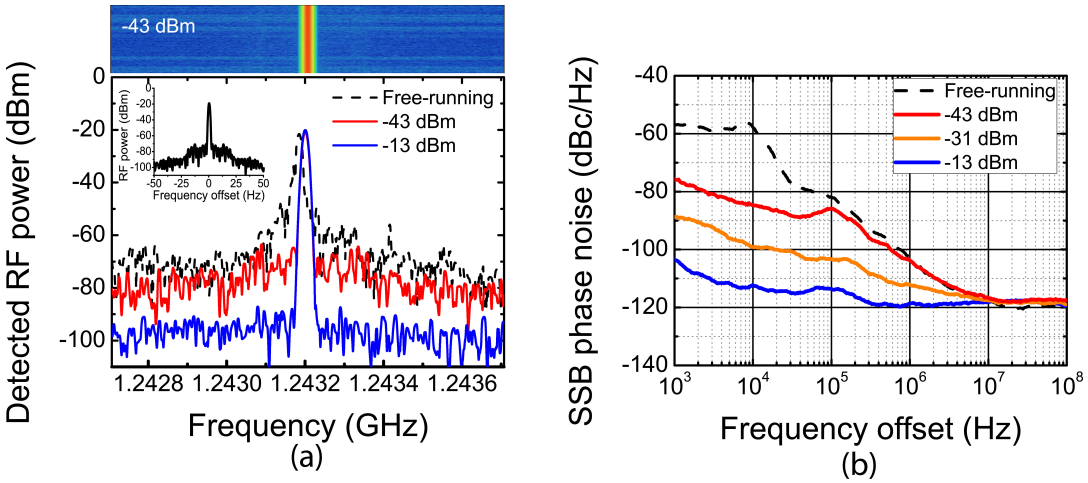

Figure 3.12: (a) Free-running and injection locked RF spectra of photo-detected RTD-LD outputs (1 MHz span and 10 kHz RBW). Inset is shown the injection locked spectrum with 100 Hz span and 1 Hz RBW at -13 dBm power level. Also shown on top is a spectrogram that represents the evolution of spectral density of the injection-locked signal recorded over approximately 60 s (time in the vertical axis). (b) SSB phase noise measurements.

We verified that the noise on the injection-locked signal followed the noise introduced from the input synthesizer signal. The injection-locked RTD-LD oscillator produced microwave signals in the LD optical sub-carrier with noise characteristics that matched those of the input signal, limited only by the measurement instrument noise floor. As the noise level of the input was changed the injection-locked signal changed accordingly. Increasing the output power of the RF synthesizer further reduced the noise on the reference signal and likewise the injection-locked signal, as observed in the spectra of Fig. 3.12(a) for a power level of -13 dBm. Inset of Fig. 3.12(a) is the

injection-locked signal with a 1 Hz resolution bandwidth phase locked to a -13 dBm low-noise RF reference signal (note the different frequency scales), confirming the output spectrum collapses to match that of the reference synthesizer. Figure 3.12(b) shows the phase noise reduction when a signal with -13 dBm power is injected with -113.69 dBc/Hz phase noise at 100 kHz carrier offset, with a suppression of more than 30 dB when compared with the free-running. Under this level of power the locking range was around 30.5 MHz, corresponding to approximately 2.45 % of the oscillation frequency. Finally, another characteristic of the injection locked RTD-LD is that the output power of the injection locked signals is approximately the same of the free-running output, as long as the injected power is lower than the injected signals.

3.6.4 Period-adding bifurcation

In order to map the RTD-LD dynamics subjected to external injection, we have characterized in detail the electro-photonics outputs in time and Fourier domains for a wide range of voltage amplitude V_{AC} and injected frequency f_{in} values. The observed dynamic trajectories were plotted in the voltage-light $(V - \ell)$ phase space, where V represents the voltage across the RTD-LD, the electrical output, and ℓ is the LD optical output. In the free-running mode, the trajectories in the $(V - \ell)$ phase space correspond to a simple attractor known as limit cycle, as shown in Fig. 3.13(a), with a free-running frequency f_0 ~0.953 GHz (the circuits described here showed free-running frequencies, f_0, ranging from 0.5 GHz to around 1 GHz, controlled by the DC voltage [49]). The free-running electrical and corresponding optical oscillations RF power spectra are presented in Fig. 3.13(b), with an harmonic content up to the 10th harmonic.

Following the injection locking phenomena discussed in the previous subsection a more complex circuit behavior known as period-adding bifurcation dynamics [45] can be obtained when free-running oscillations are perturbed by injected RF signals. In this regime, whenever a stable closed trajectory is found in the $V - \ell$ phase space the system is considered phase-locked to the driving signal. In the very weak perturbation regime, $V_{AC} << \Delta V_{NDC}$, where ΔV_{NDC} is the NDC voltage width ($\sim$ 250 mV for the circuits tested), the free-running and injected frequencies, f_0 and f_{in}, satisfy the relation $f_{in}/f_0 \rightarrow n/m$, where n and m are natural numbers. The ratios n/m are known as winding numbers [58, 59].

Figures 3.13(c)-(j) present examples of RTD-LD synchronization states for sinusoidal input amplitude voltage of 300 mV and scanning the injected frequency from 0.3 GHz to 3.5 GHz. On the left are shown $V - \ell$ phase space diagrams and on the right

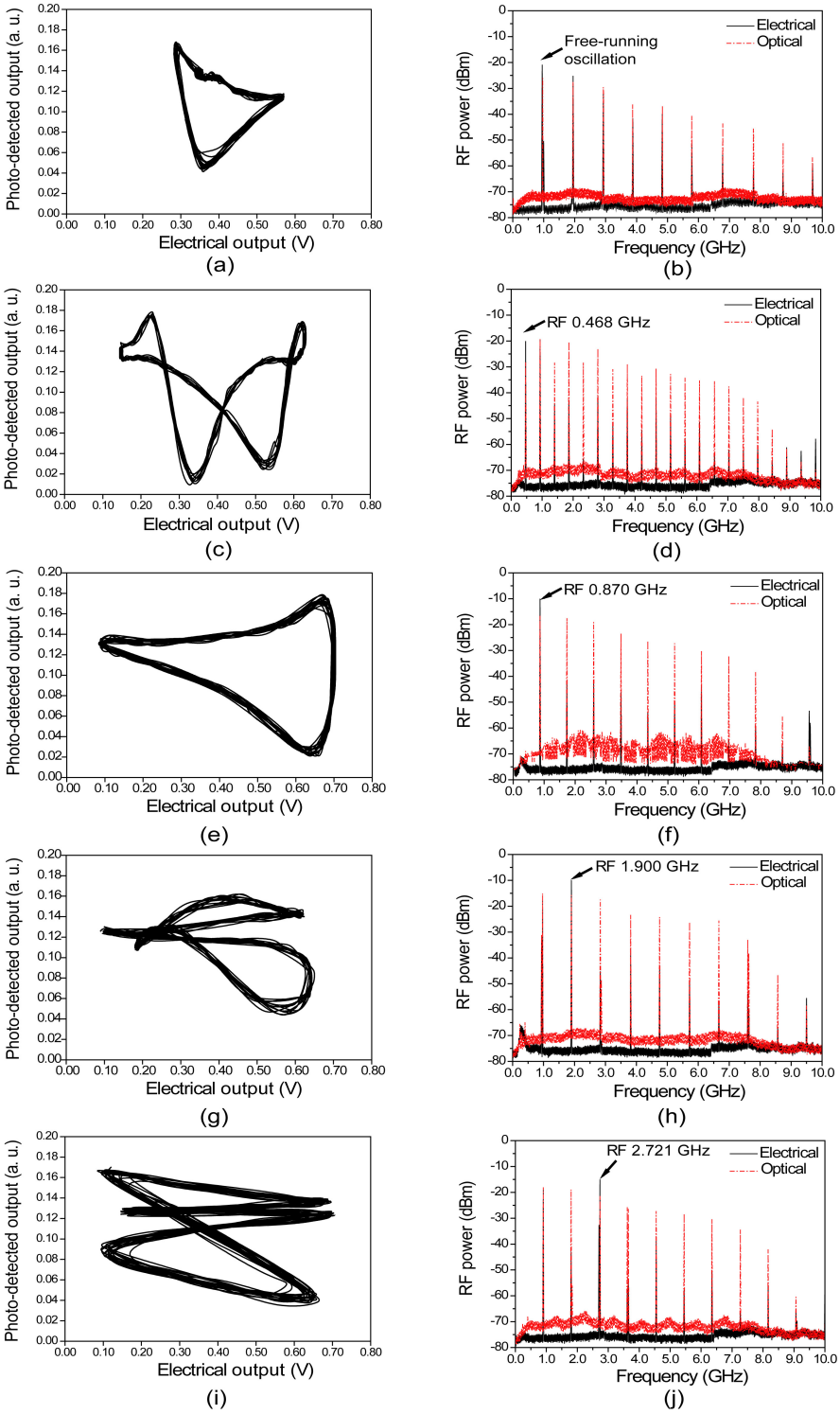

Figure 3.13: Experimental electro-photonic limit cycle regimes in the $V-\ell$ phase space (left) and corresponding spectra (right) for the following stable dynamic states: (a)(b) free-running; and locked (c)-(d) 1:2 and (e)-(f) 1:1, (g)-(h) 2:1, and (i)-(j) 3:1.

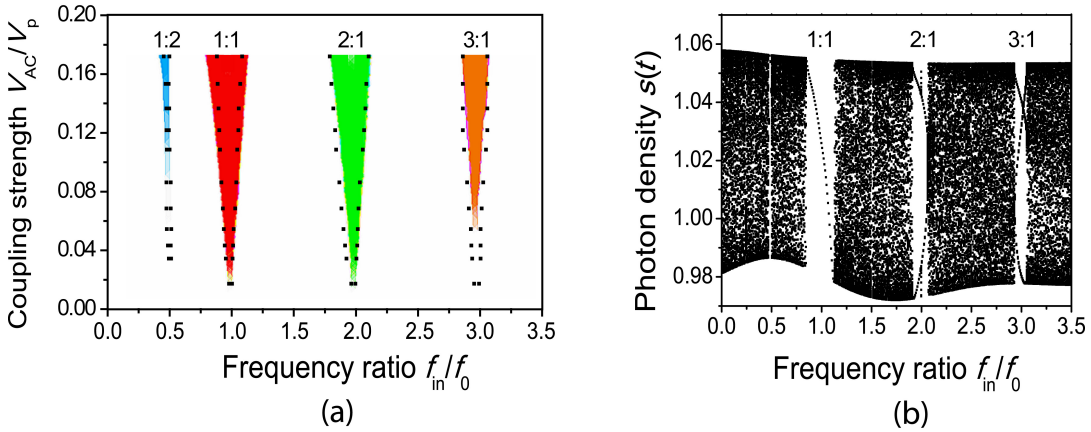

Figure 3.14: (a) RTD-LD oscillator frequency-locking structure showing the electro-photonics Arnold tongues. The results from the experiment (dotted lines) are compared with theory (colored tongues). (b) Numerical simulated bifurcation map of photon density $s(t)$ as a function of frequency for electrical injection of a periodic signal at amplitude $\upsilon = 0.3$.

the corresponding V and ℓ RF power spectra. Figs. 3.13(c)-(d), present an example of sub-harmonic locking with ratio 2:1 - the RTD-LD synchronizes at frequencies with half the circuit's free-running frequency; Figs. 3.13(e)-(f) show locking at signals with frequency close to circuit's free-running oscillation (1:1) - fundamental locking; Figs. 3.13(g)-(h) and 3.13(i)-(j) illustrate two examples of harmonic injection locking, 1:2 and 1:3, respectively, where the injected frequencies are close to RTD-LD's first and second frequency harmonics, respectively.

The overall circuit's dynamic response to perturbations was mapped in a two-dimensional Arnold tongues diagram, Fig. 3.14(a), where the tongues correspond to the regions of locking to the driving signals presented in Figs. 3.13(c)-(j). The numerical model, Eqs. (3.3)-(3.7), agrees qualitatively well with experimental tongues. The y-axis represents the perturbation strength defined as the ratio of the injected voltage amplitude V_{AC} and RTD-LD peak voltage V_p (around 2.90 V), V_{AC}/V_p; the x-axis corresponds to the frequency ratio f_{in}/f_0. The injected amplitude and frequency ranged from 50 mV to 500 mV and 0.3 GHz to 3.5 GHz, respectively. In Fig. 3.14(b) is presented the corresponding simulated bifurcation map of the photon density $s(t)$ variable, showing the period-adding bifurcation dynamics sequence between intervals of unlocked signals. The results presented in Fig. 3.14 demonstrate the RTD-LD circuit follows a period-adding bifurcation dynamics similar to the Liénard RTD oscillator

illustrated in Chapter 2. The modeling results confirm that under the regimes of operation analyzed here the RTD-LD circuits exploit only RTD's inherent non-linearity, in a way that the laser dynamics follows the overall dynamics of the RTD oscillator.

3.6.5 Quasi-periodic route to chaos

Outside the phase-locked regions the circuit produces unsynchronized complex outputs that can be regarded as result of the nonlinear mixing of the injected signal with the free-running oscillations, which gives rise to large frequency content quasi-periodic signals, and broadband (GHz wide) chaotic outputs. Figure 3.15(a) shows an example of quasi-periodic trajectories in the unsynchronized region between the winding numbers 1:1 and 2:1. Contrary to the previously synchronized orbits, quasi-periodic signals trajectories do not form closed loops. Instead, the orbits circulate around a confined region designed as quasi-periodic torus (Appendix A). Figure 3.15(b) illustrates V and ℓ RF power spectra showing spike like frequency distributions, both with the same frequency content. Increasing the nonlinearity by injecting amplitudes above 300 mV the circuit dynamics evolves from synchronization to quasi-periodicity and then onto chaos, where chaotic bursts start to appear outside the torus as the frequency ratio f_{in}/f_0 converge to certain irrational numbers. We observed experimentally this complex dynamics in a wide range of injected amplitudes. Figure 3.15(c) shows typical chaotic trajectories for driving amplitudes at 790 mV.

An example of the chaotic spectra can be seen in Fig. 3.15(d). The sharp spike like frequency peaks of quasi-periodic signals, Fig. 3.15(b), disappear in the transition to the chaotic regime, giving rise to signals with broadband continuous frequency distribution. The peaks observed in Fig. 3.15(d) correspond to the injected RF signal and to minor vestiges of some quasi-periodicity, an indication that the system dynamics evolves into a quasi-periodic route to chaos. Also observed is the substantial rise of RF power spectra noise level (up to 20 dB), also a characteristic of chaotic regimes.

The intrinsic instability and sensitivity to initial conditions of RTD-LD dynamics was numerically investigated by evaluating the rate of divergence of nearby trajectories in the unsynchronized regions. Figure 3.16 presents a histogram of the largest Lyapunov exponent λ_1, illustrating the frequency bands where the RTD-LD behaves chaotically, that is, where $\lambda_1 > 0$ (Chapter 2). The largest chaotic band corresponds to f_{in}/f_0 around the golden number $(\sqrt{5}+1)/2 \sim 1.62$ (also called the golden mean - Appendix A). The golden number, and other irrational numbers including the silver number, are commonly used in nonlinear dynamical studies [58]. The frequency range

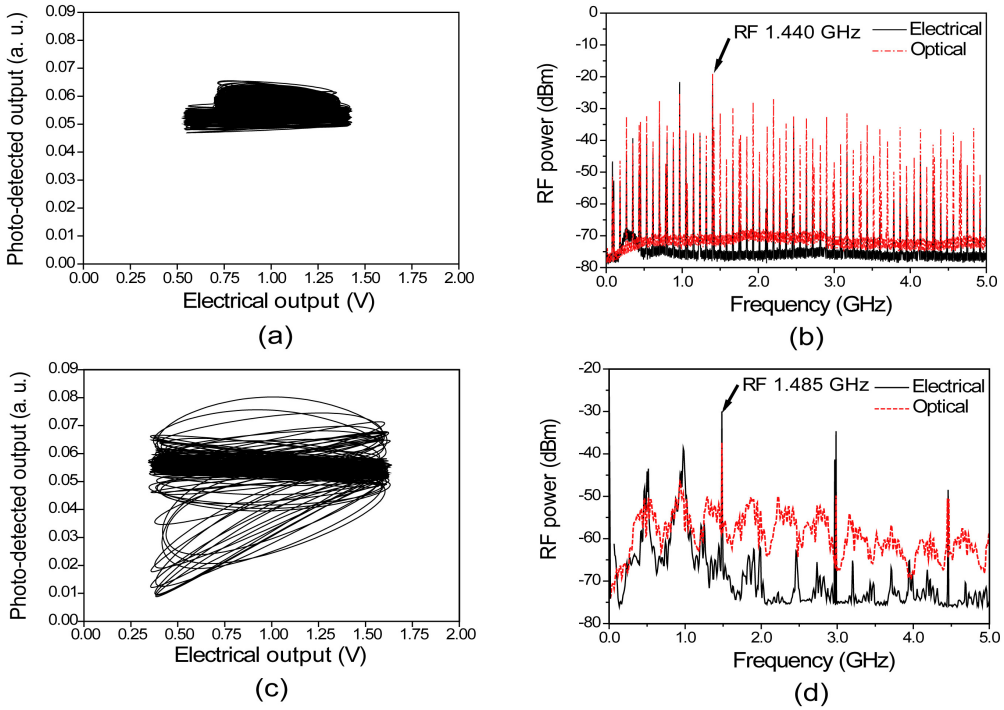

Figure 3.15: Experimental electro-photonic regimes in $V-\ell$ phase space (*left*) and corresponding power spectra (*right*) for (a)-(b) quasi-periodic, and (c)-(d) chaotic dynamic states.

of chaotic operation and the chaos signatures including broadband spectrum shown in Fig. 3.15(d), indicate the circuit is operating in the golden ratio band [58], the largest chaotic band of Fig. 3.16, since the intrinsic free-running frequency red shifts with the amplitude of the injected signal, leading to a value of f_{in}/f_0 close to the golden ratio. The analysis of Fig. 3.15(d) indicates the free-running frequency (2nd peak in the spectrum) under this level of injection was shifted from 953 MHz to ∼930 MHz, which gives $f_{in}/f_0 \sim 1.6$.

The process of producing broadband chaotic optical sub-carriers in the laser output described here is physically different from the methods presented in [27, 104, 105], and analyzed in Chapter 2, subsection 2.7.3. The generation and conversion of chaotic currents into chaotic light intensity patterns discussed here depend solely on the RTD nonlinearities. Currently under investigation are methods to increase the chaos dimensionality by exploiting the laser nonlinearities, and so extend RTD-LD capabilities. Since monolithic integration leads not only to a considerable reduction in size, energy consumption and cost but also to an increase in speed and reliability, we foresee RTD-

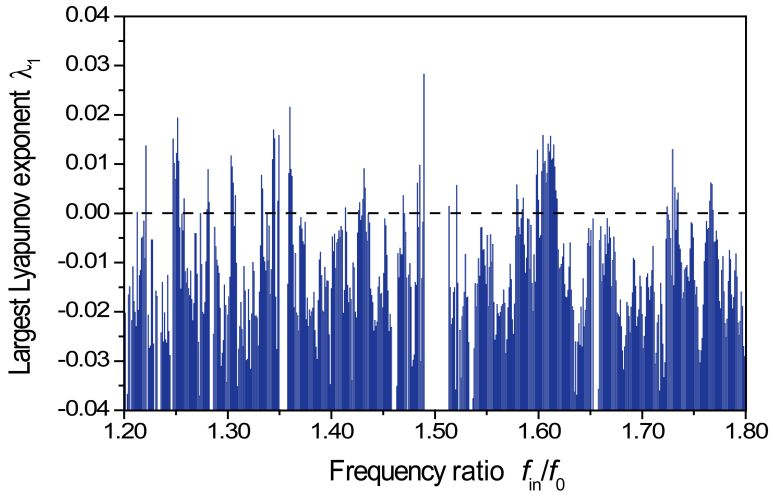

Figure 3.16: Histogram of the largest Lyapunov exponent for the unsynchronized region between 1:1 and 2:1 locking windows for the experimental conditions presented in Fig. 3.15.

LD hybrid (or monolithic) circuits as an alternative to the chaotic systems reported, like for example in [105], to operate as the core of electro-photonics chaotic broadband emitters to encode data at the physical level.

3.7 Chapter summary

A hybrid integrated RTD-LD circuit (the OEIC transmitter) operating as an oscillator and producing both electrical and optical outputs has been proposed, implemented, and characterized in time and frequency domains. By numerically solving a system of ODEs coupled to laser rate equations and obtaining a reasonably good fit to the optical and electrical results in both the time and frequency domains, we have shown that the operation of the circuit can be described by the Liénard oscillator model.

We have presented and discussed, both experimentally and numerically, the nonlinear dynamics of RTD-LD circuits in the autonomous and non-autonomous regimes. The autonomous RTD-LD operates as a OVCO producing fundamental relaxation oscillations at microwave frequencies in both electrical and optical outputs. In the non-autonomous regime the RTD-LD is driven by RF signals producing either injection locked outputs or high-dimensional chaotic carries in a quasi-periodic route to chaos. The RTD-LD circuits are simple, reproducible and versatile, and lead to a significant reduction in the complexity to generate chaotic carriers' emitters with a great potential

in secure MWP communication networks to transfer Gb/s data embedded in a chaotic electrical signal to an optical carrier. The main potential advantages of utilizing RTD-LD based systems instead of using other optoelectronic and laser systems include the simplicity and compactness of the solution which reduces considerably the number of high-speed electronics required in most of the schemes used to generate synchronized and chaotic signals, and the RTD frequency tunability as a function of the voltage. The RTD-LDs presented here operated at frequencies up to 2.1 GHz. With improved hybrid or fully monolithic integration we anticipate much higher frequencies at tens of GHz, with a great interest for future optical communication systems.

At the present the RTD-LD system exploits only RTD's inherent non-linearity, with the laser diode operating parameters being selected in a way that the laser dynamics does not influence the overall dynamics of RTD-LD oscillator, e.g., the laser is used only as a light source operating in a linear regime. In future work novel approaches may be explored using the laser relaxation oscillation frequency, as described in Chapter 2, to increase the system's dimensionality. The RTD-LD system can be explored in further applications not discussed in this chapter, namely chaos synchronization for communications [27] and chaos-controlled methods [130].

Chapter 4

Optical control of RTD-PD microwave-photonics oscillators

4.1 Introduction

Microwave-photonics (MWP) deals with OEIC devices and systems for processing signals at microwave frequencies. The key elements of MWP are optical sources capable of fast modulation, suitable transmission media, and fast optical detectors or optically controlled microwave devices. Optical injection locking of oscillators allows to synchronize the frequency and phase of free-running oscillators to optical modulated signals.

Direct optical control of microwave devices has been investigated, with early demonstrations of tuning of Gunn oscillators [131, 132], tuning and power modulation of trapped plasma avalanche and transit time (TRAPATT) oscillators [8], tuning of impact avalanche and transit time (IMPATT) oscillators [9], and injection of heterojunction phototransistors (HPT) [10] by optical illumination. More recently, optical injection locking of RTD devices [11] to intensity modulated optical signals was also achieved. RTDs are interesting alternatives for optical detection when compared with the limitations of traditional photo-detectors such as nonlinearities, saturation, and bandwidth limits. The detection results show the noise of the microwave injection-locked RTD signal matches that of the input optical signals resulting in stability and low timing jitter of the electrically detected frequency signal.

In the previous chapter, an RTD-OEIC transmitter consisting of a LD driven by a DBQW-RTD oscillator, the RTD-LD, capable of synchronization and chaos generation when perturbed by electrical periodic signals has been demonstrated. In this chapter, an optically controlled RTD-OEIC oscillator taking advantage of the photo-detection

characteristics of the DBQW-RTD structures is investigated. The process of direct optical control of RTD devices is photo-generation of carriers within the OW core of the device by the incident optical signal, through absorption. The RTD-PD driving a laser diode is realized using HIC technology. The optical control of the RTD-PD device introduces an extra port to the RTD-LD OEIC forming a new type of RTD-based MWP oscillator with both optical and electrical input and output ports.

4.2 Aim and objectives

The aim of the work described in this chapter is to investigate detection characteristics of RTD-PD devices, and the implementation and characterization of OEIC oscillators consisting of discrete RTD-PD and LD components. The main goal is to describe how optical injection locking of RTD-PD oscillators can be used for generation of low-phase noise microwave signals in both electrical and optical domains. This was achieved through the following objectives:

- Characterize the detection characteristics of DBQW-RTD OW photo-detectors under direct optical illumination.
- Implement a hybrid OEIC consisting of an RTD-PD in series with a LD, the RTD-PD-LD, with both optical and electrical input and output ports, and a DC voltage control port.
- Investigate experimentally and numerically the dynamics of RTD-PD-LD oscillators under optical injection.
- Implement RTD-based MWP systems in optoelectronic clock recovery circuits and transmission of modulated signals in wireless/photonics links.

4.3 Chapter overview

In this chapter, after a short introduction on the detection characteristics of both RTD photo-detectors and waveguide detector devices, the characteristics of DBQW-RTD OW photo-detectors utilized in this work are described. Next the experimental arrangement of OEIC oscillators formed by RTD-PD and LD devices is discussed, followed by the investigation on the optical injection-locking characteristics of RTD-PD-LD oscillators in both electrical and optical domains under direct illumination of optical modulated signals. An optically controlled Liénard oscillator model will be presented

taking in consideration the detection characteristics of the RTD optical waveguides. Ultimately, applications of RTD-PD-LD oscillators in transmission systems are discussed, including the implementation of clock recovery schemes for clock extraction of Gb/s return-to-zero (RZ) signals, and the transmission of analog and digital phase modulated signals in wireless/photonis links.

4.4 Detection characteristics of DBQW-RTD devices

DBQW-RTD structures for photo-detection emerged in the last decades as devices with high responsivities and gain-bandwidth-efficiency products, as well as low switching energies [33, 133] because of their intrinsic gain and low voltage operation characteristics. Essentially, they work as follows, a light pulse incident upon a resonant tunneling structure biased close to the peak voltage produces photo-charges that reduce the series resistance, leading to a shift of the peak and valley voltages which can induce RTD switching from the peak to the valley and give rise to changes in the current flow [134]. By taking advantage of these effects, RTD structures can be used to implement light-by-light switching [133], and optically switched RTD photo-detectors [33]. Such optically switched devices were already tested for high-speed transmission communications at Gb/s rates with very low electrical power dissipation [33]. More recently, single photon detectors were demonstrated taking advantage of DBQW-RTD detectors based on quantum dot structures [135], and light-modulated stochastic dynamics of RTDs was studied as potential candidates for artificial neurons like devices [136]. In this section, the detection characteristics of DBQW-RTD waveguide photo-detectors is analyzed for their implementation in optically injection locked oscillators.

4.4.1 DBQW-RTD detectors

An example of a surface-illuminated DBQW-RTD photo-detector consisting of InGaAs/AlAs semiconductor compounds (the same materials of the RTDs used in this work) is shown in Fig. 4.1(a). As exemplified in the conduction band diagram, since the applied external voltage drops almost entirely on the thick undoped InGaAs absorption layer, the photo-generated electrons and holes in it are separated by the electric field, the holes are accumulated at the barriers of the resonant structure whereas the electrons are collected by the external circuit. As a result, the applied electric field in the undoped layer is partially screened and that within the resonant structure is enhanced. Consequently, the NDC of the resonant tunneling device shifts to lower voltages, as exemplified in Fig. 4.1(b). If the accumulated holes have a long recombination time

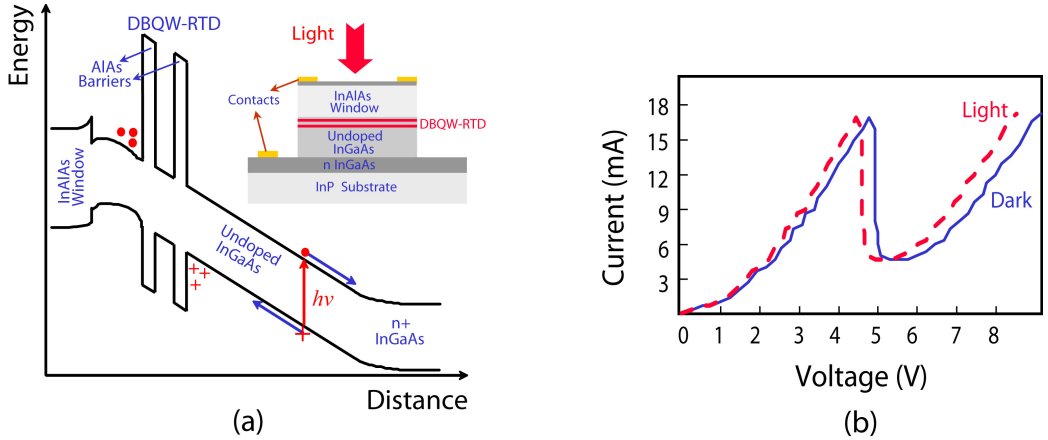

Figure 4.1: (a) Schematic of the conduction band diagram of a direct illuminated InGaAs/AlAs DBQW-RTD. Inset is shown the schematic cross-section of the surface RTD-PD. (b) Typical dark and illuminated I-V characteristics.

the sensitivity of the device is high but its frequency response is low whereas for fast hole recombination times the sensitivity is lower but high-speed can be achieved.

4.4.2 Waveguide detectors

Despite all the efforts, high efficiency and wide bandwidths cannot be simultaneously achieved by surface-illuminated structures, such as the one exemplified in the previous subsection. Therefore, side-illuminated waveguide photo-detectors were proposed as a means to ease the trade-off between the speed and responsivity. This type of detector is generally edge-illuminated with light guided parallel to the intrinsic layer and incrementally absorbed due to the fact that the photo-generated carriers and the light travel in different, perpendicular directions. In comparison with the surface transverse photodiode, the waveguide longitudinal photodiode responsivity is mainly determined by the waveguide length, and not by absorption layer thickness, therefore the waveguide detector has a larger bandwidth-efficiency performance than the surface photodiode.

The optical waveguiding structure is similar to that of the double heterostructure lasers. Figure 4.2 shows the RTD-PD OW schematic, the wafer structure and the energy band diagram of the waveguide detector used in this work. The DBQW-RTD OW layer structure is described in Chapter 3, subsection 3.4.2. Under modulated light the same epitaxial structure can be used for both modulator and photo-detector applications. In fact, the RTD-OW structure discussed here was originally designed as an RTD-EAM,

and more detail on its optical modulation characteristics can be found in [42, 43]. Light is edge-coupled to the waveguide and the responsivity is mainly limited by the coupling efficiency and the scattering loss along the waveguide. The coupling can be improved through the use of lensed fibers, antireflection coating at waveguide facet, or laterally tapered waveguide sections.

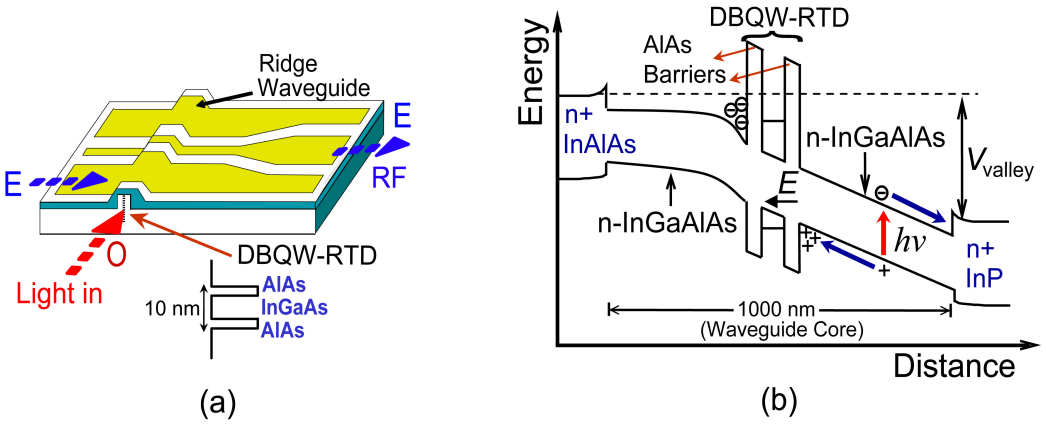

Figure 4.2: (a) Schematic diagram of RTD-PD device. The ridge waveguide dimensions were ~ 3 μm wide and 1 μm thick. (b) RTD-PD unipolar InAlAs-$In_{0.53}Ga_{0.42}Al_{0.05}As$-InP band energy diagram.

4.4.3 Detection mechanism in DBQW-RTD waveguide detectors

In this work, the RTD operates as a waveguide photo-detector by taking advantage of DBQW-RTD photoconductive layers and OW structure. An RTD-PD OW works as a waveguide photo-detector for light with energy close or above the waveguide core bandgap energy. The ridge waveguide structure, Fig. 4.2(a), gives an advantage over traditional RTD-PDs by providing light confinement along the DBQW plane. The RTD-PD presents the typical RTD nonlinear I-V characteristic with an NDC region which leads to electrical gain. The photo-detection mechanism works as follows. For the low bias condition, electron-hole pairs are created in the depleted part of the waveguide core (that is, the 500 nm undoped $In_{0.53}Ga_{0.42}Al_{0.05}As$ layer) adjacent to the double barriers, see energy band diagram of Fig. 4.2(b). However, due to the fact that the electric field is very weak under low bias, the generated electron-hole pairs tend to recombine and neutralize after the creations. As the bias is increased, the hole accumulation density at the hetero-interface increases, resulting in a enhancement of the hole tunneling current. However, for bias voltages below the peak voltage, the current

flow is still low and therefore a portion of the photogenerated carriers recombine rather than tunnel through the DBQW structure. When the bias is further increased to the valley voltage, Fig. 4.2(b), the effective conductivity of the double barriers drops as the resonant level in the quantum well becomes lower than the Fermi level of the emitter region. Consequently, the band bending on the double barriers increase, resulting in a substantially increase of the hole tunneling current. Once the hole current becomes large enough, the recombination in the photogeneration region decreases to zero, and the photogenerated carriers are collected by the electrodes.

As described previously, if the photon energy is larger than the waveguide core band-gap energy (here 0.815 eV) the RTD-PD operates as a photoconductive detector. However, if the injected photon energy is slightly lower (e.g. 0.8 eV) the Franz-Keldysh effect [137], which is associated with interband photon-assisted tunneling, plays also a role in absorption mechanism, i.e., the absorption of a photon is considerably enhanced due the presence of the electric field via the Franz-Keldysh effect.

4.4.4 Devices preparation and experimental setup

Before characterization, RTD-PD samples were prepared and separated using the thinning and cleaving processes described in Chapter 3. To operate RTDs as waveguide PDs the process of device preparation is more critical because of the need of obtaining good quality facets and the high risk of waveguide facet destruction in the scribing process. The cleaving process can also result in RTD-PDs with inferior detection performance if the devices have large guiding regions protuberant on the sample surface. After the device separation, RTD-PD bars showing good quality facets and appropriate NDC characteristics were mounted on brass sub-mounts for testing.

Photo-detection characterization of RTD-PDs consisted in coupling light into the waveguide cleave ends (endfire coupling) using a lensed SM optical fiber (spot diameter of 5 μm$\pm$0.5μm and coated on the tip). The lensed fibers and the RTD-PD devices were mounted on microblock 3-axis translation stages, in an endfire arrangement where both input optical fibers and samples could be translated and rotated independently. The endfire experimental setup is presented in Fig. 4.3(a) showing the three-axes movable stage where the mounted RTD-PD bars were placed. Figure 4.3(b) shows some RTD-PDs mounted on brass sub-mount, a SM lensed fiber aligned with the RTD-OW, and a ground-signal-ground (GSG) probe for electrical characterization.

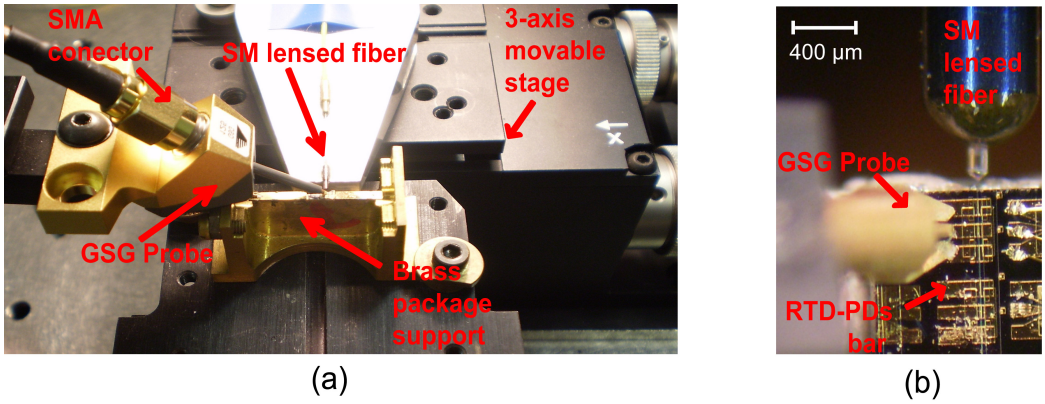

Figure 4.3: (a) Three-axes movable stage and brass package where the mounted RTD-PD bars were placed for testing. (b) Photograph of RTD-PD bars mounted on a brass sub-mount for testing.

4.4.5 DC photo-detection characteristics

The light source employed for optical detection characterization was a Photonetics Tunics laser diode tunable in the wavelength region 1457 nm - 1599 nm, with up to 10 mW optical output power, that could be used for high frequency modulation with a bandwidth up to 1 GHz. RTD-PD devices mounted on the brass fixture were characterized directly on-chip by probing the RTD CPW contacts using a GSG CPW probe with a pitch size of 125 μm, Fig. 4.3.

Due to the polarization dependence of the RTD waveguide detectors, laser light was coupled to the waveguide using a polarization controller and the position of the input fiber was optimized to obtain the highest photocurrent from the device (and hence a high response to light modulated signals), ensuring a maximized overlap between the optical mode from the input fiber and the DBQW region. In Fig. 4.4(a) is shown the I-V characteristics for both dark and illuminated conditions showing the photocurrent gradually turned on as the bias was increased to the valley voltage. Consequently, the NDC of the RTD-PD shifts to lower voltages. Also shown is the external responsivity (the photocurrent generated divided by the optical power in fiber) as a function of the bias voltage. It is possible to notice that a bias voltage of only 0.5 V was required to efficiently start to collect the photogenerated carriers. The results show clearly a higher responsivity close in or in the valley region which confirms the detection mechanism analyzed in detail in subsection 4.4.3. Fig. 4.4(b) presents the photogenerated valley current plotted versus the optical power in fiber. The straight line in the figure is the

linear regression obtained from the data. The photogenerated valley current increases approximately linearly with the illumination power level (dI/dPi) with a slope of 0.29 mA/mW, up to 10 mW in-fiber optical power level. No saturation of the photogenerated valley current was observed, indicating that photoexcited RTD waveguide detectors can operate at moderate incident power light conditions.

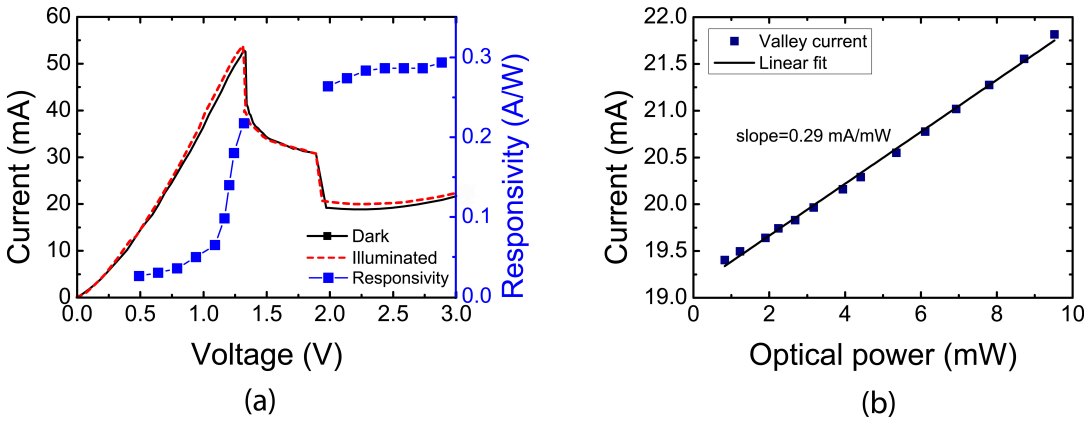

Figure 4.4: (a) Dark RTD-PD I-V characteristic and I-V curve with illumination at 1550 nm for input optical power in fiber around 5 mW. The estimated responsivity as a function of the bias voltage is also plotted. (b) Photogenerated valley current as a function of illumination intensity and the linear regression.

The RTD photo-generated current I_{ph} in response to a incident optical signal $P(\lambda)$ can be expressed by:

$$I_{ph} = \eta_{ph} \frac{q\lambda}{hc} P(\lambda) \tag{4.1}$$

where λ is the operation wavelength, h and c are the Planck constant and the speed of light in the vacuum, respectively, and η_{ph} is the waveguide photo-detector quantum efficiency given by:

$$\eta_{ph} = \kappa(1 - R_{ref})(1 - e^{-\alpha(\lambda,V)\gamma_{ph}\Lambda}) \tag{4.2}$$

with κ being the light coupling factor, R_{ref} is the waveguide facet reflectivity (sidewall imperfections and refractive index nonuniformity contribute to this kind of losses), $\alpha(\lambda, V)$ is the waveguide core absorption coefficient at wavelength λ and bias V, γ_{ph} is the overlap integral of the electric field and the optical field, and Λ is the waveguide photo-detector absorbing active length. This expression does not take into account with propagation losses.

In Table 4.1 are presented the typical physical parameters used to model the RTD photo-detector characteristics. For the waveguide structure described in Fig. 4.2, we estimate $\gamma_{ph} \sim 0.25$ and $\kappa \sim 0.35$ at 1.55 μm, and an absorption coefficient $\alpha(\lambda, V)$, in the valley region, around 400 cm^{-1}, estimated from absorption spectra characterization reported in [42], which for devices with absorbing active length $\Lambda \geq 150$ μm yields a quantum efficiency $\eta_{ph} \sim 0.2$. Finally, the external responsivity is expressed by:

$$R_\lambda = \frac{\lambda}{1.24}\eta_{ph} \tag{4.3}$$

which gives a responsivity in the valley region of 0.25 A/W, which compares well with the typical values measured between 0.25 A/W and 0.3 A/W for RTD-PD devices biased in the valley region. According to the calculations, most of the light is not coupled in the waveguide (25% coupling efficiency which gives a coupling loss of 6 dB), which seems to be the major factor limiting the responsivity. Considering the estimated losses, we expect RTD-PD devices can provide PDs with internal responsivities up to 1 A/W. The losses can be reduced by increasing the overlap integral of the input beam profile with the waveguide cross-section, reducing facet reflections, and design an optical waveguide with the RTD-PD active region closer to the input facet. In addition, calculations show that there would be no significant increase in the responsivity even with a much higher overlap, indicating that ~ 150 μm is long enough to absorb almost all light. In fact, calculations suggest there is not a substantial increase in responsivity for waveguides longer than ~ 100 μm. Therefore, the waveguide structure will occupy much less area, and the RTD could operate at higher frequencies.

Table 4.1: Description of the typical physical parameters of the waveguide photo-detector.

Symbol	Quantity	Typical order of magnitude
λ	Operation wavelength	1.55 μm
κ	Light coupling factor	0.35
R_{ref}	Waveguide facet reflectivity	0.3
$\alpha(\lambda, V)$	Waveguide core absorption coefficient (at 1.55 μm and biased in the valley)	400 cm^{-1}
γ_{ph}	Overlap integral of the electric and optical fields	0.25
Λ	Waveguide contact length	150 μm

4.4.6 Optical modulation response

The modulation response is an important characteristic for optoelectronic devices, for fabrication purposes as well as for device modeling purposes. For optical detectors, the modulation response is defined as the ratio of the change in electrical output current to the change in incident optical power. The measurement system used for the characterization of the RTD-PDs consisted of continuous wave light from a tunable SM laser modulated by an external modulator driven by an RF signal generator. A SM optical fiber was used to capture the modulated light and to illuminate the RTD-PD waveguide by means of a SM lensed fiber. The RTD-PDs, the electrical GSG probe (with high frequency response up to 40 GHz), and the optical fiber were mounted on the positioners as shown previously in the DC characterization, Fig. 4.3. The variable DC bias was applied via a wide bandwith bias-T (45 MHz - 26.5 GHz) connected to the high-frequency probe SMA cable. The RTD-PD electrical response to optical modulated injected signals was measured using a high-bandwidth spectrum analyzer and oscilloscope.

Figure 4.5(a) presents the RF injection locking capture level as function of the DC bias using light (λ = 1550 nm) modulated by a sinusoidal RF reference signal at 1.2 GHz, with optical power levels in fiber of 1 mW and 6 mW. The figure shows the dependence of 1.2 GHz photodetection signal on bias conditions. The responsitivity increases with the transition from RTD-PD peak to valley voltage, V_p and V_v, respectively, with an improvement up to 14 dB. As discussed in subsection 4.4.3, the higher response in this region occurs because the holes photo-generated in the depletion region accumulate around the collector barrier [see Fig. 4.2(b)], causing a local enhancement field which leads to higher carrier velocity and hence high current. Figure 4.5(b) presents the photo-detected RF power as function of the light wavelength with the DC bias voltage as parameter. Again, the increased responsivity under higher voltage bias has also been observed at the wavelength of 1530-1570 nm (C-band).

Figure 4.5(c) presents RTD-PD measured output RF power levels when biased in the peak and valley regions as a function of incident optical power, and Fig. 4.5(d) shows the RF power spectra of the photo-detected optical modulated signals. Up to 14 dB gain is obtained in the transition from the peak to the valley region. The results demonstrate the RTD-PD works as a high-speed O/E converter, taking advantage of the OW design. In what follows, the optical injection locking operation employing RTD-PDs is investigated when the devices are DC biased in the NDC region, i.e., when they generate self-sustained oscillations at frequencies close to the detected RF signals.

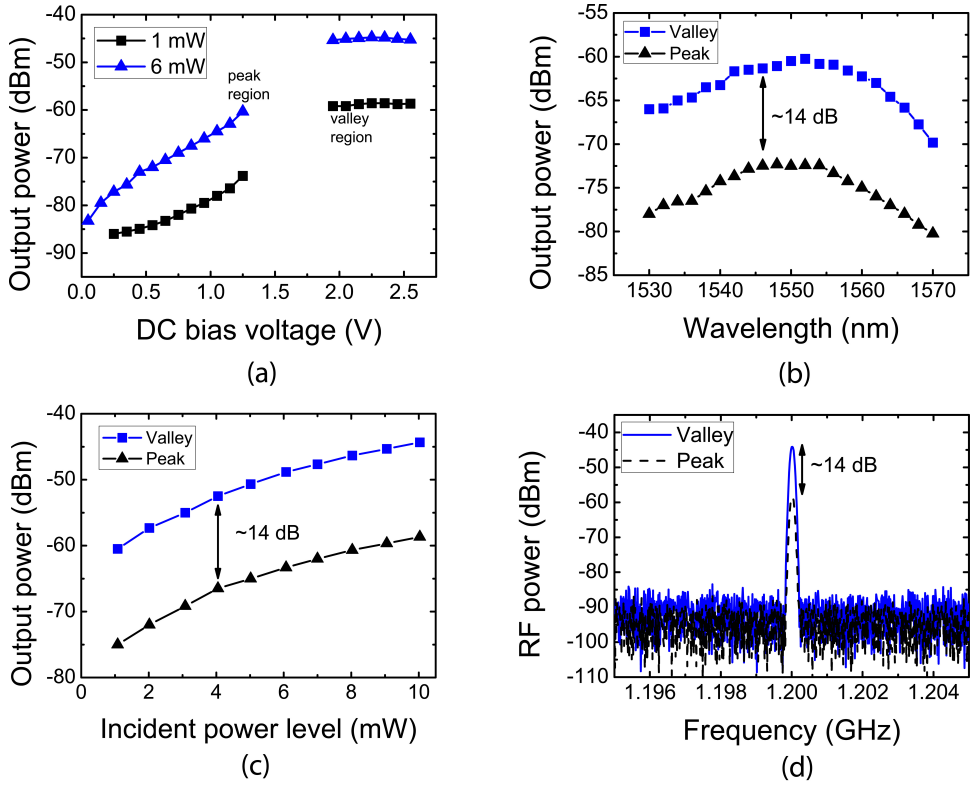

Figure 4.5: (a) RF injection locking capture level as function of the DC bias using light at $\lambda = 1550$ nm. (b) Output power as function of wavelength with DC bias voltage as parameter for 1 mW optical power in fiber. (c) Output power as function of optical power level at $\lambda = 1550$ nm. (d) Power spectra of photo-detected signal using a 10 mW optical signal ($\lambda = 1550$ nm). In figures (b), (c), and (d), the RTD-PD was DC biased in the peak $V_p = 1.2$ V and valley $V_v = 2.0$ V regions. In all figures, light was modulated by a RF reference source signal at 1.2 GHz.

4.5 Optically injection locked RTD-PD oscillators

Optical injection locking of an electrical oscillator, which allows to synchronize the frequency and phase of a free-running oscillator to the modulated optical signal, is very attractive in applications such as LO embedded in radio base station (BS) cells and in optical transmission systems, e.g. optoelectronic clock recovery circuits, which is much simpler and more suitable for higher bit-rates than a fully electrical circuit. There are two types of OILOs: the direct and indirect type. A direct OILO, whose active oscillator device itself is directly illuminated for synchronization is preferred because is much simpler and is more suitable for monolithic integration than an indirect one,

which needs an external photo-detector. A possible direct OILO can be based on DBQW-RTD devices.

Sollner et al. have proposed that photoconductivity could be used to control a RTD, resulting in a resonant tunneling phototransistor [138]. Optical injection locking of a RTD was first demonstrated using a modulated laser diode optical signal at 2.8 GHz and with 150 kHz locking bandwidth [139]. Optical injection locking of a RTD with RF-modulated 1.5 μm CW light source was also demonstrated with 300 kHz capture range of a 360 MHz RF signal [126]. Lasri et al. and Eisenstein and co-workers have converted modulated CW lasers and mode-locked diode lasers into very low phase-noise RF oscillations, and have provided very useful models for the analysis of the noise in optically injection-locked microwave oscillators [140–142]. Ramond et al. [11] reported optical injection locking of a RTD at 1 GHz taking advantage of a highly stable signal obtained from an optical frequency comb phase locked to a narrow optical transition in laser-cooled atoms, demonstrating locking ranges of $\geq$ 5 MHz, which is more than ten times greater range than previously reported.

In this work, we demonstrate a single assembled MWP oscillator having both optical and electrical input and output ports, comprising an RTD-PD and a LD, the RTD-PD-LD. The dynamics of optical injection-locking of RTD-PD-LD oscillators is analyzed showing stable and low-phase noise RF signals in both electrical and optical domains with wide capture locking ranges [50].

4.5.1 Experimental setup description

The experimental RTD-PD-LD oscillator circuit and setup are displayed in Fig. 4.6. The oscillator is a HIC consisting of RTD-PD and LD discrete components that perform the oscillator's optical input and output ports, respectively, Fig. 4.6(a). It was realized on a PCB-TL layout using a similar HIC technology described in subsection 3.5.1. In this case however, the orientations of RTD-PD OW input and laser diode output were both considered in the steps taken to package the circuit and in the layout of the circuit, to ensure a good alignment to a lensed fiber in an optical end fire set-up. The circuit disposition and end fire setup employed are shown in Fig. 4.6(a).

The RTD-PD-LD oscillator under analysis here works as an OVCO, Fig. 4.6(b), with the same principles of operation as described for the case of the RTD-LD OEIC transmitters (subsection 3.6.2). In this case the injection locking phenomena is investigated when the RTD-PD receives optical modulated signals. The circuit's diagram and experimental setup are presented schematically in Fig. 4.6(c) showing the optical

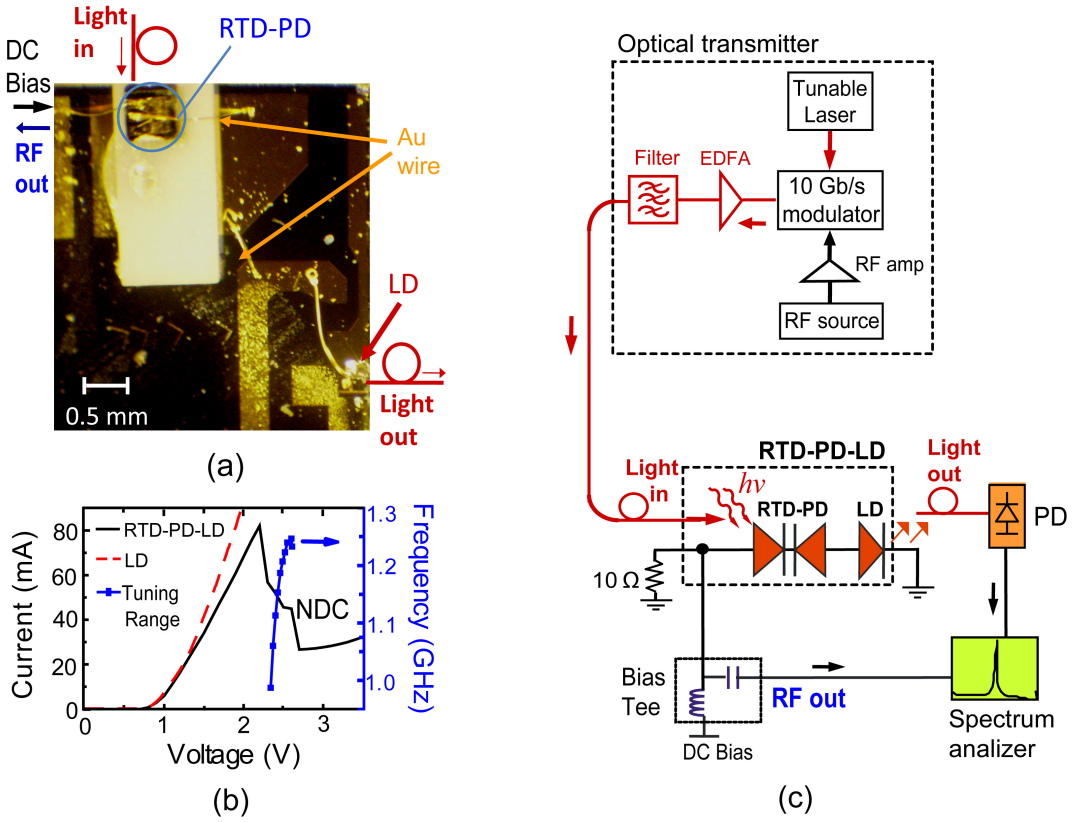

Figure 4.6: (a) Photograph of the assembled RTD-PD-LD showing both optical input and output ports. (b) I-V characteristics of LD and RTD-PD-LD, and frequency tuning curve. (c) Experimental setup and circuit schematic diagram.

transmitter and measurement setups. Optical modulated signals at communications wavelengths (typically λ =1550 nm) were generated by a tunable SM laser feeding a 10 Gb/s Mach-Zehnder modulator and amplified by an erbium-doped fiber amplifier (EDFA), and filtered to eliminate spontaneous emission noise from the EDFA. Then, optical modulated signals illuminated the RTD-PD oscillator waveguide input facet through SM lensed fiber. The free running oscillation frequency of the RTD-PD-LD oscillator was controlled by adjusting the bias voltage provided by a power supply and through an external bias tee. Optically injection locked signals were measured in the electrical output of the circuit and in the detected laser output using a high frequency oscilloscope and spectrum analyzer.

4.5.2 Optically controlled Liénard oscillator model

For numerical purposes and analysis, the incident optical modulated signal received by the RTD-PD is given by a sinusoidal optical input with:

$$P(t) = P(\lambda)\left[1 + m\sin(2\pi f_{in}t)\right] \tag{4.4}$$

where $P(\lambda)$ is the average power, m the modulation depth, and f_{in} is the frequency of the modulated signal.

Since in the operation conditions described previously in Chapter 3 the LD acts as a small series resistance the RTD-PD-LD preserves the RTD intrinsic NDC. The dynamics of the circuit in the presence of an injected optical signal can be analyzed considering the equivalent lumped circuit of Fig. 4.7(a), which is well described as a forced Liénard system subjected to external injection of a photo-generated modulated current:

$$\frac{dV(t)}{dt} = \frac{1}{C}\left[I(t) - F(V) - I_{ph}(t)\right] \tag{4.5}$$

$$\frac{dI(t)}{dt} = \frac{1}{L}\left[V_{DC} - RI(t) - V(t)\right] \tag{4.6}$$

where $I(t)$ and $V(t)$ correspond to the current flowing through and the voltage across the RTD-PD, respectively, $F(V)$ is the RTD-PD I-V curve, V_{DC} is the DC bias, $I_{ph}(t)$ is the photo-generated current taking in consideration the detection characteristics given by Eq. (4.1); C represents the RTD equivalent intrinsic capacitance and estimated parasitics, R accounts for the RTD-PD-LD series resistance, and L corresponds to the wire bonding and TL inductances. The LD dynamics is described using the photon and carrier densities rate equations as discussed in the preceding chapter, subsection 3.5.4.

In Fig. 4.7(b) is depicted a block diagram with the corresponding mathematical representation (normalized variables) of the coupled Liénard-laser diode system under injection of a periodic signal $\upsilon_{opt}\sin[z(t)]$ that accounts for the RTD-PD-LD subjected to external optical injection. In this work to avoid large running times simulations and reduce as much as possible the number of parameters, we assumed a static model of the I-V curve in the dark conditions. As shown in Fig. 4.4(a), under the moderate illuminated conditions employed in this work and considering the responsivity levels of the RTD-PDs used (around 0.25 A/W, Table 4.1), the RTD-PD-LD I-V shifts slightly to lower voltages due to the generated photo-current without having a great effect on the overall I-V characteristic. In the cases where the optical injection changes

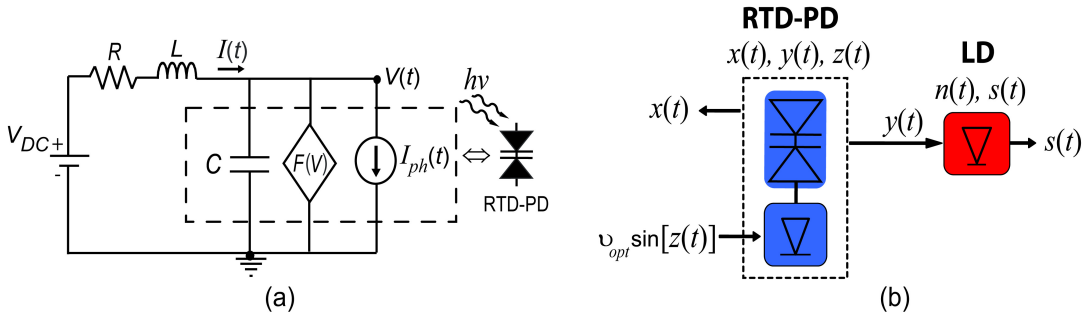

Figure 4.7: (a) RTD-PD-LD equivalent lumped electrical circuit. (b) Block diagram Liénard RTD-PD-LD oscillator dimensionless model subjected to optical injection.

substantially the I-V characteristic reducing their peak-to-valley ratio, and therefore the NDC region, refinements of the model can be employed, using for example the ones reported in [143], that include the effect of light on the static DC current-voltage model taking into account the photoconductivity and charge accumulation effects in double-barrier RTD structures.

4.5.3 Optical injection locking results

The coupling of optical modulated signals to the RTD-PD waveguide locks the self-oscillations to the optically injected RF sub-carrier for in-fiber optical powers above a given threshold that depends on the waveguide characteristics, on the frequency and the RF power of the modulated light, and on the RF power of the unperturbed self-oscillations. To investigate the influence of optical injection locking on the quality of the RF carriers, signals were observed at the output RF port of the RTD-PD-LD oscillator. The oscillator was judged injection-locked when its output spectrum matched the optical modulation reference source frequency with stable oscillation and low-noise. In the following, two RTD-PD-LD circuits employing RTD-PDs with peak currents of 84 mA and 58 mA were investigated, both with $\sim$ 25 mA valley current, and showing oscillations ranging from 0.98 GHz to 1.25 GHz, Fig. 4.6(b), and 1.04 GHz to 1.41 GHz, respectively, as the DC bias is swept across the NDC region with voltage range $\sim$ 0.4 V.

Figure 4.8(a) *top* presents the RF spectra of the unlocked electrical and LD optical output signals for optical power level in fiber around 0.4 mW, showing oscillations at around 1.2 GHz - both the free-running and photo-detected signals are present plus generated sidebands. Figure 4.8(a) *bottom* presents the RF spectra of circuit outputs

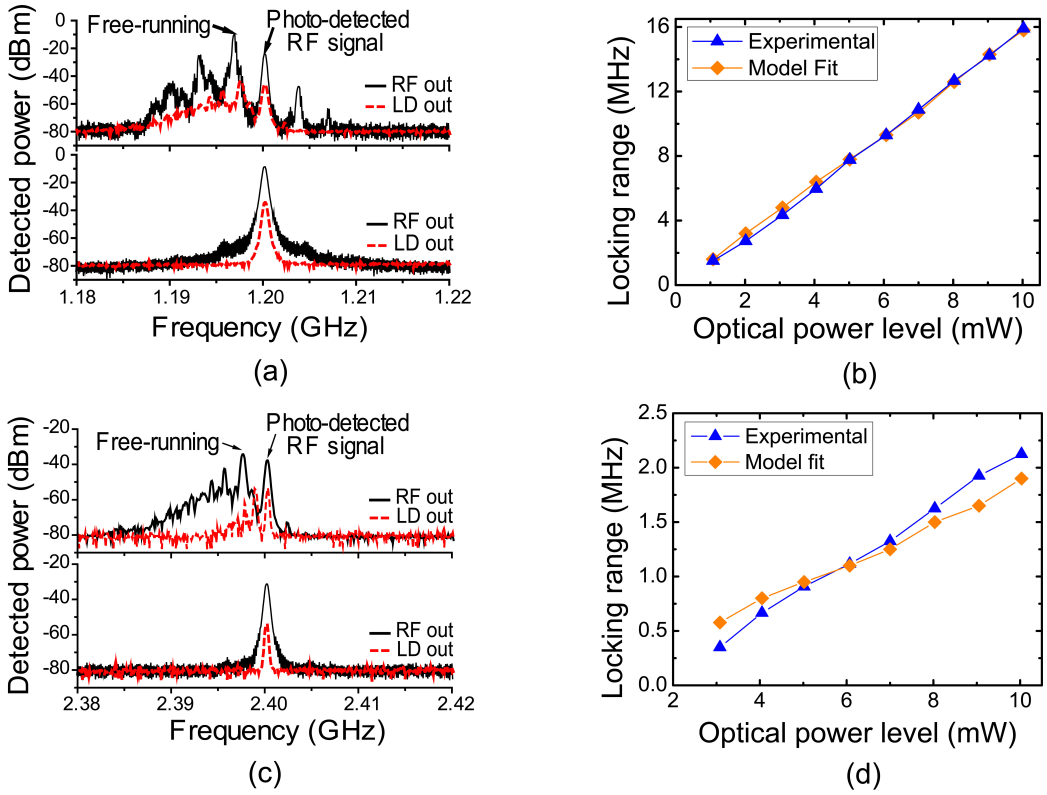

Figure 4.8: Spectra of RF and LD unlocked (*top*) and locked (*bottom*) signals for (a) 1.2 GHz, and (c) 2.4 GHz optical modulated signals. Experimental and simulated frequency locking ranges for (b) 1.2 GHz, and (d) 2.4 GHz.

for optical power in fiber around 3 mW, clearly showing optical injection-locking - the photo-detected output spectra collapses to match that of the reference source signal. Figure 4.8(b) presents the injection-locking capture range as a function of in-fiber optical power. Locking capture ranges as high as 15.9 MHz were observed, corresponding to a fractional locking bandwidth of 1.3% ($\triangle f/f_0$, where $\triangle f$ is the locking range in MHz and f_0 is the oscillation frequency in MHz), which is substantial superior to the one reported in [11]. Harmonic injection locking operation was also investigated and is displayed in Fig. 4.8(c), showing unlocking (*top*) and locking (*bottom*) regimes for a 2.4 GHz optical modulated signal. As presented in Fig. 4.8(d), injection-locking capture ranges between 0.35 MHz and 2.13 MHz were achieved using optical powers between 3 mW and 10 mW, respectively. Figures 4.8(b) and (d) also show the locking ranges given by the Liénard's oscillator model, Eqs. (4.5)-(4.6), assuming the following circuit parameters: $L = 4$ nH, $C = 3.3$ pF and $R = 8.3\ \Omega$ [see Fig. 4.7(a)]. The

Liénard's model gives a good prediction of fundamental and harmonic lockings, which is an important figure of merit of optically injection locked oscillators.

The locking capture level results reported in both fundamental and harmonic regimes are significant considering the fiber to waveguide low coupling efficiency. It is worth mentioning that when DC biased in the valley region the photo-generated RF power was around −55 dBm, see Fig. 4.5(c), a value not enough to drive the LD; when optically injection-locked the measured RF output power was around −8.7 dBm. This means that when locked the oscillator RF power does not depend on the injected optical power but is determined by the free-running oscillation power. These results clearly indicate the RTD-PD-LD oscillator can provide high-power RF signals whose characteristics can be controlled optically. Since injection-locking leads to a significant phase-noise and jitter reduction the respective oscillator performance has been further investigated. For average in fiber optical power levels around 2 mW, modulated within the oscillator frequency locking range, the electrical and optical outputs showed SSB phase noise values as low as −94 dBc/Hz at 10 kHz and −100 dBc/Hz at 100 kHz frequency offsets, respectively, Fig. 4.9(a). This is a substantial improvement since the phase noise of free-running oscillations was around −76 dBc/Hz at 100 kHz. For optical power levels around 7 mW, the circuit harmonic at 2.4 GHz showed similar phase noise suppression, Fig. 4.9(b).

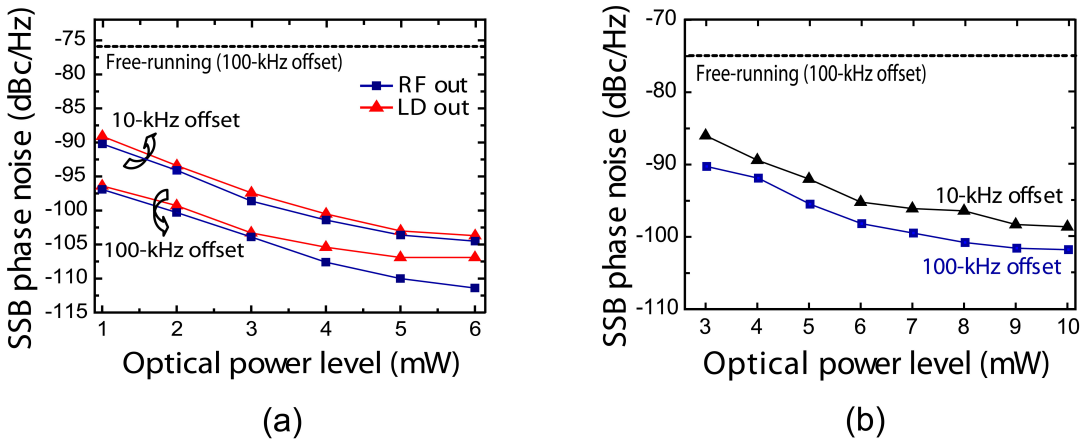

Figure 4.9: SSB phase noise of optically injection-locked signals for (a) 1.2 GHz and (b) 2.4 GHz. The RF reference signal phase noises at 1.2 GHz and 2.4 GHz were -117 dBc/Hz and -115 dBc/Hz at 10 kHz offset, respectively.

The optical injection locking investigation proceeds with a summary of the measurements using a RTD-PD-LD circuit self-oscillating at around 1.405 GHz. The circuit

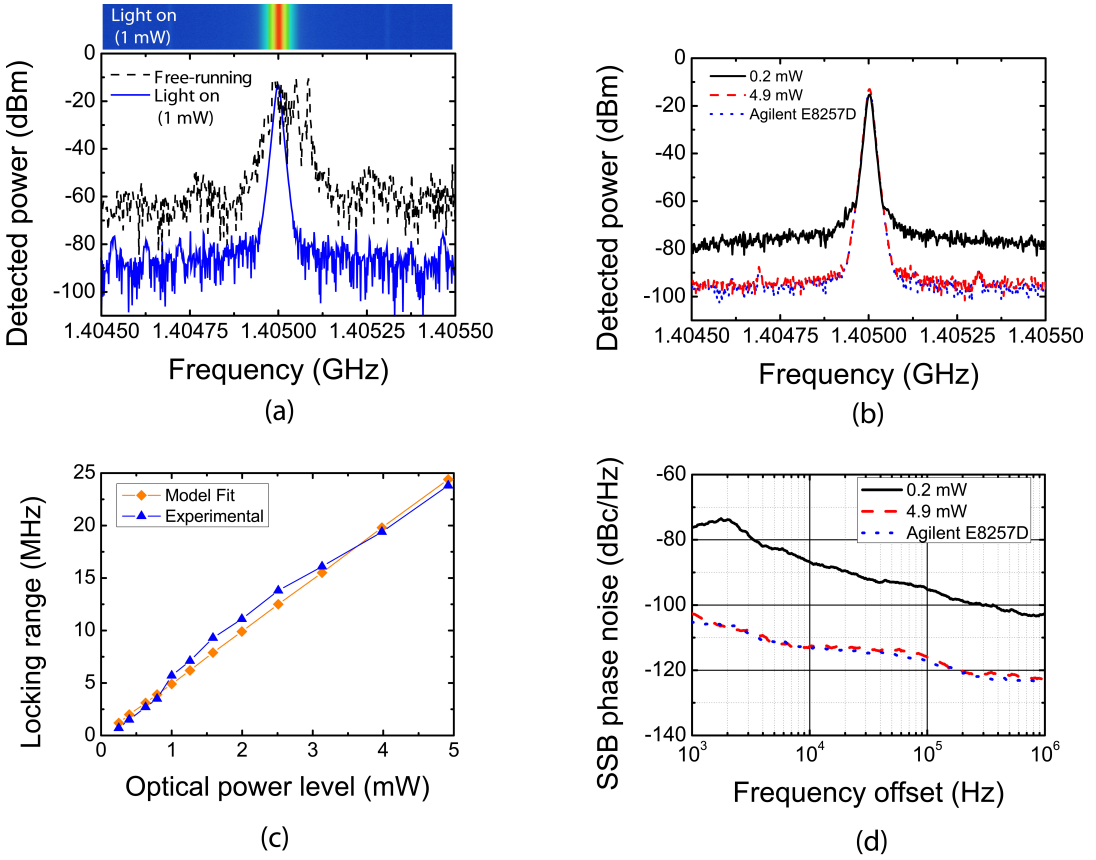

Figure 4.10: (a) Power spectra of the free-running and locked signals. (b) Spectra of RF reference and optical injection locked signals at 0.2 and 4.9 mW optical power levels. (c) Experimental and simulated locking ranges as a function of optical power using model fitting parameters $L = 3.6$ nH, $C = 3$ pF, and $R = 7.2\ \Omega$. (d) SSB phase noise measurements.

showed a substantial improved performance in terms of injection locking and spectral purity. The results are summarized in Fig. 4.10. Figure 4.10(a) presents the typical broad spectrum of free-running oscillation (light off) around 1.405 GHz. When the light is on, with an average optical power level in fiber of 1 mW, the free-running signal is pulled and the spectrum collapses showing a substantial phase noise reduction. In the inset of Figure 4.10(a)(*top*) is presented the recorded spectrum surveillance confirming the spectral long-term stability of the optical injection locking. Injection locking for optical power levels in fiber as low as 0.2 mW was observed, Fig. 4.10(b). The locking range was 23.8 MHz for 4.9 mW optical power in fiber, Fig. 4.10(c). This corresponds to an exceptional wide value with a fractional locking bandwidth of 1.7%. In Fig. 4.10(c)

is also presented the model fit with a good agreement with experimental results. Figure 4.10(d) presents the phase noise measurements showing phase noise of −112.4 dBc/Hz at 10 kHz offset, a very close match to the RF source signal for the moderate optical power levels employed (below 5 mW), which results in a noise suppression of more than 40 dB when compared with the free-running oscillator without illumination. For the in fiber optical power locking threshold the phase noise was −87.1 dBc/Hz at 10 kHz offset.

The observed locking range corresponds to the largest value reported in the literature for RTD-based devices at communication wavelengths ([11] and references therein). This improved performance is mainly due to superior fiber coupling because of facet higher quality and the use of an OW with the RTD-PD active region much closer to the input facet. The results show the RTD-PD-LD can operate as a stable optically controlled MWP oscillator to obtain a high efficient O/E conversion. The RTD-PD-LD phase noise characteristics should be sufficient for many currently microwave photonic applications that use phase modulated schemes, e.g. phase shift keying (PSK) data transmission (as discussed in the next section), as long as the locking conditions are achieved and maintained. The locking results can be further improved through RTD-PD waveguide structure redesign and facet anti-reflection coatings in order to increase light coupling efficiency.

4.6 Applications of injection locked RTD-PD oscillators

In this section, recent developments on applications of optically and electrically injection locked RTD-PD-LD oscillator devices in MWP systems are presented. The RTD-PD-LD oscillator has both optical and electrical input and output ports, with the fifth port allowing voltage control, Fig. 4.11. The ability to lock to reference RF sources by either optical or electrical injection locking techniques allows remote synchronization providing a large range of functions including generation, amplification and distribution of RF carriers, clock recovery, carrier recovery, modulation, and frequency synthesis. In what follows two main applications of RTD-PD-LD oscillators in transmission systems are discussed: optoelectronic clock-recovery of Gb/s RZ signals and transmission of modulated signals in wireless/photonis links.

4.6.1 Optoelectronic clock recovery

The ability to recover the clock signal from incoming random data is a fundamental operation in digital communications. Clock recovery consists in deriving a clock signal

from the received signal which is synchronized in both frequency and phase, avoiding its transmission along with the data, and providing a timing basis to sample the received signal. In this context, the ability to perform clock recovery using both electrical and optical techniques is an important issue in the development of circuits for novel high-speed optical communication systems.

RTD-PD-LD OEIC oscillators are candidates for that purpose, combining both electronic and photonic components to achieve highly pure microwave signals. They combine the functions of microwave oscillation and photo-detection, while offering intrinsic gain and high responsivities, being suitable to be injection locked with incoming data in both optical and electrical domains.

In what follows we present results on a recovered clock experiment using either electrical injection (E/O conversion) or optical injection (O/E conversion), Fig. 4.11. In this experiment the free running RTD-PD-LD oscillator is tuned to oscillate at a frequency sufficiently close to the incoming signal. The incoming signal can be injected into the oscillator either optically or electrically. The locking range is typically on the order of tens of MHz, and depends on the power of the injected clock frequency. The recovered signal can be accessed either at the optical output port or the electrical output port.

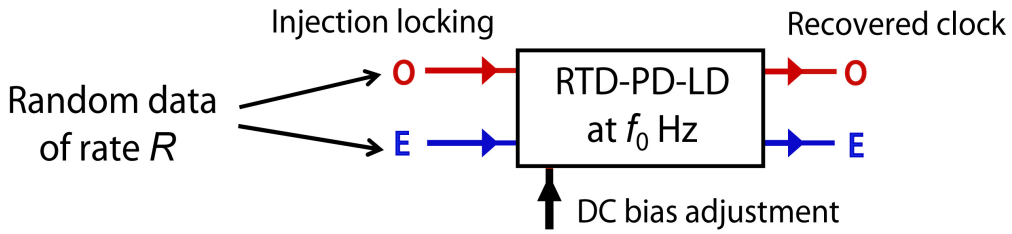

Figure 4.11: Block diagram of the RTD-PD-LD oscillator device with the functions of clock recovery via optical and electrical injection.

4.6.1.1 Clock recovery using electrical injection

In the example of the E/O clock recovery experiment we take advantage of the electrical injection locking capability of the RTD oscillator. The experimental setup consisting of an electrical input and optical output signals is shown schematically in Fig. 4.12(a). The RTD-PD-LD was DC biased in order to operate at a free-running oscillation frequency of approximately 1.25 GHz. Then an electrical input signal was injected, consisting of a RZ pseudorandom bit stream (PRBS) at 1.25 Gb/s generated from a

bit-error-rate test (BERT) transmitter, whose spectrum together with the respective eye diagram are shown in Fig. 4.12(b). The RZ data signals were injected with a range of amplitude levels between 100 mV to 500 mV. The recovered clock was accessed at the laser optical output and then converted to the electrical domain using a commercial photo-diode.

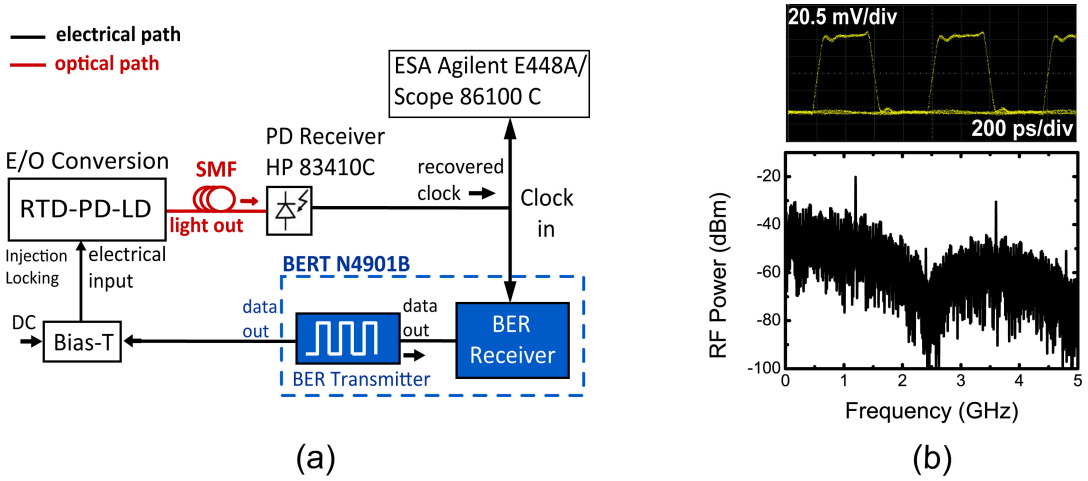

Figure 4.12: (a) RTD-PD-LD oscillator experimental schematic for timing extraction. (b) RZ data stream input of 1.25 Gb/s with 100 mV amplitude (V_{p-p}) and 50% duty cycle using a PRBS of $2^7 - 1$; (*top*): eye diagram of RZ data; (*bottom*): RZ data signal measured in the frequency domain.

Figures 4.13(a) and (b) show the frequency spectra of the data after clock recovery for injected amplitudes of 100 mV and 500 mV, respectively. The clock frequency was amplified by the RTD-PD-LD, resulting in a recovered clock with a signal-to-noise ratio of about 60 dB in both locking conditions. The other frequency components are more pronounced in Fig. 4.13(b) due to the strong injection amplitude level. Figure 4.13(c) shows the LD light detected spectra of both free-running oscillation and the injection locked RTD-PD-LD optical output using a 10 MHz window span. The RTD-PD-LD output oscillation frequency was clearly pulled to 1.25 GHz with a significant phase noise reduction of more than 30 dB, as shown in the SSB phase noise measurements presented in Fig. 4.13(d). The $1/f$ noises of the recovered signals are similar to that of the original clock signal. For example, the phase noise of the recovered clock at 10 kHz offset is -103.8 dBc/Hz and almost matches the original clock of -104.5 dBc/Hz. The locking range was verified to depend on the power of the injected signal, varying from 1 MHz up to 9.1 MHz, for the tested range of signal levels. The inset of Fig. 4.13(c)

shows the temporal waveform of the recovered clock. To perform this measurement, the oscilloscope was triggered by the original clock signal. The results demonstrate that the recovered signal is clean and synchronized to the reference incoming signal. The oscilloscope indicated a root-mean-square (RMS) jitter of 6.26 ps, which matches well with that from the phase noise measurement. The integrated timing jitter over a 90-kHz bandwidth was below 4 ps and compares with the timing jitter measured by the oscilloscope.

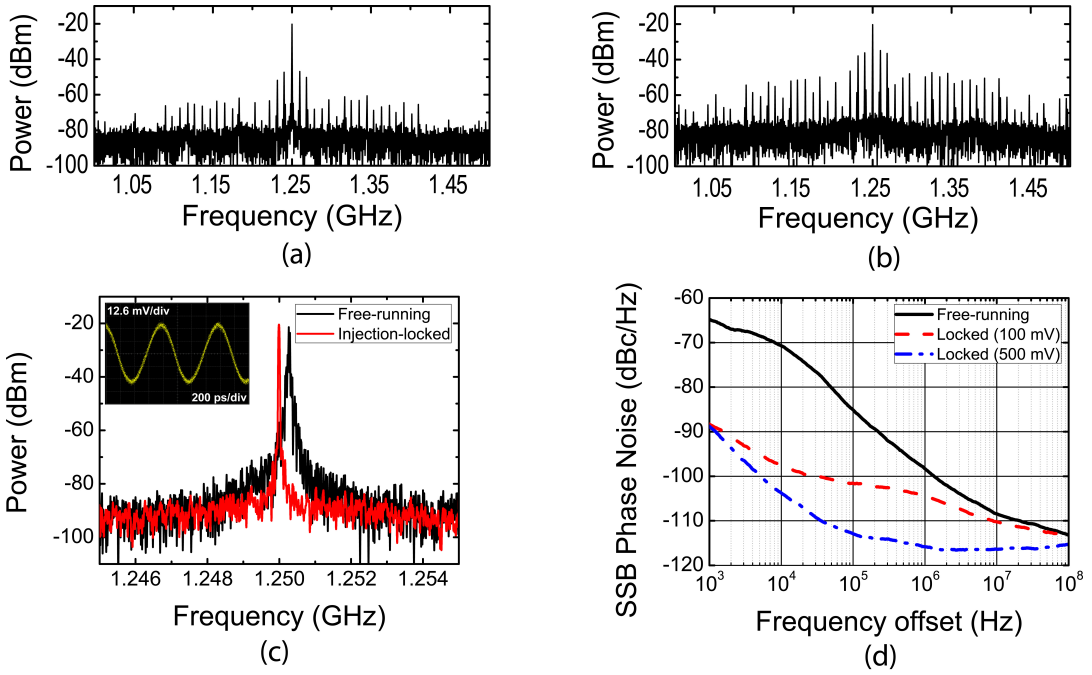

Figure 4.13: The 1.25 GHz clock recovery in the frequency domain from injected RZ data signals at (a) 100 mV, and (b) 500 mV, measured in the detected LD output. (c) The power spectra of the photo-detected LD free-running oscillation, and the recovered clock for a 100 mV amplitude injected signal (span of 10 MHz). The inset shows the LD output recovered clock in the time domain. (d) SSB phase noise measurements.

4.6.1.2 Clock recovery using optical injection

Now the O/E clock recovery experiment is investigated taking advantage of the RTD-PD-LD optical injection locking. Clock recovery via optical injection is important because it enables the clock of a high-speed data signal in a fiber-optic system to be directly recovered without first converting the data to electrical pulses. Figure

4.14 shows the experimental schematic for timing extraction and bit-error-rate (BER) measurements. The performance of the recovered clock was assessed considering the parameters timing jitter, phase noise and locking bandwidth. Additionally, BER measurements were carried out using the recovered clock accessed in the electrical domain as a timing base for the sampling of the received data.

Clock recovery and error free timing extraction results are demonstrated using RZ format data signals that optically injection locks the free-running RTD-PD-LD oscillator. A 1.24 Gb/s RZ signal was used to modulate a tunable laser diode optical carrier at 1550 nm using a 10 Gb/s modulator that then fed an EDFA which output was subsequently split in a 50/50 coupler. One of the coupler outputs went to a commercial photo-receiver whose output was connected to the error analyzer. The other part of the optical signal was coupled to the RTD-PD waveguide, Fig. 4.14.

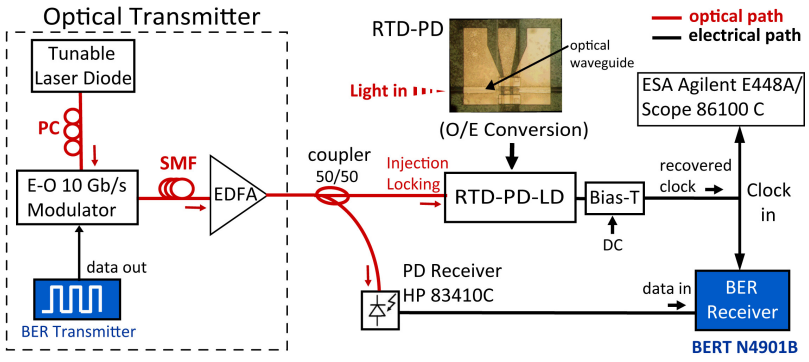

Figure 4.14: RTD-PD-LD experimental schematic for timing extraction and BER measurements via optical injection locking.

Figure 4.15(a) shows the frequency spectrum of the data after clock recovery via optical injection of a 3 mW in fiber optical power signal, showing a strong frequency component at the clock frequency. Figure 4.15(b) presents the power spectra of the free-running oscillation slightly above 1.24 GHz and the injection locked output at 1.24 GHz. The output spectrum was clearly pulled to 1.24 GHz in the presence of the optical injected signal. The inset of Fig. 4.15(b) presents also the injection locked RTD-PD output signal in time domain. A phase noise reduction of around 24 dB at 10 kHz offset from the carrier frequency was achieved for an optical injection power level in fiber of around 6 mW, Fig. 4.16(a). The minimum optical power in the fiber to obtain locking was around 1.1 mW with a locking range of 0.3 MHz. The locking range and the phase noise reduction were strongly dependent on the optical power of the optically injected

signal. The phase noise was considerably reduced as shown in Fig. 4.16(a). The RMS jitter measured by the oscilloscope was 2.16 ps, which also matches well with that from phase noise measurement. The integrated timing jitter over a 90-kHz bandwidth was below 2 ps.

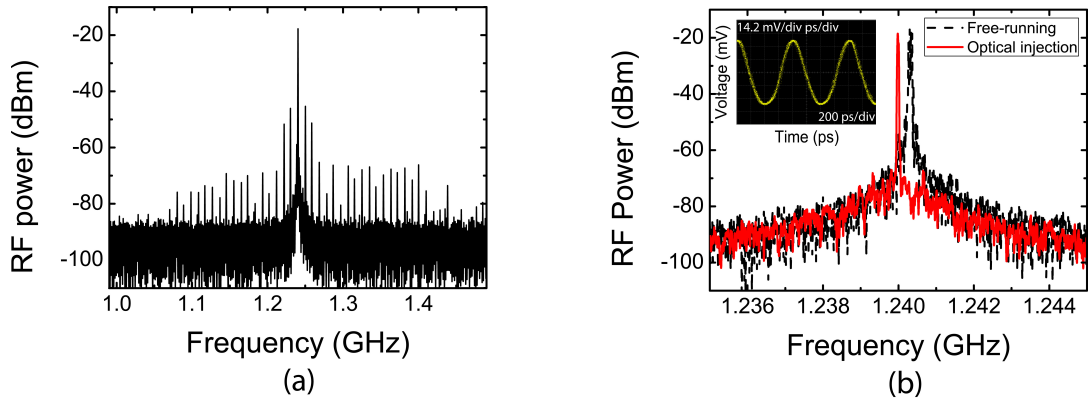

Figure 4.15: (a) The 1.24 GHz clock recovery in the frequency domain from an optically injected RZ data signal using an in fiber optical power level of $\sim$ 3 mW. (b) Power spectra of the free-running signal and the 1.24 GHz recovered clock (span of 10 MHz). The inset shows the recovered clock in the time domain.

A comprehensive way to characterize the performance of a recovered clock signal is to measure the BER. First, the quality of data detection was investigated for a direct clock situation where the clock signal from the pattern generator was used to trigger the BERT equipment. Next, clock recovery was performed and the optically injection locked RTD-PD electrical output was used to trigger the bit error tester. Figure 4.16(b) shows the BER at 1.24 Gb/s as a function of the received power for both direct and recovered clocks using a data pattern length of $2^7 - 1$. The two BER curves are similar, confirming the low jitter of the extracted clock signal. It is believed that the mismatch in some of the BER points results from environmental instabilities (vibration, temperature fluctuations) which can be reduced significantly with further optimizations in the measurement setup.

As a summary, clock recovery using RTD-PD-LD oscillator devices was demonstrated taking advantage of both electrical and optical injection locking capabilities of the devices. One of the attractive properties include the power of the recovered signal is independent of the input power of the signal to be recovered. Other attractive properties include frequency tunability and relatively wide tracking range.

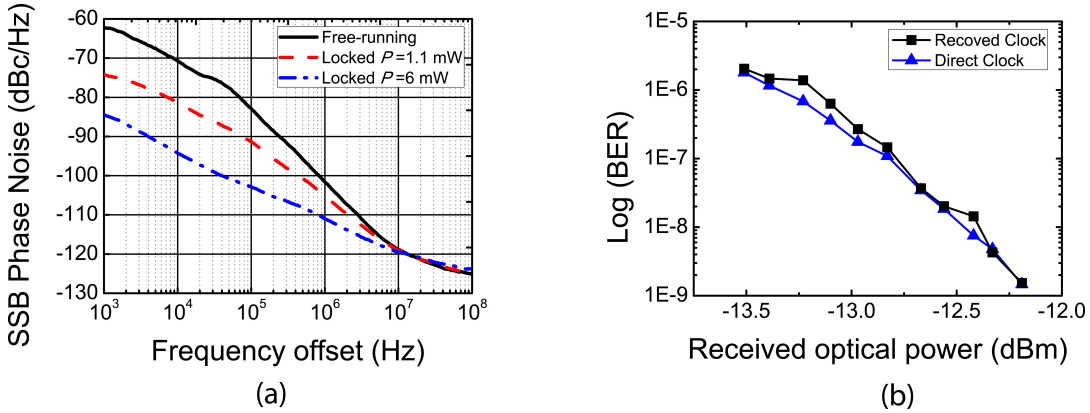

Figure 4.16: (a) SSB phase noise of free-running and recovered clock signals. (b) BER measurements of recovered and direct clocks.

4.6.2 Wireless/photonics links

The demand in the coverage and speed of optical communications networks, together with rapid growth in wireless networks, has motivated an increasing attention into hybrid wireless-photonics communication systems. The integration and transmission of RF signals over fiber, RoF systems, are expected to play an important role in broadband wireless communication systems [7]. Taking advantage of optical fiber low loss and wide bandwidth transmission characteristics, it is possible to distribute broadband data and/or high frequency signals to many wireline or wireless subscribers. Among several approaches for realizing RoF systems, much efforts are dedicated to provide economic and simple radio access points bringing the fixed network bandwidths closer to the mobile users at lower costs [12, 13].

In this subsection, results on the transmission of analog and digital modulated signals are demonstrated using two experimental wireless/photonics arrangements that take advantage of the optical and electrical injection locking characteristics of RTD-PD-LD oscillator circuits. Figure 4.17 shows the diagram of the implemented arrangements providing the downlink (a) and uplink (b) functions.

In the downlink, Fig. 4.17(a), the RTD-PD-LD oscillator locks optically and provides the O/E conversion of a RoF cell. The optical signal at the transmitter (Tx) contains the modulated data mounted directly on the RF carrier frequency used for wireless transmission and close to the oscillator free-running frequency. The photodetected signal locks the RTD-PD Tx oscillator which boosts its power for wireless propagation through the antenna. The generated electrical signals were fed directly to

a patch antenna connected to the electrical output of the RTD-PD-LD oscillator making part of the RTD circuit and broadcasted to be detected by an identical patch antenna connected to the oscilloscope or to the RF spectrum analyzer (the RF-broadcasted power level on the receiver antenna plane was measured connecting the patch antenna directly to the RF analyzer).

In the uplink, Fig. 4.17(b), the RTD-PD-LD oscillator is locked electrically and provides the E/O conversion. An antenna receives the modulated data mounted on the RF carrier frequency that is injected into the RTD-PD-LD receiver (Rx) oscillator. The locked oscillator at Rx is used to modulated the laser diode which reproduces the received wireless modulated signal containing the original information. The laser diode optical output is photo-detected and connected to the oscilloscope or to the RF spectrum analyzer.

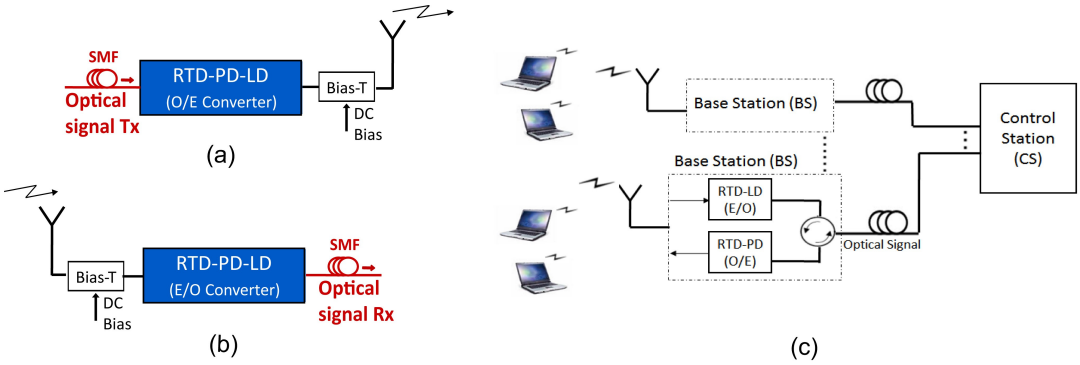

Figure 4.17: Schematic diagram of wireless/photonics architectures implemented using RTD-PD-LD oscillator circuits as (a) O/E converter in transmission, and (b) as E/O converter in reception. (c) Example of a RoF architecture based on RTD oscillators base stations.

In Fig. 4.17(c) is illustrated an example of a communications network using a RoF architecture and employing in the BS (pico-cell) RTD-LD E/O converters and RTD-PD O/E converters. In this network configuration a central station (CS) is connected to numerous simple BSs via optical fibers. Almost all processing functions including modulation, demodulation, coding, and routing are performed at the CS. The main function of a BS employing RTD wireless/optical oscillators is to convert optical signal to wireless one and conversely.

4.6.2.1 Injection locking of phase modulated signals

Using the experimental arrangements described in Figs. 4.17(a) and (b), phase modulated carriers are used in this work to lock RTD-PD-LD oscillators that convert the signals from optical to electrical domain and conversely. In the downlink arrangement, Fig. 4.17(a), the baseband modulation was initially mounted on the RF carrier frequency and then sent through an optical fibre using light with a wavelength of 1550 nm. The RF carrier was set close to the free-running oscillation operation frequency of the RTD-PD-LD oscillator device. The Agilent E8257D instrument was used to modulated the phase of the carrier at the programmed frequency. The modulation is determined by a waveform with a chosen data rate and a phase deviation. In this work the waveforms used were a sine waves and the phase deviation was varied between 90°, 180°, and 270°. The frequency of modulation was varied between 15 kHz and 1 MHz which is close to the upper limit set by the instrument.

Figure 4.18(a) presents optical injection locking of transmitted RF signals over approximately 1 m distance. The distance implies a path loss of 40 dB, which can be reduced by means of the system antenna gain. The results show phase-locking at 1.2 GHz and a modulation envelope due to the phase introduced by the RF modulator at 15 kHz sine wave frequency with phase shifts of 90° and 180°. As expected, increasing the transmitter phase deviation, the modulation index increases which results in a increase of the number of sidebands. The phase modulation was performed varying the modulation index up to 1 MHz modulating frequency. The total number of significant sidebands decreases with a higher frequency-modulating signal with the phase-locked output clearly following the phase modulation of the transmitted optical subcarrier.

Similar results were obtained in the the uplink arrangement, Fig. 4.17(b). Figure 4.18(a) shows the RF spectra of the detected laser optical output due to wireless phase-locking at 1.2 GHz frequency and side-bands due to phase modulated signals at 1 MHz with phase deviations of 90° and 270°. The RTD-LD oscillation locks to broadcasted signals with frequency close to the circuit natural frequency (or to its harmonics), with the laser output being modulated by the broadcasted signal and the phase modulated signals. Locking was observed with considerable noise reduction using received broadcasted power levels lower than -32 dBm, and the laser output clearly followed the modulation of the broadcasted RF carrier. In both uplink and downlink arrangements, due to RTD intrinsic gain, phase-locked signals were transmitted over short distances, without the need of pre-amplification. As discussed next, these characteristics can be employed for digital format modulation schemes.

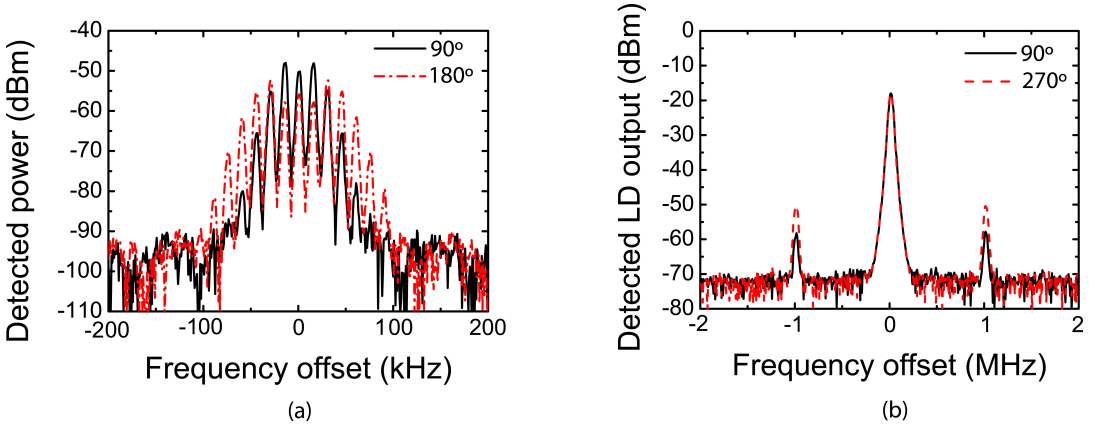

Figure 4.18: (a) Downlink: RF spectra of injection-locking to a 5.8 mW (λ =1550 nm) modulated optical signal at 1.2 GHz, phase modulated at 15 kHz with phase deviation of 90° and 180°, broadcasted over 1 m distance.(b) Uplink: RF spectra of photo-detected laser outputs due to a phase modulated broadcasted signal at 1.2 GHz and -32 dBm power. The broadcasted carriers were phase modulated by sinusoidal signals at 1 MHz with phase deviation of 90° and 270°.

4.6.2.2 Modulation accuracy of transmitted digital signals

Digital standards based on phase modulation, such as Gaussian minimum shift keying (GMSK), quadrature phase shift keying (QPSK), and quadrature amplitude modulation (QAM) are the basis for communications through the latest generation of mobile telephones and wireless local area networks (LAN). The effect of injection of sinusoidal phase modulated signals in RTD-based oscillators was demonstrated previously showing that the phase modulated signals mounted in a RF carrier are converted efficiently to both electrical and optical domains as long as the injection locking conditions are achieved. Here, optical/wireless links are investigated, exploring the possibility of distributing phase modulated digital signals.

Due to the properties of RTD-based oscillators, modulation formats that lead to large variations in the signal envelope are not recommended as the oscillator dynamics will tend to smooth these variations and introduce distortion. However, constant envelope modulation formats, such as GMSK, represent excellent candidates to be employed. In order to minimize phase transitions from the injected signal, as well as to achieve spectral efficiency at the carrier frequency, and thus containing good locking conditions, a GMSK signal using a data rate of 270.83 kbit/s has been chosen in this work as the scheme for data conversion and transmission. GMSK is widely used as

one of the global system for mobile communications (GSM) modulation standards for voice and data transmission in cellular networks. GSM operates in 124 channels that are 200 kHz wide occupying a total frequency band of 25 MHz. Although RTDs can be injection locked within frequency ranges larger than 25 MHz, the present work is concentrated on the operation of a single GMSK modulated GSM channel.

Signal bursts containing GMSK modulation using a Rohde & Schwarz SMBV100 signal generator were used in this work to injection lock the RTD free running oscillations (a detailed information about the injected GMSK signal characteristics can be found in [144]). The bursts were injected to the oscillator by means of a microwave circulator that coupled the output locked signal to a vector signal analyzer (VSA). A modulation accuracy report was generated for these measurement conditions. The report contains parameters such as error vector magnitude (EVM), magnitude error, phase error, and a constellation diagram. All reported numerical parameters are given as RMS values calculated from the constellation diagrams.

Figure 4.19 shows measured modulation accuracy metrics of the GMSK standard after injection locking of an RTD oscillator operating at around 1.3 GHz with different burst power levels. The free running power of the oscillator was -13 dBm and could be locked with a signal that was 27 dB below that level while maintaining an EVM of less than 6%. Similar results were published recently in [145] demonstrating modulation accuracy results for a 3.2 GHz RTD oscillator that was able to lock the oscillator with an EVM of less than 7%. The authors in [146] have discussed the relation between EVM and BER when specific assumptions on the source of distortion of the signals are made. If their analysis of QPSK signals could be extended to the GMSK signals used in this work, it would then be possible to expect that received signals with EVMs of 5% and SNR above 20 dB can reach BER values as low as 2.5×10^{-11} [146].

After the investigation of the relationship between the modulation accuracy metrics and injection power necessary to lock electrically the RTD oscillator, the modulation accuracy of RTD Tx, Fig. 4.17(a), and Rx, Fig. 4.17(b), was evaluated. Both Tx and Rx were tested independently to generate a modulation accuracy report after converting signals between the optical and wireless domains. For the case of the RTD-PD Tx the GMSK signal described previously was used to optically control the device while the signal was broadcast and monitored by a VSA. An antenna placed 75 cm away from the circuit was used to receive the signal and couple its power to the VSA. A plot of the received locked signal spectrum is shown in Fig. 4.20(a) working at 1.3 GHz. The spectral plot was obtained using averaging of 200 traces measured by the VSA. Constellation diagrams obtained after signal demodulation are shown inset of

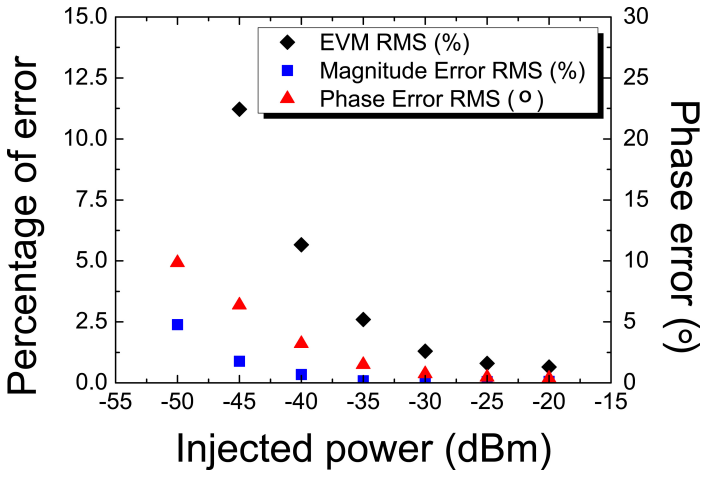

Figure 4.19: Modulation accuracy RMS parameters of GMSK signals locking RTD oscillators at a carrier frequency of 1.3 GHz.

Fig. 4.20(a). The calculated modulation accuracy metrics show an EVM of 8.1% and a phase error of 4.6°.

For the case of the RTD-LD Rx measurements a vector signal generator (VSG) and an antenna were used to broadcast GMSK bursts 75 cm away from the RTD-LD Rx circuit. The RTD was injection locked to the received signal modulating the laser diode output that was photo-detected for vector signal analysis. Figure 4.20(b) shows the measured GMSK spectrum of the photo-detected locked signal output from the RTD-LD Rx circuit. Also shown in the inset of Fig. 4.20(b) is the measured constellation diagram. The modulation accuracy results show an EVM of 4.6% and a phase error of 1.9°. These results are consistent with the parameters reported earlier in Fig. 4.19.

As a summary, the conversion and measured modulation accuracy of transmitted GMSK signals in simple optical/wireless links as been demonstrated using RTD-based oscillators. Similar results were published recently [144, 145], demonstrating modulation accuracy results of RTD transmitter and receivers operating at frequencies of 3.2 GHz. Other format schemes generally used for transmission of mobile digital communication standards, such as binary phase shift keying (BPSK), are also being tested and implemented within our group using RTD-based oscillators and will be published elsewhere [147].

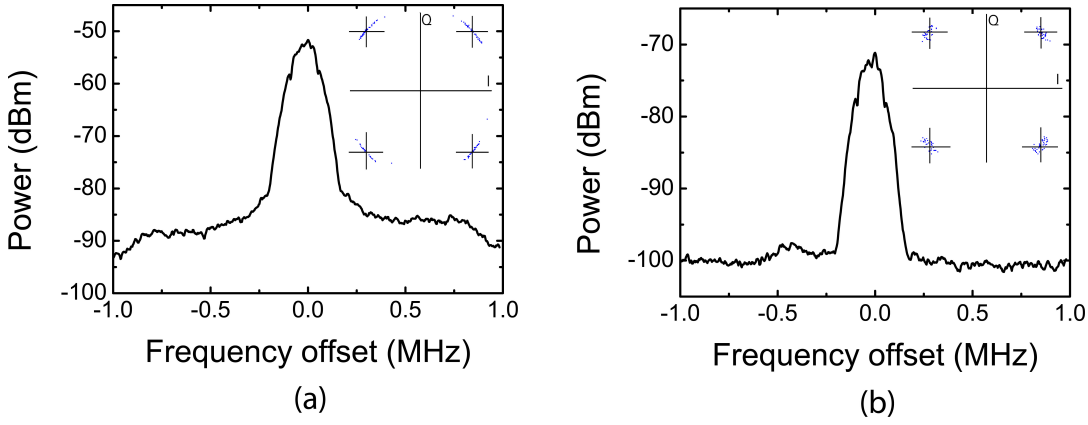

Figure 4.20: Measured spectra of GMSK signal after conversion from (a) RTD Tx and (b) RTD Rx operating at 1.3 GHz. Inset are shown the corresponding GMSK constellation diagrams.

4.7 Chapter summary

In this chapter, a simple and efficient way to obtain stable low-phase noise RF signals using optical injection locking of a RTD photo-detector laser diode oscillator, the RTD-PD-LD, was demonstrated. The oscillator provides conversion of optical RF sub-carriers from the optical to the electrical and optical domains. The optical injection-locking was observed for in fiber optical power levels below 1 mW. Phase noise suppressions of -112.4 dBc/Hz at 10-kHz with locking ranges of about 1.7% of the oscillator's free-running frequency were achieved, providing low phase noise and clean signals for electronic and optical applications. The injection locking results were also predicted by an optically controlled Liénard oscillator numerical model.

Experimental results on clock recovery from RZ format data signals were demonstrated taking advantage of optical and electrical injection of free-running oscillator circuits. The timing jitter, phase noise, and locking bandwidth aspects of recovered clocks were investigated, including the performance of the recovery clock using BER measurements. Ultimately, the feasibility of a wireless/photonics link has been investigated. The links worked under the principle of injection locking to photo-detected signals in the transmitter (RTD-PD), and injection locking to wireless signals in the receiver (RTD-LD). Analogue phase modulated and digital GMSK signals were used to test the modulation of transmitted signals in each part of the link. When injection locked with phase modulated signals, the circuits provided low phase noise and electri-

cal gain, converting the signals between wireless and optical domains, while reducing cost and complexity.

RTD-based oscillator transceivers are currently being studied under the wireless-optical-wireless interfaces for picocellular access networks (WOWi) project (PTDC/EEA-TEL/100755/2008), as simple and compact low phase-noise MWP oscillators for optical/electrical signal processing units of RoF cellular network base stations.

Chapter 5

Delayed feedback dynamics of RTD optoelectronic oscillators

5.1 Introduction

Time delayed feedback systems, where the dynamics at a given instant t depends on the state of the system at an anterior time $t - \tau_d$, where τ_d is the time delay, are common in scientific fields such as physiology, biology, epidemiology, and control systems [148]. Depending of the time delay and feedback strength, a delayed feedback loop can be added to a system to stabilize it producing highly stable periodic waveforms [24, 25], but also to obtain exceedingly complex dynamics, namely chaos [22, 23, 26]. The dynamics of such systems can be easily synchronized and controlled using either external perturbation or feedback parameters [28–30].

The effect of the delayed feedback is to reinject into the system one or more state variables, with a delay. Within the field of laser dynamics, the most prominent examples are the optoelectronic feedback [19], the optical feedback [17, 18], and the OEO system [24, 25]. The optoelectronic feedback consists of current re-injection of the detected laser output using a fast responding photodiode, which produces a current that is an image of the laser output power and that is added, after a delay time, to the laser injection current. In external optical feedback of laser systems, an external mirror is used to optically re-inject a fraction of the light produced by the laser into its active region. The round-trip time of light in the external cavity introduces a delay in the system. In OEO systems, external elements (electro-optic modulators, RF oscillators, etc.) are used to produce nonlinearities, and the laser diode is used only as a light source.

During the past few decades, time delayed OEO systems combining electronic and photonic components have been intensively studied to achieve stable and high purity RF signals. A typical OEO includes a laser source, an intensity modulator, a photodetector, a bandpass filter, and an RF amplifier [24, 25]. They have interesting applications in optical communication links and precise test and measurement equipments [25]. Several alternative OEO topologies capable of generating stable and low-phase noise RF carriers have been reported in the last few years using either direct or external modulation of laser diodes [149], or HBTs [10], among others. In order to obtain RF signals in both electrical and optical domains they require several electronic and optoelectronic components such as phase-locked local oscillators, amplifiers, photo-detectors, light emitters and/or amplifiers or modulators [7, 25, 149]. In addition, techniques including bidirectional injection [10] or self-injection locking [25, 149] may be required to achieve the very low phase-noise levels required by some applications. This makes OEOs rather complex and costly for applications such as RoF networks where compact solutions for the transmission of RF signals are needed [7].

In the preceding chapter, an RTD-PD oscillator driving a laser diode device forming a voltage controlled RTD-PD-LD circuit with both optical and electrical input and output ports was investigated. Taking advantage of this circuit topology, in this chapter a delayed feedback OEO system is demonstrated based on self-synchronization of RTD-PD oscillators by re-injecting a part of the optical output signal into the oscillator's input through a high-quality (Q) low loss optical fiber. The delayed feedback RTD-OEO system is numerically investigated providing additional insight on the OEO dynamics.

5.2 Aim and objectives

The aim of the work described in this chapter is to implement, characterize and investigate the dynamics of an optical fiber delayed feedback RTD-based OEO system. This was achieved through the following objecives:

- Implement a single and dual loop OEO comprising an RTD-PD, a laser diode and optical fiber delay lines to provide stability of free-running oscillation and noise reduction.
- Investigate the dynamics of single and dual loop RTD-OEO configurations controlled either by the re-injected optical power or the fiber delay line.
- Model the RTD-OEO dynamical behavior utilizing a system of delay differential equation (DDE) comprising a time delayed feedback Liénard oscillator with

Gaussian white noise input, and coupled with laser rate equations.

5.3 Chapter overview

In this chapter, after a short introduction on OEO systems, a description of the experimental arrangement of a self-synchronized RTD-OEO is provided, followed by the results obtained operating the device in single and dual loop fiber configurations. The experimental results will be compared with a time delayed feedback Liénard oscillator model. Examples of innovative applications of time delayed feedback RTD oscillators will be also given.

5.4 Optoelectronic oscillators

Optoelectronic oscillators enable the generation of high spectral purity oscillations and also other types of unstable behaviors including chaos in both optical and electrical domains by taking advantage of the interaction between delayed feedback signals and devices nonlinearities. The OEO relies on a intensity optical power source, a nonlinear device to modulate the optical signal, an element to compensate for any losses, and a feedback delay line with a timescale longer than the characteristic timescales of the resulting dynamics.

The first time a highly stable OEO-laser system was demonstrated was in 1996 at the Jet Propulsion Laboratory [24, 25], and its basic architecture is presented in Fig 5.1(a) (for a recent perspective review see [150]). It includes an optical fiber delay line with several kilometers long, a wide-band E/O modulator, light from a semiconductor laser CW coherent light beam, a photodiode, a narrow microwave RF filter, and microwave and/or optical amplifiers [24, 25]. It is a hybrid feedback oscillator which converts optical energy from a laser to microwave signals. In place of a resonant circuit, the OEO uses a long fiber-optic delay line as an energy-storage device [as seen in Fig. 5.1(a)]. Because of the extremely low losses and large energy storage capacities associated with fiber, a high loaded resonator quality factor can be obtained which results in oscillations with very low phase noise. The conditions for self-sustained oscillations include coherent addition of partial waves each way around the loop (the loop phase shift must be an integer multiple of 2π), and a loop gain exceeding losses for the circulating waves in the loop. These form the Barkhausen criteria [151] to obtain stable oscillations in the OEO.

Although the choice of laser can have an effect on the performance of the OEO

(specifically, with respect to the impact of laser intensity noise on the output phase noise), most traditional schemes require the use of an external (normally Mach-Zehnder) modulator to introduce a microwave sub-carrier onto the optical signal. This places a theoretical limit on the frequency of oscillation, based on the speed of the E/O modulator. Moreover, to obtain stable oscillation dynamics it is necessary to include a filter in the feedback loop to eliminate harmonics generated by the nonlinear response of the E/O modulator.

To address the limitations imposed on OEOs by the need for mode selection several other approaches have been proposed to select a single operational mode from those available. It includes the implementation of state-of-the-art OEOs based on HPT as electrical free-running oscillators [10, 149], direct modulation of semiconductor lasers [152, 153], laser self-injection locking using optical feedback feedback from high-Q whispering gallery mode (WGM) resonators [154], and photonic generators via optical frequency division [155] providing ultra-stable electrical signals comparable to that produced by the best microwave oscillators. However, most of these configurations are still quite complex and require a large number of electronic and optical high-speed components, RF amplifiers and EDFAs, which are usually the major noise contributing elements. Thus, a great deal of work on OEOs is underway to provide high-performance microwave and millimeter-wavelength oscillators that not only are of miniature size but also have power consumptions many orders of magnitude lower than existing devices.

5.5 RTD-PD optoelectronic oscillators

In this work, we demonstrate the feasibility of using RTD-PD oscillators for low powered OEO systems [55]. Figure 5.1(b) shows the basic architecture of a RTD-OEO system that considerably simplifies the reported OEO configurations reviewed in the previous section, Fig. 5.1(a). The RTD-based OEO discussed here consists of a much simpler topology whose nonlinearities arise from the NDC of the RTD-PD driving a LD device and that takes advantage of the additional low-loss high-Q cavity provided by the optical fiber delay line.

RTD-based oscillators provide low noise levels [156], with SSB noise power density as low as -86 dBc/Hz at 100-kHz offset from the carrier frequency, as reported recently in [11], which compares with the lowest noise levels for other analogous electronic free-running oscillators presented recently in [10, 149]. In order to obtain further improvement in the phase-noise of the RTD free-running oscillations, external injection locking techniques are usually employed, as demonstrated in Chapters 3 and 4 of this

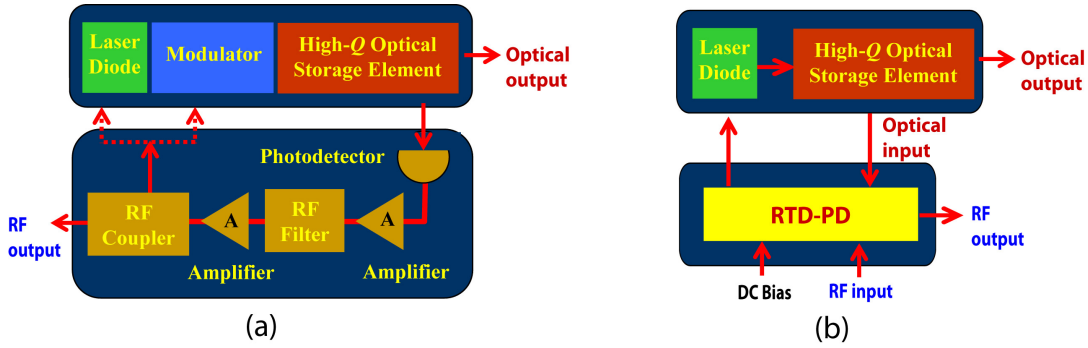

Figure 5.1: (a) Basic architecture of a typical optoelectronic oscillator. (b) A self-synchronized OEO based on a RTD-PD.

thesis. The RTD-PD based OEO topology discussed here is another way of providing stability of the free-running oscillations and further reduce fluctuations and noise without employing external reference sources. Moreover, the time delayed feedback dynamics can be further employed in innovative applications including generation and control of chaos [26].

An example of the self-synchronized OEO architecture based in a RTD-PD and a LD is shown in Fig. 5.1(b), and includes a closed loop OEO configuration consisting of an optical fiber that acts as a delay-line. The RTD-OEO obviates the need for low-noise and stable external RF amplifiers and microwave filters usually required to compensate E/O and O/E conversion losses and frequency mode selection, respectively. By eliminating the RF and EDFA amplifiers from the OEO, part of the major noise contributing elements of typical OEO architectures is eliminated. Moreover, the RTD-OEO has a low power requirement compared to previous OEOs and no high-speed high-cost extra components such as photo-detectors or modulators are used in this configuration.

5.5.1 Single loop self-synchronized RTD-OEO

In this section, the RTD-OEO basic topology is investigated consisting of a single closed loop configuration employing an optical fiber that acts as the high-Q factor optical storage element. The dynamics of the single loop RTD-OEO controlled either by the injected optical power or the fiber delay line is analyzed studying the stability and phase noise characteristics of implemented OEO systems.

5.5.1.1 Experimental setup

The self-synchronization was realized in a closed loop OEO configuration, Fig. 5.2(a), consisting of a SM optical fiber-roll that acts as a delay-line, a DBQW-RTD monolithic waveguide photo-detector oscillator, and a commercial laser diode prototype, with both RTD-PD and LD hybrid integrated on a PCB-transmission line layout, as described in Chapters 3, and 4. The RTD-PD with 0.5×0.4 mm^2 chip size (see Chapter 4 for more detailed characteristics), provided O/E conversion with ∼0.28 A/W efficiency at 1.55 μm when DC biased around 2.4 V, close to the valley region, Fig. 5.2(b). The E/O conversion was achieved by direct modulation of the laser diode operating around 1.55 μm with ∼0.25 W/A efficiency. As shown in Fig. 5.2(a) this arrangement provided a simple configuration not requiring external amplification. However, because the RTD-PD devices were not optimized for this particular experiment, in some experiments, namely in the dual loop fiber experiment presented in subsection 5.5.2, EDFA amplifiers were used to compensate the losses of coupling the light in more than one fiber.

The RTD-OEO works as a self-synchronized OVCO, e.g., the free-running frequency of the RTD-PD-LD oscillator is controlled by adjusting the DC bias voltage. When it is biased in the NDC region, electrical free-running current oscillations build-up, directly modulating the LD. The LD optical modulated output is then decoupled using a lensed SM fiber, sent through an optical fiber delay line, and finally re-injected into the RTD-PD waveguide using a similar lensed SM fiber. The optical re-injection induces self-injection locking of RTD free-running oscillations. The operation frequency of the RTD-OEO is essentially determined by the RTD-PD parallel capacitance and the series equivalent inductance of the wire bonding used to connect the RTD-PD to the LD (the wire length was ∼3-4 mm, giving an equivalent inductance around 3.6 nH), which for the circuit reported here gives an operation frequency up to ∼1.4 GHz. Using an appropriate circuit configuration, one estimates the RTD-PD oscillators used in this experiment could operate up to ∼14 GHz (see subsection 3.4.2). Since the LD used had a cut-off frequency of 11 GHz, the LD is the device that can limit the upper frequency of our OEO circuit for layouts that significantly reduce the series inductance. For operation at frequencies above the maximum achievable laser operating frequencies (>30 GHz), one can replace the laser by an RTD-EAM [42, 43], or other external modulator devices [7].

The utilization of fiber-rolls with different lengths provided an easy way of changing the optical feedback route of the RTD-OEO. With this simple feedback route configuration, we obtained an RTD-OEO having both electrical and optical input and output

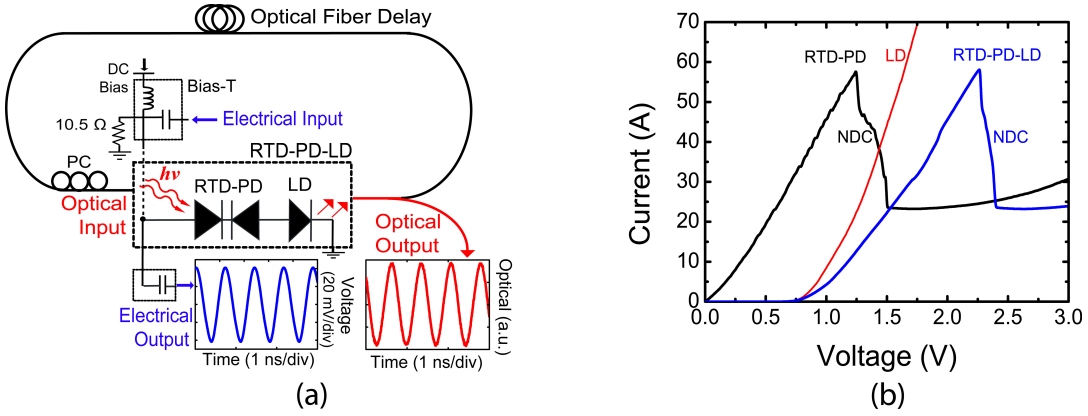

Figure 5.2: (a) Schematic of the self-synchronized RTD-OEO setup. (b) I-V characteristics of the RTD-PD-LD, and of the RTD-PD and LD devices.

ports, with the RTD-OEO frequency and phase-noise fluctuations substantially reduced after passing the high-Q optical delay line. In what follows, we present and discuss the self-synchronization results.

5.5.1.2 Results and discussion

Without optical re-injection, the RTD-PD-LD circuit reported here oscillated with a free-running frequency tunable from 1.05 to 1.41 GHz, depending on DC bias voltage. When the RTD-PD-LD was DC biased close to the valley region, ~2.4 V, it produced electrical and optical modulated free-running oscillations at around 1.4052 GHz [the oscillations in time domain are shown in the inset of Fig. 5.2(a)] with power consumption of 0.55 W. The power consumption can also be further reduced below 0.1 W inserting a capacitor in series with the shunt resistor shown in Fig. 5.2(a). Figure 5.3(a) presents the free-running oscillation spectrum trace, showing the typical broad spectrum caused by the frequency oscillation fluctuations. The electrical power produced is determined by RTD circuit and I-V characteristic. Although the output power reported here was around -14 dBm, more than 10 dB higher output powers were already demonstrated using similar RTD-PD oscillators [48].

The RTD-OEO characteristics were investigated using fiber delay lines with lengths, L_f, as low as 0.4 km, and above 1 km. In Figs. 5.3(b) and (c) are presented the self-synchronized free-running oscillations produced for two fiber-roll lengths of 0.814 km and 1.219 km, respectively. The average in-fiber optical power was $P \sim 5$ dBm. Also shown inset on top of each figure is the spectrum surveillance screening the plot density

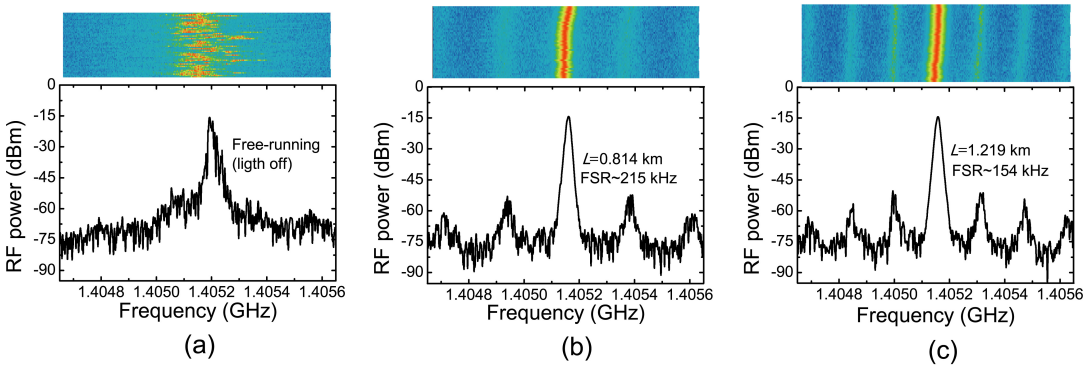

Figure 5.3: RF power spectrum traces of the RTD-OEO output. (a) Free-running. Self-synchronization at $P \sim 5$ dBm using fiber loops of (b) $L_f = 0.814$ km, and (c) $L_f = 1.219$ km. The frequency span and resolution bandwidth settings of all figures were 1 MHz and 10 kHz, respectively. The top part of each figure shows a spectrogram that represents the evolution of spectral density recorded over 30 s (time in the vertical axis).

spectrum. The results show the self-injection enhances the signal quality, improving considerable the frequency stability with a substantially phase noise reduction.

The side modes presented in Figs. 5.3(b) and (c) are separated from the center frequency by about 215 kHz and 154 kHz, respectively, with single mode suppression ratio (SMSR) of 38 dB and 36 dB. These are the mode spacing of the free spectral range (FSR) of the RTD-OEO and are related to the re-injected signal time delay τ_d, which in this case depends on the electrical time delay τ_e, introduced by the electrical components, and the optical time delay τ_{op}, mainly due to optical fiber length. For the feedback routes employed here the optical time delay τ_d is much larger than the electrical time delay τ_e:

$$FSR = \frac{1}{\tau_e + \tau_{op}} \simeq \frac{1}{\tau_{op}} \simeq \frac{c}{n_F L_f} \tag{5.1}$$

where $\tau_{op} = n_F L_f / c$, with n_F being the optical fiber effective refractive index and c the velocity of light: that is, the RTD-OEO mode spacing is determined by the fiber length. From Eq. 5.1 the following FSR values are estimated: $L_f = 0.814$ km, $FSR = 251$ kHz; $L_f = 1.219$ km, $FSR = 167.6$ kHz, which compares with the experimental values for lengths presented in Figs. 5.3(b) and (c).

In order to verify phase-noise reduction performance, SSB phase noises of output signals were measured and shown in Fig. 5.4. For an in-fiber optical power of $P \sim 9$

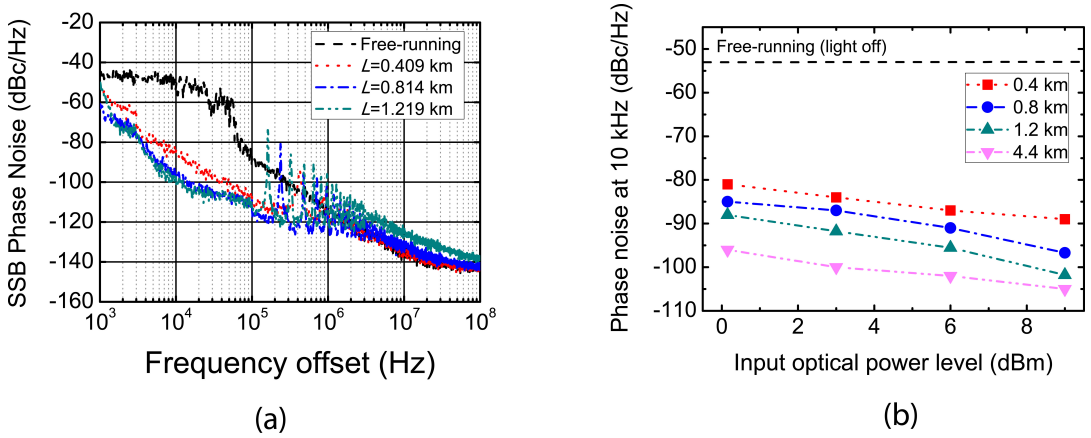

Figure 5.4: (a) Measured SSB phase noises for $P \sim 9$ dBm and free-running oscillation. (b) RTD-OEO SSB phase noise measurements at 10 kHz offset from the center frequency as a function of in-fiber optical power.

dBm and optical fiber lengths of 0.409 km, 0.814 km, and 1.219 km, the corresponding self-injection locked phase noise values were -89 dBc/Hz, -96.7 dBc/Hz, and -101.8 dBc/Hz, respectively, as shown in Fig. 5.4(a). A phase noise reduction more than 40 dB at 10 kHz offset was achieved when compared to the free-running oscillations without light re-injection. In the self-synchronized mode the SSB phase noise at 10 kHz offset from the center frequency was substantially reduced with the increase of the in-fiber optical injection power and also the fiber delay, as shown in Fig. 5.4(b).

In Fig. 5.4(b) is also presented the results of SSB phase noise for a very long delay line using a fiber roll with $L_f = 4.4$ km. A considerable phase noise reduction of up to 50 dB was achieved at frequencies offsets below the side modes (< 45 kHz) when compared to the free-running oscillations without light re-injection. Phase noise values below -100 dBc/Hz at 10 kHz offset were measured at power levels close to 3 dBm which corresponds to ~17 dB improvement when compared with $L_f = 0.4$ km. In Fig. 5.5(a), is shown an example of the self-injection locked output spectra for an average in-fiber optical power $P \sim 6$ dBm. The inset on top of the figure presents the spectrum surveillance of the self-injection locked output. Figure 5.5(b) presents the corresponding SSB phase noise measurement. A considerable improvement of the frequency stability was achieved, however, comparing these results with the ones of Fig. 5.3(b) and (c), the side modes are considerably amplified with the increasing of the delay line loop because of the proximity of the modes. Also, as the power level increases, the optical loop losses are reduced, and the side modes become stronger as well. As discussed next,

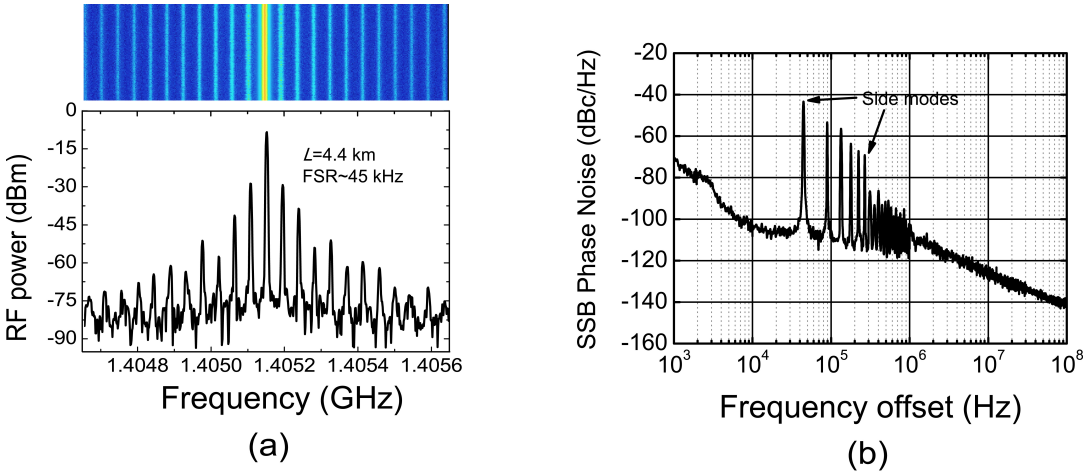

Figure 5.5: (a) RF power spectrum of the self-synchronized RTD-OEO output at $P \sim 9$ dBm using a fiber loop of $L_f = 4.4$ km. The frequency span and resolution bandwidth settings were 1 MHz and 1 kHz, respectively. The top part shows a spectrogram that represents the evolution of spectral density recorded over 30 s. (b) Measured SSB phase noise for $P \sim 9$ dBm.

in order to maintain the low phase noise levels and frequency stability due to the very long delay line, and at the same time suppress unwanted signals that deteriorate the performance of the RTD-OEO around frequency offsets close to the FSR of the delay line, a multi-loop fiber configuration [157] provides a good solution for mode selection.

In order to summarize the results of the single loop RTD-OEO, a comparison of recently reported OEOs based in fiber-looped configurations is presented in Table 5.1 showing the most relevant characteristics of a single loop OEO. The system presented here is simpler, providing an OEO configuration without the need of extra RF or optical amplification in the single loop.

5.5.2 Dual loop self-synchronized RTD-OEO

As verified in the previous subsection, a disadvantage of using a single fiber loop is the production of side mode oscillations. These modes - highly undesirable for certain applications - are caused by the propagation of waves multiple times around the OEO loop. There are two effective solutions for the removal or suppression of side modes. One scheme involves using multiple loops of fiber, which essentially functions as a narrow band filter. Another technique is to use a high-Q optical cavity to filter out the unwanted modes [154].

Table 5.1: A comparison of recently reported single loop OEOs and the RTD-OEO.

Parameter	RTD	VCSEL [152]	HPT [149]	HPT* [10]
Frequency (GHz)	1.40515	2.49	10.79	9.6
Power output (dBm)	-14	18	-11	-2
Fiber-loop length (km)	1.219	1.0	2.4	3
Phase noise @ 10 kHz (dBc/Hz)	-101.8	-107.57	-100	-114
FSR (kHz)	154	180	84	68
SMSR (dB)	36	53	35	43
RF/EDFA amplifier	No	Yes	Yes	Yes
Optical/RF filter	No	Yes	Yes	Yes

Yao and Maleki demonstrated a dual loop OEO configuration where the optical power was split by an optical decoupler with both portion of the optical signal being subsequently detected by two photo-detectors [157]. The two converted RF signals were coupled by an RF coupler and then fed to the modulator after amplification. In each loop, the process was equivalent to a single-loop OEO. In this configuration, the method uses the natural structure of the OEO cavity to obtain filtering through an additional fiber loop or loops having shorter lengths, in parallel with the long fiber loop. Under the cooperation of the two loops, the side modes are efficiently reduced due to the gain competition between the two sets of modes. In this case, there is no random interference and beat noise because the RF signals have the same oscillation frequency and are coupled in the electrical domain. Although this design gave the expected result, two high-speed photo-detectors were needed.

5.5.2.1 Experimental setup

Here, substantial improvements in the reduction of the level of the side modes using a carrier suppression scheme in a dual loop RTD-OEO configuration is demonstrated. As illustrated in Fig. 5.6, the portion of the laser optical output is split into two parts each propagating through fibers having different lengths and then combined in a single fiber to be coupled to the single RTD-PD. That is, the RF signals are coupled in the optical domain without adding extra active electrical devices. Due to the interference between the two combined optical signals, the dual loop RTD-OEO presents strong mode selectivity with low power side modes. The RTD-PD-LD circuit configuration and components used in the dual-loop experiment showed identical characteristics of the one presented in the single-fiber experiment. Depending on DC bias, the circuit

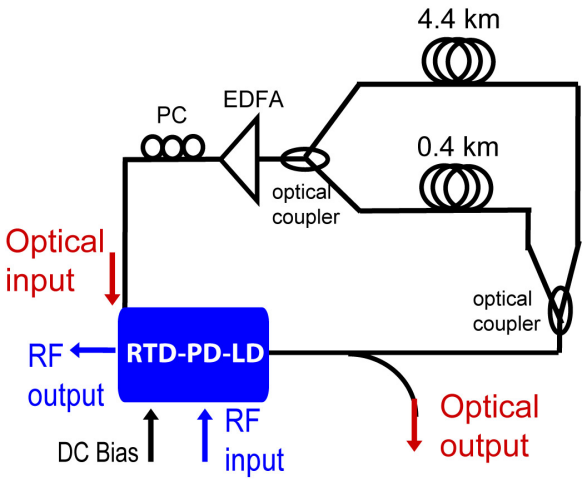

Figure 5.6: Schematic of the dual loop self-synchronized RTD-OEO setup.

under analysis here generated oscillations with natural frequencies ranging from 0.944 GHz to 1.129 GHz. In this investigation the RTD-PD-LD was DC biased at 2.33 V (close to the valley), showing oscillations around 1.121 GHz. The responsivity of the RTD-PD device was 0.25 A/W at 1550 nm when biased in the valley region.

5.5.2.2 Results and discussion

The effect of the dual-loop RTD-OEO using a 4.4 km and a 0.4 km fiber loop lengths, Fig. 5.6, was studied experimentally measuring the phase noise and level of side modes characteristics. The longer fiber leads to high spectral purity and low phase noise at low offsets. The short fiber is able to suppress the side modes close to the carrier.

Breaking either path, there is a complete single-loop OEO, which is able to freely run, similarly as demonstrated in the previous subsection. With the long path broken (4.4 km fiber loop), the mode spacing is 425 kHz and the measured side mode suppression ratio was -53 dBc at $P \sim 6$ dBm [see Fig. 5.7(a)]. With the short path broken (0.4 km fiber loop), the mode spacing is 45 kHz and the measured side mode suppression ratio was around -20 dBc [see Fig. 5.7(b)]. In the case of the dual-loop configuration, the side mode suppression ratio was improved up to -60 dBc [see Fig. 5.7(c)]. Compared with the single-loop results, the side modes can be effectively suppressed by 20-40 dB, depending on the input optical power launched into the RTD-PD.

The SSB phase noises of the single [Fig. 5.8(a)] and dual loop [Fig. 5.8(b)] con-

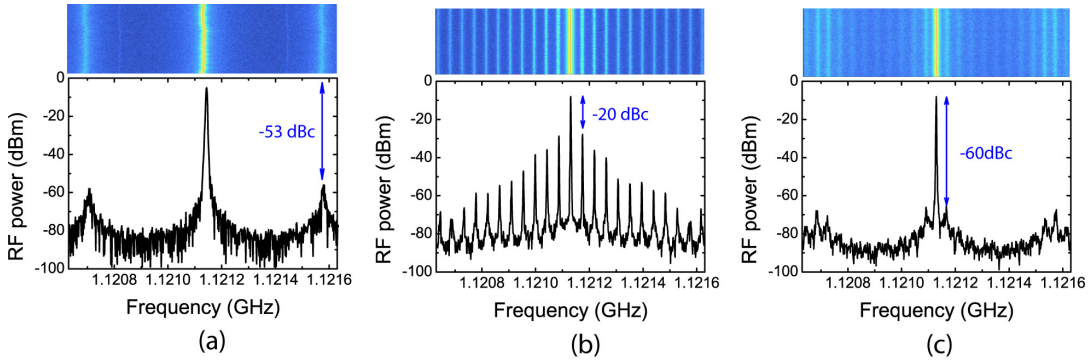

Figure 5.7: RF power spectra output showing the SMSR for (a) 0.4 km, (b) 4.4 km single loop, and (c) dual-loop configuration. The top part of each figure shows a spectrogram that represents the evolution of spectral density recorded over 1 min (time in the vertical axis).

figurations were measured. The phase noise at 10 kHz away from the carrier of the dual loop RTD-OEO was -99.28 dBc/Hz for 6 dBm in-fiber re-injected optical power, and -102.88 dBc/Hz for 9 dBm in-fiber re-injected optical power [Fig. 5.8(b)], which compares with the single loop at 4.4 km, showing -101.67 dBc/Hz at 10 kHz away from the carrier [Fig. 5.8(a)]. Therefore, besides maintaining the quality of the phase noise below -100 dBc/Hz at low offset, successfully suppression of the side modes was achieved in the spectral region above 45 kHz frequency offset of the carrier frequency which confirms the efficient side mode suppression function of the dual loop configuration. The measurements also showed that little close-to-carrier noise is introduced by the dual-loop configuration resulting sometimes in poor noise levels at lower carrier offsets when compared with the single 4.4 km long path. Figure 5.8(b) also shows results of a similar dual-loop setup without using optical amplification at $P = 3$ dBm, which demonstrate a dual-loop RTD-OEO not requiring either electrical or optical amplification. The EDFA was mainly used in the dual loop experiments to compensate the losses of coupling the light in more than one fiber, and due to the experimental difficulties of coupling and decoupling light in free-space conditions, mainly because the waveguide RTD-PD was not optimized for this application.

As a final comment, the dual loop OEO implementation reported here uses only a single RTD-PD which reduces considerably the number of components usually required in a dual-loop OEO configuration. However, it may suffer of problems related with coupling in the optical domain, namely interference and beating. This occurs mainly because the RF signals are coupled in the optical domain instead of other configurations

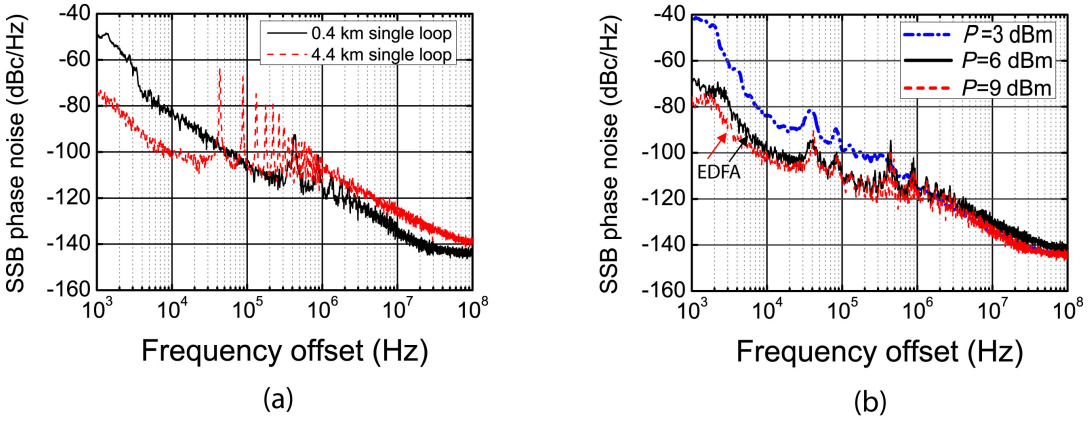

Figure 5.8: SSB phase noise plots. (a) 0.4 km and 4.4 km single-loop paths at $P \sim 6$ dBm optical power. (b) Dual loop configuration with and without EDFA.

where the coupling is achieved electrically. In order to avoid these two effects and retain the function of the dual-loop, an effective and simple way is to utilize, for example, a polarization beam splitter and combiner. The fluctuation of polarization and loop length are also considerable problems in the RTD-OEO dual-loop scheme presented here. If the polarization has large deviations, the optimized power distribution among the fibers is destroyed, and the side mode suppression ratio is degraded. To eliminate this effect, polarization-maintaining fibers can be used in the system. In the case of the loop length fluctuations, which are usually caused by environmental changes, these effects are difficult to overcome unless temperature control or feedback control is employed.

As a summary, the results of both single and dual loop schemes demonstrate the self-synchronization enhances the phase quality of free-running output signals with a compromise between the time delayed feedback loop configuration and the phase noise suppression. Although in terms of phase noise the RTD-OEO is still below commercial available voltage-controlled modules, such as CRO operating at the same range of frequencies that typically show phase noise values around -120 dBc/Hz at 10 kHz offset, it is expected that further techniques including temperature and vibration control can have a great impact in the RTD-OEO performance. It is worth mentioning that the results presented here are limited by the responsivity of the RTD-PD used in the experiment, and can be further improved using anti-reflection coating facets and maximizing waveguide external quantum efficiency, which for the devices employed is estimated to be $\eta_{ph} \sim 0.2$ (see Chapter 4 for more details). Furthermore, since there

is still considerable scope for optimization in many aspects of the OEO configuration including monolithic integration of the RTD-PD with LD, plus high-Q feedback route, the OEO topologies using self-injection locking of RTD oscillators can be interesting alternatives for novel low cost OEOs that not only are of miniature size (excluding the fiber loop) but also have power consumptions lower than existing devices.

5.6 Time delayed feedback Liénard oscillator

In Chapter 2 and in the remaining chapters on modeling of RTD and LD dynamical systems, we have considered systems that can be modeled by a set of first-order ODEs. However, the delayed feedback RTD-OEO system analyzed here belongs to a different class of systems: delay systems.

Delay systems possess a delayed feedback loop and can be modeled be a system of first-order delay-differential equations:

$$\frac{d\mathbf{x}(t)}{dt} = \mathbf{F}(\mathbf{x}(t), \mathbf{x}(t-\tau_d); \mathbf{p}), \tag{5.2}$$

where τ_d is the delay of the system and $\mathbf{F}$ is a vector field. The derivative of $\mathbf{x}(t)$ at time t depends on the value of of $\mathbf{x}(t)$ at time t and on the value that $\mathbf{x}(t)$ took in the past at time $t - \tau_d$. This means that it is necessary to know the vectorial function on the time interval of length τ_d to determine the state of the system and its evolution, because the phase space is an infinite-dimensional functional space. This infinite dimensionality of the phase space means that delay systems have the potential to produce very high-dimensional dynamics [22].

5.6.1 Liénard's OEO model

Developing a computational model of the RTD-OEO capable of reproducing the important dynamical effects observed experimentally, namely the level of the side modes due to the long delay line and the various noise sources, can be a challenging task since the round trip time scale corresponding to the optical fiber cavity mode spacing is much higher (typically in the μs range) than the time scale of the oscillation frequency of the oscillator. This means long run simulations and large amount of memory storage are usually required leading to time consuming simulations. In this section, we present a comprehensive numerical model of the single-loop delayed-feedback RTD-OEO system using DDEs [56, 57]. The DDE RTD-OEO system comprises a time-delayed feedback Liénard oscillator that models the RTD electrical dynamics and the feedback loop of

the OEO, laser rate equations describing the LD dynamics (see Chapter 2 for more details), and white Gaussian input noise to describe the dominant OEO noise sources, the thermal and shot noises [57].

5.6.1.1 Time delayed feedback system

The dynamics of the RTD-PD-LD oscillator is analyzed considering the lumped electrical circuit of Fig. 5.9. This circuit is equivalent to a Liénard oscillator [46, 48], that includes photocurrent (I_{ph}) and current noise (I_n) terms. The RTD-PD is represented by its intrinsic capacitance in parallel with a voltage dependent current source $F(V)$, and its photo-detection characteristics is modeled as an optical power dependent current source, I_{ph} [50]. Table 5.2 summarizes the typical values used in the simulations, estimated from the detection characteristics of experimental RTD-PD devices [50]. (see Chapter 4 for more details on the photo-detector model.)

Table 5.2: Parameters of the electrical circuit and of the RTD waveguide photo-detector.

Symbol	Parameter	Value
R	Resistance	7.8 Ω
L	Inductance	3.1×10^{-9} H
C	Capacitance	3.25×10^{-12} F
λ	Operation wavelength	1.55 μm
κ	Light coupling factor	0.35
R_{ref}	Waveguide facet reflectivity	0.3
α_v	Waveguide core absorption coefficient (valley)	400 cm^{-1}
γ_{ph}	Overlap integral of the electric and optical fields	0.25
Λ	Waveguide contact length	150 μm

Using the Kirchhoff's rules, the same procedure discussed in Chapter 2 was applied to obtain the two dimensionless first-order differential equations that describe the electrical circuit of Fig. 5.9. Then, the electrical system was coupled to the laser diode rate equations that model the laser system. As previously, time is normalized to the characteristic frequency of oscillation of the solitary RTD-PD-LD, $\omega_0 = (\sqrt{LC})^{-1}$, hence $\tau = \omega_0 t$. Finally, redefining τ as t and introducing into the system the optical delayed feedback $s(t - \tau_d)$, where η is the feedback strength and τ_d is the time-delay with respect to the dimensionless time t, the Liénard oscillator-laser diode dynamical system is transformed into the following dimensionless coupled DDEs:

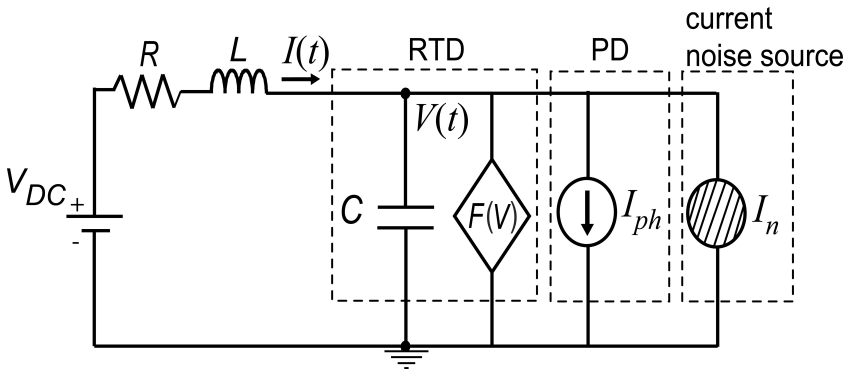

Figure 5.9: Equivalent electrical circuit schematic of the resonant tunneling diode photo-detector oscillator with current noise injection. The resistor R and inductor L account to the circuit series and parasitic resistance and inductance of RTD-PD-LD circuit, respectively.

$$\frac{dx(t)}{dt} = \frac{1}{\mu}\left[y(t) - f(x) - \chi\xi(t) - \eta s(t-\tau_d)\right] \tag{5.3}$$

$$\frac{dy(t)}{dt} = \mu\left[\upsilon_0 - \gamma y(t) - x(t)\right] \tag{5.4}$$

$$\frac{dn(t)}{dt} = \frac{1}{\tau_n'}\left[\frac{i_m(t)}{i_{th}} - n(t) - \frac{n(t)-\delta}{1-\delta}\{1-\epsilon s(t)\}s(t)\right] \tag{5.5}$$

$$\frac{ds(t)}{dt} = \frac{1}{\tau_p'}\left[\frac{n(t)-\delta}{1-\delta}\{1-\epsilon s(t)\}s(t) - s(t) + \beta n(t)\right] \tag{5.6}$$

Equations (5.3)-(5.6) represent the system of equations of the RTD-PD-LD with optical feedback control through the variable $s(t-\tau_d)$. The feedback strength η parameter depends on the fraction of the laser optical output power introduced into the delayed feedback loop and on the RTD-PD detection characteristics (Table 5.2). The function $f(x)$ comes from the normalization of $F(V)$, and $\mu = V_0/I_0\sqrt{C/L}$ is dimensionless. Equations (5.5)-(5.6) are the dimensionless rate equations describing LD normalized photon $s(t)$ and injected carrier $n(t)$ densities, respectively, where $\delta = N_0/N_{th}$ and $\epsilon = \epsilon_n S_0$ are two dimensionless parameters, $i_m(t)$ accounts for the bias current and the current oscillations produced by RTD-PD electrical model, Eqs. (5.3)-(5.4), and i_{th} is the dimensionless laser diode threshold current. The parameters τ_n' and τ_p' come from the time rescaling. Table 5.3 presents the dimensionless parameters used in the numerical simulations.

Table 5.3: Parameters used in the RTD-OEO simulation.

Symbol	Parameter	Value
μ	$V_0/I_0\sqrt{C/L}$	3.238×10^{-2}
γ	$R(I_0/V_0)$	7.8
τ_n'	Dimensionless carrier lifetime	0.30578
τ_p'	Dimensionless photon lifetime	0.01395
δ	N_0/N_{th}	0.613
ϵ	$\epsilon_n S_0$ (dimensionless laser gain saturation)	1.72×10^{-3}
β	Spontaneous emission	4×10^{-4}

In real systems, the unavoidable noise sources affect the dynamics by introducing amplitude and period fluctuations even in the most stable periodic signals. In our case, several sources or random processes are at play, like e.g. thermal and shot noises. We model their overall effect as an effective delta-correlated Gaussian white noise of zero mean input source $\chi\xi(t)$, Eq. (5.3), where the parameter χ is the dimensionless variance of the distribution and denote the noise strength.

For purposes of numerical simulation, Eqs. (5.3)-(5.6) were integrated with a standard constant step size Runge-Kutta method of fourth order [90]. As discussed previously, since long run simulations and large amount of memory storage are required, we interfaced a C++ time integrator with Matlab & Octave [158] via the mex interface [159]. This allows for high performances, efficient scripting capabilities as well as easy cluster deployment, three characteristics that are useful for extended parametric studies. The presence of a delayed contribution in Eq. (5.3) demand a special care. Indeed, to advance the solution with a step h from $t_n = nh$ to $t_{n+1} = (n+1)h$, the Runge-Kutta algorithm requires evaluating the values of $s(t-\tau_d)$ at intermediate points $t_{mid} = (n+1/2)h$. However, $s(t_{mid} - \tau_d)$ is not known and must be interpolated from past values, e.g., $s(t_{n-1} - \tau_d), s(t_n - \tau_d), s(t_{n+1} - \tau_d)$, etc., with an order consistent with the algorithm of integration. Therefore, in addition of the past values of $s(t)$ we also kept the time derivative $\dot{s}(t)$, that is, a quantity readily available upon time integration which allows building a third order Hermite polynomial between $t_n - \tau_d$ and $t_{n+1} - \tau_d$. By evaluating this interpolant of the delayed term at $t_{mid} - \tau_d$, we ensure an overall fourth order accuracy. The stochastic noise contribution $\chi\xi(t)$ in Eq. (5.3) is added after the deterministic step by simply using the Euler method [160]. Figure 5.10 presents a block diagram showing the corresponding mathematical representation of the OEO modeled by Eqs. (5.3)-(5.6) with time-delayed feedback $s(t-\tau_d)$ and noise input source.

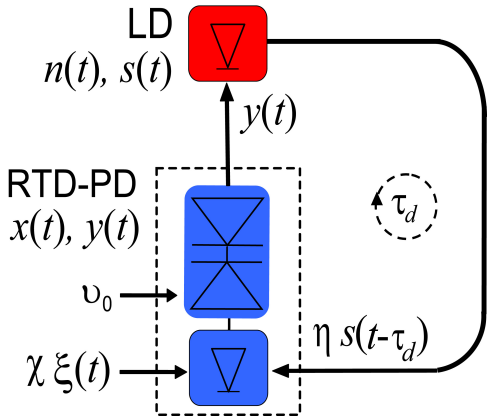

Figure 5.10: Block diagram of the mathematical representation of the delayed feedback Liénard oscillator laser diode dimensionless system.

In what follows the noise contribution in RTD-based OEO dynamical systems is discussed and the typical physical values of the noise intensities are derived.

5.6.1.2 Noise in RTD-PD OEO systems

The fundamental noise sources in the RTD-PD OEO system consist of thermal noise, the shot noise, and laser's RIN, which for the purpose of analysis can be viewed as all originating from the photo-detector. Since the photo-detector is monolithically integrated with the RTD structure, the noise can be viewed as entering the RTD-PD at the input current of the Liénard oscillator model, Eq. (5.3). Therefore, we are mainly interested in the thermal and shot noise sources of the RTD-PD. In a RTD-PD device, thermal noise or Johnson noise consists of thermal induced random fluctuations in the charge carriers of the material with a finite resistivity. These fluctuations are characterized by a Gaussian random process and they can be modeled as an equivalent current noise source in parallel with a noise-free resistor. Electronic shot noise is associated with the passage of carriers across a potential barrier such as those encountered in $p-n$ junctions of semiconductor diodes and transistors. The statistics that describe charge motion determine the noise characteristics. When the number of events that occur per unit time observation is large then the Poisson distribution can be replaced by a distribution of a zero mean Gaussian process with a white power spectral density.

The RTD-PD's thermal noise can be estimated from Nyquist generalized formula

[161], where the power spectral density is given by:

$$S_T = 4\kappa_B T G \tag{5.7}$$

with G being the differential conductance of the RTD-PD. For a typical RTDs with $G = 0.2$ S at $T = 300$ K we obtain $S_T = 0.33 \times 10^{-20}$ A^2/Hz. The power spectral density of RTD-PD electronic shot noise is given by:

$$S_I = 2q\gamma' I \tag{5.8}$$

where I is the average current, q is the magnitude of the electron charge, and γ' is the shot noise factor. In double barriers structures a phenomenon called shot noise suppression has been reported due to the reduction of γ' below 0.5 [162], in the I-V PDC region, prior to the NDC. When the device is DC biased in the NDC, enhanced shot noise is expected with respect of the full shot noise [163]. Here, for simplicity of the model, we are assuming $\gamma' = 1$. Therefore, for a DC current of 25 mA [RTD-PD biased close to the valley region, Fig. 5.2(b)], we obtain $S_I = 0.8 \times 10^{-20}$ A^2/Hz. These values compare with the RTD current noise caused by shot noise reported in [161] for InGaAlAs structures similar with the ones discussed here.

It is possible to relate the dimensionless noise intensity χ with the physical value of the noise found in the experimental RTD-OEO systems considering the thermal and shot noises discussed previously in Eqs. (5.7) and (5.8). The parameter χ defines the noise strength and $\xi(t)$ defines the Gaussian distribution added in Eq. (5.3) after the deterministic step. Therefore, if we want to relate χ to the physical noise intensity values we must pay attention to the time scaling and simulation time step. Since the model of Eqs. (5.3)-(5.6) is dimensionless, the time variable t, is dimensionless too, and reflects the physical time $\tilde{t}$ in units of $\sqrt{LC} \cong 100$ ps (assuming physical circuit parameters L and C presented in Table 5.2). Furthermore, we use the dimensionless stochastic force χ, with I_0 as the scale parameter of the physical dimension of current (here $I_0 = 1$ A). Therefore the dimensionless noise is given by:

$$\chi = (\sigma_T + \sigma_I)/I_0 = \left(\sqrt{4\kappa_B T G/\tau_a} + \sqrt{2q\gamma' I/\tau_a}\right)/I_0 \tag{5.9}$$

where σ_T and σ_I, are the thermal and shot noises in units of current, respectively, and $1/\tau_a$ is the bandwidth to be examined (equal to sampling frequency). For example, for a typical time step used in the simulations of $h = 0.01$ (corresponding to a time scale of 1 ps which is of the order of magnitude of typical Johnson noise correlation

at room temperature), and considering the values used to calculate the power spectral densities presented previously in Eqs. (5.7) and (5.8), we obtain a typical χ level of around 1.5×10^{-4}.

In Fig. 5.11 we evaluate the stochastic noise contribution in the free-running oscillator dynamics without time delayed feedback, that is $\eta = 0$. Figure 5.11(a) shows a typical experimental RF power spectrum of a free-running RTD-PD-LD electrical output at around 1.12207 GHz, and Fig.5.11(b) the simulated power spectrum of the voltage $x(t)$ at approximately the same oscillation frequency with noise contribution, and using parameters shown in Table 5.3. The introduction of noise with amplitude $\chi = 5 \times 10^{-4}$ into the system produces a broader peak in the Fourier domain. Also observed is a reduction of the signal-to-noise ratio at the free-running oscillation frequency. This value of noise amplitude fits relatively well with the experimental data. In what follows, we consider the noise value constant and for simplicity of analysis we define the new parameter $\theta = \eta/\chi$ that stands for the feedback strength to noise ratio of the Liénard OEO system.

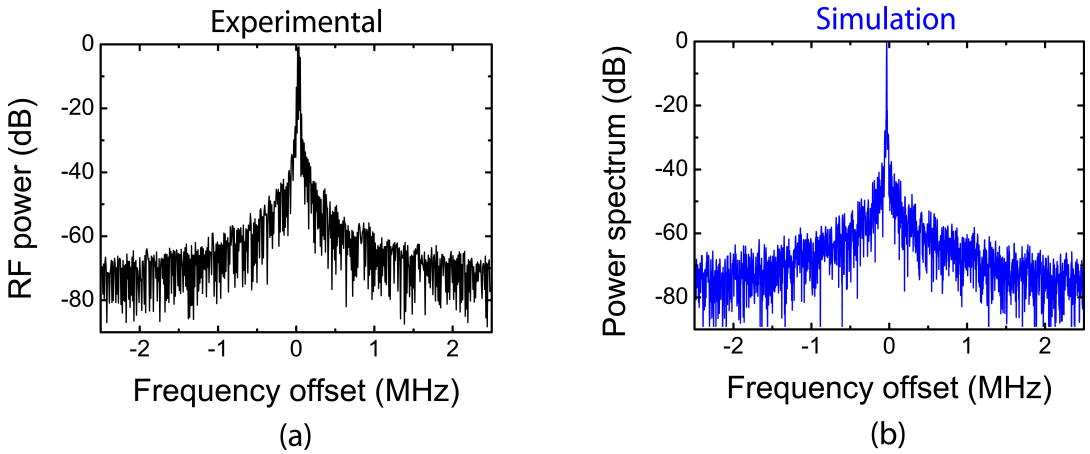

Figure 5.11: (a) Experimental RF power spectrum of RTD-PD-LD free-running electrical output. (b) Simulated power spectra of free-running fundamental oscillation of $x(t)$ output without stochastic noise $\chi = 0$, and with noise contribution $\chi = 5 \times 10^{-4}$. In both plots the span was 5 MHz and the central frequency was 1.12207 GHz.

5.6.2 Dynamics of delayed feedback Liénard oscillators

In this subsection, we describe the main results of the delayed feedback Liénard OEO model in the single and dual loop configurations. When the time delayed feedback is

included, important dynamical effects are observed that include close-to-carrier noise reduction and the appearance of side modes due to the delay contribution, similar to the experimental results reported previously in the single loop configuration.

We have simulated the numerical model using three round trip times $\tau_d \cong 2.35$ μs, $\tau_d \cong 4.25$ μs, and $\tau_d \cong 6.09$ μs, which correspond to the fiber lengths of 0.4 km, 0.8 km, and 1.2 km utilized in the experiments. The round trip times were obtained from the FSR of experimental results, which in our case depends on the electrical time delay τ_e, introduced by the electrical components, and the optical time delay τ_o, due to optical fiber length, Eq. (5.1). As discussed previously in the single loop configuration, for long feedback routes (optical fiber lengths above 1 km) the optical time delay is much larger than the electrical time delay, and $\tau_d \cong \tau_o = n_F L_f/c$.

Equations (5.3)-(5.6) were integrated with a time step of $h = 0.01$, which corresponds to $dt = 1$ ps, over l round trips in the external fiber loop. At each round trip the signal was propagated in the OEO and computed according to the Runge-Kutta algorithm described previously. In order to avoid very long time simulations and large memory requirements, we have chosen round trip times up to $\tau_d \cong 6.09$ μs and a time sampling of 10, i.e., 1 point every 10 was sampled.

Figure 5.12 presents the experimental (a) and simulated (b) power spectra around the fundamental free-running oscillation with and without delayed feedback. Figure 5.12(a) presents the experimental results of self-synchronized electrical output using a in-fiber optical re-injected power P of $\sim$ 6 dBm and 0.4 km fiber length. The results show phase noise and linewidth reductions at offsets below 250 kHz of the carrier frequency, and side-modes separated by about 425 kHz with a SMSR of -43 dBc. Note that the linewidth of the self-synchronized output could not be resolved by the 3 kHz resolution limit set by the instrument. Figure 5.12(b) shows the corresponding simulation for a time delay of $\tau_d = 2.35$ μs, and a feedback strength to noise ratio of $\theta = 2.0$ (corresponding to a feedback strength $\eta = 1 \times 10^{-3}$, for an injected optical power of 6 dBm). As observed experimentally, the introduction of time delayed feedback variable in the Liénard OEO model narrows the linewidth of the fundamental oscillation frequency and generates frequency side peaks due to the time-delay τ_d, which corresponds to the FSR of the RTD-OEO system. The SMSR of -44 dBc compares with the experimental result shown in Fig. 5.12(a).

Figure 5.13 shows the dynamics of the RTD-OEO as a function of the optical power level for a fixed delay, $\tau_d = 2.35$ μs. The minimum experimental optical power threshold necessary to self-synchronize the RTD-OEO and observe the presence of the side-modes close to the noise floor was around -2.36 dBm, Fig. 5.13(a), and compares

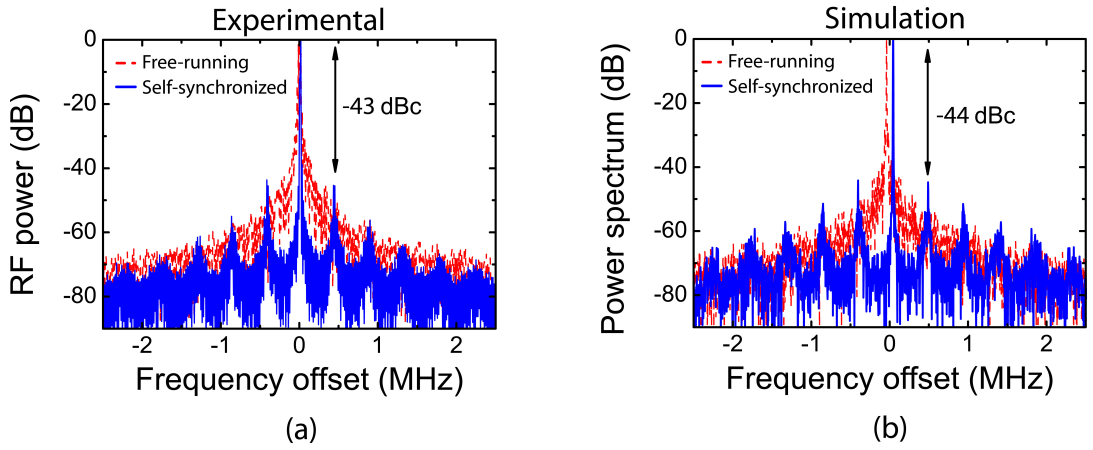

Figure 5.12: (a) Experimental RF power spectra of free-running oscillation and self-synchronized electrical output at $P \sim 6$ dBm and 0.4 km fiber length. (b) Simulated power spectra of free-running fundamental oscillation and self-synchronized $x(t)$ outputs with time delay of $\tau_d = 2.35$ μs and feedback strength to noise ratio of $\theta = 2.0$. In both plots the span was 5 MHz and the central frequency was 1.12207 GHz.

with the simulated results at a feedback strength to noise ratio of $\theta = 0.4$, Fig. 5.13(b). As the optical power increases, the reduction of noise close to the carrier frequency also improves. However, the presence of the side modes with SMSR around -45 dBc deteriorates the spectra at offsets around the FSR, as demonstrated experimentally and numerically in Figs. 5.13(c) and (d), respectively.

In Fig. 5.14 we investigate the influence of increasing the time delay in the dynamics of the RTD-OEO at a fixed feedback strength to noise ratio, $\theta = 1.2$. When $\tau_d = 4.25$ μs the side modes are present at levels around -39 dBC and -41 dBc in the experimental and simulated results, Figs. 5.14(a) and (b), respectively. The influence of the delay is more pronounced in Figs. 5.14 (c) and (d) at $\tau_d = 6.09$ μs showing several side modes with a SMSR above -35 dBc. In both the experimental and simulation results, the mode spacing decreased from about 236 kHz to 162 kHz when the delay line was increased from 0.8 km to 1.2 km. The results provide evidence that there is a compromise between the delay and the oscillator stability because increasing the time delay produces higher power side peaks close to the carrier. To overcome this limitation delayed configurations using multiple delayed-feedbacks can be implemented to suppress the side modes [157], as demonstrated in subsection 5.5.2.

Finally, we demonstrate that a dual loop Liénard OEO numerical model can accurately simulate the observed experimental results. We use Eqs. (5.3-5.6), with a

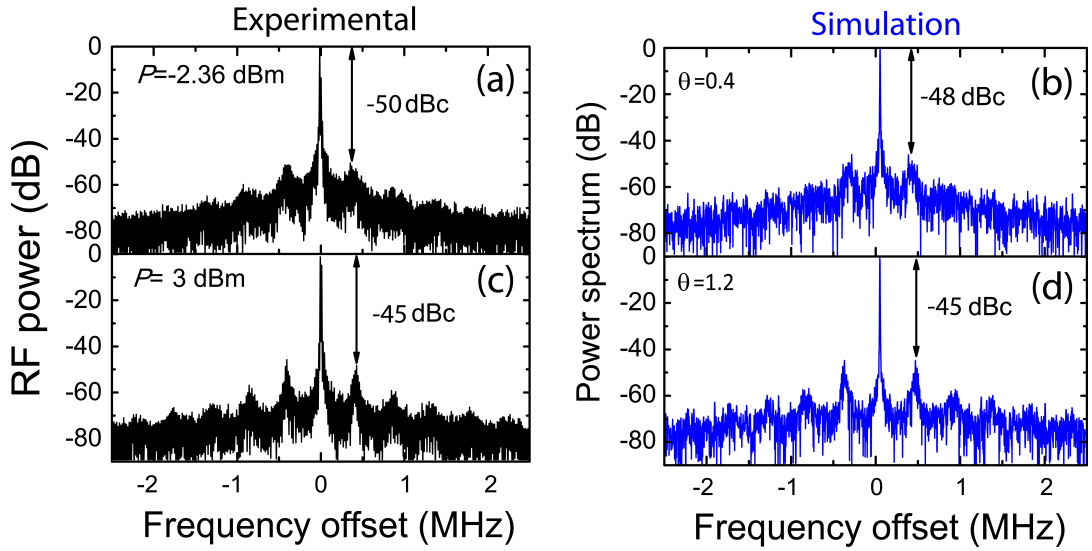

Figure 5.13: Experimental RF power spectra of self-synchronized electrical output: (a) $P \sim -2.36$ dBm, and (c) $P \sim 3$ dBm for 0.4 km fiber length. Simulated power spectra of self-synchronized $x(t)$ outputs with time delay $\tau_d = 2.35$ μs and feedback strength to noise ratio: (b) $\theta = 0.4$, and (d) $\theta = 1.2$. In all plots the span was 5 MHz and the central frequency was 1.12207 GHz.

modification in Eq. (5.3) to include two time delay contributions from the dual-loop configuration. Therefore, we change the single feedback from $\eta s(t - \tau_d)$ to the dual feedback $\eta_1 s(t - \tau_1) + \eta_2 s(t - \tau_2)$ where $\tau_1 < \tau_2$. Such a simple addition of the two photocurrents sources can be performed since after such a long propagation time the two signals are not coherent anymore with respect to each other. As such their interference average out. In addition, the fiber being not polarization preserving the two re-injected signals may also have partially orthogonal polarization.

In the numerical simulations we have chosen the round trip times $\tau_1 \cong 2.35$ μs and $\tau_2 \cong 22.2$ μs, which correspond to the fiber lengths of 0.4 km and 4.4 km, respectively, used in the dual loop experiments. In Fig. 5.15 we present a comparison between experimental data and the simulated power spectra. Figures 5.15(a) and (b) show the experimental and simulated multimode oscillation, respectively, of a single-loop RTD-OEO (in which the shorter loop is disconnected). Figures 5.15(c) and (d) present the single-mode oscillation of a dual-loop RTD-OEO in which both loops are closed. It is evident that the presence of the shorter loop effectively suppresses other modes of the longer loop and only leaves the fundamental oscillation signal. In both experimental and simulated results we can also observe the presence of additional side modes due

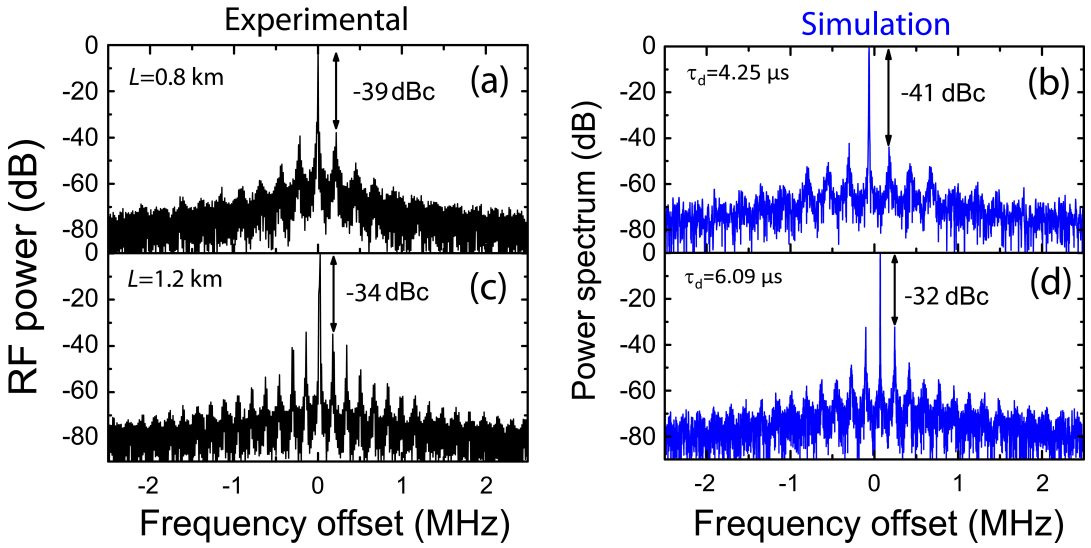

Figure 5.14: Experimental RF power spectra of self-synchronized electrical output at $P \sim 3$ dBm: (a) 0.8 km, and (c) 1.2 km fiber length. Simulated power spectra of self-synchronized $x(t)$ outputs with time delay: (b) $\tau_d = 4.25$ μs, and (d) $\tau_d = 6.09$ μs, and fixed feedback strength to noise ratio of $\theta = 1.2$. In all plots the span was 5 MHz and the central frequency was 1.12207 GHz.

to the shorter fiber with a spacing of about 425 kHz with an interference pattern that results of the combination of the two delayed-feedback signals. In Fig. 5.15(d) the mode-suppression ratio is -48 dBc which is in a good agreement with the experimental value of -51 dBc presented in Fig. 5.15(c). The results clearly demonstrate the model presented here can be extremely useful for design purposes to select the appropriate cavity characteristics to achieve efficient suppression of side modes.

The model dynamics investigated here follows the dynamics observed experimentally where the characteristics of the OEO can be controlled using optical delay lines. The large number of side-bands spaced by FSR (inversely proportional to the time delay) is an indication that more complex dynamics may occur, strongly depended of the feedback level and the length of the external cavity. In the results presented here, considering the moderate levels of feedback employed, $\eta << \Delta I/I_0$, where ΔI is the peak-to-valley current ratio, only stable self-synchronized oscillations were observed. The model can be used either to map the RTD-OEO dynamical regimes in order to avoid unstable signals or to take advantage of the rich dynamics which can be used to investigate innovative applications such as generation of frequency combs [25], or even chaotic transitions [26] controlled by the delayed feedback parameter.

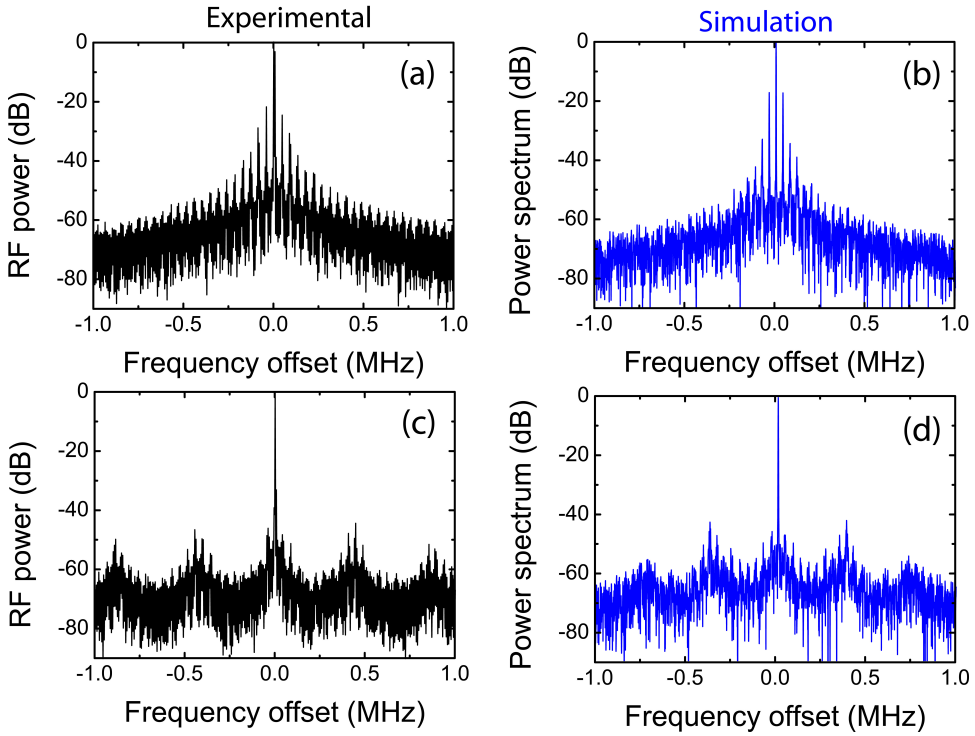

Figure 5.15: (a) Experimental RF power spectra of self-synchronized electrical output at $P \sim 0$ dBm and 4.4 km fiber length, and (c) dual-loop configuration. Simulated power spectra of self-synchronized $x(t)$ using (b) single delay at $\theta = 0.3$, and (d) dual delay at feedback strength to noise ratios $\theta_1 = 1.0$ (shorter delay), and $\theta_2 = 0.3$ (longer delay). In all plots the span was 2 MHz and the central frequency was 1.12219 GHz.

5.7 Chapter summary

In conclusion, we have demonstrated a simple optoelectronic self-synchronized oscillator that is based on the integration of a RTD-PD for O/E conversion, a laser diode for E/O conversion, and an optical fiber delay line. With this configuration we achieved stable free-running self-locked oscillations with a phase-noise reduction more than 40 dB at 10 kHz frequency offset from the center free-running frequency for single loop optical fiber lengths around 1.2 km, without the need of RF or optical amplification. Successful suppression of the side modes associated with the delay line was achieved using a dual loop topology. The level of the side modes was improved by 20-40 dB resulting with side mode suppression ratio of -60 dBc.

Numerical modeling based on a system of DDE comprising a time delayed feedback Liénard oscillator driven by white Gaussian noise and coupled with laser rate equations

provided additional insight on the dynamics of the OEO in both single and dual loop configurations. The model predicted the experimental behavior of the RTD-OEO as a function of the time delay and the feedback strength, predicting the free-spectral range and the side mode suppression ratio to within 2-3 dB. This model, once extended to include the different noise contributions of a typical OEO such as flicker noise from environmentally driven changes in the fiber length, will enable users to accurately design OEOs based on RTD-PD devices and to investigate a variety of multi-loop configurations. Furthermore, the complex behavior induced by the delayed feedback configuration enriches the nonlinear dynamics of RTD-based oscillators which can be explored in other applications not discussed in this thesis, namely chaos-controlled methods [130] to stabilize a desired dynamical behavior, and noise-induced stochastic oscillatory behavior [164, 165], using the time delayed feedback as a control parameter [166].

Chapter 6

Conclusions and future work

In this research work, a new type of OEO-based system was investigated. It comprises a resonant tunneling diode photo-detector oscillator and laser diode that takes advantage of RTD's nonlinear behavior subjected to optical and electrical perturbations, and to time delayed feedback. The objective of the work was to develop RTD-based OEO topologies and investigate their dynamical operation regimes in both electrical and optical domains. The topologies were numerically evaluated using two sets of ordinary and delay differential equations consisting of a Liénard RTD oscillator model, and laser diode single mode rate equations for the analysis of the dynamics of RTD and LD-based systems, respectively.

6.1 Conclusions

In Chapter 2 an overview on the theory of nonlinear dynamic systems was given employing resonant tunneling diode and the laser diode devices. A dynamical system theory to model nonlinear RTD-based systems, the Liénard oscillator model, was introduced consisting of a system of ordinary differential equations obtained from the circuit analysis of RTD oscillators. The dynamical regimes of these oscillators ranged from self-sustained relaxation oscillations controlled by voltage to synchronization when subjected to external periodic injection, and chaos generation in a quasi-periodic route to chaos. Finally, the laser diode optical system using the rate equation model was discussed. The numerical simulation showed the LD dynamics was strongly depended on the factor of spontaneous emission and the nonlinear gain saturation, and the period-doubling bifurcation routes to chaos were the predominant instabilities found in directly modulated lasers.

Chapter 3 provided a description of the experimental key steps needed for producing the RTD-OEICs considered in this work. We gave particular attention to the processes needed to obtain a high-frequency RTD oscillator driving a LD in a hybrid integrated circuit, the RTD-LD. The dynamical regimes of RTD-LD oscillators subjected to RF signals were investigated in both electrical and optical domains. The results of injection locking at the fundamental oscillation demonstrated locking with power levels 40 dB below the free-running output power. The injection power, locking range, and phase noise reduction aspects of the locked outputs were characterized. At moderate levels, clean signals were obtained with more than 30 dB noise suppression when compared with the free-running mode, and locking ranges of tens of MHz, corresponding to more than 2% of the RTD-LD oscillation frequency. We have also observed complex dynamics that included period-adding bifurcation, and generation of quasi-periodic and high-dimensional chaotic electrical and optical signals. Ultimately, in Chapter 3 the experimental results were analyzed using the Liénard-laser diode oscillator model system, providing additional insight on the dynamics followed by the RTD-LD system.

In Chapter 4 the detection characteristics of DBQW-RTD optical waveguide devices working as photo-detectors were investigated. Optically controlled RTD-OEICs were successfully implemented, consisting of an RTD-PD in series with a LD, the RTD-PD-LD, with both optical and electrical input and output ports, and a DC voltage control port. The circuits provided a simple and efficient way to obtain stable low-phase noise RF signals and conversion of optical RF sub-carriers from the optical to the electrical and optical domains via optical injection locking perturbation. We measured optical injection locking for in fiber optical power levels below 1 mW, and phase noise suppressions of -112.4 dBc/Hz at 10 kHz offset with locking ranges of 1.7% of the oscillator free-running frequency, providing low phase noise and clean signals for electronic and optical applications. The corresponding dynamics was also investigated utilizing the optically controlled Liénard oscillator model that took in consideration the detection characteristics of the RTD-PD waveguide. Finally, a clock-recovery circuit utilizing injection locking of RTD-PD-LD circuits was implemented, followed by the successfully transmission of phase modulated signals in a wireless/photonics link using analogue phase modulation and GMSK digital modulation formats.

At last, in Chapter 5 was demonstrated for the first time a delayed feedback RTD-

OEO comprising a self-synchronized RTD-PD oscillator driving a LD and utilizing an optical delay line. With this configuration we achieved stable free-running self-locked oscillations with a phase-noise reduction more than 40 dB at 10 kHz frequency offset from the center frequency for single loop optical fiber lengths around 1.2 km, without the need of RF or optical amplification. Successful suppression of the spurious modes associated with the delay line was also achieved utilizing a dual fiber loop topology. The level of the spurious mode suppression was improved by up to 40 dB resulting with side mode suppression ratio of -60 dBc. The RTD-OEO dynamics was numerically investigated utilizing a system of delay differential equations comprising a time delayed feedback Liénard oscillator with Gaussian white noise input, and coupled with laser rate equations. The time delayed feedback Liénard oscillator model provided a reasonably good fit to the observed RTD-OEO dynamics as a function of the re-injected optical power and the delay line in both single and dual loop configurations.

The main achievements of this work can be summarized as follows:

- Hybrid integrated circuit oscillators were designed and successfully implemented consisting of a DBQW-RTD connected electrically in series with a communications LD, forming the RTD-LD circuits.

- RTD-LD circuits operating as optoelectronic voltage controlled oscillators were demonstrated for the first time, producing both electrical and optical signals with fundamental relaxation oscillation at microwave frequencies.

- The following dynamical regimes were observed when the RTD-LD oscillators where electrically perturbed by periodic signals: fundamental and harmonic injection locking, period-adding bifurcation, and generation of quasi-periodic and chaotic signals.

- A numerical model that helped to understand the aforementioned dynamical behaviors was implemented consisting of a system of ordinary differential equations formed by a Liénard RTD oscillator model coupled to laser single mode rate equations.

- An optically controlled RTD-OEIC oscillator taking advantage of the photodetection characteristics of the DBQW-RTD structures was implemented. The RTD-PD-LD, with both optical and electrical input and output ports, and DC

voltage control port, provided simple O/E conversion and amplification of optical modulated signals.

- Clock-recovery circuits utilizing injection locking of RTD-PD-LD circuits were successfully implemented, followed by the demonstration of transmission of phase modulated analogue and digital signals in wireless/photonis links.

- First demonstration of a time delayed feedback RTD-OEO comprising a self-synchronized RTD-PD oscillator driving a LD and utilizing single and dual-loop optical delay lines for phase noise reduction.

- A numerical model utilizing a system of delay differential equations consisting of a time delayed-feedback Liénard oscillator with Gaussian white noise input, and coupled with laser rate equations was demonstrated to understand and predict the dynamics of RTD-OEO circuits.

6.2 Future work

The achievements of this work established a variety of dynamical regimes found in RTD-based OEO systems. Following these results, this work suggests, the synchronization and chaotic dynamics found in RTD-based OEOs can have many applications such as in highly stable oscillators, and in generation of random numbers, novel spread spectrum, ultra wide bandwidth, and chaos-based optical communication schemes [27]. There are an increasing number of novel applications in optoelectronic systems that can take advantage of these operation modes including high speed, and low power optoelectronic converters. The main potential advantages of utilizing RTD-based OEO systems instead of using other optoelectronic and laser systems subjected to optical injection or feedback include the simplicity and compactness of this OEO solution, the RTD frequency tunability as a function of the voltage, and the electrical and optical input ports provided by the RTD detector which reduces considerably the number of high-speed electronics required in most of the schemes used to generate chaotic and synchronized outputs.

At the present the RTD-based OEO exploits mainly RTD's inherent non-linearity, with the laser diode parameters being selected in a way that the laser dynamics does not influence the overall dynamics of RTD-OEO oscillator, e.g., the laser is used only as a light source. In future work novel approaches may be explored experimentally

and in the Liénard OEO model using the laser relaxation oscillation frequency (or other perturbation methods) to increase the system's dimensionality and investigate the resultant dynamics. The RTD-OEO system can be explored in further applications not discussed in this thesis, namely chaos-controlled methods [130] using time delayed feedback to stabilize a desired dynamical behavior. This can be used to implement novel microwave-photonic dynamical systems for applications requiring the ability to control the chaotic trajectories.

Ultimately, taking advantage of the random noise fluctuations, RTD-OEO systems can be used to produce noise-induced stochastic oscillatory behavior using time delayed feedback as a control parameter. The occurrence of oscillatory behavior due to noise is a remarkable effect discovered in stochastic excitable dynamics perturbations and has been recently explored in RTD-based devices [136], as an example of novel types of excitable systems [164, 165]. Because of the similarity of these behaviors with the patterns found in nature, RTD-OEO systems could provide a novel way to analyze and understand in laboratory environment many complex interactions influenced by noise, like for example in neural circuits [3].

Appendix A

Bifurcations in Dynamic Systems

The aim of this appendix is to review basic concepts of the theory of dynamical systems. This summary provides the basic notions and definitions necessary to understand the concepts and methods used to characterize the resonant tunneling diode and laser diode systems investigated in this thesis.

Continuous-time systems

Generally, a dynamic system is specified by a set of dynamic variables $\mathbf{x} = (x_1, x_2, ..., x_d)$ that depend upon time t, together with a law or rule determining the temporal evolution $\mathbf{x}(t)$ (in continuous-time systems, the governing rule is a set of differential equations) that determines the present state in terms of past states, for given initial conditions, and a set of control parameters by which the dynamic law can be changed.

Continuous-time systems can be described by a set of differential equations $d\mathbf{x}/dt$ governing the autonomous flow of a system with dimension d and initial conditions $\mathbf{x}(t_0)$. The dynamic system is given by:

$$\frac{d\mathbf{x}}{dt} = \mathbf{F}(\mathbf{x}; \mathbf{p}), \tag{A.1}$$

$$\mathbf{x}(t_0) = \mathbf{x}_0, \tag{A.2}$$

where $\mathbf{F}[\mathbf{x}; \mathbf{p}]$ is a nonlinear vector function, called vector field, that characterizes the system. This depends on a set of parameters $\mathbf{p} = (p_1, p_2, ...)$ which describe the features of a particular system modeled by the vector field. When the vector field depends explicitly on time, the system is said to be non-autonomous.

It is common to represent the evolution of a given system in its phase space. This space is generated by the set of all the variables that are necessary to describe the dynamical state of the system. For every phase point $\mathbf{x}$, except for the fixed points $\mathbf{x}_F$ (the fixed points represent time-independent steady states far from thermodynamic equilibrium), where $\mathbf{F}(\mathbf{x}_F; \mathbf{p}) = 0$, the differential equations A.1 give a unique direction of the phase flow $\mathbf{x}(t)$. Thus one can construct a phase portrait of the trajectories or orbits in the phase space, similar to the streamlines of a fluid. Any solution $\mathbf{x}(t)$, which may be regarded as the path of a particle in $\mathbf{x}$-space, is uniquely determined by its initial value $\mathbf{x}_0$ at the initial time t_0, denoted by $\mathbf{u}_{x0}(t)$. A trajectory is said to be locally stable if other trajectories, obtained from other initial conditions, different from, but close to, $\mathbf{x}_0$, remain close to the original trajectory for all later times. Is is locally asymptotically stable if, for all trajectories $\mathbf{u}_{x'0}$, whose phase points satisfy the stability criterion, the condition:

$$|\mathbf{u}_{x0}(t) - \mathbf{u}_{x'0}| \to 0, t \to \infty \tag{A.3}$$

also holds. A subset of the phase space that satisfies the stability criterion is called an attractor. The knowledge of the geometry of the attractor is very important in the characterization of the type of asymptotic behavior a system experiences. In what follows, the main characteristics of attractors found in dynamic systems are characterized.

Classification of attractors

A bounded, undecomposable, invariant, and locally asymptotically stable subset of the phase space is called an attractor. An attractor is globally stable if its basin of attraction includes the whole phase space. Note that attractors can occur only in dissipative dynamic systems, in which phase volumes contract. The following attractors can be observed.

- **fixed point**. The asymptotic behavior is stationary. Therefore the Fourier transform of the steady-state solution is a Dirac impulse.
- **periodic attractor (limit cycle)**, i.e. a closed curve if the phase space is at least two-dimensional. The steady state solution is periodic and the spectrum is discrete and constituted by a fundamental frequency and its harmonics.
- **torus** T^m. The asymptotic solution is quasi-periodic and its spectrum has m base frequencies. In the case of a two-dimensional torus ($m = 2$), this obviously

means that the spectrum has two base frequencies. When the ratio of the two frequencies is irrational, the trajectories lie on the torus in a dense way and the spectrum is itself dense. When the ratio is rational, the solution is periodic and the period is the smallest common multiple of the two base frequencies. The asymptotic solution is a closed curve on the torus and the spectrum is discrete.

- **strange attractor**. The steady-state is chaotic. Three dynamic degrees of freedom are required for a qualitatively chaotic attractor. It consists in an attracting, bounded set of phase points with the property that trajectories within the attractor that are initially very close to each other become separated exponentially fast with time. Hence, this implies that there is a sensitive dependency upon initial conditions, and an unstable motion within the attractor.

Deterministic chaos

In two-variable autonomous purely temporal dynamic systems, the field of directions of the phase flow is uniquely defined, and therefore trajectories can not cross. All trajectories in a bounded dissipative system must tend asymptotically to either a fixed point or a limit cycle, i.e. a zero- or one-dimensional attractor. When autonomous systems involving at least three dynamic variables are considered, this third degree of freedom adds a qualitatively new type of behavior, which is associated with an irregular and unpredictable temporal evolution of the system. If such irregular but bounded motion depends sensitively upon the initial conditions it is called chaotic. It is distinct from the irregularities caused by stochastic fluctuations in systems with many microscopic degrees of freedom since here we are considering a deterministic system with few degrees of freedom.

Chaos is sometimes defined by exclusion: a steady state solution of a deterministic system can be said to be chaotic if it is neither stationary, nor periodic, nor quasi-periodic. Practically, a series of properties are used to characterize a chaotic signal. We are going to enumerate the most important ones. A first property is that the spectrum of a chaotic signal is continuous and broadband . The spectrum usually resembles that of a noisy process with sometimes a few dominant frequencies appearing. This also means that the autocorrelation function, which is the inverse Fourier transform of the power spectral density, tends rapidly toward zero. Therefore the temporal correlation of the signal with itself decreases rapidly with time. Another important property is the sensitivity to initial conditions: two trajectories, initially even very close, diverge over

time and the distance between the trajectories increases, on average, exponentially over time. This sensitivity is also linked to the unpredictability of chaotic systems. Indeed, if the same experience is repeated two times on the same chaotic systems, two completely different evolutions of the system over time will be observed. We see that chaotic signals have common characteristics with random processes even if chaotic systems are fundamentally deterministic.

Routes to chaos

In order to determine the route to chaos of a given system, the trajectories in the phase space are analyzed. Depending on the dynamical system under analysis, several geometrical structures can be found in the phase space plots, which are generally called attractors. Using the bifurcation diagrams' analysis that represent the evolution of the type of solution when one or more parameters are changed, a qualitative change of a steady-state solution can be easily identified. Several routes to chaos have been reported using the analysis of bifurcation diagrams. In the following we discuss three common scenarios that have universal features and appear in many systems of quite different physical origin: (i) period doubling cascades, (ii) quasi-periodicity and (iii) intermittency.

- **(i) period doubling cascades**. As a control parameter is increased, the period will successively double until the system becomes chaotic. When a limit cycle embedded in a three-dimensional phase space becomes unstable, it bifurcates into another limit cycle with doubled period, i.e. half the frequency (subharmonic bifurcation). Upon further increase of the control parameter, a sequence of period-doubling bifurcations may occur at successive values of the control parameter p_n with n = 1, 2, 3,... with periods $2^n T$. For $n \to \infty$ the k_n converge to a critical value k_∞ at which the motion ceases to be periodic, and becomes chaotic.

- **(ii) quasi-periodicity**. In the case (ii), the Ruelle-Takens scenario [58], a limit cycle with frequency ω_1 undergoes a second Hopf bifurcation leading to a quasi-periodic motion on a two-torus with incommensurate frequencies ω_1 and ω_2. A subsequent bifurcation may either take the system back to a limit cycle with a single frequency (which is called frequency-locking), or add a third fundamental frequency ω (which transforms the two-torus into a three-torus). A condition for the latter is that the frequencies must be sufficiently irrational with respect to each other. However, this is a structurally unstable situation, and small structural

perturbations will destroy the three-torus and lead to a strange attractor. The observed scenario again obeys a universality law, which can be most easily studied in terms of an iterated map, the circle map [58]:

$$\Theta_{n+1} = \Theta_n + \Omega - \frac{K}{2\pi}\sin(2\pi\Theta_n) \tag{A.4}$$

where Θ is the iterated angular variable on the circle, and the parameters Ω and K denote the frequency ratio and the coupling strength of the two competing oscillatory modes, respectively. Increasing the strength of the nonlinear coupling between the oscillators develops an increasing tendency to lock into incommensurate motion for which the ratio of the oscillation frequencies is rational. The resonance-frequency-locked states form horn-like structures within the (Ω, K) control parameter plane known as Arnold tongues. They are ordered hierarchically according to the Farey tree, which orders all rationals in the interval [0, 1] with increasing denominator according to the rule that the rational with the smallest denominator between p/q and p'/q' is $(p+p')/(q+q')$, where p, p', q, and q' are integers. At the critical line $K = 1$, the frequency-locking intervals form a characteristic self-similar structure (a devil's staircase), i.e. it looks the same at any scale of magnification, and the Arnold tongues cover the entire Ω interval. For $K > 1$ the map ceases to be invertible, and chaos may set in, especially if Ω is chosen equal to the golden mean $(\sqrt{5}-1)/2$, which is in some sense the most irrational number. Other irrational numbers including the silver mean may also provide the necessary conditions for chaos.

- **(iii) intermittency**. A third common route to chaos is the intermittency scenario (Pomeau-Manneville). The intermittent motion of a dynamic system is characterized by the alternation of bursts of apparently chaotic behavior and intervals of almost periodic oscillations. The repetition frequency of the chaotic bursts depends upon the external control parameter.

Analysis of dynamical systems

- Power spectra

The analysis of oscillation and chaotic phenomena in Fourier space, known as spectral analysis, provides a useful tool, especially for those that imply transitions, such as from periodicity to chaos. A single scalar signal of the signal, $x(t)$, is enough to perform a

spectral analysis. A common procedure is to compute the Fourier transform, $F[x]$, of the signal, which is given by:

$$F[x] = X(f) = \int_{-\infty}^{\infty} s(t) e^{i2\pi f t} dt \tag{A.5}$$

and is a function of the frequency, $X(f)$. The one sided power spectral density for a real function, $x(t)$, is given by the square of its Fourier transform:

$$P(f) = 2|X(f)|^2 \tag{A.6}$$

The power spectrum provides an idea of how important the motions with frequency f are in the system dynamics. For discrete finite signals which are usually found in experiments and numerical studies, the power spectral density can be straightforwardly computed by means of the Fast Fourier Transform (FFT) technique. This is described in many standard textbooks on numerical analysis, and is frequently implemented in numerical and graphical software packages found for example in Mathematica and Matlab.

Two structural features of the power spectrum, sharp peaks and broadband noise, are useful to distinguish chaotic from non-chaotic signals. The power spectra, $P(f)$, of periodic attractors are made of Dirac $\delta-$peaks at the dominant frequencies of the attractor, f_1, and at its harmonics, kf_1, with k a whole number:

$$P(f) = \sum_{k=1}^{\infty} A_k \delta(kf_1 - f) \tag{A.7}$$

with A_k a decreasing amplitude, and $\delta(x)$ the Dirac delta function [$\delta(x) \to \infty$ for $x = 0$, and $\delta(x) = 0$ for $x \neq 0$]. This feature of periodic attractors, however, is lost to some extent when the power spectrum is computed from time series that are finite and discrete; but even in this case the power spectrum is significant, because the $\delta-$peaks become acute peaks with finite height and a finite width (of the order of the inverse of the length of the time series), which are usually clearly distinguishable. The main feature of the power spectrum of chaotic attractors is its continuity: it presents a broad noise-like band structure in general, with finite and broad peaks in many systems. These qualitative differences make the power spectrum useful to distinguish between chaotic and non-chaotic signals, and to determine the main frequencies of periodic oscillators.

- Lyapunov exponents

The essential property of chaos is an intrinsic instability of chaotic trajectories that causes unpredictability of the future state of the chaotic system. This unpredictability is called sensitivity to initial conditions because two trajectories of the same system, that start in states so close that they are indistinguishable within experimental uncertainties, would diverge exponentially.

The basic idea of the Lyapunov exponent is to measure the average rate of the divergence for the neighboring trajectories on the attractor. The direction of the maximum divergence or convergence locally changes on the attractor. The motion must be monitored at each point along the trajectory. Therefore, a small sphere is defined, whose center is a given point on the attractor and whose surface consists of phase points from nearby trajectories. As the center of the sphere and its surface points evolve in time, the sphere becomes an ellipsoid with the principal axes in the directions of the contraction and the expansion. The average rates of the expansion or the contraction along the principal axes are the Lyapunov exponents. For the $i-$th principal axis, the corresponding exponent is defined by:

$$\lambda_i = \lim_{t\to\infty} \left\{ \frac{1}{t} \ln \frac{L_i(t)}{L_i(0)} \right\} \tag{A.8}$$

where $L_i(t)$ is the radius of the ellipsoid along the $i-$th principal axis at time t. In this expression, the growth rate is always measured along the $i-$th principal axis, but the absolute orientation in the phase space of that axis is not fixed. It is impractical to perform the actual computation in the way suggested in the definition, because the initially close phase points would soon diverge from each other by distances approaching the size of the attractor, and the computation would then fail to capture the local rates of the divergence and the contraction. Therefore, vectors connecting the surface of the ellipsoid to the center must be shrunk periodically or renormalized to ensure that the size of the ellipsoid remains small and that its surface points correspond to trajectories near that of the center point.

Bibliography

[1] J. Marion and W. Hornyak, *Physics for Science and Engineering*. Saunders College Publishing, Philadelphia, 1982. 2

[2] B. V. der Pol, "A theory of the amplitude of free and forced triode vibrations," *Radio Rev.*, vol. 1, pp. 701–710, 754–762, 1920. 2, 26

[3] A. Pikovsky, M. Rosenblum, and J. Kurths, *Synchronization: A Universal Concept in Nonlinear Sciences*. Cambridge University Press, 2003. 3, 30, 141

[4] B. V. der Pol and J. V. der Mark, "Frequency demultiplication," *Radio Rev.*, vol. 120, pp. 363–364, 1927. 3, 26, 32

[5] R. Adler, "A study of locking phenomena in oscillators," *Proc. IEEE*, vol. 61, pp. 2804–2810, 1973. 3, 67, 68

[6] H. L. Stover and W. H. Steier, "Locking of laser oscillators by light injection," *Appl. Phys. Lett.*, vol. 8, pp. 91–93, 1966. 3

[7] A. J. Seeds and K. J. Williams, "Microwave photonics," *J. Lightw. Technol.*, vol. 24, pp. 4628–4641, 2006. 4, 45, 101, 110, 114

[8] R. A. Kiehl, "Behavior and dynamics of optically controlled TRAPATT oscillators," *IEEE Trans. Electron Devices*, vol. 25, pp. 703–710, 1978. 4, 77

[9] H. W. Yen, M. K. Barnoski, R. G. Hunsperger, and R. T. Melville, "Switching of GaAs IMPATT diode oscillator by optical illumination," *Appl. Phys. Lett.*, vol. 31, pp. 120–122, 1977. 4, 77

[10] E. Shumakher, T. Magrisso, S. Kraus, D. C. Elias, A. Gavrilov, S. Cohen, G. Eisenstein, and D. Ritter, "An InP HBT-based oscillator monolithically integrated with a photodiode," *J. Lightwave Technol.*, vol. 26, pp. 2679–2683, 2008. 4, 77, 110, 112, 119

[11] T. Ramond, L. Hollberg, P. W. Juodawlkis, and S. D. Calawa, "Low noise optical injection locking of a resonant tunneling diode to a stable optical frequency comb," *Appl. Phys. Lett.*, vol. 90, p. 171124, 2007. 4, 66, 77, 88, 92, 95, 112

[12] M. Sauer, A. Kobyakov, and J. George, "Radio over fiber for picocellular network architectures," *J. Lightw. Technol.*, vol. 25, pp. 3301–3320, 2007. 4, 101

[13] N. J. Gomes, M. Morant, A. Alphones, B. Cabon, J. E. Mitchell, C. Lethien, M. Csornyei, A. Stohr, and S. Iezekiel, "Radio-over-fiber transport for the support of wireless broadband services," *J. Opt. Netw.*, vol. 8, pp. 156–178, 2009. 4, 101

[14] T. B. Simpson, J. M. Liu, K. F. Huang, and K. Tai, "Nonlinear dynamics induced by external optical injection in semiconductor lasers," *Quantum Semicl. Opt.*, vol. 9, pp. 765–784, 1997. 5

[15] S. Wieczorek, B. Krauskopf, and D. Lenstra, "A unifying view of bifurcations in a semiconductor laser subject to optical injection," *Opt. Commun.*, vol. 172, pp. 1–6, 1999. 5

[16] R. Lang and K. Kobayashi, "External optical feedback effects on semiconductor injection laser properties," *IEEE J. Quantum Electron.*, vol. 16, pp. 347–355, 1980. 5

[17] B. Dahmani, L. Hollberg, and R. Drullinger, "Frequency stabilization of semiconductor-lasers by resonant optical feedback," *Opt. Lett.*, vol. 12, pp. 876–878, 1987. 109

[18] J. Mork, B. Tromborg, and J. Mark, "Chaos in semiconductor-lasers with optical feedback - theory and experiment," *IEEE J. Quantum Electron.*, vol. 28, pp. 93–108, 1992. 5, 109

[19] S. Tang and J. M. Liu, "Chaotic pulsing and quasi-periodic route to chaos in a semiconductor laser with delayed opto-electronic feedback," *IEEE J. Quantum Electron.*, vol. 37, pp. 329–336, 2001. 5, 45, 109

[20] J. Ohtsubo, *Semiconductor Lasers: Stability, Instability and Chaos.* Springer, 2005. 5, 16, 36, 42

[21] J. Sacher, D. Baums, P. Panknin, W. Elsasser, and E. O. Gobel, "Intensity instabilities of semiconductor lasers under current modulation, external light injection, and delayed feedback," *Phys. Rev. A*, vol. 45, pp. 1893–1905, 1992. 5, 36, 37

[22] K. Ikeda, K. Kondo, and O. Akimoto, "Successive higher-harmonic bifurcations in systems with delayed feedback," *Phys. Rev. Lett.*, vol. 49, pp. 1467–1470, 1982. 5, 109, 123

[23] T. E. Murphy, A. B. Cohen, B. Ravoori, K. R. B. Schmitt, A. V. Setty, F. Sorrentino, C. R. S. Williams, E. Ott, and R. Roy, "Complex dynamics and synchronization of delayed-feedback nonlinear oscillators," *Phil. Trans. R. Soc. A.*, vol. 368, pp. 343–366, 2010. 5, 7, 109

[24] X. S. Yao and L. Maleki, "Optoelectronic microwave oscillator," *J. Opt. Soc. Am. B*, vol. 13, pp. 1725–1735, 1996. 6, 109, 110, 111

[25] X. S. Yao and L. Maleki, "Optoelectronic oscillator for photonic systems," *IEEE J. Quantum Electron.*, vol. 32, pp. 1141–1149, 1996. 6, 109, 110, 111, 133

[26] K. E. Callan, L. Illing, Z. Gao, D. J. Gauthier, and E. Schöll, "Broadband chaos generated by an optoelectronic oscillator," *Phys. Rev. Lett.*, vol. 104, p. 113901, 2010. 6, 109, 113, 133

[27] A. Argyris, D. Syvridis, L. Larger, V. Annovazzi-Lodi, P. Colet, I. Fisher, J. Garcia-Ojalvo, C. Mirasso, L. Pesquera, and K. A. Shore, "Chaos-based communications at high bit rates using commercial fibre-optic links," *Nature*, vol. 438, pp. 343–346, 2005. 6, 36, 45, 73, 75, 140

[28] Y. C. Kouomou, P. Colet, L. Larger, and N. Gastaud, "Chaotic breathers in delayed electro-optical systems," *Phys. Rev. Lett.*, vol. 95, p. 203903, 2005. 6, 109

[29] L. Illing, D. J. Gauthier, and R. Roy, "Controlling optical chaos, spatiotemporal dynamics, and patterns," *Adv. At., Mol., Opt. Phys.*, vol. 54, pp. 615–697, 2006.

[30] M. Peil, M. Jacquot, Y. K. Chembo, L. Larger, and T. Erneux, "Routes to chaos and multiple time scale dynamics in broadband bandpass nonlinear delay electro-optic oscillators," *Phys. Rev. E*, vol. 79, p. 045201, 2009. 6, 109

[31] L. L. Chang, L. Esaki, and R. Tsu, "Resonant tunneling in semiconductor double barriers," *Appl. Phys. Lett.*, vol. 24, pp. 593–595, 1974. 6, 18

[32] S. K. Diamond, E. Ozbay, M. J. W. Rodwell, D. M. Bloom, Y. C. Pao, and J. S. Harris, "Resonant tunneling diodes for switching applications," *Appl. Phys. Lett.*, vol. 54, pp. 153–155, 1989. 7

[33] T. S. Moise, Y.-C. Kao, C. L. Goldsmith, C. L. Schow, and J. C. Campbell, "High-speed resonant-tunneling photodetectors with low-switching energy," *IEEE Photon. Technol. Lett.*, vol. 9, pp. 803–805, 1997. 7, 79

[34] E. R. Brown, J. R. Söderström, C. D. Parker, L. J. Mahoney, K. M. Molvar, and T. C. McGill, "Oscillations up to 712 GHz in InAs/AlSb resonant-tunneling diodes," *Appl. Phys. Lett.*, vol. 58, pp. 2291–2293, 1991. 7, 23

[35] S. Suzuki, M. Asada, A. Teranishi, H. Sugiyama, and H. Yokoyama, "Fundamental oscillation of resonant tunneling diodes above 1 THz at room temperature," *Appl. Phys. Lett.*, vol. 97, p. 242102, 2010. 23

[36] M. Feiginov, C. Sydlo, O. Cojocari, and P. Meissner, "Resonant-tunnelling-diode oscillators operating at frequencies above 1.1 THz," *Appl. Phys. Lett.*, vol. 99, p. 233506, 2011. 7, 23

[37] E. S. Hellman, K. L. Lear, and J. S. Harris, "Limit-cycle oscillation in negative differential resistance devices," *J. Appl. Phys.*, vol. 64, pp. 2798–2800, 1988. 7

[38] S. G. Zhou, M. Sweeny, J. M. Xu, and O. Berolo, "Chaotic behavior of quantum resonant tunneling diodes," *Physica D*, vol. 52, pp. 544–550, 1991. 7

[39] J. H. Davies, *The physics of low-dimensional semiconductors: an introduction.* Cambridge University Press, Cambridge, 1998. 7, 18, 21

[40] H. Mizuta and T. Tanoue, *The physics and applications of resonant tunneling diodes.* Cambridge University Press, Cambridge, 1995. 16, 18

[41] J. P. Sun, G. I. Haddad, P. Mazumder, and J. N. Schulman, "Resonant tunneling diodes: models and properties," *Proc. IEEE*, vol. 86, pp. 641–660, 1998. 7, 20

[42] J. M. L. Figueiredo, C. N. Ironside, and C. R. Stanley, "Electric field switching in a resonant tunneling diode electroabsorption modulator," *IEEE J. Quantum Electron.*, vol. 37, pp. 1547–1552, 2011. 7, 48, 49, 81, 85, 114

[43] J. M. L. Figueiredo, B. Romeira, T. J. Slight, and C. N. Ironside, *Resonant Tunnelling Optoelectronic Circuits.* Book Chapter In: Advances in Optical and Photonic Devices, Ki Young Kim (Ed.), ISBN 978-953-7619-76-3, InTech, 2010. 7, 81, 114

[44] T. J. Slight and C. N. Ironside, "Investigation into the integration of a resonant tunnelling diode and an optical communications laser: Model and experiment," *IEEE J. Quantum Electron.*, vol. 43, pp. 580–587, 2007. 7, 47, 48

[45] J. M. L. Figueiredo, B. Romeira, T. J. Slight, L. Wang, E. Wasige, and C. N. Ironside, "Self-oscillation and period adding from a resonant tunnelling diode - laser diode circuit," *Electron. Lett.*, vol. 44, pp. 876–878, 2008. 10, 69

[46] T. J. Slight, B. Romeira, L. Wang, J. M. L. Figueiredo, E. Wasige, and C. N. Ironside, "A Liénard oscillator resonant tunnelling-laser diode hybrid integrated circuit: Model and experiment," *IEEE J. Quantum Electron.*, vol. 44, pp. 1158–1163, 2008. 10, 27, 58, 124

[47] B. Romeira, J. M. L. Figueiredo, T. J. Slight, L. Wang, E. Wasige, C. N. Ironside, J. M. Quintana, and M. J. Avedillo, "Observation of frequency division and chaos behavior in a laser diode driven by a resonant tunneling diode," *Conference on Lasers and Electro-Optics (CLEO)/Quantum Electronics and Laser Science Conference and Photonic Applications Systems Technologies (QELS) (Optical Society of America, Washington, DC, 2008)*, vol. paper CMY5, San Jose, CA, USA, May 4-9, pp. 766–767, 2008. 10

[48] B. Romeira, J. M. L. Figueiredo, T. J. Slight, L. Wang, E. Wasige, C. N. Ironside, A. E. Kelly, and R. Green, "Nonlinear dynamics of resonant tunneling optoelectronic circuits for wireless/optical interfaces," *IEEE J. Quantum Electron.*, vol. 45, pp. 1436–1445, 2009. 10, 58, 68, 115, 124

[49] B. Romeira, J. M. L. Figueiredo, C. N. Ironside, and T. J. Slight, "Chaotic dynamics in resonant tunneling optoelectronic voltage controlled oscillators," *IEEE Photon. Technol. Lett.*, vol. 21, pp. 1819–1821, 2009. 10, 69

[50] B. Romeira, J. M. L. Figueiredo, C. N. Ironside, A. E. Kelly, and T. J. Slight, "Optical control of a resonant tunneling diode microwave-photonic oscillator," *IEEE Photon. Technol. Lett.*, vol. 22, pp. 1610–1612, 2010. 10, 88, 124

[51] B. Romeira, J. M. L. Figueiredo, T. J. Slight, L. Wang, E. Wasige, and C. N. Ironside, "Synchronizing optical to wireless signals using a resonant tunneling diode laser diode circuit," *21st Annual Meeting of the IEEE Lasers and Electro-Optics Society (LEOS 08)*, vol. paper TuB1, pp. 145-146, Newport Beach, CA, USA, November 9-13, 2008. 10

[52] B. Romeira, J. M. L. Figueiredo, T. J. Slight, L. Wang, E. Wasige, and C. N. Ironside, "Wireless/photonics interfaces based on resonant tunneling diode optoelectronic oscillators," *Conference on Lasers and Electro-Optics (CLEO)/The International Quantum Electronics Conference (IQEC) (Optical Society of America, Washington, DC, 2009)*, vol. paper CTuT4, Baltimore, Maryland, USA, May 31-June 5, 2009. 10

[53] B. Romeira, L. M. Pessoa, H. M. Salgado, S. Silva, and J. M. L. Figueiredo, "Clock recovery of an injection-locked resonant tunneling diode microwave-photonics oscillator," *13th International Conference on Transparent Optical Networks (ICTON 11)*, vol. paper We.C5.6, Stockholm, Sweden, June 26-30, 2011. 10

[54] B. Romeira, K. Seunarine, C. N. Ironside, A. E. Kelly, T. J. Slight, and J. M. L. Figueiredo, "An optoelectronic oscillator based on a resonant tunneling diode photo-detector integrated chip," *The 23rd Annual Meeting of the IEEE Photonics Society*, vol. paper MD4, Denver, Colorado, USA, November 7-11, 2010. 10

[55] B. Romeira, K. Seunarine, C. N. Ironside, A. E. Kelly, and J. M. L. Figueiredo, "A self-synchronized optoelectronic oscillator based on an RTD photo-detector and a laser diode," *IEEE Photon. Technol. Lett.*, vol. 23, pp. 1148–1150, 2011. 10, 112

[56] B. Romeira, K. Seunarine, C. N. Ironside, J. Javaloyes, A. E. Kelly, and J. M. L. Figueiredo, "A Liénard optoelectronic oscillator with time-delayed feedback," *The European Conference on Lasers and Electro-Optics (CLEO) and the European Quantum Electronics Conference (EQEC) Conference Digest, OSA Technical Digest (CD) (Optical Society of America, 2011)*, vol. paper CI3.2, Munich, Germany, May 22-26, pp. 766–767, 2011. 11, 123

[57] B. Romeira, J. Javaloyes, J. M. L. Figueiredo, C. N. Ironside, H. I. Cantu, and A. E. Kelly, "Delayed feedback dynamics of Liénard-type resonant tunneling-photo-detector optoelectronic oscillators," *IEEE J. Quantum Electron.*, vol. 49, pp. 31–42, 2013. 11, 123, 124

[58] E. Ott, *Chaos in Dynamical Systems*. Cambridge, U.K.: Cambridge Univ. Press, 1993. 13, 67, 69, 72, 73, 146, 147

[59] S. H. Strogatz, *Nonlinear dynamics and chaos*. Addison-Wesley, New York, 1994. 13, 67, 69

[60] E. N. Lorenz, "Deterministic nonperiodic flow," *J. Atmos. Sci.*, vol. 20, pp. 130–141, 1963. 13

[61] D. J. Watts and S. H. Strogatz, "Collective dynamics of 'small-world' networks," *Nature*, vol. 393, pp. 440–442, 1998. 13

[62] M. C. Cross and P. C. Hohenberg, "Pattern-formation outside of equilibrium," *Rev. Mod. Phys.*, vol. 65, pp. 851–1112, 1993. 13

[63] E. Ott, , C. Grebogi, and J. A. Yorke, "Controlling chaos," *Phys. Rev. Lett.*, vol. 90, pp. 1196–1199, 1990. 13

[64] K. Pyragas, "Continuous control of chaos by self-controlling feedback," *Phys. Lett. A*, vol. 170, pp. 421–428, 1992.

[65] K. M. Cuomo and A. V. Oppenheim, "Circuit implementation of synchronized chaos with applications to communications," *Phys. Rev. Lett.*, vol. 71, pp. 65–68, 1993. 13, 45

[66] E. Scholl, *Nonequilibrium Phase Transitions in Semiconductors*. Springer, Berlin, 1987. 13

[67] H. Haug, *Optical Nonlinearities and Instabilities in Semiconductors*. Academic Press, New York, 1988. 13

[68] J. Unkelbach, A. Amann, W. Just, and E. Scholl, "Time-delay autosynchronization of the spatiotemporal dynamics in resonant tunneling diodes," *Phys. Rev. E*, vol. 68, no. 2, p. 026204, 2003. 16

[69] P. Orellana, E. Anda, and F. Claro, "Dynamic instabilities in resonant tunneling induced by a magnetic field," *Phys. Rev. Lett.*, vol. 79, pp. 1118–1121, 1997. 16

[70] Y. H. Zhang, J. Kastrup, R. Klann, and K. H. Ploog, "Synchronization and chaos induced by resonant tunneling in GaAs/AlAs superlattice," *Phys. Rev. Lett.*, vol. 77, pp. 3001–3004, 1996. 16

[71] L. L. Bonilla and H. T. Grahn, "Non-linear dynamics of semiconductor superlattices," *Rep. Prog. Phys.*, vol. 68, p. 577, 2005. 16

[72] D. Bohm, *Quantum theory*. Prentice-Hall Inc., New Jersey, 1951. 17

[73] L. V. Iogansen, "The possibility of resonance transmission of electrons in crystals through a system of barriers," *Sov. Phys. JETP*, vol. 18, p. 146, 1964. 17

[74] R. Tsu and L. Esaki, "Tunneling in a finite superlattice," *Appl. Phys. Lett.*, vol. 22, pp. 562–564, 1973. 18

[75] T. C. L. G. Sollner, W. D. Goodhue, P. E. Tannenwald, C. D. Parker, and D. D. Peck, "Resonant tunneling through quantum wells at frequencies up to 2.5 THz," *Appl. Phys. Lett.*, vol. 43, pp. 588–590, 1983. 18, 56

[76] M. Tsuchiya and H. Sakaki, "Room temperature operation of high-performance AlAs/GaAs/AlAs resonant tunneling diodes with atomically controlled barrier width," *IEEE Int. Electron Devices Meeting*, vol. 31, pp. 662–665, 1985. 18

[77] M. Tsuchiya, H. Sakaki, and J. Yoshino, "Room-temperature observation of differential negative-resistance in an AlAs/GaAs/AlAs resonant tunneling diode," *Jpn. J. Appl. Phys. 2*, vol. 24, pp. L466–L468, 1985. 18

[78] E. R. Brown, O. B. McMahon, L. J. Mahoney, and K. M. Molvar, "SPICE model of the resonant-tunneling diode," *Electron. Lett.*, vol. 32, pp. 938–940, 1996. 20, 24

[79] T. H. Kuo, H. C. Lin, U. Anandakrishnan, R. C. Potter, and D. Shupe, "Large-signal resonant tunneling diode model for SPICE3 simulation," *Electron Devices Meeting*, pp. 567–570, 1989. 20

[80] K. Maezawa, "Analysis of switching time of monostable-bistable transition logic elements based on simple model calculation," *Jpn. J. Appl. Phys.*, vol. 34, pp. 1213–1217, 1995. 21

[81] Z. Yan and M. J. Deen, "New RTD large-signal dc model suitable for PSPICE," *IEEE Trans. Comput.-Aided Design Integr. Circuits Syst.*, vol. 14, pp. 167–172, 1995. 21

[82] J. N. Schulman, H. J. D. L. Santos, and D. H. Chow, "Physics-based RTD current-voltage equation," *IEEE Electron Device Lett.*, vol. 17, pp. 220–222, 1996. 21, 54, 55

[83] E. R. Brown, C. D. Parker, and T. C. L. G. Sollner, "Effect of quasibound-state lifetime on the oscillation power of resonant tunneling diodes," *Appl. Phys. Lett.*, vol. 54, pp. 934–936, 1989. 24

[84] E. R. Brown, W. D. Goodhue, and T. C. L. G. Sollner, "Fundamental oscillations up to 200 GHz in resonant tunneling diodes and new estimates of their

maximum oscillation frequency from stationary-state tunneling theory," *J. Appl. Phys.*, vol. 64, pp. 1519–1529, 1988. 25

[85] E. R. Brown, T. C. L. G. Sollner, W. D. Goodhue, and C. D. Parker, "Millimeter-band oscillations based on resonant tunneling in a double-barrier diode at room temperature," *Appl. Phys. Lett.*, vol. 50, pp. 83–85, 1987. 25

[86] A. Liénard, "Etude des oscillations entretenues," *Rev. Gen. Electr.*, vol. 28, pp. 901–946, 1928. 26

[87] A. Lins, W. Melo, and C. Pugh, *On Liénards Equation. Lecture Notes in Mathematics*. Springer-Verla, New York, 1977. 26

[88] J. K. Hale, *Theory of Functional Differential Equations*. Springer-Verla, New York, 1977. 26

[89] J. M. Quintana and M. J. Avedillo, "Analysis of frequency divider RTD circuits," *IEEE Trans. Circuits Syst. I, Reg. Papers*, vol. 52, pp. 2234–2247, 2005. 26, 32

[90] W. H. Press, S. A. Teukolsky, W. T. Vetterling, and B. P. Flannery, *The Art of Scientific Computing*. Cambridge University Press, Cambridge, 2007. 29, 126

[91] V. I. Arnold, *Geometrical Methods in teh Theory of Ordinary Differential Equations*. Springer, New York, 1983. 31

[92] H. S. Zuckerman, H. L. Montgomery, I. M. Niven, and A. Niven, *An Introduction to the Theory of Numbers*. John Wiley, New York, 1991. 32

[93] M. Sandri, "Numerical calculation of lyapunov exponents," *The Mathematica Journal*, vol. 6, pp. 78–84, 1996. 35

[94] G. P. Agrawal and N. K. Dutta, *Semiconductor lasers*. Van Nostrand Reinhold, New York, 1993. 36

[95] K. Petermann, *SLaser Diode Modulation and Noise*. Kluwer Academic Publishers, Dordrecht (NL), 1988. 36

[96] C.-H. Lee, T.-H. Yoon, and S.-Y. Shin, "Period doubling and chaos in a directly modulated laser diode," *Appl. Phys. Lett.*, vol. 46, pp. 95–97, 1985. 36, 42

[97] H. G. Winful, Y. C. Chen, and J. M. Liu, "Frequency locking, quasiperiodicity, and chaos in modulated self-pulsing semiconductor lasers," *Appl. Phys. Lett.*, vol. 48, pp. 616–618, 1986. 36

[98] G. D. Vanwiggeren and R. Roy, "Communication with chaotic lasers," *Science*, vol. 279, pp. 1198–1200, 1998. 36, 45

[99] P. V. Mena, S. Kang, and T. A. DeTemple, "Rate-equation-based laser models with a single solution regime," *J. Lightw. Technol.*, vol. 15, pp. 717–730, 1997. 37, 63

[100] L. M. Pecora and T. L. Carroll, "Synchronization in chaotic systems," *Phys. Rev. Lett.*, vol. 64, pp. 821–824, 1990. 45

[101] C. Kurtsiefer, P. Zarda, M. Halder, H. Weinfurter, P. M. Gorman, P. R. Tapster, and J. G. Rarity, "Quantum cryptography: A step towards global key distribution," *Nature*, vol. 419, p. 450, 2002. 45

[102] L. L. J. P. Goedgebuer and H. Porte, "Optical cryptosystem based on synchronization of hyperchaos generated by a delayed feedback tunable laser diode," *Phys. Rev. Lett.*, vol. 80, pp. 2249–2252, 1998. 45

[103] S. Bennett, C. M. Snowden, and S. Iezekiel, "Nonlinear dynamics in directly modulated multiple-quantum-well laser diodes," *IEEE J. Quantum Electron.*, vol. 33, pp. 2076–2083, 1997. 45

[104] M. Yousefi, Y. Barbarin, S. Beri, E. A. J. M. Bente, M. K. Smit, R. Nötzel, and D. Lenstra, "New role for nonlinear dynamics and chaos in integrated semiconductor laser technology," *Phys. Rev. Lett.*, vol. 98, p. 044101, 2007. 45, 73

[105] A. Argyris, M. Hamacher, K. E. Chlouverakis, A. Bogris, and D. Syvridis, "Photonic integrated device for chaos applications in communications," *Phys. Rev. Lett.*, vol. 100, p. 194101, 2008. 45, 73, 74

[106] A. Katz, *Indium phosphide and related materials: processing, technology, and devices*. Artech House, London, 1992. 46

[107] A. Katz, *Optoelectronic integration: physics, technology and applications*. Kluwer Academic Publishers, Massachusetts, 1994. 46

[108] K. Y. Liou, S. Chandrasekhar, A. G. Dentai, E. C. Burrows, G. J. Qua, C. H. Joyner, and C. A. Burrus, "A 5 Gb/s monolithically integrated lightwave transmitter with 1.5 μm multiple quantum well laser and HBT driver circuit," *IEEE Photon. Technol. Lett.*, vol. 3, pp. 928–930, 1991. 47

[109] P. R. Berger, N. K. Dutta, D. L. Sivco, and A. Y. Cho, "GaAs quantum-well laser and heterojunction bipolar-transistor integration using molecular-beam epitaxial regrowth," *Appl. Phys. Lett.*, vol. 59, pp. 2826–2828, 1991. 47

[110] C. Vanhoof, J. Genoe, R. Mertens, G. Borghs, and E. Goovaerts, "Electroluminescence from bipolar resonant tunneling diodes," *Appl. Phys. Lett.*, vol. 60, pp. 77–79, 1992. 47

[111] I. Grave, S. Kan, G. Griffel, S. Wu, A. Saar, and A. Yariv, "Monolithic integration of a resonant tunneling diode and a quantum-well semiconductor-laser," *Appl. Phys. Lett.*, vol. 58, pp. 110–112, 1991. 47

[112] Y. Kawamura, H. Asai, and H. Iwamura, "Fabrication of resonant-tunneling optical bistable laser-diodes," *Electron. Lett.*, vol. 30, pp. 225–227, 1994. 47

[113] J. M. L. Figueiredo, *Optoelectronic properties of Resonant Tunnelling Diodes*. PhD Thesis, Universidade do Porto, 2000. 49

[114] N. V. Alkeev, V. E. Lyubchenko, C. N. Ironside, J. M. L. Figueiredo, and C. R. Stanley, "Super high-frequency characteristics of optical modulators on the basis of InGaAlAs resonance-tunnel heterostructures," *J. Commun. Technol. Electron.*, vol. 45, pp. 911–914, 2000. 50

[115] N. Hassaine, K. Sauv, A. Konczykowska, and R. Lefevre, "Parasitic element influence on laser driver performances for 1.3 μm fiber optical communication," *J. Phys. III*, vol. 3, pp. 1751–1759, 1993. 54

[116] G. W. Roberts and A. S. Sedra, *SPICE*. 2nd ed. Oxford: Oxford University Press, 1997. 55

[117] C. Kidner, I. Mehdi, J. R. East, and G. I. Haddad, "Bias circuit instabilities and their effect on the dc current-voltage characteristics of double-barrier resonant tunneling diodes," *Solid-State Electron.*, vol. 34, pp. 149–156, 1991. 56

[118] E. R. Brown, "Resonant-tunneling transmission-line relaxation oscillator," *in Proc. OSA Ultrafast Elec. and Optoelectron.*, 1993. 56

[119] . Boric-Lubecke, D. S. Pan, and T. Itoh, "RF excitation of an oscillator with several tunneling devices in series," *IEEE Microw. Guided Wave Lett.*, vol. 4, pp. 364–366, 1994. 56

[120] K. Maezawa, Y. Ookawa, S. Kishimoto, T. Mizutani, M. Takakusaki, and H. Nakata, "High-power oscillations in resonant tunneling diode pair oscillator ICs fabricated with metamorphic devices," *Jpn. J. Appl. Phys.*, vol. 46, pp. 2306–2308, 2007. 56

[121] M. R. amd R. Y. Yu, H. Kroemer, M. J. W. Rodwell, S. C. Martin, R. E. Muler, and R. P. Smith, "Bias stabilisation for resonant tunnel diode oscillators," *IEEE Microw. Guided Wave Lett.*, vol. 5, pp. 219–221, 1995. 56

[122] C. Kidner, I. Mehdi, J. R. East, and G. I. Haddad, "Power and stability limitations of resonant tunnelling diodes," *IEEE Trans. Microw. Theory Tech.*, vol. 38, pp. 864–872, 1990. 56, 57

[123] B. Romeira, J. M. L. Figueiredo, T. J. Slight, L. Wang, E. Wasige, C. N. Ironside, J. M. Quintana, and M. J. Avedillo, "Synchronisation and chaos in a laser diode driven by a resonant tunneling diode," *IET Optoelectron.*, vol. 2, pp. 211–215, 2008. 58

[124] E. R. Brown, C. D. Parker, S. Verghese, M. W. Geis, and J. F. Harvey, "Resonant-tunneling transmission-line relaxation oscillator," *Appl. Phys. Lett.*, vol. 70, pp. 2787–2789, 1997. 59, 63

[125] J. Rutman, "Characterization of phase and frequency instabilities in precision frequency sources: Fifteen years of progress," *Proc. IEEE*, vol. 66, pp. 1048–1075, 1978. 65

[126] M. Kahn, J. Lasri, M. Orenstein, D. Ritter, and G. Eisenstein, "Phase-locking of an InP/InGaP/InGaAs resonant tunneling diode relaxation oscillator by direct optical injection," *Solid-State Electron.*, vol. 45, pp. 1827–1830, 2001. 66, 88

[127] C.-L. Yang and Y.-C. Chiang, "Low phase-noise and low-power CMOS VCO constructed in current-reused configuration," *IEEE Microw. Wireless Compon. Lett.*, vol. 18, pp. 136–138, 2008. 66

[128] A. Brannon, J. Breitbarth, and Z. Popovic, "A low-power, low phase noise local oscillator for chip-scale atomic clocks," *Microwave Symposium Digest, 2005 IEEE MTT-S International.* 66

[129] Y. Jeong, S. Choi, and K. Yang, "A sub-100 μw ku-band rtd vco for extremely low power applications," *IEEE Microwave and Wireless Components Letters*, vol. 19, pp. 569–571, 2009. 67

[130] J. N. Blakely, L. Illing, and D. J. Gauthier, "Controlling fast chaos in delay dynamical systems," *Phys. Rev. Lett.*, vol. 92, p. 193901, 2004. 75, 135, 141

[131] P. Guetin, "Interaction between a light beam and a Gunn oscillator near the fundamental edge of GaAs," *J. Appl. Phys.*, vol. 40, pp. 4114–4122, 1969. 77

[132] X. Zhu, X. Jiang, W. Hong, and Y. Chen, "Investigations on optically controlled millimeter wave Gunn oscillators," *Int. J. Infrared Milli.*, vol. 14, pp. 347–354, 1993. 77

[133] P. England, J. E. Golub, L. T. Florez, and J. P. Harbison, "Optical switching in a resonant tunneling structure," *Appl. Phys. Lett.*, vol. 58, pp. 887–889, 1991. 79

[134] T. S. Moise, Y.-C. Kao, L. D. Garrett, and J. C. Campbell, "Optically switched resonant tunneling diodes," *Appl. Phys. Lett.*, vol. 66, pp. 1104–1106, 1995. 79

[135] H. W. Li, B. E. Kardynał, D. J. P. Ellis, A. J. Shields, I. Farrer, and D. A. Ritchie, "Quantum dot resonant tunneling diode single photon detector with aluminum oxide aperture defined tunneling area," *Appl. Phys. Lett.*, vol. 93, p. 153503, 2008. 79

[136] F. Hartmann, L. Gammaitoni, S. Höfling, A. Forchel, and L. Worscheche, "Light-induced stochastic resonance in a nanoscale resonant-tunneling diode," *Appl. Phys. Lett.*, vol. 98, p. 242109, 2011. 79, 141

[137] S. L. Chuang, *Physics of Optoelectronic Devices*. Wiley, 1995. 82

[138] T. C. L. G. Sollner, E. R. Brown, and H. Q. Le, "Microwave and millimeter-wave resonant-tunneling devices," *The Lincoln Laboratory Journal*, vol. 1, pp. 89–105, 1988. 88

[139] T. P. Higgins, J. F. Harvey, D. J. Sturzebecher, A. C. Paolella, and R. A. Lux, "Direct optical frequency modulation and injection locking of resonant tunnel diode oscillator," *Electron. Lett.*, vol. 28, pp. 1574–1576, 1992. 88

[140] J. Lasri and G. Eisenstein, "Phase dynamics of a timing extraction system based on an optically injection-locked self-oscillating bipolar heterojunction phototransistor," *J. Lightwave Technol.*, vol. 20, pp. 1924–1932, 2002. 88

[141] J. Lasri, P. Devgan, R. Tang, and P. Kumar, "Self-starting optoelectronic oscillator for generating ultra-low-jitter high-rate (10 GHz or higher) optical pulses," *Opt. Express*, vol. 11, pp. 1430–1435, 2003.

[142] E. Shumakher and G. Eisenstein, "On the noise properties of injection-locked oscillators," *IEEE Trans. Microw. Theory Tech.*, vol. 52, pp. 1523–1537, 2004. 88

[143] I. J. S. Coelho, J. F. Martins-Filho, J. M. L. Figueiredo, and C. N. Ironside, "Modeling of light-sensitive resonant-tunneling-diode devices," *J. Appl. Phys.*, vol. 95, p. 8258, 2004. 91

[144] H. I. Cantu, B. Romeira, A. E. Kelly, C. N. Ironside, and J. M. L. Figueiredo, "Resonant tunneling diode optoelectronic integrated circuits applications in radio over fiber networks," *IEEE Trans. Microw. Theory Tech.*, vol. 60, pp. 2903–1912, 2012. 105, 106

[145] H. I. Cantu, B. Romeira, K. Seunarine, A. E. Kelly, C. N. Ironside, and J. M. L. Figueiredo, "Conversion of phase modulated signals from optical network to wireless domain using resonant tunneling diode optoelectronic integrated circuits," *The Optical Fiber Communication Conference and Exposition and the National Fiber Optic Engineers Conference (OFC/NFOEC'12), OSA Technical Digest (Optical Society of America, 2012)*, vol. paper JTh2A.19, Los Angeles, CA, USA. 105, 106

[146] R. Hassun, M. Flaherty, R. Matreci, and M.Taylor, "Efffective evaluation of link quality using error vector magnitude techniques," *in Wireless Communications Conference Proceedings.* 105

[147] H. I. Cantu, B. Romeira, A. E. Kelly, C. N. Ironside, and J. M. L. Figueiredo, "Modulation accuracy of binary phase-shift keying signal broadcast after injection locking of a resonant tunnelling diode microwave oscillator," *to be published in Microw. Opt. Techn. Let.* 106

[148] T. Erneux, *Applied delayed differential equations.* Springer Science + Business Media, 2009. 109

[149] K. H. Lee, J. Y. Kim, W. Y. Choi, H. Kamitsuna, M. Ida, and K. Kurishima, "Low-cost optoelectronic self-injection-locked oscillators," *IEEE Photon. Technol. Lett.*, vol. 20, pp. 1151–1153, 2008. 110, 112, 119

[150] L. Maleki, "Sources: The optoelectronic oscillator," *Nature Photon.*, vol. 5, pp. 728–730, 2011. 111

[151] L. V. Wangenheim, "On the Barkhausen and Nyquist stability criteria," *Analog Integr. Circ. S.*, vol. 66, pp. 139–141, 2011. 111

[152] A. Hayat, M. Varon, A. Bacou, A. Rissons, and J.-C. Mollier, "2.49 GHz low phase-noise optoelectronic oscillator using 1.55 μm VCSEL for avionics and aerospace applications," *in Proc. Int. Topical Meeting on Microwave Photonics*, pp. 98–101, 2008. 112, 119

[153] H.-K. Sung, X. Zhao, E. K. Lau, D. Parekh, C. J. Chang-Hasnain, and M. C. Wu, "Optoelectronic oscillators using direct-modulated semiconductor lasers under strong optical injection," *IEEE J. Sel. Topics Quantum Electron.*, vol. 15, pp. 572–577, 2009. 112

[154] W. Liang, V. S. Ilchenko, A. A. Savchenkov, A. B. Matsko, D. Seidel, and L. Maleki, "Whispering-gallery-mode-resonator-based ultranarrow linewidth external-cavity semiconductor laser," *Opt. Lett.*, vol. 35, pp. 2822–2824, 2010. 112, 118

[155] T. M. Fortier, M. S. Kirchner, F. Quinlan, J. Taylor, J. C. Bergquist, T. Rosenband, N. Lemke, A. Ludlow, Y. Jiang, C. W. Oates, and S. A. Diddams, "Generation of ultrastable microwaves via optical frequency division," *Nature Photon.*, vol. 5, pp. 425–429, 2011. 112

[156] S. Verghese, C. D. Parker, and E. R. Brown, "Phase noise of a resonant tunneling relaxation oscillator," *Appl. Phys. Lett.*, vol. 90, pp. 2550–2552, 1998. 112

[157] X. S. Yao and L. Maleki, "Multiloop optoelectronic oscillator," *IEEE J. Quantum Electron.*, vol. 36, pp. 79–84, 2000. 118, 119, 131

[158] J. W. Eaton, *Gnu Octave Manual*. Network Theory Ltd., 2002. 126

[159] *http://www.gnu.org/software/octave/doc/interpreter/Mex_002dFiles.html*. 126

[160] C. W. Gardiner, *Handbook of Stochastic Methods*. Edited by Hermann Haken, Springer-Berlag Berlin Heidelberg, New York, 1985. 126

[161] N. V. Alkeev, V. E. Lyubchenko, C. N. Ironside, J. M. L. Figueiredo, and C. R. Stanley, "Current noise in resonance tunnel diodes based on InGaAlAs heterostructures," *Journal of Communications Technology and Electronics*, vol. 47, pp. 228–231, 2002. 128

[162] A. Przadka, K. J. Webb, D. B. Janes, H. C. Liu, and Z. R. Wasilewski, "Microwave measurement of shot noise in resonant tunneling diodes," *Appl. Phys. Lett.*, vol. 71, pp. 530–532, 1997. 128

[163] G. Iannaccone, G. Lombardi, M. Macucci, and B. Pellegrini, "Enhanced shot noise in resonant tunneling: Theory and experiment," *Phys. Rev. Lett.*, vol. 80, pp. 1054–1057, 1998. 128

[164] A. S. Pikovsky and J. Kurths, "Coherence resonance in a noise-driven excitable system," *Phys. Rev. Lett.*, vol. 78, pp. 775–778, 1997. 135, 141

[165] B. Lindner, J. Garcia-Ojalvo, A. Neiman, and L. Schimansky-Geier, "Effects of noise in excitable systems," *Phys. Rep.*, vol. 392, pp. 321–424, 2004. 135, 141

[166] A. G. Balanov, N. B. Janson, and E. Scholl, "Control of noise-induced oscillations by delayed feedback," *Physica D: Non linear Phenomena*, vol. 199, pp. 1–12, 2004. 135